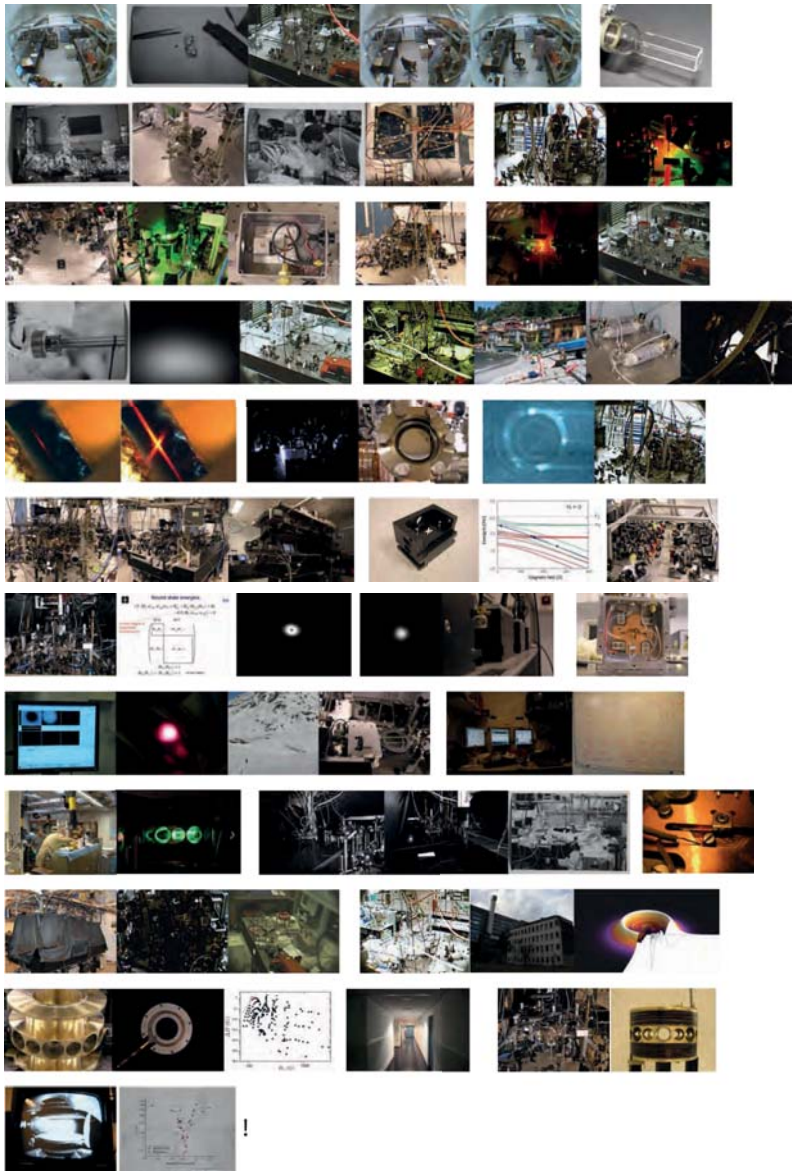

!

Feshbach resonances in ultracold mixtures of fermionic quantum gases

Tobias Tiecke 2009

Feshbach resonances in ultracold mixtures of the fermionic quantum gases ^{6}Li and ^{40}K

Tobias Tiecke

Uitnodiging

Voor het bijwonen van de openbare verdediging van mijn proefschrift, getiteld:

Feshbach resonances in ultracold mixtures of the fermionic quantum gases ^{6}Li and ^{40}K

dinsdag 15 december
om 16:00 uur

In de Agnietenkapel
van de
Universiteit van
Amsterdam
Oudezijds Voorburgwal
231

Na afloop is er een receptie

Paranimfen:
Michelangelo Vargas Rivera
Aaldert van Amerongen

Tobias Tiecke
Utrechtsedwarsstraat 133-2
1017 WE Amsterdam
06-24801430

Feshbach resonances in ultracold mixtures of the fermionic quantum gases ^{6}Li and ^{40}K

ACADEMISCH PROEFSCHRIFT

ter verkrijging van de graad van doctor
aan de Universiteit van Amsterdam
op gezag van de Rector Magnificus
prof. dr. D.C. van den Boom
ten overstaan van een door het college voor promoties ingestelde
commissie, in het openbaar te verdedigen in de Agnietenkapel
op dinsdag 15 december 2009, te 16:00 uur

door

Tobias Gerard Tiecke

geboren te Meyrin, Zwitserland

Promotiecommissie:

Promotor:	prof. dr. J.T.M. Walraven
Overige leden:	prof. dr. J.J. Engelen
	prof. dr. M.S. Golden
	dr. T.W. Hijmans
	dr. S.J.J.M.F. Kokkelmans
	prof. dr. H.B. van Linden van den Heuvell
	prof. dr. C. Salomon
	prof. dr. G.V. Shlyapnikov

Faculteit der Natuurwetenschappen, Wiskunde en Informatica

ISBN: 978-90-9024900-1

Front cover: ^{6}Li and ^{40}K, both at a temperature of 20° C.

The work described in this thesis was carried out
in the group "Quantum Gases & Quantum Information", at the
Van der Waals-Zeeman Instituut of the University of Amsterdam,
Valckenierstraat 65, 1018 XE Amsterdam, The Netherlands,
where a limited number of copies of this thesis is available.
A digital version of this thesis can be downloaded from
`http://www.science.uva.nl/~walraven`
or: `http://dare.uva.nl`
This work is part of the research programme of the
Foundation for Fundamental Research on Matter (FOM),
which is financially supported by the Netherlands Organization
for Scientific Research (NWO).

Contents

1 Introduction **1**
- 1.1 Ultracold gases . . . 1
- 1.2 This thesis . . . 1
- 1.3 Strongly interacting systems . . . 2
- 1.4 Universality . . . 3
- 1.5 Outline . . . 4

2 Theoretical Background **5**
- 2.1 Introduction . . . 5
- 2.2 Cooling of fermions . . . 5
- 2.3 Ultracold scattering . . . 7
  - 2.3.1 Two body hamiltonian . . . 7
  - 2.3.2 Feshbach resonances . . . 11
  - 2.3.3 Ultracold scattering at finite energy . . . 13
  - 2.3.4 Accumulated phase method . . . 14
- 2.4 Trapping of ultracold atoms . . . 17
  - 2.4.1 Optical dipole potentials . . . 17
  - 2.4.2 Magnetic potentials . . . 19
  - 2.4.3 Properties of trapped gases . . . 21

3 Experimental Setup **25**
- 3.1 Introduction . . . 25
- 3.2 Vacuum . . . 26
- 3.3 Laser Systems . . . 30
  - 3.3.1 Potassium . . . 30
  - 3.3.2 Lithium . . . 31
- 3.4 Trapping and Cooling . . . 35
  - 3.4.1 2D MOTs . . . 35
  - 3.4.2 3D MOTs . . . 37
  - 3.4.3 Optically Plugged Magnetic Trap . . . 40
  - 3.4.4 Optical Trapping and Optical Transport . . . 42
- 3.5 Manipulation and Diagnostics . . . 43
  - 3.5.1 Computer Control . . . 43
  - 3.5.2 Radio-frequency and microwave sources . . . 45
  - 3.5.3 Imaging . . . 48
  - 3.5.4 Spin state preparation and purification . . . 50
  - 3.5.5 Feshbach Coils . . . 55

3.6 Ultracold Fermionic Mixtures . . . 60
3.6.1 Quantum degenerate ^{40}K spin mixture . . . 60
3.6.2 Ultracold ^{6}Li-^{40}K mixture . . . 62

4 Lithium 2D MOT 67
4.1 Introduction . . . 67
4.2 Experimental . . . 69
4.2.1 Vacuum system . . . 69
4.2.2 Lithium oven . . . 69
4.2.3 The 2D MOT configuration . . . 71
4.2.4 Hyperfine structure of ^{6}Li levels . . . 71
4.2.5 Laser system . . . 72
4.3 Source model . . . 73
4.3.1 Oven flux . . . 73
4.3.2 Capture and cooling . . . 73
4.4 Experimental results . . . 75
4.4.1 Oven flux . . . 75
4.4.2 Fluorescence detection - TOF distribution . . . 77
4.4.3 Beam flux - dependence on push beam . . . 79
4.4.4 Beam flux - dependence on 2D MOT . . . 81
4.4.5 Beam flux - dependence on oven temperature . . . 81
4.5 Discussion . . . 82
4.5.1 Recapture in the 3D MOT . . . 82
4.5.2 Loss mechanisms . . . 84
4.5.3 Comparison with Zeeman slowers . . . 86
4.6 Summary and conclusion . . . 86

5 Asymptotic Bound-state Model 89
5.1 Introduction . . . 89
5.2 Asymptotic Bound-state Model . . . 90
5.2.1 Internal energy . . . 91
5.2.2 Relative Hamiltonian . . . 91
5.2.3 Free parameters . . . 93
5.2.4 Asymptotic bound states . . . 94
5.3 Application to various systems . . . 95
5.3.1 ^{6}Li–^{40}K . . . 95
5.3.2 ^{40}K-^{87}Rb . . . 97
5.3.3 ^{3}He* - ^{4}He* . . . 97
5.4 Coupling to the open channel . . . 98
5.4.1 Tailored Feshbach theory . . . 99
5.4.2 The dressed Asymptotic Bound state Model . . . 102
5.5 Summary and Conclusion . . . 103

6 Feshbach resonances in Li-K 105
6.1 Introduction . . . 105
6.2 Experimental procedure . . . 106
6.3 Extended ABM . . . 107

6.4 Feshbach resonance width measurement 108
6.5 Conclusion 111

A Potassium Properties **113**
A.1 Introduction 113
A.2 General Properties 113
A.3 Optical properties 115
A.4 Fine structure, Hyperfine structure and the Zeeman effect 117
A.5 Scattering properties 120

B Li-K properties **123**
B.1 General properties 123
B.2 Feshbach resonances 124

Summary **145**

Samenvatting **147**

Acknowledgments **149**

List of Publications **153**

Chapter 1
Introduction

1.1 Ultracold gases

During the past decades the field of ultracold gases has experienced a tremendous growth. The large interest in ultracold gases comes from the fact that when a gas is cooled to a temperature close to zero the quantum nature of the atomic motion starts to play a dominant role. This is quantified by the size of an atomic wavepacket, given by the thermal de Broglie wavelength, becoming of the order of the interparticle spacing. When these two length scales are comparable the wavefunction of neighboring particles overlap and the system has to be described by many-body wavefunctions. For bosonic atoms (atoms with integer spin) the appearance of the quantum nature is associated with the occurrence of Bose-Einstein Condensation (BEC). For fermionic atoms (atoms with half-integer spin) the appearance of the quantum nature is not associated with a phase-transition but with a gradual suppression of atoms occupying low energy states due to the phenomenon of Pauli-blocking. Initially the studies of ultracold gases were mainly aimed towards bosonic systems due to the possibility to achieve Bose-Einstein Condensation. The first theoretical prediction for a quantum gas was for the groundstate of spin-polarized hydrogen [1, 2]. By means of quantum Monte-Carlo calculations it was shown that spin-polarized hydrogen was expected to remain a gas even at 0 K. This prediction was confirmed in 1980 by stabilizing spin-polarized hydrogen [3]. However, the achievement of Bose-Einstein Condensation was realized in the alkali-metals rubidium [4] and sodium [5] in 1995.
The field of ultracold fermionic gases naturally emerged out of the research performed on ultracold bosonic gases. Shortly after spin-polarized hydrogen was stabilized, the fermionic gas of spin-polarized deuterium was also stabilized in 1980 [6]. Quantum degeneracy in an ultracold fermionic gas was achieved in 1999 with the alkali-metal potassium [7]. The realization of fermi-degeneracy has shown to be the starting point for many fascinating experiments on fermionic systems. In recent years ultracold fermionic gases have shown to exhibit remarkable unexpected phenomena. In particular the stability of fermionic systems for strong interaction [8, 9] was unexpected and has led to the possibility to use ultracold gases to study strongly-interacting fermionic systems.
The realization of a strongly-interacting fermionic system was achieved by tuning the interaction strength using a so-called Feshbach resonance. This phenomenon was first pointed out in the context of ultracold gases in 1976 [10], observed in 1986 [11] and theoretically described in the beginning of the 90's [12, 13]. The spectacular possibilities in the field of fermionic quantum gases were only realized in 2003 with the observation of long lived molecules consisting of two fermionic atoms [8, 14].

1.2 This thesis

This thesis project, to study a system of heteronuclear mass-imbalanced Fermi gases, was started shortly after the discovery of the strongly interacting homonuclear Fermi gas. At

that time very little was known about the properties of a mixture of ^{6}Li and ^{40}K. Only few theoretical studies had been performed and from the experimental point of view it was unclear if the mixture could be cooled to degeneracy. Additionally, it had become clear that Feshbach resonances are essential to study ultracold fermionic gases. However, for the ^{6}Li-^{40}K system it was unknown what the Feshbach resonance structure was and if there was a Feshbach resonance suitable to perform studies on a strongly-interacting system of ^{6}Li-^{40}K. At that time quantum degenerate gases of only ^{6}Li and ^{40}K had been realized. Additionally, ^{6}Li and ^{40}K are the only two stable fermionic alkali atoms, which allows relatively easy laser-cooling. Therefore, the obvious system to realize a mass-imbalanced heteronuclear Fermi-Fermi system was the ^{6}Li-^{40}K mixture.
This thesis describes the experimental realization of the ultracold ^{6}Li-^{40}K system and pioneering experiments on the scattering properties. A priori it was unknown if it would be possible to realize an ultracold mixture of ^{6}Li and ^{40}K, and this thesis describes the approach we have taken. From the experimental side four major developments are presented. First, the development of a novel source for cold ^{6}Li is presented. It was expected the principle of a two-dimensional magneto-optical trap (2D MOT) would not work efficiently for a light atom as ^{6}Li. The source has proven to generate a high-flux cold beam, comparable to the common solution of a Zeeman slower. Second, an optically plugged magnetic trap has been realized. Prior to this thesis it had only been realized for sodium [5, 15] and it was not expected to work for a light atom like ^{6}Li. Third, the sympathetic cooling of lithium ^{6}Li by a large bath of multiple spin states of ^{40}K has been demonstrated. Fourth, the optical transport of an ultracold sample. This had previously been realized [16], however it was considered to be an involved and unstable approach. The reasons why our approach has turned out to work easily and reliably are explained in Sect. 3.4.4. From the theoretical side a model has been developed allowing to completely map the Feshbach resonance structure in any system. The model has been applied to ^{6}Li-^{40}K to theoretically assign observed loss features [17] and to find the resonance most suitable to study the strongly-interacting mixture [18]. This resonance is experimentally characterized, which allows to define experimental conditions for studying strongly interacting ^{6}Li-^{40}K.
During the coarse of this thesis the topic of fermionic mixtures with a mass imbalance has tremendously gained in interest. Two other experiments on ^{6}Li-^{40}K were started nearly simultaneously in Munich and Innsbruck and at the moment of writing two more are being set up at the ENS in Paris and at MIT in Boston. From the theoretical side a vast number of publications have appeared on unequal mass fermionic systems (see e.g. Ref. [19, 20, 21, 22, 23, 24, 25, 26, 27, 28, 29, 30] and references therin), many of them assume a Feshbach resonance broad enough to exhibit universal behavior. By using the Feshbach resonance presented in this thesis many of these theories can be tested.

1.3 Strongly interacting systems

A key topic of present-day physics is the understanding of strongly interacting systems. Many fascinating phenomena observed in nature appear to find their origin in strongly interacting systems. These systems range from the fields of condensed-matter to high-energy physics. For example the phenomena of high-temperature superconductivity [31] and nuclear matter [32] are systems where strongly interacting fermions play a key role. However, the theoretical understanding of these phenomena is not complete. In the study

of strongly-interacting fermions, the field of ultracold gases has come to play a special role. Not only does it provide an elegant way to study fundamental aspects of quantum mechanics, but it has also proven to be a powerful tool to simulate other quantum systems. The extraordinary degree of tunability of the confining potential and interaction strength are key features of quantum gases which allow to accurately model quantum many-body systems. In particular the realization of a stable strongly-interacting fermionic system [33, 8] provided the possibility to draw analogies to other strongly interacting systems.
An ultracold gas is not by definition strongly interacting. However, due to the ability to change the interaction strength it can be tuned to become strongly interacting. Already in 1992 [12], before the realization of the first BEC, it was realized that the two-body interaction parameter, the scattering length a, could be modified in favor of the experiment by an external magnetic field. The theory used to describe these resonant phenomena [13] is strongly based on Feshbach's theory describing nuclear reactions [34, 35], hence these resonances are called *Feshbach resonances*. The application of Feshbach resonances in ultracold atom experiments has allowed to create and study strongly interacting fermionic systems with very large versatility. The interaction strength can be changed *in-situ,* therefore the interaction can be tuned to be attractive, repulsive, non-interacting or strongly interacting in a continuous manner *during* the coarse of an experiment. There are two other realizations of strongly-interacting systems. First, reduced dimensionality can enhance the effect of interactions leading to strongly correlated quantum system, in particular the Tonks-Girardeau [36, 37] gas is an example of such a system. Second, the use of optical lattices in ultracold gases [38] provide the possibility to achieve a strongly correlated system in the form of Mott insulator. In this thesis we will discuss only strongly interacting systems related to Feshbach resonances.
For a long time the work on ultracold fermionic gases has been limited to homonuclear systems. Quantum degeneracy has been achieved for four different fermionic elements: ^{3}He* [39], ^{6}Li [40, 41], ^{40}K [7] and ^{173}Yb [42]. The addition of a second fermionic element to create a fermionic heteronuclear system tremendously enriches the system and adds more degrees of tunability. In particular a mass-imbalance between two species allows to mimic a whole new class of quantum systems. For example, the ^{6}Li-^{40}K system is expected to exhibit long-lived p-wave trimers [30]. Furthermore, exotic forms of superfluidity are expected due to interaction between ^{40}K atoms mediated by ^{6}Li atoms. Another prospect for this system is to create ground state molecules [43, 44]. These molecules will be bosonic and exhibit a large dipole-moment [45, 46]. Finally, a novel analogy to condensed matter systems can be made by applying a lattice potential selectively to one species and have the other move freely through the artificially created crystal. These few examples of novel quantum systems illustrate the richness of studies which can be performed using the ^{6}Li-^{40}K system.

1.4 Universality

In order to use ultracold gases to model strongly-interacting fermions, it is required that experiments can be generalized to a generic system of strongly-interacting fermions. If a system of ultracold fermions is prepared as such, it is called to exhibit *universal behavior.* This implies that the behavior of the system is determined entirely by the fermionic nature of the particles and their interaction strength. The possibility of achieving universal

behavior with ultracold fermions strongly depends on the properties of the Feshbach resonance used to tune the interaction. For ultracold fermions universal behavior has only been achieved in spin mixtures of ^{6}Li or spin mixtures of ^{40}K. Both atomic species exhibit Feshbach resonances with properties favorable to achieve universal behavior, i.e. the resonances are strong.
Knowledge about Feshbach resonances is thus of great importance to be able to study universal behavior. However, for any system other than hydrogen the potentials describing the interaction between two atoms cannot be calculated a-priori with sufficient accuracy to predict Feshbach resonances. Therefore, without experimental input it is unknown if universal behavior can be achieved in a certain system. For the homonuclear systems of ^{6}Li and ^{40}K the scattering properties have been studied in great detail [47, 48, 49, 50]. At the start of this project the Feshbach resonance structure of a heteronuclear mixture of ^{6}Li and ^{40}K was unknown. A careful study of the resonances occurring in the ^{6}Li-^{40}K system is presented in this thesis. We show that the ^{6}Li-^{40}K system exhibits Feshbach resonances suitable to study universal behavior in a mass-imbalanced fermionic mixture.

1.5 Outline

This thesis describes the study of Feshbach resonances in the ^{6}Li-^{40}K mixture both from the experimental and theoretical point of view. Chapter 2 provides a brief summary of theoretical concepts used throughout this thesis. However, the largest part of the research for this thesis consists of the development of a state-of-the-art machine to study an ultracold mixture ^{6}Li with ^{40}K, which is presented in Chapter 3. In addition to the technical aspects and novel approaches as have been discussed above, the realization of a quantum degenerate spin mixture of ^{40}K and an ultracold mixture of ^{6}Li and ^{40}K are described. A significant innovation in the techniques used for ultracold gases is performed by developing the first 2D MOT source for lithium. It is presented in Chapter 4, and it yields a very large cold flux of ^{6}Li atoms. On the theoretical side a computationally simple, intuitive model has been developed to accurately describe all Feshbach resonance positions and widths in a system. The model is presented in Chapter 5. Using this model all possible Feshbach resonances of the ^{6}Li-^{40}K system are examined and the resonance most suitable to study universal behavior is selected. Furthermore, all these efforts have been combined in Chapter 6 by experimentally characterizing the selected resonance. These results show that the ^{6}Li-^{40}K systems can be used to realize a strongly interacting Fermi-Fermi mixture in the universal limit, opening a wide area of research for studying mass-imbalanced Fermi-Fermi systems.

Chapter 2
Theoretical Background

2.1 Introduction

This chapter provides a background of the theoretical concepts used in this thesis. This chapter is by no means a review of the discussed subjects, it is rather a description of the different approaches as compared to common treatments, a description of the approximations which have been made and an introduction of notations. The field of ultracold gases is tremendously active and many up-to-date reviews are available, covering a very large part of the field. Here I will summarize some of the review articles which have shown to be very useful. An extensive description of optical trapping is given in Ref. [51] and for magnetic trapping in Ref. [52, 53, 54, 55]. Evaporative cooling, in particular in magnetic traps, is described in Ref. [56, 57] and the description of trapped ultracold Fermi gases is well covered in Ref. [58, 59]. Basic experimental techniques for experiments on ultracold gases can be found in [55, 60, 61, 58]. An extensive description of Feshbach resonances is given in Ref. [62], and in particular the square well problem, which offers a very good insight in the basic properties of Feshbach resonances, is discussed in various places [63, 58, 64]. Finally, many PhD theses offering very detailed descriptions of ultracold gases experiments have been written, see e.g. [65, 66, 67]
Three aspects of the theoretical background for this thesis require a bit of extra attention. First, the quantum statistics of particles are of great importance in experiments with ultracold gases, this will be addressed in Sect. 2.2. Second, the experimental and theoretical results presented in this thesis are in many aspects based on ultracold scattering theory. In Sect. 2.3 a brief description of ultracold scattering and in particular resonant scattering is given. Third, both magnetic and optical traps are used in the experiments presented in this thesis. A clear introduction on what assumptions are made to analyze and model the trapping is given in Sect. 2.4.

2.2 Cooling of fermions

Experiments with ultracold fermionic gases are in many aspects similar to experiments with ultracold bosonic gases, however there are a few distinct differences. For two indistinguishable particles the wavefunction describing both particles $\psi(\mathbf{r}_1, \mathbf{r}_2)$ can be constructed from the two single-particle wavefunctions $\psi_1(\mathbf{r}_1)$ and $\psi_2(\mathbf{r}_2)$ in two manners

$$\psi_{\pm}(\mathbf{r}_1, \mathbf{r}_2) = C\left[\psi_1(\mathbf{r}_1)\psi_2(\mathbf{r}_2) \pm \psi_1(\mathbf{r}_2)\psi_2(\mathbf{r}_1)\right]$$

where C is a normalization factor. The $+$ sign yields a two-particle wavefunction which is symmetric under exchange of particle 1 and 2 and the $-$ sign yield an anti-symmetric wavefunction under exchange of the two particles. The former type of particles are called *bosons* and the latter *fermions*. The anti-symmetry of the fermionic wavefunction is called the *Pauli exclusion principle* and implies that two fermions cannot occupy the same internal state $\psi_1 = \psi_2$, because $\psi_-(\mathbf{r}_1, \mathbf{r}_2) = C\left[\psi_1(\mathbf{r}_1)\psi_1(\mathbf{r}_2) - \psi_1(\mathbf{r}_2)\psi_1(\mathbf{r}_1)\right] = 0$.

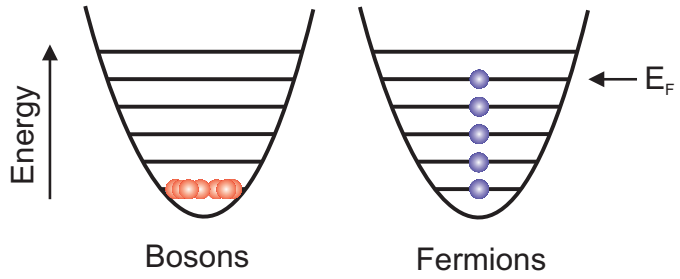

Figure 2.1: The different behavior of bosons and fermions at zero temperature: bosons pile up in the ground state, and fermions fill up all states up to the Fermi energy E_F.

Additionally, two fermions cannot be at the same spatial position $\mathbf{r}_1 = \mathbf{r}_2$, since $\psi_-(\mathbf{r}_1, \mathbf{r}_1) = C\left[\psi_1(\mathbf{r}_1)\psi_2(\mathbf{r}_1) - \psi_1(\mathbf{r}_1)\psi_2(\mathbf{r}_1)\right] = 0$. These two properties of fermions have dramatic consequences for experiments with ultracold atoms. The first aspect concerning the internal states is depicted in Fig. 2.1 for both types of particles in a harmonic trap. For $T = 0$ the bosons pile up in the ground state resulting in a macroscopic occupation of the ground state, a so-called *Bose-Einstein condensate*. The fermions cannot occupy the same state, therefore they will fill up each state up to a certain energy referred to as the *Fermi-Energy* E_F.

The second property of fermions, that they cannot exist at the same spatial position $\mathbf{r}_1 = \mathbf{r}_2$ has different consequences. The wavefunction of the two bosons is symmetric under exchange of the two particles, therefore, the total probability density $|\psi_+(\mathbf{r}_1, \mathbf{r}_2)|^2$ has a finite value for $\mathbf{r}_1 = \mathbf{r}_2$. The fermionic two particle wavefunction has to be anti-symmetric under exchange of the particles, resulting in the fact that the total probability density $|\psi_-(\mathbf{r}_1, \mathbf{r}_2)|^2$ will vanish for $\mathbf{r}_1 = \mathbf{r}_2$. This has the important consequence that two indistinguishable fermions will not collide for $T \to 0$.

To achieve quantum degeneracy in ultracold gases only one method has been demonstrated to be successful, namely, evaporative cooling [56, 57]. To achieve an increase in phase-space density by means of evaporative cooling, rethermalizing collisions are essential down to $T \to 0$. Three fundamentally different pre-cooling steps have been successfully employed to achieve ultracold samples, laser-cooling [4], cooling by contact with a cryogenic surface [68] and very recently buffer gas cooling [69]. However, the final step to achieve quantum degeneracy has always been evaporative cooling, therefore collisions are essential for ultracold gases experiments. This has an important consequence for experiments with fermionic gases, namely, that at least *two* distinguishable species are required to obtain rethermalizing collisions and allow to perform evaporative cooling.

The second species next to the fermion can be another internal (spin)state of the same atomic species, a different bosonic species, or a different fermionic species. The first quantum degenerate Fermi gas was obtained by a spin mixture of two internal hyperfine states of ^{40}K [7]. Surprisingly, this method was proven to be very efficient, however, this approach has never been repeated until this thesis project. In the past decade many other combinations of species have been used to cool fermions to quantum degeneracy. Cooling by means of rethermalization with a boson has been used to achieve quantum degeneracy in ^{6}Li by cooling with ^{7}Li [40, 41], ^{23}Na [70] or ^{87}Rb [71], for degeneracy in ^{40}K by cooling with ^{87}Rb [72], and for degeneracy in ^{3}He* by cooling with ^{4}He* [39] and for ^{173}Yb by cooling with ^{174}Yb [73]. The method using a homonuclear spin mixture to assure rether-

malizing collisions has been used for ^{40}K in two spin states [7], for ^{6}Li in two spin states [74] and for ^{173}Yb in six spin states [42].
Cooling fermionic atoms to quantum degeneracy by rethermalizing collisions with other fermions had not been performed prior to this thesis. Very recently in experiments performed in Innsbruck, simultaneous to the experiments presented in this thesis, quantum degeneracy has been achieved in ^{40}K by cooling with two spin states of ^{6}Li [75]. In this thesis the first results on cooling ^{6}Li by rethermalizing collisions with a ^{40}K spin-mixture are presented. The Fermi-Fermi mixture is cooled close to quantum degeneracy limited by technical aspects of the optical dipole trap. Cooling of two different fermionic species both in a single spin state by means of forced evaporation on both species has not been achieved at the moment this thesis is being written.
The cooling of ^{6}Li with ^{40}K or vice-versa has an additional problem of the mass-imbalance between the two species. To achieve rethermalization of a sample, not only collisions are required, but also momentum transfer has to occur. If the mass imbalance is very large, many collisions are required to achieve rethermalization. It can be easily shown [64] that for two particles with mass m_1 and m_2 the thermalization time τ_{th} is related to the collision rate τ_c^{-1} by

$$\tau_{th}^{-1} = \frac{\xi}{2(\gamma + 3/2)} \tau_c^{-1}$$

where $\xi = 4m_1m_2/(m_1 + m_2)^2$ is the mass-imbalance factor and γ is the trap parameter, $\gamma = 3/2$ for a harmonic trap and $\gamma = 3$ for a linear trap. For the ^{6}Li-^{40}K system $\xi \simeq 0.455$ therefore rethermalization of the ^{6}Li-^{40}K mixture takes about twice as long compared to a homonuclear system only due to the effect of the mass difference.

2.3 Ultracold scattering

Atomic scattering theory has been treated extensively in literature, see e.g. [76, 64]. In this section we will summarize the background required for Chapters 5 and 6. We will start in Sect. 2.3.1 with the Hamiltonian describing two body scattering. Subsequently, we will treat resonance scattering at $T = 0$ (Sect. 2.3.2) and at finite temperature (Sect 2.3.3). We will conclude the chapter with a brief description of the accumulated phase method in Sect. 2.3.4.

2.3.1 Two body hamiltonian

The two-body Hamiltonian of two interacting atoms can be written as:

$$\mathbf{H} = \mathbf{H}^{\mathrm{rel}} + \mathbf{H}^{\mathrm{int}},$$

where $\mathbf{H}^{\mathrm{rel}}$ is the Hamiltonian of the relative motion and $\mathbf{H}^{\mathrm{int}}$ is the internal energy of the two atoms, given by

$$\mathbf{H}^{\mathrm{rel}} = \frac{\mathbf{p}^2}{2\mu} + \mathbf{V}, \tag{2.1}$$

$$\mathbf{H}^{\mathrm{int}} = \mathbf{H}_{\alpha}^{\mathrm{hf}} + \mathbf{H}_{\beta}^{\mathrm{hf}} \tag{2.2}$$

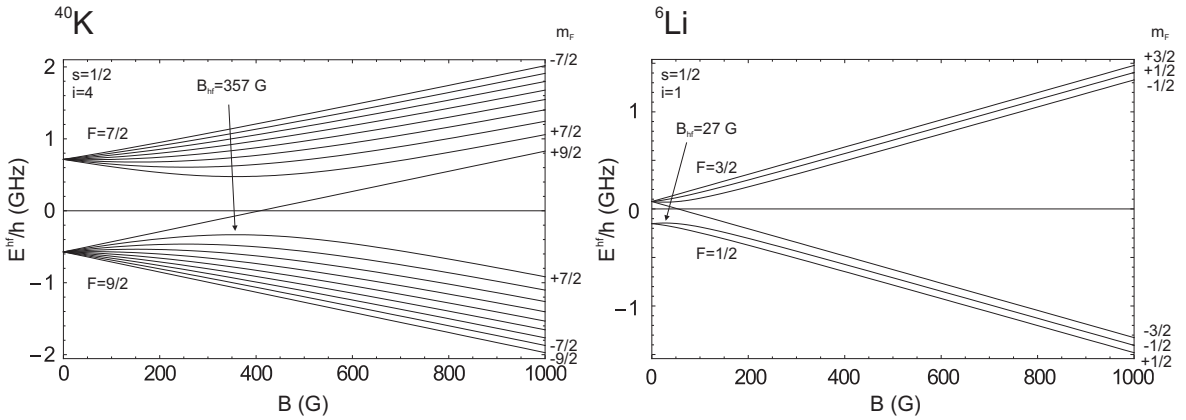

Figure 2.2: The single atom hyperfine energies as a function of the magnetic field B for the electronic groundstates of ^{6}Li and ^{40}K. The states are labeled with their zero-field quantum numbers $|fm_f\rangle$. Note the inverted hyperfine structure for ^{40}K and the relatively small hypefine field B_{hf} of ^{6}Li.

where $\mathbf{p}^2/2\mu$ is the relative kinetic energy operator, $\mathbf{V}$ is the effective interaction among the atoms, and $\mathbf{H}^{\rm hf}_\alpha$ and $\mathbf{H}^{\rm hf}_\beta$ are the single-atom hyperfine hamiltonian for both atoms, labelled with α and β. The single-atom internal Hamiltonian is given by the sum of the hyperfine interaction and the Zeeman interaction

$$\mathbf{H}^{\rm hf} = \frac{a^{hf}}{\hbar^2}\mathbf{i}\cdot\mathbf{s} + (\gamma_e\mathbf{s} - \gamma_i\mathbf{i})\cdot\mathbf{B}, \tag{2.3}$$

where a^{hf} is the hyperfine constant, $\gamma_e \equiv g_s\mu_B/\hbar$ and $\gamma_i \equiv g_i\mu_B/\hbar$[1] are the electronic and nuclear gyromagnetic factors, $\mathbf{B}$ is the magnetic field and $\mathbf{i}$ and $\mathbf{s}$ are the nuclear and electronic spin operators with the respective quantum numbers m_i and m_s. The hyperfine structure of the ground state of ^{6}Li and ^{40}K play a central role throughout this thesis. In Fig. 2.2 the eigenvalues E^{hf} of Eq. 2.3 are plotted as a function of the magnetic field dependence of the various hyperfine states of ^{6}Li and ^{40}K. Both atoms have an electron spin of $s = 1/2$, ^{6}Li has a nuclear spin of $i = 1$ and ^{40}K has a nuclear spin of $i = 4$ (see Appendix A for more details on potassium). The hyperfine constants for ^{6}Li and ^{40}K are $a^{hf}_{Li}/h = 152.1368407(20)$ MHz and $a^{hf}_K/h = -285.7308(24)$ MHz respectively [77]. The states are labeled with the low-field quantum numbers $|fm_f\rangle$ where $\mathbf{f} = \mathbf{i} + \mathbf{s}$ is the total spin operator with the corresponding quantum numbers f and m_f. Note that for finite magnetic field $\mathbf{H}^{\rm hf}$ is not diagonal in the $|fm_f\rangle$ basis.

Relative Hamiltonian

The Hamiltonian of the relative motion, given by Eq. 2.1, describes the interaction of two particles with an effective interaction $\mathbf{V}$ and a relative kinetic energy $p^2/2m$. The effective interaction $\mathbf{V}$ can be written as the central Coulomb interaction $V^{cen}(r)$ of the two atoms, where r is the internuclear distance. The central interaction is a function of

[1] Note that the common reference for g_i, Ref. [77], uses a different sign convention. We use the convention [78] where the magnetic moment is parallel to the nuclear spin: $\boldsymbol{\mu}$=$g_i\mu_B\mathbf{i}$, i.e. g_i of the proton and ^{6}Li is positive and g_i of ^{40}K is negative.

the internuclear distance and depends on the total spin $\mathbf{S} = \mathbf{s}_\alpha + \mathbf{s}_\beta$. It can be decomposed as

$$V^{cen}(r) = \sum_S |S\rangle V_S(r) \langle S| \tag{2.4}$$

where $V_S(r)$ is the interaction potential for total electron spin quantum number S. For spin 1/2 atoms the total electron spin has a singlet ($S = 0$) or triplet ($S = 1$) symmetry. The singlet and triplet potentials are then given by $V_s(r)$ and $V_t(r)$ respectively and Eq. 2.4 can be rewritten as:

$$V^{cen}(r) = V_D(r) + J(r)\mathbf{s}_\alpha \cdot \mathbf{s}_\beta \tag{2.5}$$

where $V_D(r) = \frac{1}{4}(V_s(r) + 3V_t(r))$ is called the *direct* interaction and $J(r) = V_t(r) - V_s(r)$ the *exchange* interaction. Asymptotically $V_D(r)$ corresponds to the van der Waals tail[2]:

$$V_D(r) = -\frac{C_6}{r^6} \tag{2.6}$$

The characteristic length of this potential can be expressed in the so called van der Waals range

$$r_0 = \frac{1}{2}\left(\frac{2\mu C_6}{\hbar^2}\right)^{1/4} \tag{2.7}$$

The exchange term in Eq. 2.5 can be well described by [79]

$$J(r) = J(\gamma_\alpha, \gamma_\beta, r) r^{\frac{2}{\gamma_\alpha} + \frac{2}{\gamma_\beta} - \frac{1}{\gamma_\alpha + \gamma_\beta} - 1} e^{-(\gamma_\alpha + \gamma_\beta)r} \tag{2.8}$$

where $-\gamma_\alpha^2/2$ and $-\gamma_\beta^2/2$ are the ionization energies of both atoms and $J(\gamma_\alpha, \gamma_\beta, r)$ is a normalization function, which reduces to a constant for homonuclear systems, ($\gamma_\alpha = \gamma_\beta$). For heteronuclear systems, $\gamma_\alpha \neq \gamma_\beta$, a parameterization of $J(\gamma_\alpha, \gamma_\beta, r)$ can be found in Ref. [79], the values for the LiK system are given in Appendix B. Knowledge about the energy scales of the direct and exchange interactions are required to perform accumulated-phase calculations as described below in Sect. 2.3.4.

Scattering in a central potential The elastic scattering properties can be obtained by solving the one-dimensional radial Schrödinger equation [80]

$$\left[\frac{\hbar^2}{2\mu}\left(\frac{\partial^2}{\partial r^2} + \frac{2}{r}\frac{\partial}{\partial r}\right) + V_S^l(r)\right] R(r) = E R(r) \tag{2.9}$$

where $V_S^l(r) = V_S(r) + \hbar^2 l(l+1)/2\mu r^2$ and correspondingly, $V_S^0(r) = V_S(r)$. For $E < 0$ the solutions correspond to the vibrational levels of the $V_S^l(r)$ potential and for $E \downarrow 0$ and $l = 0$ the influence of the scattering potential $V_S(r)$ on the scattered wavefunction at $r \to \infty$ can be expressed in the so-called s-wave phase-shift η_0 [76]. This phase shift is related to the s-wave scattering length a by

$$a = -\lim_{k \to 0} \frac{\tan \eta_0}{k} \tag{2.10}$$

[2]For a more accurate description of the direct term Eq. 2.6 can be easily extended with the $-C_8/r^8$ and $-C_{10}/r^{10}$ dispersive terms.

We define a_s and a_t as the s-wave scattering lengths for the $V_0(r)$ and $V_1(r)$ potentials. In the case of resonant scattering ($\eta_0 \to \pi/2$) the scattering length diverges, this is referred to as a potential resonance due to the resonance being induced by the scattering potential $V^{cen}(r)$.

Internal Hamiltonian

The internal Hamiltonian, given by Eq. 2.2, can be rewritten in a more convenient form

$$\mathbf{H}^{\text{int}} = \mathbf{H}_\alpha^{\text{hf}} + \mathbf{H}_\beta^{\text{hf}} \equiv \mathbf{H}_+^{\text{int}} + \mathbf{H}_-^{\text{int}}$$

where

$$\begin{aligned}\mathbf{H}_+^{\text{int}} &= \frac{1}{2\hbar^2}(a_\alpha^{hf}\mathbf{i}_\alpha + a_\beta^{hf}\mathbf{i}_\beta)\cdot\mathbf{S} + (\gamma_e\mathbf{S} - \gamma_{i,\alpha}\mathbf{i}_\alpha - \gamma_{i,\beta}\mathbf{i}_\beta)\cdot\mathbf{B}\\ \mathbf{H}_-^{\text{int}} &= \frac{1}{2\hbar^2}(a_\alpha^{hf}\mathbf{i}_\alpha - a_\beta^{hf}\mathbf{i}_\beta)\cdot(\mathbf{s}_\alpha - \mathbf{s}_\beta)\end{aligned}$$

where $\mathbf{H}_+^{\text{int}} (= \mathbf{H}_+^{\text{hf}}$ for $\mathbf{B} = 0)$ contains all terms which conserve the total electron spin and $\mathbf{H}_-^{\text{int}} (\equiv \mathbf{H}_-^{\text{hf}})$ gives rise to the coupling between different S, additionally we have set $\gamma_{e,\alpha} = \gamma_{e,\beta} \equiv \gamma_e$. We define the total spin of the two-body system as $\mathbf{F} = \mathbf{S} + \mathbf{i}_\alpha + \mathbf{i}_\beta$. For distinguishable atomic species the nuclear spin does not need to be symmetrized and we take the basis $|SM_S i_\alpha \mu_\alpha i_\beta \mu_\beta\rangle = |SM_S \mu_\alpha \mu_\beta\rangle$, where we omit the total nuclear spin i_α and i_β of both atoms to simplify the notation. For indistinguishable atoms one has to define the total nuclear spin $\mathbf{I} = \mathbf{i}_\alpha + \mathbf{i}_\beta$ with its associated quantum number I and projection M_I, allowing to use the symmetrized basis $|SM_S I M_I\rangle$. We have neglected dipole-dipole coupling and second-order spin-orbit interaction, therefore, the relative Hamiltonian $\mathbf{H}^{\text{rel}}$ conserves the total spin and only acts on the spatial part of the wavefunction. In contrast, $\mathbf{H}^{\text{int}}$ only acts on the spin states and not on the spatial wavefunction.

Inelastic Scattering

The relative Hamiltonian (Eq. 2.1) conserves the total spin $\mathbf{F}$ and its projection M_F. However, the exchange term of the central interaction (Eq. 2.5), $\mathbf{s}_\alpha \cdot \mathbf{s}_\beta$, couples the electron spins of both atoms and can couple different hyperfine states while conserving the total electron spin $\mathbf{S}$. These collisions, which change the hyperfine state of a colliding atom pair, are called *spin-exchange collisions*. Only certain combinations of hyperfine channels are allowed due to conservation of total angular momentum and energy. For spin 1/2 atoms we can rewrite the exchange term of Eq. 2.5 as

$$\mathbf{s}_\alpha \cdot \mathbf{s}_\beta = \frac{1}{2}\left(\mathbf{S}^2 - \mathbf{s}_\alpha^2 - \mathbf{s}_\beta^2\right) = \frac{1}{2}\mathbf{S}^2 - \frac{3}{4} \tag{2.11}$$

The spin-exchange rate K_2 of a certain inelastic collision channel is given by [60]

$$K_2 = 4\pi(a_t - a_s)^2 v_f |\langle f'_\alpha m'_{f,\alpha} f'_\beta m'_{f,\beta}|\mathbf{s}_\alpha \cdot \mathbf{s}_\beta| f_\alpha m_{f,\alpha} f_\beta m_{f,\beta}\rangle|^2 \tag{2.12}$$

where $|f_\alpha m_{f,\alpha} f_\beta m_{f,\beta}\rangle$ and $|f'_\alpha m'_{f,\alpha} f'_\beta m'_{f,\beta}\rangle$ are the initial and final hyperfine states respectively and v_f is the relative velocity of the two atoms in the final state, given by

$$v_f = \sqrt{\frac{2}{\mu}\left(E_{kin} + E_\alpha^{hf} + E_\beta^{hf} - E_\alpha^{hf\prime} - E_\beta^{hf\prime}\right)}.$$

Here E_α^{hf} and E_β^{hf} are the hyperfine energies of the initial states with kinetic energy E_{kin} and $E_\alpha^{hf\prime}$ and $E_\beta^{hf\prime}$ are the hyperfine energies of the final states. Note that the hyperfine energies depend on the magnetic field value. The value of v_f reflects the amount of phase-space available for the final scattering states: a large energy difference between the initial and final state will result in a large inelastic collision rate. To obtain a numerical value for the spin-exchange rate for a certain magnetic field B and temperature T (see Sect. 3.6) we perform a basis transformation from the $|f_\alpha m_{f_\alpha} f_\beta m_{f_\beta}\rangle$ basis to the total spin basis $|Sm_S\mu_\alpha\mu_\beta\rangle$, this allows us to calculate the coupling term given in Eq. 2.11.

2.3.2 Feshbach resonances

For a collision of two atoms the scattering properties are determined by the scattering potential $V^{cen}(r)$ (see Sect. 2.3.1). The properties of the scattering potential $V^{cen}(r)$ determine the s-wave scattering length a for $k \to 0$. However, the value of a can be drastically influenced due to resonant coupling to a two-body bound state, referred to as a *closed channel*. Since this closed channel can have a different hyperfine structure than the open channel the presence of an external magnetic field can modify the position of the closed-channel bound state with respect to the open channel. This phenomenon is depicted in Fig. 2.3. The hyperfine energy of the two colliding atoms at large separation ($r \to 0$) defines the total energy of the initial atom pair. Since the s-wave scattering is energetically allowed in this channel, even at $T \to 0$, this channel is called the *open channel*. Any scattering potential with a higher asymptotic energy is referred to as a closed channel (see Fig. 2.3a) Since the hyperfine energy of different channels vary different due to the influence of an external magnetic field, the closed channel shifts with respect to the open channel (see Fig. 2.3b). If the closed channel has a bound state with binding energy ϵ_S, it can become resonant with the asymptotic energy of the open channel for a certain magnetic field B_0. If a coupling between the open and closed channel exists the scattering length can de dramatically altered due to resonant coupling to the bound state. On this resonance the scattering length diverges (see Fig 2.3b). This phenomenon is known as a *Feshbach resonance*. [34, 35].Occasionally these resonances are referred to as *Fano-Feshbach resonances* referring to the work of Fano in 1961 [81]. However, the resonances in the context of ultracold atoms differ significantly from the original Feshbach and Fano resonances. In the field of ultracold atoms the resonance occurs due to tuning of the internal structure of the collision partners even down to zero kinetic energy. Fano and Feshbach resonances occur due to the variation of energy of the collision partners, and not their internal structure.
In the context of ultracold atoms it was first pointed out in 1976 [10] that these resonances can result in losses for certain magnetic fields. The first observation of such losses due to coupling to a closed channel was done in 1986 [11]. Only in 1992 Tiesinga, *et al* [12] showed these resonances can be used in a positive manner to tune the scattering length to any favorable value.
In the presence of only one closed channel the scattering length can be written as:

$$a(B) = a_{bg} + a_{res}(B)$$

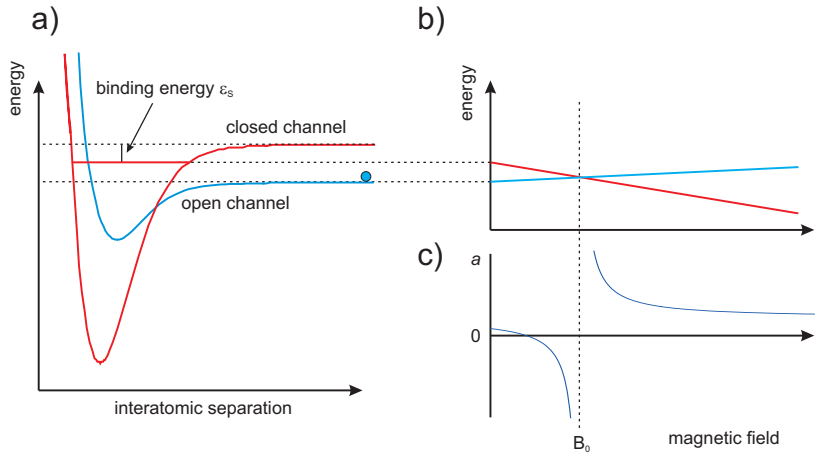

Figure 2.3: Principle of a Feshbach resonance. a) a pair of atoms is prepared in a hyperfine state collides through an energetically open channel. A energetically closed channel has a bound state with binding energy ϵ_S. b) due to the hyperfine structure both the open and closed channel shift as a function of the externally applied magnetic field. For a certain magnetic field B_0 the open channel asymptote becomes resonant with the bound state in the closed channel. c) at B_0 the scattering length diverges and around the resonance all values of a can be accessed.

where a_{bg} is the scattering length in the open channel, the so-called background scattering length and $a_{res}(B)$ is the magnetically induced scattering length due to the presence of the closed channel. This resonance term is commonly denoted as

$$a_{res}(B) = -a_{bg}\frac{\Delta B}{B - B_0} \tag{2.13}$$

where B_0 is the resonance position and ΔB is the resonance width defined as the difference between the magnetic field resonance B_0 and the magnetic field where $a(B) = 0$, hence, ΔB is a function of a_{bg} itself. By introducing $\Delta\mu = \mu_o - \mu_c$ as the difference in magnetic moment between the open and closed channel[3] we can write

$$a(B) = a_{bg} - \frac{a_{bg}\Delta B\Delta\mu}{\Delta\mu(B - B_0)}$$

where the numerator of the second term $a_{bg}\Delta B\Delta\mu \equiv C$ corresponds to the coupling strength between the open and closed channel and is always positive [82]. Figure 2.4 shows the possible configurations of the scattering length divergence. A Feshbach resonance width is fully characterized by the three parameters a_{bg}, ΔB and $\Delta\mu$, and the position solely by B_0. In the literature various expressions are used to describe the resonance width for $k \to 0$. The length scale R^* [83] and the width Γ are commonly used and are related by

$$R^* \equiv \frac{\hbar^2}{2\mu a_{bg}\Delta B\Delta\mu}, \qquad \Gamma \equiv \frac{\hbar^2 k}{\mu R^*} = 2Ck$$

Additionally the dimensionless parameter $s_{res} = R^*/r_0$ [62] is a convenient measure to describe the resonance strength.

[3] Note that $\mu = -\partial E/\partial B$

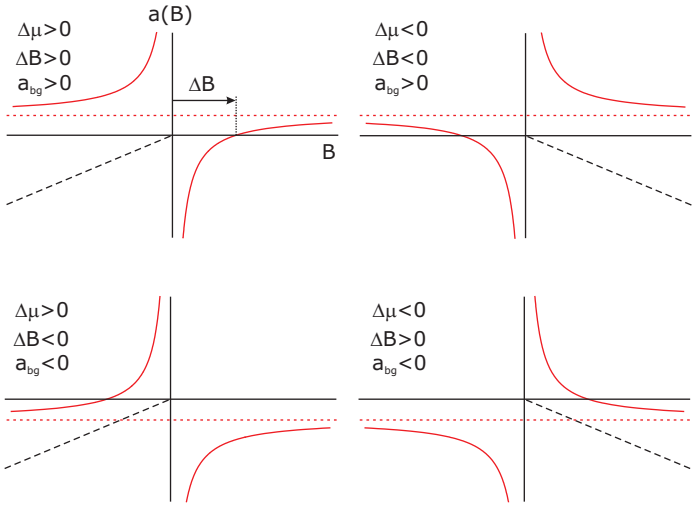

Figure 2.4: The scattering length (solid red) is plotted as a function of magnetic field for the four possible symmetries of the divergence around a Feshbach resonance. The red dotted line indicates the a_{bg} and the black dashed line indicates $\Delta\mu$.

2.3.3 Ultracold scattering at finite energy

Up till now we have considered scattering at $T = 0$. However, even at ultracold temperatures the finite temperature plays a significant role. In this section we discuss the s-wave scattering properties in the presence of a Feshbach resonance. We do this in the context of the scattering amplitude f_0 given by

$$f_0 = \frac{1}{k \cot \eta_0 - ik} \tag{2.14}$$

where η_0 is the s-wave phase-shift as defined in 2.3.1. The cross-section of s-wave collisions for distinguishable particles is given by

$$\sigma(k) = 4\pi |f_0|^2 = 4\pi \frac{1}{k^2 \cot^2 \eta_0 + k^2} \tag{2.15}$$

where the $\sigma(k)$ has an energy dependence reflected in the unitarity-limit term k^2 in the denominator and in η_0. The s-wave phase shift is given by

$$\eta_0(E) = \eta_{bg}(E) + \eta_{res}(E) \tag{2.16}$$

where the resonant term is expressed as

$$\tan \eta_{res}(E) = -k \frac{a_{bg} \Delta B \Delta\mu}{\hbar^2 k^2 / 2\mu - \Delta\mu(B - B_0)} \tag{2.17}$$

where $E = \hbar^2 k^2 / 2\mu$, this equation reduces to equation 2.13 for $k \to 0$. Generally, the finite energy behavior is described in terms of the effective range expansion. This method expands the $\cot \eta_0$ in terms of $-ka$. However, due to the resonant structure of a we choose to not perform this expansion, instead we calculate the energy dependent cross section by assuming a non-resonance background scattering length ($\tan k a_{bg} \simeq k a_{bg}$). We readily obtain

$$\sigma(k) = \frac{4\pi}{k^2} \frac{\left(\Gamma/2 - k a_{bg}\delta\right)^2}{\left(1 + k^2 a_{bg}^2\right)\left(\delta^2 + (\Gamma/2)^2\right)} \tag{2.18}$$

where $\delta = \Delta\mu(B - B_0) - E$ represents the detuning from the resonance. In the absence of a resonance ($\Gamma = 0$) this expression reduces to the familiar form

$$\sigma(k) = 4\pi \frac{{a_{bg}}^2}{1 + k^2 a_{bg}^2} \tag{2.19}$$

The cross-section has an asymmetric shape around the Feshbach resonance, this shape is called the *Fano-profile*. In the absence of a background scattering length Eq. 2.18 reduces to

$$\sigma(k) = \frac{4\pi}{k^2} \frac{\left(\Gamma/2\right)^2}{\delta^2 + (\Gamma/2)^2}$$

which has a symmetric Lorentz-shape and is the familiar *Breit-Wigner resonance* [84].
To obtain a thermally averaged cross-section we need to average over all possible k-vectors. In particular we want to study the collision rate $\Gamma = n\langle\sigma v\rangle$, where n is the density and $v = \hbar k/\mu$ is the relative velocity of a collision pair. The distribution in position and momentum space is given by $f(\mathbf{r}, \mathbf{p}) = \exp(-\mathbf{H}(\mathbf{r}, \mathbf{p})/k_B T)$, where the single-atom Hamiltonian $\mathbf{H}(\mathbf{r}, \mathbf{p})$ describes the system at position $\mathbf{r}$ with momentum $\mathbf{p}$, and is given by

$$\mathbf{H}(\mathbf{r}, \mathbf{p}) = \frac{p^2}{2m} + U(\mathbf{r}) \tag{2.20}$$

where $U(\mathbf{r})$ is the trapping potential. Using $\mathbf{p} = \hbar\mathbf{k}$ and the fact that $\langle\sigma v\rangle$ is independent of $\mathbf{r}$ we obtain

$$\langle\sigma v\rangle = \frac{\int \frac{\hbar k}{\mu} \sigma(k) e^{-\mathbf{H}(\mathbf{r},\mathbf{k})/k_B T} d\mathbf{k} d\mathbf{r}}{\int e^{-\mathbf{H}(\mathbf{r},\mathbf{k})/k_B T} d\mathbf{k} d\mathbf{r}} \tag{2.21}$$

$$= \frac{2^{3/2}}{\sqrt{\pi\mu}(k_B T)^{3/2}} \int_0^\infty \sigma(E) E e^{-E/k_B T} dE \tag{2.22}$$

In particular a finite energy collision $k > 0$ results in a shift of the resonance position and of the zero-crossing. Additionally, the on-resonance scattering cross section is reduced due to the unitarity limited term $1/k^2$. For a thermal sample with a distribution of k-values this results in a washing out of the zero crossing of the scattering length. This is depicted in figure 2.5: the finite temperature of the sample results in a shift of the maximum cross section.

2.3.4 Accumulated phase method

The Asymptotic Bound-state Model as described in Chapter 5 utilizes the Accumulated phase method [85]. Recently, an extensively discussion of this method with additional extension is presented in Ref. [86]. The accumulated phase method enables to neglect details of the inner part of the potential, i.e. for a internuclear separation of $r < r_{in}$.

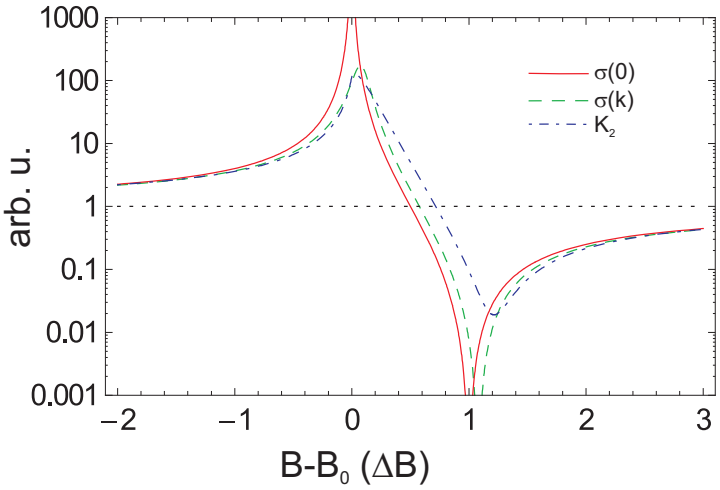

Figure 2.5: The scattering cross section $\sigma(k)$ and the thermally averaged rate constant $\langle\sigma v\rangle$, both normalized to a background value of 1. The solid red and dashed green curves shows Eq. 2.18 for $k = 0$ and $k > 0$. The dash-dotted blue curve shows the thermally averaged rate constant $\langle\sigma v\rangle$ given by Eq. 2.22. Note the shift of the maxima for finite temperatures.

At the distance r_{in} a boundary condition is imposed on the wavefunction in the form of a phase. This phase represents the accumulated phase behavior of the wavefunction for $r < r_{in}$. A proper choice of r_{in} allows the inner potential to be neglected and a very good approximation of the wavefunctions near the scattering threshold can be made. In particular to describe Feshbach resonances, originating from near-threshold bound states, this tool has proven to be very powerful as demonstrated on the ^{40}K^{87}Rb system in Chapter 5. The idea is to expand the radial wavefunctions in a singlet and triplet basis, if this is possible, knowledge about the singlet and triplet radial wavefunctions suffice to describe any superposition occurring due to hyperfine mixing by $\mathbf{H}_{-}^{\mathrm{hf}}$ of the singlet and triplet potentials.

Three conditions on r_{in} have to be fulfilled to use the accumulated phase method. First, the accumulated phase radius r_{in} has to be small enough that the exchange energy is larger than the hyperfine energy. If this is the case the hyperfine coupling term $\mathbf{H}_{-}^{\mathrm{hf}}$ can be neglected and the singlet-triplet basis is a good basis for the radial wavefunctions. Second, r_{in} should be large enough that the singlet-and triplet potentials are known. This condition can be fulfilled if the exchange energy is smaller than the van der Waals energy and the potentials are well described by the van der Waals tail. Finally, the energy and angular momentum scales should be small enough that varying the energy or angular momentum l does not significantly alter the accumulated phase at r_{in}[4].

The conditions given above are depicted in Fig. 2.6 for the ^{6}Li^{40}K system. The first condition is fulfilled for $r \lesssim 22$ a$_0$, the second for $r \gtrsim 14$ a$_0$, therefore taking $r_{in} = 18$ a$_0$ yields a good choice for the accumulated phase method. The third condition is always satisfied in the calculations presented in this thesis, for more detail on this condition we refer the reader to Ref. [86].

[4] If this condition can not be fulfilled a first order correction can be made to allow the phase to vary proportional to E or $l(l+1)$ [86].

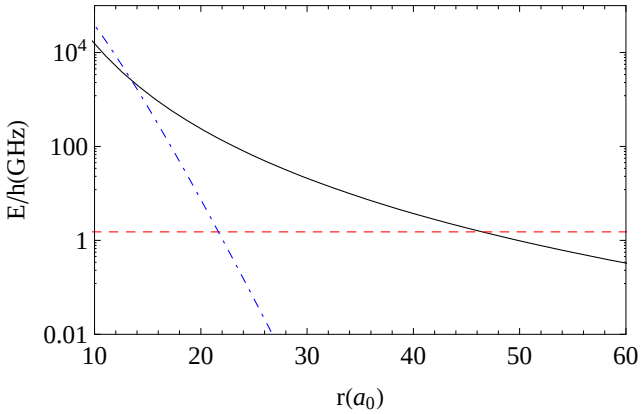

Figure 2.6: Determination of the accumulated phase point r_{in} for the ^{6}Li^{40}K system. The solid line is the van der Waals energy, (Eq. 2.6), the red dashed line is the hyperfine energy ($E_{hf}^{\alpha} + E_{hf}^{\beta}$) and the blue dash-dotted line is the exchange energy (Eq. 2.8).

Figure 2.7 illustrates an application of accumulated phase method where the first bound state E_1 of the ^{6}Li^{40}K triplet potential is calculated from the triplet scattering length $a_t = 63.5$ a$_0$ [17]. First, the accumulated phase at $r = r_{in}$ is obtained by solving the radial Schrödinger equation (Eq. 2.9) for $E = k_B \times 1$ nK using as a boundary condition at $r \to \infty$ the s-wave phase shift obtained with equation 2.10. The obtained wavefunction is depicted as the blue solid curve in Fig. 2.7. Subsequently, the triplet binding energy is obtained by varying E using as boundary conditions the phase at r_{in} and $\psi', \psi \to 0$ for $r \to \infty$. The obtained binding energy is $E_1 = h \times 434$ MHz, well in agreement with full coupled channel calculations yielding $E_1 = h \times 427.44$ MHz [17]. The procedure can also be applied in a reversed manner to relate the binding energy to the scattering length. Using $E_1 = h \times 427.44$ MHz as input parameter we obtain a scattering length of $a_t = 63.9$ a$_0$, well in agreement with the coupled-channel calculation value ($a_t = 63.5$ a$_0$).

The accumulated phase method is very useful for Feshbach resonance studies due to its accurate description of near-threshold states. For example calculating the Franck-Condon factors of singlet and triplet wavefunctions can be performed very accurately with the accumulated phase method. These Franck-Condon factors are essential for the generalized version of the ABM presented in Chapter 5.

In Fig. 2.8 another illustration of the accumulated phase method is given. The grey line is the triplet potential of ^{6}Li^{40}K, and the solid blue line depicts the radial wavefunction of the least bound state with binding energy $E_1 = h \times 427.44$ MHz. Two other wavefunctions are plotted, first the red dashed line represents the wavefunction with the accumulated phase method up to $r_{in} = 18$ a$_0$. This wavefunction is obtained by solving Eq. 2.9 using $V_S^l(r) = V_{vdW}(r) = -C_6/r^6$ and as a boundary condition $\chi(r) \to 0$ for $r \to \infty$, where $\chi(r) = rR(r)$. We will refer to such a state as an *asymptotic-bound state* since the probability density of the wavefunction extends far outside the range of the potential. The inner part of the wavefunction, i.e. for $r < r_{in}$, contains less than 1% of the probability density of the wavefunction. Therefore, summarizing the short-range behavior in the phase of the wavefunction yields a good approximation. As a comparison the wavefunction where the least bound state is treated as a halo state is plotted (green dash-dotted curve). For a halo state the potential is approximated by a contact potential with a bound state at an

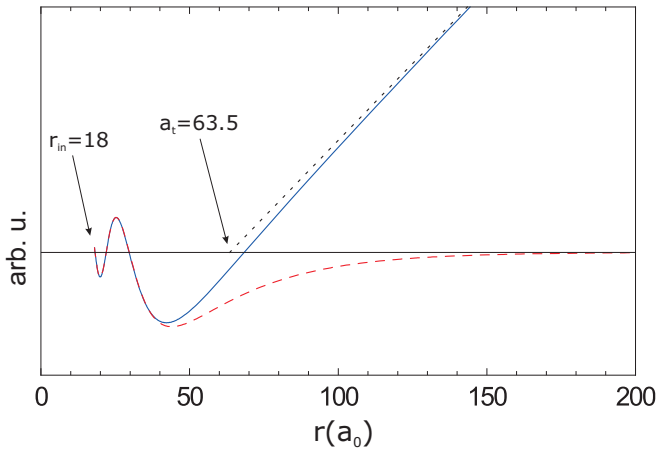

Figure 2.7: Relating the triplet scattering length for ^{6}Li^{40}K to the binding energy E_1 by making use of the accumulated phase method. The solid blue line is the scattering wave function at $E = k_B \times 1$nK, the red dashed curve is the wavefunction of the bound state and the dotted black line is the asymptotic behavior of the scattering wavefunction, yielding the scattering length.

energy E_1. The radial wavefunction is given by $\chi(r) = \sqrt{2\kappa}e^{-\kappa r}$, where $\kappa = \sqrt{2\mu E_1/\hbar^2}$. It is clear that for this case the halo state is a too crude approximation to describe the radial wavefunction. The asymptotic-bound state, however, yields a good approximation.

2.4 Trapping of ultracold atoms

In this section the principles of trapping will be briefly resumed, in particular a background is given for the aspects special to our experimental setup which is presented in Chapter 3. In Sect. 2.4.1 optical trapping is discussed, followed by Sect. 2.4.2 on magnetic trapping. Finally, density distributions of thermal and degenerate gases are discussed in Sect. 2.4.3.

2.4.1 Optical dipole potentials

Optical dipole potentials for neutral atoms are based on the *AC Stark effect*. An intense laser beam is far-detuned from an optical transition, inducing an electric transition dipole-moment on the atom. The induced dipole moment in the external driving field results in a potential energy proportional to the driving intensity[87]. An extensive discussion of optical dipole potentials for neutral atoms can be found in Ref. [51]. Here we consider the approximations required to describe the optical potentials used in our setup.
An optical potential formed by a far detuned laser beam with an intensity $I(\mathbf{r})$ interacting with a two-level system is given by [51]

$$U(\mathbf{r}) = -\frac{3\pi c^2}{2\omega_0^3}\left(\frac{\Gamma}{\omega_0 - \omega_L} + \frac{\Gamma}{\omega_0 + \omega_L}\right) I(\mathbf{r}), \tag{2.23}$$

where $\omega_0 = 2\pi c/\lambda_0$ and $\omega_L = 2\pi c/\lambda_L$ are the angular frequency of the atomic transition and of the laser respectively and Γ is the spontaneous decay rate of the excited state. For

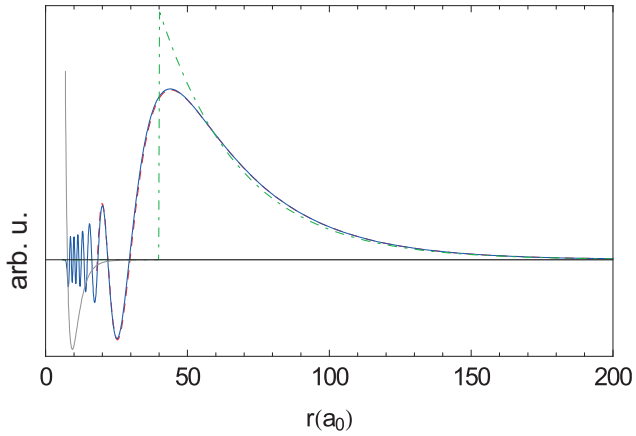

Figure 2.8: Various approximations for the radial wavefunction of ^{6}Li^{40}K in the triplet potential. The grey curve depicts the potential, the solid blue curve the wavefunction for the complete potential, the red dashed curve for only the $V_{vdW}(r)$ potential and the green dash-dotted for a contact potential.

laser beams tuned relatively close to resonance $\omega_L/\omega_0 \approx 1$ the rotating wave approximation (RWA) is generally made. This approximation assumes $\omega_0 + \omega_L \gg \omega_0 - \omega_L$, however for lithium in a trap with $\lambda_L \simeq 1\mu$m the counter-rotating term $\Gamma/(\omega_0 + \omega_L)$ has a contribution of 19% to the trapping potential, therefore we do not perform the RWA. For alkali atoms the excited state of the D-lines has an orbital angular momentum of $l = 1$ which results in a fine-structure splitting in the D1 and D2 lines. The optical transition can still be approximated by a two-level (ground state/exited state) model if the detuning of the laser from the atomic resonance, $\Delta \equiv \omega_0 - \omega_L$, is much larger than the fine structure splitting, ΔE_{FS}, of the excited state. We take the atomic transition frequency ω_0 at the average of the D1 and D2 lines. For all dipole potentials considered in this thesis $\Delta \gg \Delta E_{FS}$ and we can use the two-level model.

The intensity profile of a focused Gaussian beam is described by the cylindrically symmetric intensity distribution [88]:

$$I(\rho, z) = I_0 \frac{e^{-2(\rho/w(z))^2}}{1 + (z/z_R)^2} \tag{2.24}$$

where $w(z) = w_0\sqrt{1 + z/z_R}$ is the beam waist as a function of z, w_0 is the focal waist, $z_R = w_0^2\pi/\lambda_L$ is the Rayleigh range, λ_L is the wavelength of the far off resonant laser beam and $I_0 = 2P/(\pi w_0^2)$ is the peak intensity for a total laser power P. Substituting Eq. 2.24 into 2.23 we obtain the total trapping potential, with a peak value U_0 given by

$$U_0 = \frac{6Pc^2}{w_0^2\omega_0^2}\left(\frac{\Gamma}{\omega_L^2 - \omega_0^2}\right).$$

This results in an attractive potential for a red-detuned laser ($\omega_L < \omega_0$) or a repulsive potential for a blue detuned laser ($\omega_L > \omega_0$).

Repulsive potentials

For a laser blue detuned with respect to the $ns\ ^2S \rightarrow\ np\ ^2P$ transition, it is red detuned with respect to all $ns\ ^2S \rightarrow (n+i)p\ ^2P$ $(i > 0)$ transitions. Summing over all these attractive terms potentially attenuates the repulsive potential originating from the lowest transition. The total trapping potential U_{total} is given by the sum over the contributions of all possible $^2S \rightarrow\ ^2P$ transitions up to the ionization threshold [51]:

$$U_{total} = \sum_i U_i$$

where ω_i and Γ_i are the angular frequency and decay rate of the $ns\ \rightarrow (n+i)p$ optical transition. Since the linewidths of the higher excited states Γ_i become increasingly smaller for larger i, the effective detuning becomes much larger. As an example we consider a blue detuned laser beam with $\lambda_L = 532$ nm. For potassium the $i = 1$ transition ($4s^2S_{1/2} \rightarrow 5p^2P_{3/2}$) has a wavelength of $\lambda_1 = 404.4$ nm and a decay rate of $\Gamma_1 = 2\pi \times 0.2$ MHz [89], therefore $U_1 = 7 \times 10^{-3} U_0$. Summing over all transitions results in an attenuation of the potential by 0.7% for potassium and 0.4% for lithium, therefore we can safely consider it as a two-level system, also for far-off-resonance blue-detuned laser beams.

Attractive Potentials

For a red detuned laser $\omega_L < \omega_0$, the optical dipole potential is attractive ($U_0 < 0$) and can be used as a trap for an ultracold atomic sample, with the shape given by

$$U(\rho, z) = U_0 \frac{e^{-2(\rho/w(z))^2}}{1 + (z/z_R)^2} \tag{2.25}$$

The bottom can be well approximated by a harmonic potential with trapping frequencies in radial (ω_r) and axial (ω_z) directions of:

$$\omega_r = \sqrt{\frac{4U_0}{m w_0^2}}, \qquad \omega_z = \sqrt{\frac{2U_0}{m}} \frac{\lambda}{w_0^2 \pi} \tag{2.26}$$

where m is the mass of the trapped atom.

2.4.2 Magnetic potentials

Magnetic trapping of neutral atoms is based on the Zeeman effect: an atom in an externally applied magnetic field experiences an energy shift proportional to the magnetic field value. For an extensive discussion of magnetic trapping of neutral atoms see e.g. [60, 55, 90], here we will briefly introduce the concepts required to describe the magnetic trap used in our setup. Atoms in different hyperfine ground-states experience a different Zeeman effect and therefore a different trapping potential. The internal energy of a ground state ($l = 0$) atom in an externally applied magnetic field is given by Eq. 2.3. The hyperfine interaction couples the nuclear and electronic spin to a total angular momentum $\mathbf{f} = \mathbf{i} + \mathbf{s}$, therefore, we take the appropriate $|fm_f\rangle$ basis.
In the case of $s = 1/2$ Eq. 2.3 can be diagonalized resulting in an analytic expression for the hyperfine energies, called the *Breit-Rabi formula* [91]

$$E^{hf}(B) = -\frac{a^{hf}}{4} + g_i \mu_B m_f B \pm \frac{a^{hf}(i+1/2)}{2}\left(1 + \frac{4m_f x}{2i+1} + x^2\right)^{1/2} \tag{2.27}$$

where $\mu_B = 9.27400915 \times 10^{-24}$ JT^{-1} is the Bohr-magneton, $x = (g_s - g_i)\mu_B B/(a^{hf}(i + 1/2))$ and the sign corresponds to the manifolds with $f = i \pm s$. Figure 2.2 shows the hyperfine diagrams for ^{6}Li and ^{40}K respectively. For low magnetic fields the atomic energy shift is well described by the linear Zeeman effect. For typical magnetic fields achieved in our magnetic trap this assumption can be made for ^{40}K, however for ^{6}Li at relatively high temperatures the quadratic Zeeman effect cannot be neglected as will be discussed in Sect. 3.4.3. In this section we will consider clouds cold enough ($T_{Li} \ll 0.6$ mK, $T_K \ll 4$ mK) that the linear Zeeman effect yields a good description.
For an atom in the hyperfine state m_f of the $f = i + s$ manifold the energy shift due to the magnetic field is given by:

$$U(B) = -\mu \cdot \mathbf{B} = m_f g_f \mu_B |B|$$

where g_f is the Landé g-factor of the hyperfine manifold (see e.g. [55]). The magnetic field generating our trap is created by a pair of coils mounted in approximately an anti-Helmholtz configuration. This results in a three-dimensional quadrupole field, where the field-gradient along the symmetry axis of the coil is twice the gradient in the two orthogonal directions. The absolute value of the magnetic field is given by $B(x, y, z) = \frac{\alpha_B}{2}\sqrt{x^2 + y^2 + 4z^2}$, where α_B is the magnetic field gradient and z is the symmetry axis of the coils (see Fig. 3.10). This magnetic field results in a potential given by:

$$U(x, y, z) = m_f g_f \mu_B \frac{\alpha_B}{2}\sqrt{x^2 + y^2 + 4z^2} \tag{2.28}$$

which results in a magnetic trap for low-field seeking states ($m_f g_f > 0$) simultaneously expelling high-field seeking states ($m_f g_f < 0$). In the origin of the coordinate system the magnetic field vanishes and different m_f states within a f-manifold are degenerate, therefore, transitions from trapped to untrapped states can occur, resulting in trap loss. This process is known as *Majorana loss* and limits the densities which can be achieved in quadrupole traps[5].

Optically plugged magnetic trap

The linear trap offers very tight confinement and is therefore attractive to experiments with ultracold gases. Evaporative cooling in such a trap can be performed more efficient than in e.g. harmonic confinement. Therefore, it is favorable to use a linear trap which is stable against Majorana spin flips, rather than a harmonic confinement[6]. Trap losses due to Majorana spin flips can be suppressed, without sacrificing the linear confinement, by applying a strong repulsive potential at the trap origin. This method has been first demonstrated in 1995 at MIT allowing to reach Bose-Einstein condensation in sodium [5]. The method was abandoned mainly because of the complex shape of the combined trap, making analytic descriptions of the trapped BEC's complicated. In 2005 D. Naik et al [15] reintroduced the method demonstrating it as an efficient pre-cooling stage before

[5] For an experimental demonstration see Sect. 3.6.1 or e.g. Ref. [92].
[6] For an extensive discussion on evaporative cooling in power-law traps see e.g. [57, 56].

loading an optical dipole trap. In both references [5, 15] the magnetic field gradient had to be decreased during the evaporative cooling to minimize three-body losses. This requires low stray fields to avoid the magnetic field zero to move with respect to the plug position while reducing the field gradient. In the presented experiments the gradient is constant during the evaporative cooling process, and therefore the setup is insensitive to even large (though constant) stray fields generated by the environment.

2.4.3 Properties of trapped gases

Fermi Energy

We start by discussing the Fermi energy E_F which is defined as the energy of the highest occupied single particle state in a Fermi gas at $T = 0$ (see Fig. 2.1). This is related to the Fermi-temperature $T_F = E_F/k_B$. To obtain the Fermi energy we need to consider the density of states $\rho(\epsilon)$. The density of states describes the number of classical states with energy ϵ per unit phase-space. The density of states for an ideal gas, confined in a trapping potential $U(\mathbf{r})$, is given by

$$\rho(\epsilon) = \frac{1}{(2\pi\hbar)^3}\int \delta\left(\epsilon - \frac{p^2}{2m} - U(\mathbf{r})\right) d\mathbf{r}d\mathbf{p} \tag{2.29}$$

For a harmonic trap, given by

$$U(x,y,z) = \frac{1}{2}m(\omega_x^2 x^2 + \omega_y^2 y^2 + \omega_z^2 z^2) \tag{2.30}$$

we can obtain the density of states by evaluating the integral in Eq. 2.29. This results in $\rho(\epsilon) = (1/\hbar\bar{\omega})^3\epsilon^2/2$, where $\bar{\omega} = (\omega_x\omega_y\omega_z)^{1/3}$. To obtain the Fermi energy we integrate the density of states, $\rho(\epsilon)$, up to the Fermi energy E_F. By definition of E_F we know that this equals the total number of atoms

$$\int_0^{E_F} d\epsilon\ \rho(\epsilon) \equiv N \tag{2.31}$$

For the harmonic confinement evaluating the integral 2.31 yields

$$k_B T_F = \hbar\bar{\omega}(6N)^{1/3} \tag{2.32}$$

For the pancake shaped linear trap, described by Eq. 2.28, we obtain the density of states by evaluating the integral

$$\rho(\epsilon) = \frac{128\sqrt{2}}{105\pi}\left(\frac{\sqrt{m}}{\mu_B\alpha_B\hbar}\right)^3 \epsilon^{7/2} \tag{2.33}$$

And for the Fermi energy in a linear trap we substitute Eq. 2.33 into Eq. 2.31. and obtain:

$$k_B T_F \simeq 1.5961 N^{2/9}\left(\mu_B\alpha_B\hbar/\sqrt{m}\right)^{2/3}.$$

depending even weaker on the atom number than for the case of the harmonic trap.

Density distributions

In the classical limit, i.e. the temperature T is much larger than T_F, the statistical nature of the particles is irrelevant and the probability distribution for an atom with energy ϵ is given by the Maxwell-Boltzmann distribution

$$f(\epsilon) = e^{-\epsilon/k_B T}$$

For a non-interacting ideal gas the energy is given by the one-body Hamiltonian $\epsilon = \mathbf{H}(\mathbf{r}, \mathbf{p})$, given by Eq. 2.20. The density distribution is obtained by integrating the Boltzmann distribution over all possible momenta

$$n_{th}(\mathbf{r}) = \int d\mathbf{p} e^{-\mathbf{H}(\mathbf{r},\mathbf{p})/k_B T} \tag{2.34}$$

For a harmonic confinement solving the integral yields a Gaussian density distribution given by

$$n_{th}(\mathbf{r}) = n_0 e^{-m(\omega_x^2 x^2 + \omega_y^2 y^2 + \omega_z^2 z^2)/2k_B T}$$
$$n_0 = N \left(\frac{m\bar{\omega}^2}{2\pi k_B T} \right)^{3/2}$$

where n_0 is the peak density and $\bar{\omega} = (\omega_x \omega_y \omega_z)^{1/3}$.

Degenerate density distributions For the quantum-degenerate gas we take a different approach. We assume the thermal energy $k_B T$ is much larger than the quantum mechanical level spacing $\hbar\omega$, this allows us to calculate the density distribution $n_{FD}(\mathbf{r})$ of a trapped fermionic gas by using the *semi-classical* approximation

$$n_{FD}(\mathbf{r}) = \frac{1}{(2\pi\hbar)^3} \int d\mathbf{p} \frac{1}{e^{(\mathbf{H}(\mathbf{r},\mathbf{p})-\mu)/k_B T} + 1} \tag{2.35}$$

where the integrand is the Fermi-Dirac distribution function. To calculate the density distribution of a Fermi-degenerate cloud at a finite temperature, $T < T_F$, we evaluate the integral 2.35. This results in the expression

$$n(\mathbf{r}) = -\left(\frac{m k_B T}{2\pi\hbar^2} \right)^{3/2} \mathrm{Li}_{3/2}\left(-\zeta e^{-U(\mathbf{r})/k_B T} \right)$$

where $\mathrm{Li}_n(z) \equiv \sum_{k=1}^{\infty} z^k/k^n$ is the polylogarithm function and $\zeta \equiv \exp(\mu/k_B T)$ is the fugacity.

In typical experiments the density distribution is analyzed by absorption imaging. This method projects the three-dimensional density distributions onto a two-dimensional optical density distribution (see Sect. 3.5.3). We can calculate this two-dimensional density profile for a harmonic potential (Eq. 2.30) by integrating over the y-dimension. Additionally, we integrate over the z-dimension to obtain the one-dimensional density profile and once more over the x-dimension to obtain the total atom number. We readily obtain

$$n_{2D}(x,z) = -\frac{1}{\hbar^3}\frac{m\,(k_BT)^2}{2\pi\omega_y}\mathrm{Li}_2\left(-\zeta e^{-m(\omega_x^2x^2+\omega_z^2z^2)/(2k_BT)}\right) \tag{2.36}$$

$$n_{1D}(x) = -\frac{1}{\hbar^3}\sqrt{\frac{m}{2\pi}}\frac{(k_BT)^{5/2}}{\omega_y\omega_z}\,\mathrm{Li}_{5/2}(-\zeta e^{-m(\omega_x^2x^2)/(2k_BT)}) \tag{2.37}$$

$$N = -\left(\frac{k_BT}{\hbar\bar{\omega}}\right)^3\mathrm{Li}_3(-\zeta) \tag{2.38}$$

The fugacity ζ can be related to the degeneracy parameter T/T_F by combining Eq. 2.38 and 2.32

$$\frac{T}{T_F} = (-6\mathrm{Li}_3(-\zeta))^{-1/3} \tag{2.39}$$

In the case of a time-of-flight experiment the gas is released from the trap and starts ballistically expanding. For a harmonic confinement the single particle Hamiltonian 2.20 is quadratic in momentum and in position space. Therefore, in the semiclassical approximation the time-of-flight distribution can be related to the spatial distribution by simply rescaling the coordinates

$$\omega_i \rightarrow \frac{\omega_i}{\sqrt{1+\omega_i^2t^2}}$$

where ω_i is ω_x, ω_y or ω_z. A quantum mechanical treatment of this problem yields the same result [93].

Chapter 3
Experimental Setup

3.1 Introduction

This chapter describes the experimental setup developed for this thesis. A brief discussion of the design considerations will be made followed by an extensive description of all techniques required to achieve the ultracold mixture of ^{6}Li-^{40}K. At the time of the start of this thesis no experiment regarding mass-imbalanced Fermi-Fermi mixtures existed. However, next to our experiment two others were started, one by F. Schreck and R. Grimm in Innsbruck and another one in Munich by K. Dieckmann. Interestingly, all three experiments took the ^{6}Li-^{40}K system, but different technical approaches were chosen to achieve the ultracold Fermi-Fermi mixture. In all three experiments collisions between different species provide the rethermalization of the ultracold mixture required for efficient evaporative cooling. The Innsbruck group took an all-optical approach [94], trapping a large amount of lithium in two hyperfine states and a small amount of potassium in a pure hyperfine state. Rethermalizing collisions occur by *intra*-species collisions of the two lithium hyperfine states where the collision cross-section is enhanced by the broad ^{6}Li Feshbach resonance [95]. *Inter*-species collisions between the potassium and any of the two lithium hyperfine states yields the rethermalization of the potassium. At the start of this experiment the s-wave scattering lengths between ^{6}Li-^{40}K were not known and yielded an uncertainty in the possibility to succeed in cooling the mixture. It was unclear which approach would be the best: using a large amount of both spin-polarized ^{6}Li and ^{40}K and only relying on inter-species collisions or sympathetic cooling of a small amount of spin-polarized ^{6}Li with a large spin mixture of ^{40}K or vice-versa. The Munich group took a different approach to circumvent this uncertainty, namely by adding a third element, the bosonic ^{87}Rb, as a coolant. A large amount of ^{87}Rb is evaporatively cooled relying on intra-species collisions and small amounts of the ^{6}Li and ^{40}K are sympathetically cooled along relying on inter-species collisions of ^{6}Li-^{87}Rb and ^{40}K-^{87}Rb. The choice of ^{87}Rb as a third species was obvious since both the scattering lengths of ^{6}Li-^{87}Rb [71] and ^{40}K-^{87}Rb [96, 97] were known and sympathetic cooling of both fermions to quantum degeneracy by sympathetic cooling with ^{87}Rb had been achieved [71, 72].

Our approach is somewhat in between the two other approaches. We use only the two fermionic species, and use a combination of magnetic and optical traps. A big advantage of magnetic traps is the large trapping volume yielding large atom numbers and in the case of a linear quadrupole trap also the tight confinement. The largest quantum-degenerate atomic gases have been obtained in magnetic traps [98, 99]. The initial design was to prepare both the ^{6}Li and the ^{40}K atoms in the fully stretched hyperfine states which are stable against spin-exchange losses. Rethermalization only occurs due to inter-species collisions and forced evaporative cooling is performed on both species simultaneously. To be able to perform this approach two high flux cold atom sources have been developed, capable of loading 2×10^9 ^{40}K atoms simultaneous with 3×10^9 ^{6}Li atoms. During the coarse of the experiment we discovered in a collaboration with the Innsbruck group [17]

that the singlet and triplet scattering lengths of ^{6}Li-^{40}K collisions are nearly identical, $a_s = 52.1(3)$ a_0 and $a_t = 63.5(1)$ a_0, yielding a suppression of the spin exchange losses. Therefore, we found that sympathetic cooling of a small amount of ^{6}Li in a large bath of three hyperfine states of ^{40}K is more efficient than the initial approach of using a large amount of both atoms in their doubly polarized states.
Additionally, two design considerations have been made which are emphasized here. First, we have used an optically plugged magnetic quadrupole trap rather than the commonly used Ioffe-Pritchard type of magnetic traps. This trap was originally used at MIT to achieve BEC, but was abandoned because of the non-harmonic confinement in the trap bottom which complicates analysis of the trapped clouds. However, since most research on ultracold fermions is performed in optical dipole traps the optically plugged quadrupole trap is an excellent option for pre-cooling close to quantum degeneracy. The combination of simple coil design, good optical access, large trapping volume and tight confinement provides a fast manner to achieve large ultracold atomic samples.
Second, the design incorporates an optical transport of the ultracold sample to an appendix of the vacuum system, which will be referred to as the science cell. The choice of transporting a sample close to degeneracy rather than a relatively hot cloud, as it is done by using a magnetic transport [100], was made to have no equipment around the science cell required to cool the sample and only equipment to perform experiments on the degenerate cloud. This allows a very small science cell with superb optical access to the sample, for example high-resolution imaging can be performed with standard microscope objectives as will be discussed in section 3.5.3.
This chapter is ordered as follows. Sect. 3.2 describes the vacuum system, followed by the description of the laser systems for both species in Sect. 3.3. Subsequently, the various trapping and pre-cooling methods are discussed in Sect. 3.4 and in Sect. 3.5 the methods used for manipulating and diagnosing the samples are explained. The chapter concludes in Sect. 3.6 with the experimental results on the ultracold ^{6}Li-^{40}K mixture and the quantum degenerate spin mixture of ^{40}K-^{40}K.

3.2 Vacuum

The vacuum system consists of four chambers, a source chamber for a two-dimensional magneto-optical trap (2D MOT) for each atomic species, a main trapping and cooling chamber and a science cell as depicted in figure 3.1 and 3.2.
The potassium 2D MOT chamber is a glass cell (Technical Glass Inc.) as depicted in figure 3.1, 3.3 and 3.9. It consists of a four way cross of optical quality windows ($\varnothing = 30$ mm) to provide access for two pairs of 2D MOT beams. Along the long side of the cell there is on one side a glass to metal seal connecting to a CF40 flange. This flange connects the chamber to the main vacuum system through a differential pumping tube of 23 mm length and 2 mm diameter. A gold mirror with in its center a 2 mm diameter orifice is mounted in front of the differential pumping tube, keeping a 1 mm distance between the mirror and the differential pumping tube to facilitate pumping between the surfaces. This mirror can be used for a 1D optical molasses or for reflecting a probe beam. On the other side there is an optical quality window for an axial cooling beam or push beam. On the side of the cell a 13 mm glass tube is connected by a T-piece to a break-seal ampule containing enriched potassium-40 and a glass to metal seal connecting through a

bellows to a CF16 flange. This flange is connected to a valve for pumping of the source chamber. During the coarse of the research performed for this thesis the valve has never been opened for pumping. The source cell has been baked while mounted on the main vacuum without the differential pumping section. Subsequently, the differential pumping tube was mounted under a protective atmosphere of Argon. Finally, the source cell has been evacuated through the differential pumping tube by the main vacuum pumps. As a source for ^{40}K we use KCl enriched to an abundance of 6% ^{40}K purchased from Trace Science International and distilled into a break-seal ampule by Technical Glass Inc. This break-seal ampule circumvents the use of home-built potassium dispensers [101][1]. The required vapor pressure for efficient operation of the 2D MOT is achieved by heating the source chamber. During the baking the temperature of the ampule has been kept below 100 °C to avoid the potassium reacting and avoid pressure building up in the ampule which could potentially break the seal.
The lithium 2D MOT chamber is described in detail in Chapter 4. We will briefly resume the design of the vacuum chamber here. It has a configuration similar to the potassium 2D MOT chamber, consisting of stainless steel rather than glass. Lithium is chemically reactive with glass, therefore the design is such that there is no direct line of sight from the oven to any window. The lithium source chamber is connected to the main vacuum by a differential pumping tube of 23 mm length and 2 mm diameter. A gold mirror with a 2 mm diameter orifice, identical to the one in the potassium setup, is mounted in front of the differential pumping tube. The source is connected to a four way cross which connects to a titanium sublimation pump (Leybold V150) and a 40 l/s ion pump (Vacion Plus 40 Starcell). The ion pump is valved off by an all-metal valve (VAT MAV-150-V). The titanium sublimation pump is only used once after closing the vacuum. As a source for lithium we use a combination of 6 g of enriched ^{6}Li (95% purity from Sigma Aldrich) with 2 g of bosonic ^{7}Li from natural abundance lithium for possible future use. The lithium is shipped as chunks in oil to protect reaction with water vapor in the air, additionally, the lithium contains a large amount of LiH. To clean out the lithium and obtain an oven with pure metallic lithium we degassed the lithium oven for about 2 h at a temperature of 670 °C on a separate vacuum system. During this procedure the oven was connected through a liquid nitrogen cold trap to a turbo pump. About 25% of the lithium was lost during this process. Subsequently, the oven was mounted under a protective atmosphere of argon onto the main vacuum chamber. When the oven is operated, no gas load is observed on the 40 l/s ion pump, indicating that the lithium is properly degassed. Additionally, during the coarse of the experiment the lithium sticking on the vacuum system acts as a getter itself. The lithium oven is connected with a nickel gasket (Caburn MDC) to the source chamber.
The main chamber is built around a spherical octagon (Kimball Physics Inc. MCF800-SO2000800-A). The lithium source is connected by a gate-valve (Leybold UHV 28699) and a close-coupler (Kimball Physics Inc. MCF275-CC200-700-A) to port no. 1 of the CF-40 ports (numbered clockwise from the top as in figure 3.1). The potassium source is connected without a gate valve directly to the opposing port (no. 5). On the port next to the potassium source (no. 6) a four way cross connects a titanium sublimation pump (Leybold V150) and a 55 l/s ion pump (Vacion Plus 55 Starcell) by a 60 cm long 2 1/2" tube. The ion pump is valved off by an all-metal valve (Varian 951-5027). On the top

[1] At the time of writing this thesis enriched potassium dispensers have become commercially available from Alvatec.

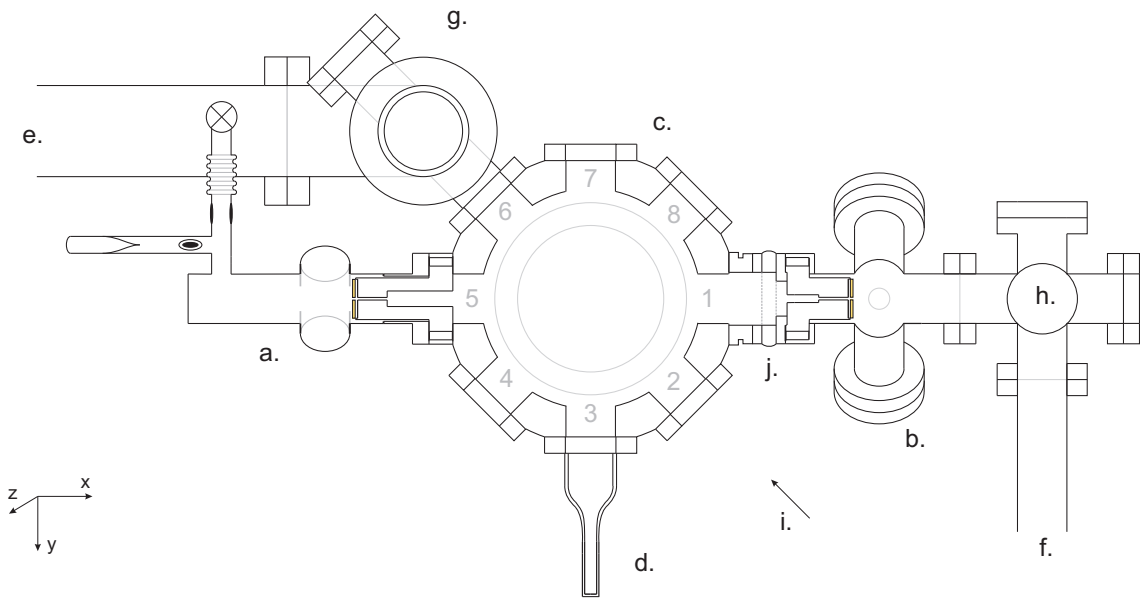

Figure 3.1: A schematic top view of the vacuum system. The following parts are shown: a) potassium 2D MOT source chamber, b) lithium 2D MOT source chamber, c) main UHV chamber, d) science cell, e) to 55 l/s ion pump, f) to 40 l/s ion pump, g/h) titanium sublimation pumps (mounted upwards), i) viewing direction of figure 3.10, j) gate valve

and bottom of the octagon two re-entry flanges provides space for magnetic field coils to be mounted close to the atomic sample. Each re-entry flange consists of an uncoated quartz window ($\varnothing = 113$ mm) connected to a CF-150 re-entry flange with a non-magnetic glass-to-metal seal (VACOM). The port numbers 2,4,6,7 and 8 have uncoated optical quality vacuum windows. Port no. 3 connects the science cell. The science cell consists of a $12.7 \times 12.7 \times 42$ mm square cell of uncoated quartz (Technical Glass Inc.) which is connected by a glass to metal seal to a CF40 flange. The end facet of the science cell extends to 23 cm out of the center of the main vacuum.

The vacuum is baked to a temperature of 180° C (limited by the glass-to-metal seals) for four days. The potassium cell is baked out separately before mounting the differential pumping tube. The vacuum operates at a pressure below the reading of the 55 l/s ion pump ($< 0.1\ \mu\text{A} = 5 \times 10^{-10}$ mbar) and the complete system is leak tested to a level of 10^{-10} mbar $\times$ l/s. The system is continuously pumped by the two ion pumps. About twice a year the 55 l/s ion pump has to be regenerated due to saturation, most likely by argon leaking from the potassium 2D MOT chamber. At these events the ion pump is baked to a temperature of 350 °C for a few hours, followed by running a current of 50 A for 1 minute through one of the titanium sublimation filaments. The gas load generated by the ion pump bake and the titanium sublimation pulse is dumped on a turbo pump connected to the back end of the ion pump. The saturation of the ion-pump within a few months suggests a pump with a larger pumping speed would elongate the time between the regeneration events and might elongate the lifetime of the ultracold sample.

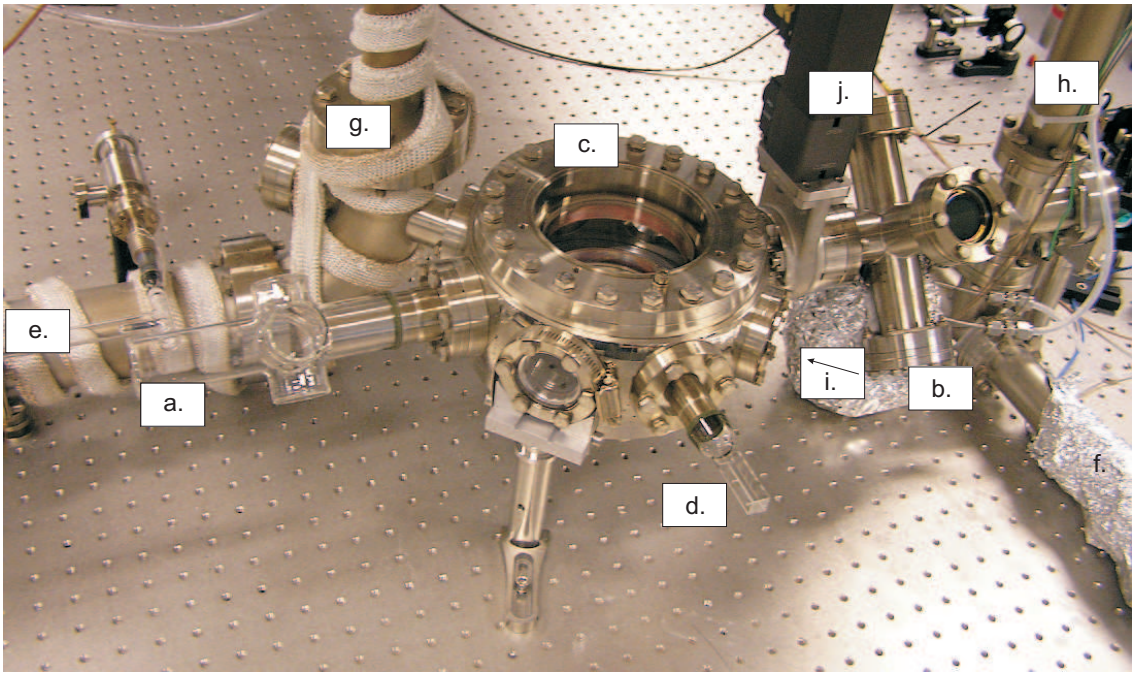

Figure 3.2: Photograph of the vacuum system, the parts indicated with a) to j) are explained in the caption of Fig. 3.1.

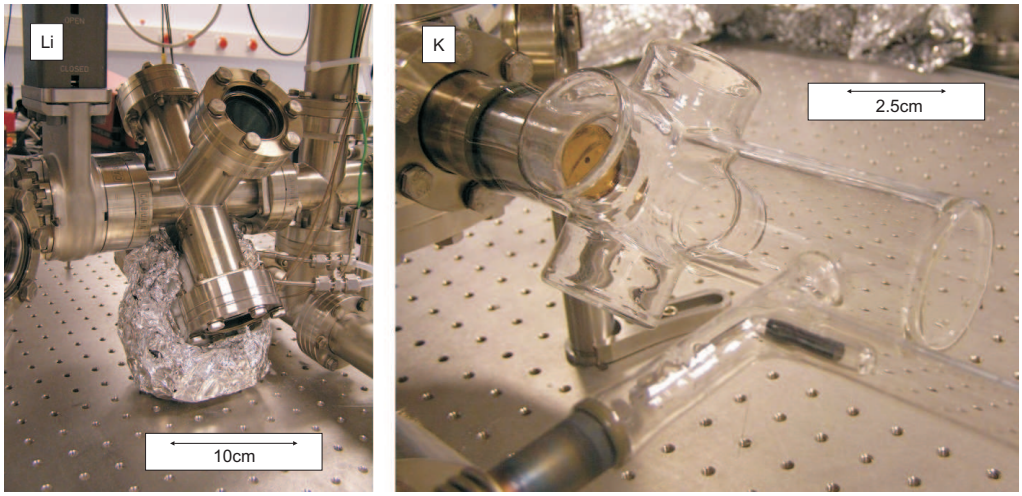

Figure 3.3: Photographs of the 2D MOT source chambers. The lithium 2D MOT (left) is described in detail in Chapter 4. Due to the perspective are the dimensions only a rough indication. The flanges on the lithium source chamber are CF40-flanges ($\varnothing = 70$ mm), the glass cross on the potassium source chamber has windows with $\varnothing = 38$ mm.

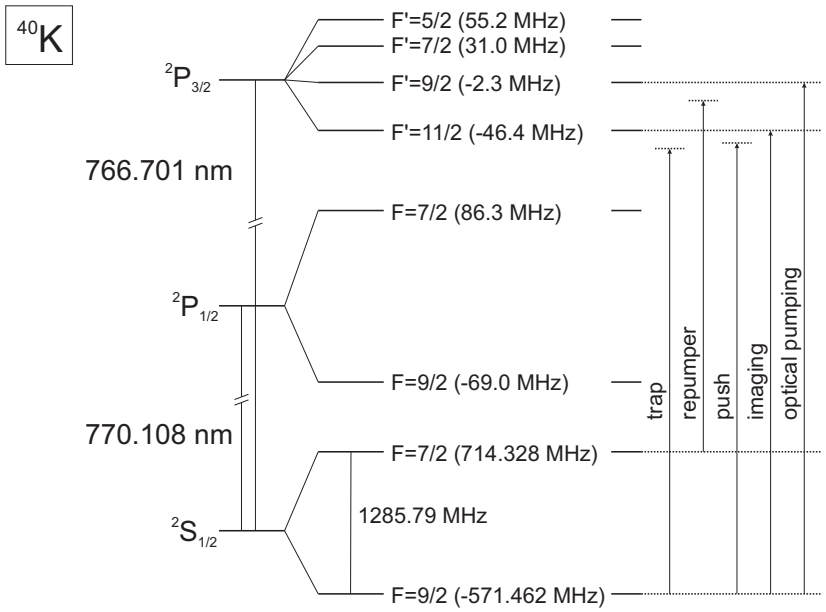

Figure 3.4: Optical transitions of the D1 and D2-lines of ^{40}K and the transitions used for trapping, cooling and diagnostics. Numerical values are taken from [102] and [77]. Note the inverted hyperfine structure.

3.3 Laser Systems

3.3.1 Potassium

We use the D2-line transitions for trapping and cooling of potassium-40, where we will refer to the $^2S_{1/2}|F = 9/2\rangle \rightarrow {}^2P_{3/2}|F' = 11/2\rangle$ transition as the *trap transition* and to the $^2S_{1/2}|F = 7/2\rangle \rightarrow {}^2P_{3/2}|F' = 9/2\rangle$ transition as the *repump transition* (see figure 3.4). The potassium-40 isotope has a hyperfine splitting of the $^2S_{1/2}$ level of 1285.79 MHz (see Appendix A), therefore it is possible to derive the repump light from the trap light by making use of an acousto-optical modulator (AOM). Figure 3.5 depicts the potassium laser setup. One master laser is used as a stable frequency reference and two tapered-amplifier (TA) chips as amplification stages, a number of AOMs are used to shift the laser frequencies. For low frequencies (< 300 MHz) ISOMET AOMs are used, and for the hyperfine frequency of 1.3 GHz a Brimrose AOM (GPF-1240-200-.766) is used. Optical fibers are employed to distribute the light and to provide an accurate reference point for the beam alignment between certain parts of the experiment. The fibers used are the Schäfter + Kirchhoff PMC-630 models and homebuilt Thorlabs PM630-HP fibers. Schäfter + Kirchhoff fiber couplers (60FC-4-A6,2S-02) are used for in- and out-coupling of the fiber.

Master Laser and locking A Toptica DLX 110 is employed as a stable frequency source (see figure 3.5). The laser is operated at an output power of 350 mW which is distributed over five beams. Two beams are used for injecting the tapered amplifiers, one beam is used for low-field absorption imaging, one beam as a push beam for the 2D MOT and one for high-field absorption imaging. The laser is locked based on polarization Zeeman spectroscopy. Here we briefly describe the configuration. A linear polarized beam

is passed through a natural abundance potassium vapor cell heated to $\sim 40°$ C. Ten percent of the beam is retro-reflected as a probe beam, detecting a doppler-free saturated absorption spectrum. A quarter waveplate combined with a cube splits the beam in its σ^+ and σ^- components. A homogeneous magnetic field of a few Gauss effectively shifts both signals in opposite directions due to the difference in Clebsch-Gordan coefficients for the $m_F + q$ and $m_F - q$ transitions, where $q = \pm 1$ for $\sigma^\pm$ polarized light. The intensity of these beams are measured by two OPT 101 photodiodes. The two signals are electronically subtracted to create a dispersive signal used for locking. The laser is locked by two separate feedback loops: one slow integrator stage ($\sim$ 1 Hz) to the piëzo and one fast ($\sim$ 4 kHz) integrator feedback to the laser current. The former tunes the piëzo over a range of ± 15 V to compensate slow thermal drifts. The latter provides short term stability, additionally it is limited in amplitude by the frequency span of the locking feature. This combination of amplitude-limited fast-feedback and large-range slow feedback eliminates the possibility of 'hopping' to another line due to electrical or acoustical noise spikes, common reasons for 'breaking lock'. The long term stability of this spectroscopic method was characterized by spectroscopy on the MOT and found to fluctuate over less than 1 MHz over the coarse of a few years. The lockpoint chosen is the spectral line of the ^{39}K $^2S_{1/2}$ $F = 1$ to the unresolved $^2P_{3/2}$ transitions (see Fig. 3.8).

Tapered Amplifiers We use two Eagleyard (EYP-TPA-0765-01500-3006-CMT03-0000) Tapered Amplifier chips as optical amplification stages. The chips are mounted in a homebuilt housing designed for optimum position stability of the chip, the mount is described in detail in Ref. [103]. The chip is mounted on a copper cross which temperature is actively stabilized by two Peltier elements (Eureca Messtechnik GmbH TEC 1H-30-30-44/80-BS). The cross itself is mounted by four spring loads and PEEK mounting studs to an aluminium base. The PEEK mounting studs provide electrical isolation of the diode and the spring loads keep the cross in place but allow it to marginally rotate around the diode laser center. Thermal expansion of the copper will therefore result in a rotation of the diode rather than a displacement. The collimation lenses are mounted in a PEEK holder, machined slightly too big for the aluminium housing such that longitudinal alignment can be done very accurately. During the operation period of a year we did not see any decay in the output power of both Tapered Amplifier chips, nor did the in- or out-coupling need any realignment.
The trap TA is operated by a Sacher Pilot 2000 temperature and current controller and is run at a temperature of 25° C and a current of 2.0 A. Its typical input (output) powers are 46(766) mW. The repumper TA is temperature stabilized by a Thorlabs TED 200C temperature controller at a temperature of 31° C and it runs a current of 1.7A, provided by a homebuilt power supply around a Thorlabs LD3000 module. Its typical input (output) powers are 8(200) mW.

3.3.2 Lithium

The D-lines of lithium have a wavelength of 671 nm (see figure 3.6). For a long time high power narrow band laser light at 671 nm has been an issue for experiments on ultracold lithium. At the time of the writing of this thesis, various options are commercially available, these include tapered amplifiers from Toptica, dye lasers (see e.g. Radiant Dyes Laser), diode lasers (Mitshubishi ML101J27) and broad area diode lasers from Eagleyard.

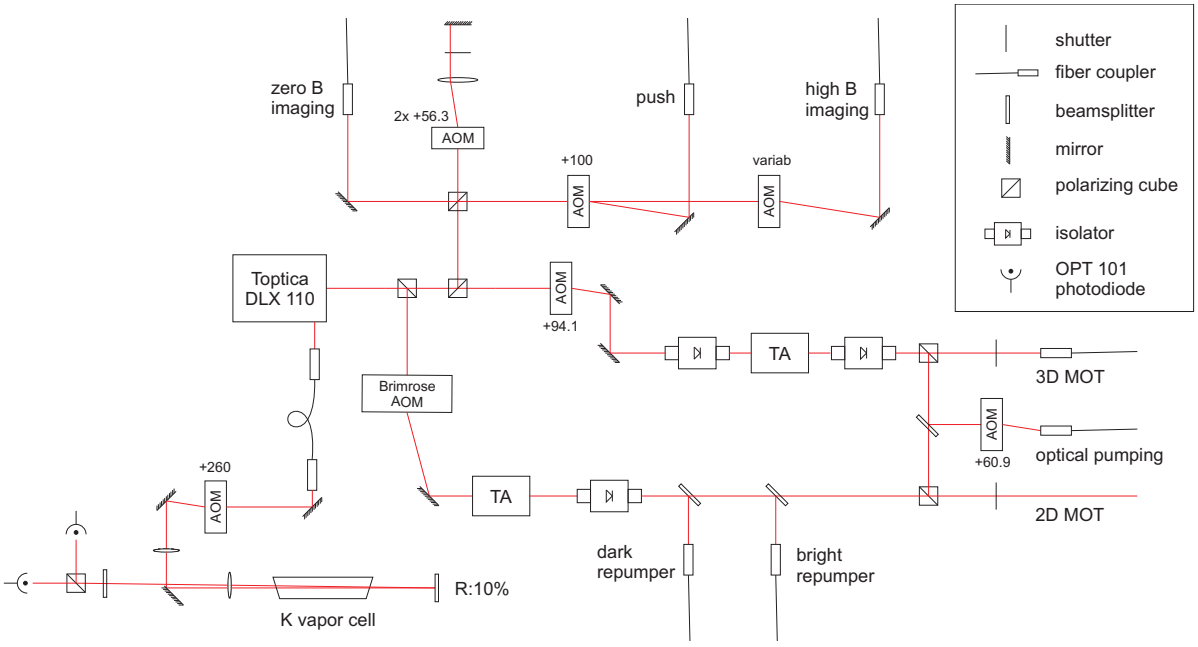

Figure 3.5: Optical setup of the potassium laser system. The Toptica DLX 110 provides a narrowband frequency which is actively stabilized on the spectral line of the ^{39}K $^2S_{1/2}$ $F = 1$ to the unresolved $^2P_{3/2}$ transitions. The laser beam is split in total into five beams which are independently frequency shifted (see text), the typical frequencies used are indicated at each AOM. Two beams are amplified by Tapered Amplifiers (TA). Additional mirrors, beam shaping telescopes and shutters have been left out of the drawing.

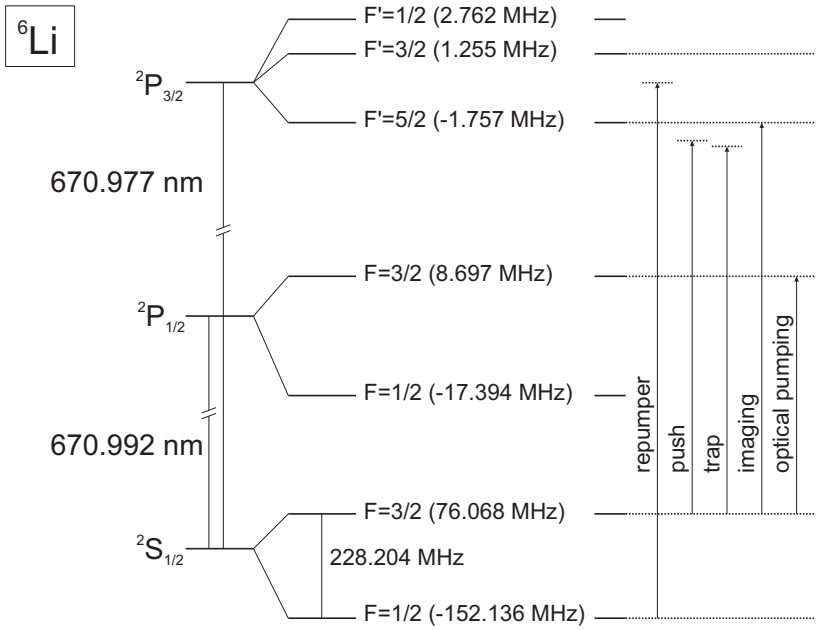

Figure 3.6: Optical transitions of the D1 and D2-lines of ^{6}Li and the transitions used for trapping, cooling and diagnostics. Numerical values are taken from [104] and [77]. Note the unresolved and inverted hyperfine structure in the $^2P_{3/2}$ excited state.

When this project was started neither the tapered amplifiers, nor the high power diode lasers were available. Therefore we started with a Coherent 699 dye laser pumped with 5W at 532nm from a Verdi V10, using LD688 laser dye dissolved in Dowanol EPH. However due to its lack of stability we developed an injection locked dye laser, where an external low power diode laser was made narrowband by optical feedback from the dye cavity. The dye cavity itself was a compact bow-tie cavity consisting of four mirrors and the dye jet as optical elements. The concept of placing the bandwidth narrowing parts out of the cavity greatly improved the power output and stability of the system. At that time however the high power diode lasers had become available and to characterize the lithium 2D MOT behavior we needed independent control of the four frequencies for the 2D and 3D MOT beams. Therefore the ease of use of diode lasers and remaining instabilities due to the dye jet made us switch to the diode laser system as it is used now in the experiment. Two master lasers and four slave lasers provide ample power for the conducted experiments (see figure 3.7).

Master Lasers As stable frequency sources we operate two external cavity diode lasers (ECDL), similar to Ref. [105], operating a 120 mW wavelength selected diode (Mitshubishi ML101J27). One laser is locked on the D1-line and used for optical pumping, the other laser is locked on the D2-line and used for imaging beams, the push beam and injection locking of the slave lasers. The grating-mount and diode are temperature stabilized to $T = 70°$ C (Thorlabs TED 200C temperature controller) to tune the free running wavelength close to 671 nm. By tuning the grating, the laser can be tuned mode-hop free over a spectral range of 3 GHz. The current of the laser is provided by homebuilt power supplies based on the design of Libbrecht, et al. [106], providing a current stability on the timescale of hours of $\sim 10^{-5}$ on a current of up to 300 mA. Frequency stabilization of the master

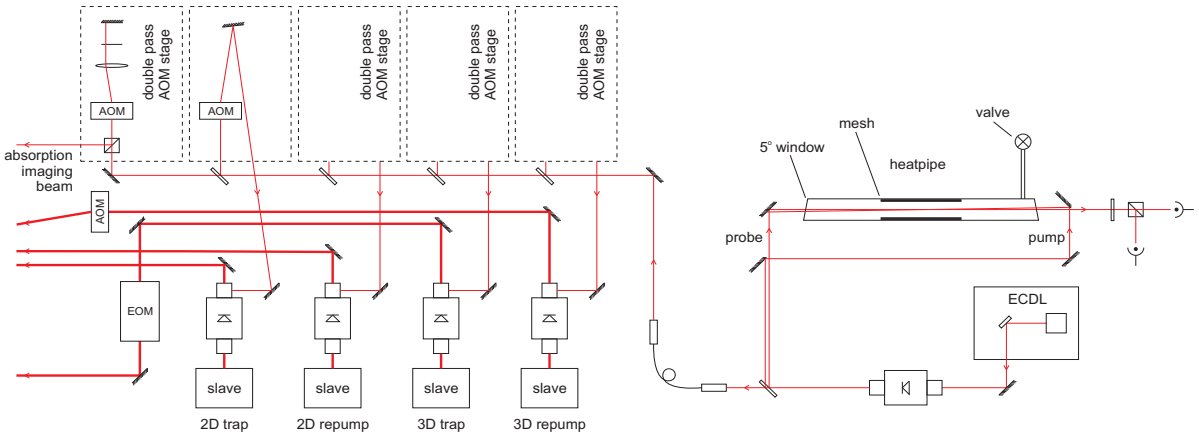

Figure 3.7: Schematic of the lithium laser setup. For a legend see figure 3.5. The ECDL is locked to a saturated absorption spectroscopy and distributed over 5 beams which can independently be shifted in frequency. Four beams are used for injecting slave lasers. The push beam is derived from the 3D-repumper. The intensity of the 3D-trap light can be controlled by the EOM and the intensity of the 3D repumper by an AOM. Additional mirrors, beam shaping telescopes and shutters are not shown.

laser is performed identical to the method used for the potassium. Saturated absorption spectroscopy in a heat pipe oven [107] yields a dispersive signal for locking (see Fig. 3.8). The heat pipe consists of a stainless steel tube of 40cm length, 1.6cm inner diameter and two CF16 windows on each side mounted under 5° to avoid interference effects. Three layers of stainless steel mesh (wire $\varnothing = 0.112$ mm, mesh opening 0.142 mm) over a distance of 15cm around the center of the heatpipe improve the mobility of the lithium by capillary action. The central part is heated to a temperature of $\sim 300°$ C adjusted to have $\sim 30\%$ absorption on the D2 resonance, where the Lamb dip of the F=3/2 transition is 7% of the total signal. Water cooling is applied 5 cm from the windows to prevent overheating of the optics and distillation of the lithium towards the windows. A buffer gas pressure of 0.1 mbar of argon[2] prevents contamination of the windows by the lithium vapor. A 6 mm tube close to one of the windows connects to a Swagelok valve and is used for evacuating and the argon inlet.

Slave Lasers The four slave lasers are operating the same diodes as the master lasers (Mitshubishi ML101J27). The diodes are mounted in homebuilt housings optimized for operating at elevated temperatures. A small aluminium block ($12 \times 12 \times 12$ mm) which houses the diode laser, a 10 kΩ thermistor, a thermal switch (AIRPAX - 67F070) and a collimation lens (Thorlabs C230TM-B), is clamped on a Peltier element (Melcor CP1.0-127-05L). The small thermal mass yields a fast response time and combined with an airtight housing the lasers have proven to be very stable and reliable. Injection locking of the lasers is performed by feeding in ~ 0.5 mW of frequency shifted light originating from the master laser. Using this design concept four 120 mW beams of independently tunable frequencies are fully available for the 2D/3D MOT operation and characterization.

[2]The actual buffer gas pressure in the heat-pipe oven is likely to be higher due to the presence of hydrogen outgassing from the lithium.

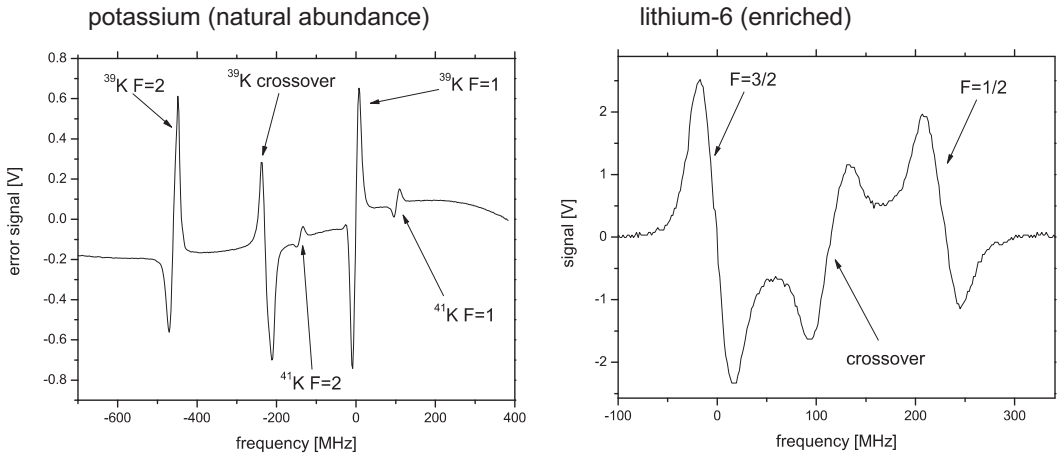

Figure 3.8: Spectroscopic signals obtained from the difference of the two photodiodes detecting the σ^+ and σ^- saturated absorption signal. The spectroscopic features are labeled by the quantum number of the hyperfine groundstate. For both species the excited states are unresolved. Positive frequency refers to blue detuning. The current locking range is limited to $\pm$50 MHz for the potassium and $\pm$25 MHz for the lithium (see text). The potassium is locked to the ^{39}K F=1 line and the lithium to the crossover feature.

3.4 Trapping and Cooling

This section describes the various techniques used for trapping and cooling of both species. As sources for lithium and potassium we use two 2D MOTs. The lithium 2D MOT is described in detail in Chapter 4. In Sect. 3.4.1 the potassium 2D MOT is described followed by the double 3D MOT in Sect. 3.4.2. In Sect. 3.4.3 the optically plugged magnetic trap is described. This is the first realization of such a trap for lithium. The chapter concludes in Sect. 3.4.4 with a description of the optical trap and the optical transport.

3.4.1 2D MOTs

Two-dimensional magneto-optical traps have become a widely used method to obtain a high flux cold atom source. Although the largest fluxes up to date have been achieved with designs incorporating Zeeman slowers, alternative sources like the 2D MOT are very popular due to their compactness, the absence of hot flux in the main vacuum chamber and the little engineering required to set them up. The 2D MOT is formed by a combination of a 2D quadrupole magnetic field and two pairs of orthogonal trapping laser beams (see Fig. 3.9b), detuned to the red of the atomic resonance line. As in a standard 3D MOT [55], counter-propagating lasers have σ^+/σ^- polarization, so that the Zeeman shift relative to the two opposing lasers is opposite. As a result, a cold atom that moves toward one side of the trap finds that the Zeeman shift places it closer to resonance with the laser whose propagation direction points toward the trap center. Thus cold atoms will tend to be pushed toward a line that coincides with the zero of the quadrupole magnetic field. Since there is no confinement in the axial direction, atoms are free to leave the trapping region along this axis, and cooled, trapped atoms stream out of the trapping region along this line. Furthermore, due to the negative detuning of the trapping lasers, the atoms are cooled in the radial directions, producing a well collimated beam. We distinguish two types

parameter	value
trap laser detuning	-3Γ
repump laser detuning	-2Γ
beam waist	15 mm
trap power per beam	120 mW
repump power per beam	40 mW
field gradient	20 G/cm

Table 3.1: The optimal parameters for operating the potassium 2D MOT. Note that the 2D MOT is operated in a retro-reflected configuration.

of two-dimensional cooling. First, axially-loaded 2D MOTs like, for example, the original atom funnel [108] to which we will refer as beam brighteners since a beam source is needed to load this type of 2D MOT. Second, isotropically or radially-loaded 2D MOTs operated as a beam source, to which we shall refer as 2D MOTs. Isotropically loaded 2D MOTs are widely used for rubidium [109, 110, 111], cesium [112, 113] and also potassium [114, 115]. Our setup employs two 2D MOTs, for lithium and potassium. The lithium 2D MOT is the first 2D MOT for a light species like lithium, additionally it is the first 2D MOT radially loaded from an effusive source, therefore the setup and requires an extensive description to which we refer the reader to Chapter 4. The isotropically loaded potassium 2D MOT is described below. For both species a separate source chamber is used to have fully independent control over the vapor pressures and optical setup of the sources. Lithium is chemically reactive with glass and various groups working with potassium MOTs reported the potassium adsorbing on the stainless steel vacuum chamber. To avoid these problems we developed a stainless steel chamber for the lithium and a separate glass vacuum cell for the potassium.

Potassium 2D MOT Figure 3.9 depicts the setup of the potassium 2D MOT. A break-seal ampule containing enriched potassium (Technical Glass Inc.) is connected to the vacuum cell. A glass-encapsulated magnet is placed in the tube of the break-seal, and after the bake the magnet is hit against the break-seal to open the enriched potassium ampule. The complete vacuum cell is heated to a temperature of $T \simeq 50°$ C to achieve a vapor pressure optimal for the 2D MOT operation. Two circularly polarized beams are retro-reflected with additional quarter-waveplates to obtain two pairs of counter-propagating cooling and trapping beams. The magnetic quadrupole field required for the trapping is provided by two sets of $Nd_2\,Fe_{14}B$ magnets (Eclipse magnets N750-RB) with a measured magnetization of $8.8(1) \times 10^5$ A/m. Each set consists of two $25 \times 10 \times 3$ mm magnet bars separated by 12 mm to make an effective dipole bar of 62 mm total length. The magnets are displaced from the symmetry axis by 35 mm, resulting in a two-dimensional quadrupole field with a gradient of 20 G/cm along the optical axes. The 2D MOT is operated at the parameters as shown in table 3.1. For these parameters a 3D MOT loading rate of 3×10^8 s^{-1} is obtained, nearly two orders of magnitude more than the previously reported ^{40}K 2D MOT [115, 116]. During the writing of this thesis a 2D+ MOT for ^{40}K, employing additional axial cooling, has been realized at the ENS in Paris yielding a 3D MOT loading rate of up to 2×10^9 s^{-1} [117].

3.4.2 3D MOTs

Setup

Single species three-dimensional Magneto Optical Traps (3D MOTs) for lithium [118, 119] and potassium [120, 121, 122] have been extensively described elsewhere. This section describes the double-species 3D MOT and for which conditions it operates optimally. In contrast to other groups, the largest atom numbers for the potassium 3D MOT have been obtained by applying a very low power dark MOT operating close to resonance.
The trapping and cooling beams of the 3D MOT are formed by three orthogonal pairs of counter-propagating beams (see figure 3.10). Each beam consists of four colors: trap and repump light for the lithium, trap light for the potassium and (optional) bright repump light for the potassium. The six beams are clipped at roughly the $1/e$ diameter of $\varnothing = 18$ mm, and are derived from one single beam by making use of polarization cubes and dichroic waveplates. We use $\varnothing = 18$ mm dichroic quarter waveplates (Casix custom $670 + 767$ nm) for the circularly polarized light of the MOT beams. The lithium trap (repump) light has a power of $P = 10$ mW (11 mW) per beam corresponding to a peak-intensity of $I = 1.8I_s$ ($2.0I_s$). The trapping light is red-detuned from the $F = 3/2 \rightarrow F' = 5/2$ D2 transition by $\delta_t = -6\Gamma$, and the repump light by $\delta_r = -4.5\Gamma$ from the $F = 1/2 \rightarrow F' = 3/2$. The potassium trapping (bright repumper) beams have $P = 10$ mW (1.5 mW) per beam corresponding to $I = 2.7I_s$ ($0.4I_s$). The trapping light is red-detuned from the $F = 9/2 \rightarrow F' = 11/2$ D2 transition by $\delta_t = -3\Gamma$, and both the bright and dark repump beams are detuned by $\delta_r = -2\Gamma$ from the $F = 7/2 \rightarrow F' = 9/2$ transition, significantly closer to resonance compared to other ^{40}K 3D MOTs [123, 115]. We use a separate dark repumper beam for the MOT loading stage to achieve a high atom number and corresponding density. The dark repumper beams consist of two counter-propagating beams with both the same dark spot imaged on the MOT position. At the position of the MOT the dark spot has a diameter of 3 mm and an extinction ratio of $1 : 50$ corresponding to the surrounding repump light. Both beams have 1.4 mW per beam ($\simeq 0.4I_s$). The magnetic quadrupole field for the MOT is formed by the magnetic trap coils and operates at a gradient of 14 G/cm. The double species 3D MOT is loaded simultaneously from the two 2D MOT sources in a continuous (non-pulsed) manner. The potassium MOT is typically loaded for 20 s, and the lithium MOT is loaded for the first few seconds of the potassium loading time. Depending on the experiment which is performed the atom number in the lithium MOT can be well controlled by means of the oven temperature and loading time. During the loading of the 3D MOTs the three trim coils apply a field of a few Gauss at the trap center to optimize the trapped atom number. We load simultaneously up to 2×10^9 ^{40}K atoms with 3×10^9 ^{6}Li atoms, where the MOT field gradient and beam alignment is optimized for maximum potassium atom number. The potassium MOT temperature is 190 μK, colder MOTs have been achieved for different MOT parameters resulting in a smaller number of trapped atoms. The lithium MOT temperature is 1.6 mK. In an optimized single species lithium MOT we can load up to 10^{10} ^{6}Li atoms (see chapter 4).

Compressed MOT and Optical Pumping

After loading of the double species MOT we apply a short modification of the MOT parameters to increase the phase-space density of both clouds before loading the mixture

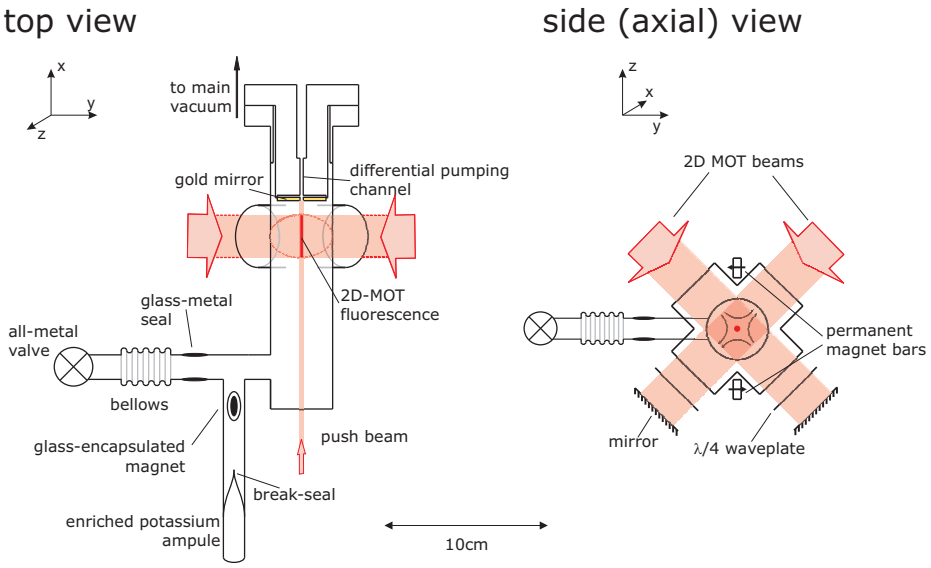

Figure 3.9: Schematic of the potassium 2D MOT system. The glass cell is filled with enriched potassium, distilled out of the break seal ampule after baking the vacuum. The vapor pressure of the cell is kept at a temperature of $T \sim 50°\mathrm{C}$ to achieve a vapor pressure optimal for operating the 2D MOT. Two beams are retroreflected to perform two-dimensional cooling on the vapor. The magnetic quadrupole field is applied by two bars of permanent magnets.

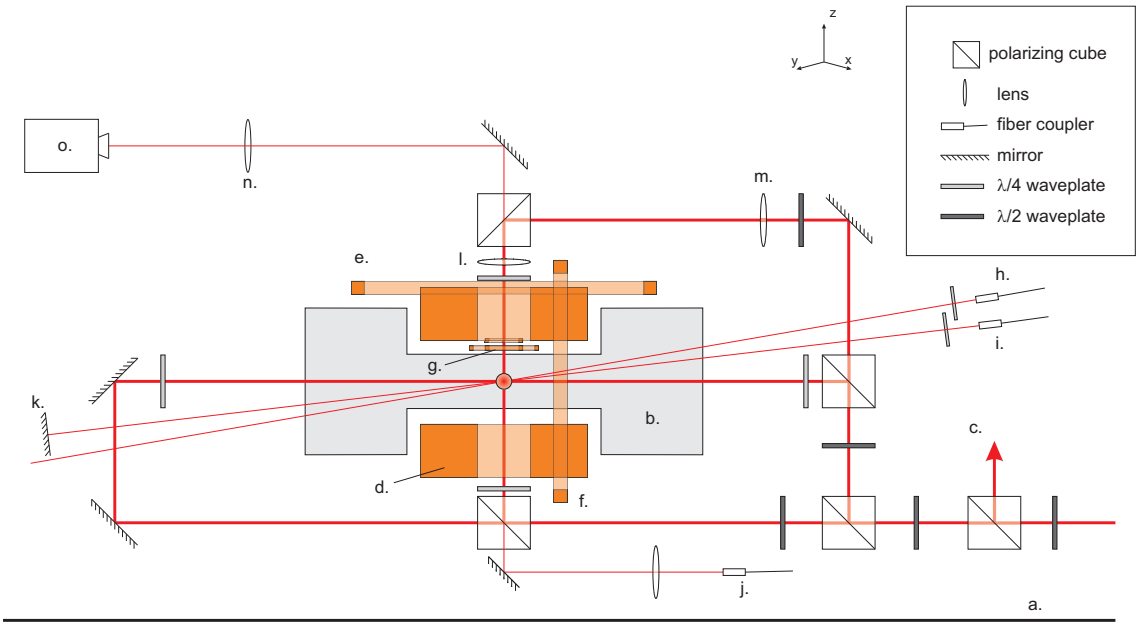

Figure 3.10: Schematic side view of the MOT optics and coils. The viewing direction is under 45° with the x and y axes (see figure 3.1). The dark repumper is not shown and propagates along the viewing axis. The parts shown in the figure are: a) optical table, b) main vacuum chamber, c) optical beams towards the MOT axis along the viewing direction, d) MOT/MT coils, e) vertical trim coils, f) horizontal trim coil, g) RF/MW antenna's (see Sect. 3.5.2), h) potassium optical pumping beam, i) lithium optical pumping, j) imaging fiber with $f = 25\mathrm{mm}$ lens making a collimated beam with $\varnothing = 20\mathrm{mm}$, k) mirror for retro-reflecting lithium optical pumping beam, l) imaging lens $f = 160\mathrm{mm}$ forms $1:1$ telescopes with m) to collimate MOT beams and n) to image the ultracold sample, o) Sony X710 camera.

into the magnetic trap. During this compressed MOT stage the magnetic field gradient is linearly increased to $B' = 44$ G/cm in 25 ms and the position of the field zero is shifted to optimize the transfer to the magnetic trap. During the last 3 ms of the compression the lithium 3D trap(repump) laser intensity is reduced to 1% (2%) of the original power and the trap(repump) detuning is decreased to $-1.5\Gamma(-2\Gamma)$. This reduces the lithium temperature to $T_{Li} = 0.6$ mK, increases the density to $n_{0,Li} = 3 \times 10^{10}$ cm^{-3} and increases the degeneracy parameter by almost a factor 40 to $D = n_0\Lambda^3 \simeq 7 \times 10^{-7}$, where $\Lambda = \sqrt{2\pi\hbar^2/mk_BT}$ is the thermal de Broglie wavelength.
After the compression and cooling the mixture is optically pumped towards low field seeking states in the $F = 9/2$ and $F = 3/2$ manifolds for the potassium and lithium respectively. The potassium is optically pumped by a 60 μs flash of intensity $1.4I_{sat}$ resonant with the $F = 9/2 \rightarrow F' = 9/2$ transition, simultaneously the bright repumper is switched on to avoid leaking to the $F = 7/2$ manifold. The transfer efficiency of total atom number is $\sim 60\%$ optimized for a spin mixture in the $F = 9/2, m_F = +5/2$, $+7/2$, and $+9/2$ states. Transfer efficiencies of up to 80% can be achieved, however this results in an excess of atoms in the fully stretched state which is unfavorable for rethermalization in the magnetic trap. The lithium is optically pumped by a 150 μs flash on the D1-line. The pulse consists of two colors with intensities $I = 1.0I_{sat}$ resonant with the $F = 3/2 \rightarrow F' = 3/2$ transition and $I = 2.4I_{sat}$ resonant with the $F = 1/2 \rightarrow F' = 3/2$ transition. These parameters are optimized to achieve a maximum number of lithium atoms in the fully stretched state. We obtain a transfer efficiency of $\sim 80\%$ in magnetically trapped states. A 3.6 G homogeneous field is pulsed on during the optical pumping pulses to provide a quantization field for the hyperfine states.

Light induced collisions

Figure 3.11a and 3.11b show the fluorescence decay curves of the single species lithium and potassium dark-spot MOT's respectively. The curves are fitted to a decay model

$$\frac{dN}{dt} = -\frac{1}{\tau}N - \beta\int n^2 dV \tag{3.1}$$

where τ is the background lifetime of the MOT and β is the loss coefficient due to homonuclear light induced collisions. The density distributions n of the lithium and potassium clouds are obtained by absorption imaging. The lithium has an optimal fit for $\tau_{Li} = 65$ s and $\beta_{Li,Li} = 5 \times 10^{-13}$ cm^{3}s^{-1}. For the potassium the optimal fit values yield $\tau_K = 166$ s and $\beta_{K,K} = 2 \times 10^{-12}$ cm^{3}s^{-1}, for a bright MOT we obtain a loss coefficient of $\beta_{K,K} = 7 \times 10^{-12}$ cm^{3}s^{-1}. The discrepancy of the background lifetimes of the lithium and potassium MOTs is most likely due to an imbalance of the lithium MOT beams since these measurements are performed in a MOT optimized for the potassium. The low value of $\beta_{Li,Li}$ is attributed due to the trap depth of the lithium MOT being larger than the fine structure splitting of lithium [124]. The large trap depth allows atoms to stay trapped after having undergone a fine-structure changing collision from the $^2P_{3/2}$ to the $^2P_{1/2}$ excited state, picking up a kinetic energy of $E = k_B \times 0.48$ K. Our obtained value for the ^{6}Li loss parameter agrees the values from Ref. [124] and [119] for ^{7}Li.
Figure 3.11c shows the fluorescence of the single MOTs and of the double MOT. We observe very low losses in the double MOT due to the interspecies light induced collisions, this can be attributed to the dark spot of the potassium. To obtain the heteronuclear loss

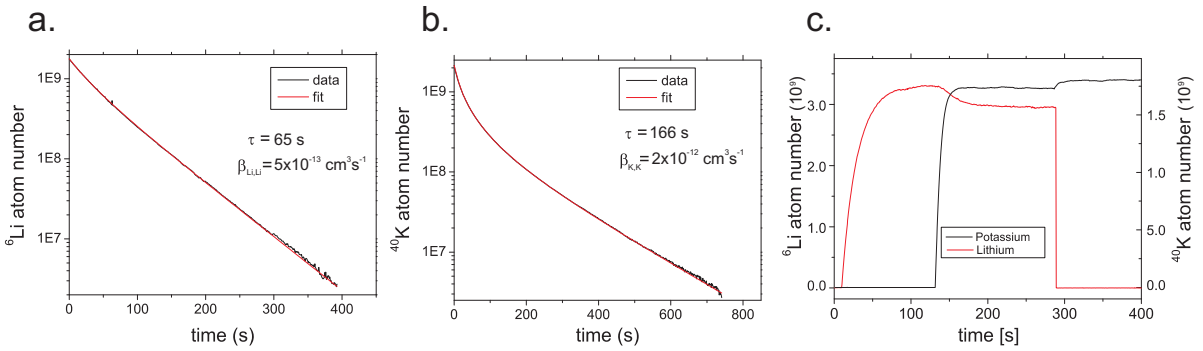

Figure 3.11: a) decay curve of a single ^{6}Li MOT and b) decay curve of a single ^{40}K MOT, the lithium MOT is less lossy due to the small fine structure splitting [124]. The black lines are the fluorescence signals of the MOTs and the red lines are fits to Eq. 3.1. c) loading curves of the double MOT of ^{6}Li and ^{40}K, the losses for the double MOT are suppressed due to the dark spot in the repump light (see text).

coefficient $\beta_{Li,K}$ we use the following rate equation

$$\frac{dN_{Li}}{dt} = L_{Li} - \frac{1}{\tau}N_{Li} - \beta_{Li,Li}\int n_{Li}^2 dV - \beta_{Li,K}\int n_{Li}n_K dV \tag{3.2}$$

In the case of the steady state, $dN_{Li}/dt = 0$, we can obtain the heteronuclear loss coefficient from Eq. 3.2. We obtain a value of $\beta_{Li,K} = 4 \times 10^{-12}$ cm^{3}s^{-1}. Similarly we obtain a value of $\beta_{K,Li} = 5 \times 10^{-12}$ cm^{3}s^{-1}. We attribute these low losses due to the suppression of light-induced collisions by the potassium dark-spot. Due to the dark spot in the repump light most of the ^{40}K atoms in the high density region are in the $F = 7/2$ manifold. Since the trap light is blue detuned with respect to the $^2S_{1/2}|F = 7/2\rangle \rightarrow {}^2P_{3/2}$ levels it will not couple to any molecular bound states in the K(4p)+Li(2s) excited state potentials which could lead to photo-association losses. Molecular bound states in the K(4s)+Li(2p) excited state potentials extend to a maximum of 15.5 a$_0$ [125], much smaller than the interparticle spacing of atoms in a MOT. These properties suppress light induced collisions resulting in the relatively low values of $\beta_{K,Li}$ and $\beta_{Li,K}$.

3.4.3 Optically Plugged Magnetic Trap

After spin preparation of the laser cooled sample, the mixture is transferred into an optically plugged quadrupole trap [5, 15]. The quadrupole field is formed by a pair of commercially available foil-wound coils (Canatron). The foil has a cross-section of 25 × 0.25 mm with on both sides 50 μm Kapton isolation foil. Each coil has 76 windings yielding a coil with an inner radius of 17.5 mm and an outer radius of 45 mm. The coil is mounted on a copper, water cooled plate, where the largest thermal resistance occurs at the 0.2 mm electrical isolation between the coil and the copper plate. A current of 100 A (corresponding to an axial magnetic field gradient of 180 G/cm) results in a temperature rise of 35° C with a time-constant of 2 minutes. During a typical experimental cycle the temperature of the coils varies by about 8° C. The current for the coils is provided by a Delta Elektronica power supply (model SM 15-200 D/P104). The current switching electronics is homebuilt inspired by the design of Ref. [126]. Four IGBT's (Semikron SKM100GB123D) in parallel with 2 × 15 transient voltage suppressors (ST Microelectronics SM15T39A) are capable

of switching 100 A off in 100 μs. A high voltage stage can switch the current on from 0 to 100 A in 120 μs. Two industrial relays (Stancor part no. 586-914) can be switched to reverse the current in one coil and provide the possibility of applying a homogeneous field up to 850 G for a current of 200 A.
At the zero point of the magnetic field Majorana spin-flips can occur which lead to heating and a limited lifetime of the sample. To prevent this depolarization we apply an 'optical plug' as a repulsive barrier to the atoms approaching the zero in magnetic field [5]. As an optical plug we use 532 nm light, which is far detuned from any $^2S \rightarrow P$ transition of a lithium or potassium atom.
The optical plug is generated by a Verdi V10 (532 nm), of which 7 W is focused to a waist of $w_0 = 16$ μm. This creates a repulsive barrier for the lithium and potassium both of ~ 1 mK and a magnetic field in the trap bottom of $B_0 \simeq 260$ mG (490 mG) along the weak (tight) axis of the quadrupole field. The optical plug can be switched by an Isomet 1205C-2 AOM. The plug position is monitored in real time with a CCD camera (see fig 3.14). From a Gaussian fit to the image we obtain the center position. We find the jitter during the experiment to be ~ 0.5 μm along both transverse directions, well below the beam diameter. We have operated the plug on a daily basis for a month without having to realign it. The plug beam is combined with the optical dipole trap on a dichroic beamsplitter (CVI laser BSR-15-1940), where the dipole trap is reflected and the plug beam is transmitted. This imposes an astigmatism on the plug beam which displaces the focal positions along the x and y axes by about 2.2 mm. Majorana losses only occur around the center of the magnetic trap, over an axial distance much smaller than the Rayleigh range of the plug beam. Therefore the astigmatism yields a tunability of the aspect ratio of the plugged volume from $r_x/r_y \approx 0.3$ to 3, where y is the tight axis of the quadrupole field. A slight increase of the aspect ratio to match the magnetic field aspect ratio is found to yield similar results as a circular plug. An aspect ratio in the range of $1 \lesssim r_x/r_y \lesssim 2$ yields comparable results in the performance of the plug. Figure 3.12 shows an image of a potassium cloud with in the optically plugged trap after a time of flight of 1 ms. The plug is kept on during the time of flight to magnify the hole size.
Four of the six spin states of lithium are trapped in an optically plugged quadrupole trap. The $|3/2, +3/2\rangle$ and $|3/2, +1/2\rangle$ states are trapped for all magnetic fields, and for an energy $k_B T \lesssim 310$ μK the $|1/2, -1/2\rangle$ and $|3/2, -1/2\rangle$ states are trapped as well, the former in the trap center and the latter in a hollow pancake around the trap center due to the low hyperfine field of lithium (see Fig. 2.2). For a typical magnetic field gradient of 180 G/cm the $|3/2, -1/2\rangle$ forms a pancake with a radius of about 1.5 mm along the tight quadrupole axis, additionally the pancake trap forms a stable trap without any field zeroes for $T \lesssim 310$ μK. The hyperfine field of the potassium is $B_{hf,K} = 357$ G (see appendix A), the potentials for the various spin states are thus well described by the linear Zeeman shift.

Magnetic field trim coils

Four magnetic field coils of 80 windings each allow trimming of the magnetic field in the main chamber. Two coils generate a vertical field and two orthogonal coils generate horizontal fields (see figure 3.10), all create a homogeneous field up to ~ 10 G. The coils are controlled by Delta Elektronica power supplies (model ES030-5) and the current can be quickly switched between a coil and a dummy load by means of a set of MOSFETs.

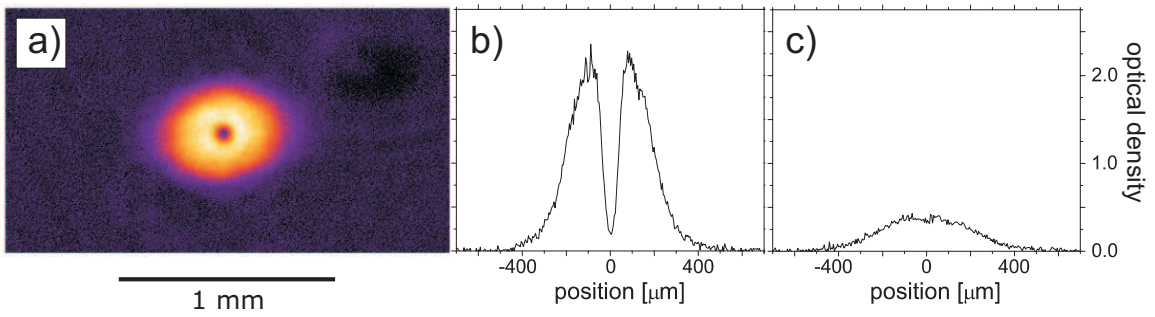

Figure 3.12: The effect of the optical plug for a ^{40}K cloud, evaporatively cooled to $T \simeq 20$ μK. a) optical density of an image taken after 1 ms of time-of-flight where the plug beam has been kept on to visualize the hole. This simplifies the alignment of the plug beam tremendously. b) horizontal cut through the density distribution c) the same but with the plug off, the absence of the plug clearly suppresses a high density in the trap center.

3.4.4 Optical Trapping and Optical Transport

After pre-cooling in the plugged trap we transfer the mixture in a far-off- resonance dipole trap (FORT) as described in section 2.4.1. The optical trap is formed by focusing up to 2 W of 1070 nm light (IPG Photonics YLD-5-LP) to a waist of $w_0 = 19$ μm yielding a maximum trap depth for the potassium (lithium) of 360 μK (160 μK). The position of the focus is displaced by ~ 50 μm from the plug position in the horizontal plane. The harmonic trapping frequencies at maximum laser power are $\omega_{r,K} = 2\pi \times 4.72$ kHz, $\omega_{z,K} = 2\pi \times 59$ Hz and $\omega_{r,Li} = 2\pi \times 8.11$ kHz, $\omega_{z,Li} = 2\pi \times 101$ Hz. The trap depth can be controlled by modifying the beam power by means of an AOM (Crystal Technology Inc. 3080-197).

The optical trapping beam is focused down to the $w_0 = 19$ μm waist by an achromatic lens ($f = 100$ mm), mounted on a linear air bearing stage (Leuven Air Bearings LAB-LS). The translation stage is connected to a geared DC motor (Maxon Motor part no. 118751 equipped with a 111:1 gearbox) by means of a rubber belt to minimize vibrations transmitted from the motor to the stage. A motion controller (Maxon Epos 24/5) in combination with an encoder (HEDL 5540 part no. 110512) controls the stage movement. The stage can displace the lens over a distance of 22 cm and after each transport the absolute position of the stage is re-calibrated on a laser beam focused on a razorblade. The focus is translated onto the atoms by a $1:1$ telescope to maintain the numerical aperture and maintain constant trapping frequencies during the transport. The optical trap light is combined with the optical plug by means of a dichroic beamsplitter (CVI laser BSR-15-1940).

Due to the large Rayleigh range of a typical optical dipole trap the requirements on the longitudinal reproducibility are far less stringent than on the transverse reproducibility. A simple tachometer on the DC motor and an optical switch consisting of a focused laser beam and a razorblade are sufficient to achieve the required longitudinal accuracy. After adiabatic loading of the dipole trap in 250 ms the trap focus is shifted by a sinusoidal profile to its end position in the science cell. The position of the trap focus in the main chamber is monitored by a CCD camera collecting the light transmitted ($\ll 1\%$) by the beamsplitter. The transverse position reproducibility over 20 transports is $\sigma_\perp = 1$ μm.

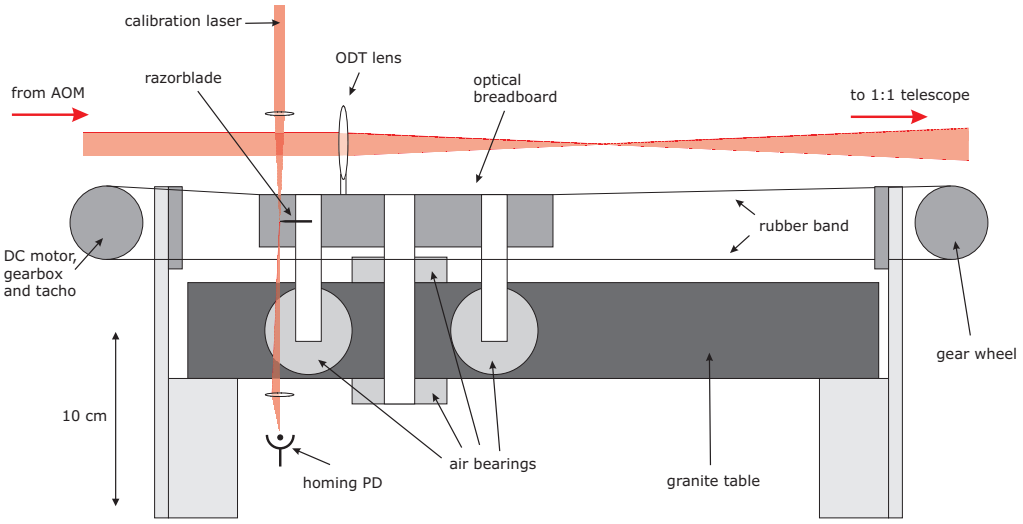

Figure 3.13: A schematic drawing of the optical transport stage. The ODT lens focuses the optical trap beam in free space. A 1 : 1 telescope translates this focus onto the atoms, while preserving the numerical aperture and the trap shape. A razorblade is mounted on the stage to have an absolute calibration point after each transport.

The longitudinal reproducibility is measured by placing the CCD camera out of focus and monitoring the reproducibility of the focal waist on the CCD camera. The longitudinal reproducibility is $\sigma_{\shortparallel} = 40$ μm, much smaller than the typical cloud size ($2r_z \approx 1$ mm). Future experiments will incorporate a crossed dipole trap. In that geometry the alignment of the crossing beam will define the final longitudinal position of the ultracold sample and the reproducibility achieved with this encoding system.
In the original demonstration of the optical transport of ultracold atoms a degenerate cloud was transported [16]. Here we transport only thermal clouds and we have not observed significant losses or heating due to the higher temperature and trapping frequencies during the transport. The lowest trapping frequencies in our trap are nearly an order of magnitude higher compared to Ref. [16] ($\omega_r = 4.72$ kHz/$\omega_z = 59$ Hz vs $\omega_r = 440$ Hz/$\omega_z = 4$ Hz).

3.5 Manipulation and Diagnostics

3.5.1 Computer Control

The experiment is controlled by one main computer, this computer runs Windows XP as operating system and controls all digital and analog output lines and the cameras. A second Windows XP computer is used for visualizing CCD camera's to monitor the plug or optical trap beams, magnetic field sensors and to control the optical transport system. The third computer is running a Fedora Core 6 Linux distribution and is used for real-time analysis of the measurements. The experimental system is running on a Windows XP machine because of the vast availability of drivers for any type of hardware and of the Control system described below. The choice to perform the data analysis on a Linux machine and to use open-source software has been made because of the high compatibility and portability for future experiments. Additionally the general properties of the Linux

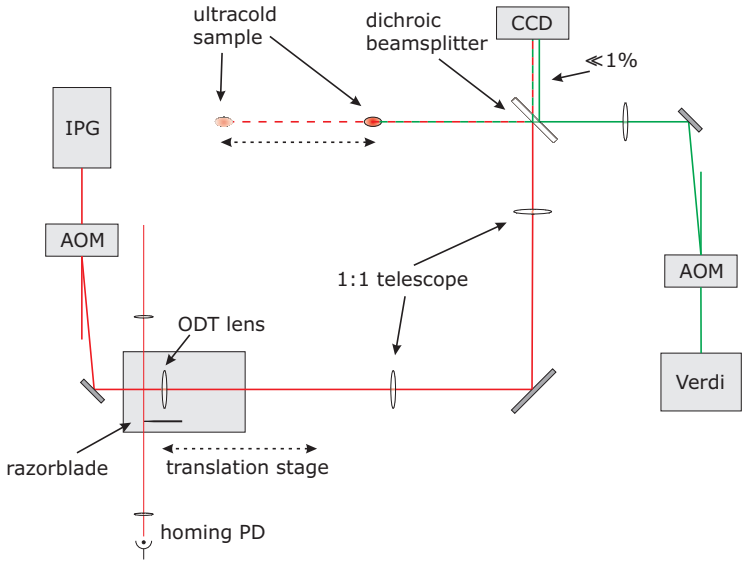

Figure 3.14: A schematic drawing of the push and optical transport optics. The optical trap is focused in free space and translated by a 1:1 atom on the ultracold atoms. The focusing lens is moved by a linear air bearing stage (see text) to transport the ultracold sample to the science cell. After each transport the stage is recalibrated on a laser beam focused onto a razorblade. The plug is focused onto the atoms through a dichroic beamsplitter combining it with the optical trap light. A small amount of the plug and optical trap beams which are reflected and transmitted respectively is imaged on a CCD camera to monitor the focal positions.

operating systems simplify batch processing and remote processing of data.

Hardware

The hardware used to control the experiment is built around the Control system developed by Todd Meyrath and Florian Schreck [127]. This system uses a 25-bit bus system to program various types of devices. At the moment of writing of this thesis the modules available include: digital outputs, analog outputs, analog inputs, an RF synthesizer and RF amplifier. In our setup only digital output and analog output modules have been implemented. Additionally a module to interface DDS evaluation boards on the bus system has been developed (see section 3.5.2), the design concept is a simple variant of the digital output boards. The bus operates with 16-data bits, 8 address bits and 1 strobe bit, running at a clock speed of 300 kHz. Each analog output is programmed by a 16-bit DA-converter occupying one of the 256 available addresses. The analog output can be programmed from -10 to +10V and is capable of driving a current of 250 mA. For the digital output, one address is occupied by every 16 digital output. The outputs are TTL-compatible and capable of driving 50Ω loads. For our experiment 80 digital output lines and 40 analog output lines have been implemented. The controlling PC is connected to the bus system by means of a 32-bit National Instruments Digital I/O card (NI6533). The system is very cost-effective and has proven to be very reliable.

Additional devices are programmed by the same computer through various protocols, including RS232 (for the fiber laser and the Feshbach coil power supply), USB (for the

AD9956 DDS's and an Apogee U13 CCD camera), GPIB (for a Fluke PM3394B oscilloscope and a Tulby Thandar Instruments 1906 multimeter) and Firewire (for the Sony X710 and SX90 CCD cameras).

Software

The software controlling the experiment is based on the Control software as developed in combination with the hardware described above, a detailed description can be found in Ref. [127]. The Control software is interfaced by a set of Visual C++ functions in which all outputs can be accessed. Variables can be defined which are accessible by a graphical user interface and which can be automatically scanned to perform measurements. The code is executed once to prepare the order of which digital/analog output lines have to be executed and peripheral devices can be pre-programmed. Subsequently the code is executed for a second time actually switching the digital/analog outputs and synchronized command are sent to peripheral devices. The digital/analog output commands are executed with a timing resolution of 3 μs. The free availability of this system in combination with its ease of use make it a good choice for ultracold atom experiments. In particular the programming of waveforms on any channel simultaneously can be done without any effort.

Some modifications to the software had to be made to adapt it to our setup. The main modification is that only the Control software is used, and not the data acquisition part Vision. We have developed image acquisition software capable of interfacing with the Control software while running on the same computer. The Firewire cameras are interfaced through a Visual C++ program exploiting the open-source driver 1394Camera [128]. The Apogee U13 Camera is controlled by a Visual C++ program exploiting the Apogee Alta driver, and is permanently running in the background. At the beginning of an experimental sequence the Apogee program is armed and for each Firewire camera an instance of the Firewire program is started. The exact triggers for all cameras are given by hardware triggers from a digital output. Images are acquired and saved in a Portable Gray Map format (PGM) to a local harddrive. All acquired images and experimental parameters are copied to a network drive from where the data analysis software analyzes the images. This configuration allows data acquisition to continue when network delays occur. The program to control the Maxon motor controller for the optical transport is written in Visual Basic 6.0 and is running on a separate computer. The program initializes the controller and programs the endpoints and sinusoidal trajectory of the transport. Triggers to start the transport and the homing sequence are provided by digital outputs of the main computer connected to the Maxon controller.

All on-line data analysis software is written in GNU C++ running on the Linux computer. The routines for fitting various 1D and 2D distributions to PGM images are compiled into a dynamic library. This library is accessed from command line programs to perform manual batch fitting to images, or from the graphical user interface. The graphical interface is written in Python 2.5.1 and uses the wxPython library for interfacing to the X-Windows environment and the cTypes library for interfacing the GNU C++ fitting library. The fitting program displays the absorption image, an optical density image, basic fit information like atom number and cloud sizes and an x and y-integrated 1D-profile to compare the fit result to the data. An instance of this program is run for each camera separately.

3.5.2 Radio-frequency and microwave sources

Due to the hyperfine structure of the alkali atoms being in the range of MHz-GHz energy scales, many radio-frequency (RF) and microwave (MW) have to be employed in experiments to manipulate the atoms. The RF and MW sources can be divided into two categories: sources used related to optical transitions and sources related to ground state hyperfine transitions. The former are used to shift the frequency of light by means of AOM's or EOM's and require frequency stability on the sub-MHz level (smaller than the natural linewidth). For this purpose voltage controlled oscillators (VCO's) are being used. These oscillators are cheap and easy to setup. The hyperfine states do not experience spontaneous decay and therefore the linewidth of the transition is determined by the coupling strength of the RF or microwave. This requires high frequency and power stability of the sources to drive coherent transitions between the hyperfine levels. For this purpose we employ Direct Digital Synthesis (DDS) technology.
Most AOMs in our setup are being controlled by VCO's from the ZOS series by Mini-Circuits. The only exception to this scheme is the Brimrose AOM (see figure 3.5), which shifts the light by the frequency corresponding to the potassium hyperfine splitting of about 1.2 GHz. A VCO with sub-MHZ drift would require a long term stability of the tuning voltage of the order of 1 mV. To avoid drifts we use a DDS as a frequency source for this AOM.

Analog Devices AD9956 DDS

Three AD9956 DDS's from Analog Devices are used in our setup. The DDS's are mounted on standard evaluation boards containing the circuitry for a VCO and a loop filter. These evaluation boards offer USB programming and the possibility of phase-locking a VCO to the DDS. All three boards are mounted with Crystek Microwave VCO's, two have a CV55BE1000-1500 for frequencies from $0.9 - 1.35$ GHz and one has a CV55CL225-425 for frequencies ranging from $200 - 350$ MHz. Each evaluation board is equipped with a loop filter adapted for the used frequency range, and configured in a manner as depicted in figure 3.15a. The devices are programmed through USB and to assure time-critical control over the frequencies, the I/O update and Profile Select lines are rewired to digital output ports of the main control system. Reprogramming of all three DDS boards are performed through the USB bus, synchronized with the experimental sequence. Triggers for frequency updating are subsequently given by a digital output line.

Analog Devices AD9858 DDS

During the coarse of the experiment the setup was extended with four additional DDS sources. We chose for an alternative to the AD9956 to have a more flexible control over the frequencies as compared to the USB programmed AD9956's. Four Analog Devices AD9858 DDS evaluation boards are used in our setup. These DDS's are parallel programmed through the bus system, facilitating the change of DDS frequency to its full 32-bit frequency accuracy every five clockcycles (15 μs). An interface to the bus system has been developed based on the design of the 16-bit digital output card, with the addition of a demultiplexer stage to allow control over all 18 bits of the evaluation board with a single 16-bit bus module. One of the DDS boards is equipped with a CV55BE1000-1500 VCO to access the 1.0-1.3 GHz frequency range. This VCO is phase-locked to the

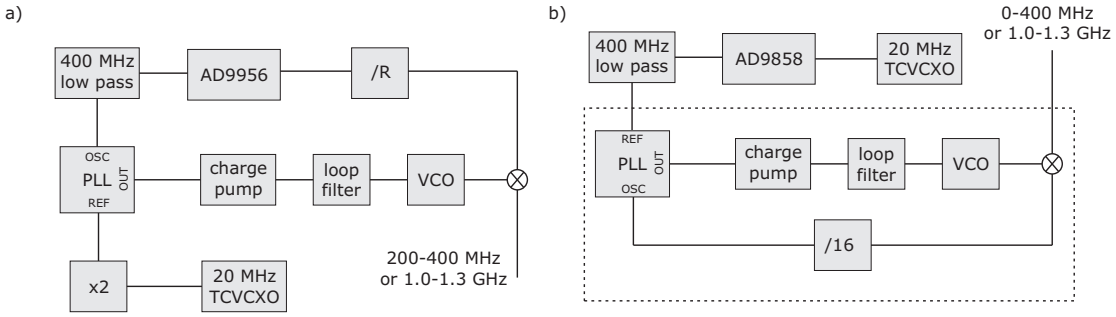

Figure 3.15: The two DDS setups. a) the setup of the USB programmed AD9956 set up in a fractional divider loop, the divider /R divides by 4 for the 1.0-1.3 GHz boards and is bypassed for the 200-400 MHz board. b) the parallel programmed AD9858 is set up in a direct upconversion scheme. The dotted box in b) is only present for the 1.0-1.3 GHz output.

application	Manufacturer	model	P (W)
AOM f<150 MHz	MiniCircuits	ZHL-3a-S	1
AOM f>150 MHz	MiniCircuits	ZHL-2-S	1
Brimrose AOM	Hughes	700-1400MHz 2W	15
K hyperfine	MiniCircuits/RSE	ZHL-2-12/PA 15-23	15
Li hyperfine	MiniCircuits	ZHL-20W-13	20
Zeeman levels	MiniCircuits	TIA-1000-1R8	4

Table 3.2: The RF and microwave amplifiers used in the setup. The various AOMs are described in Sect. 3.3.1, the potassium and lithium hyperfine manipulation in Sect. 3.5.2 and state preparation on the Zeeman levels for potassium and hyperfine for lithium in Sect. 3.5.4.

DDS according to figure 3.15b. All four boards use a 2 GHz clock provided by an Analog Devices AD9516 clock generator evaluation board.

The clock generator is running with an external 20 MHz clock as a reference. This clock is provided by a temperature compensated voltage controlled crystal oscillator (TXVCXO) from IQD Frequency Products (LF PTXO000006), which has a long term stability of ± 1 ppm. Both the AD9956 and AD9858 DDS's with the phase locked VCO's have a measured linewidth smaller than 100 Hz, more than sufficient for the experiments performed in this thesis.

RF and MW amplification

The amplitude of the RF and MW from the frequency sources is controlled by various combinations of amplifiers, voltage controlled attenuators and switches. Table 3.2 lists the amplifiers used for the different applications. The power of the RF signals are controlled by MiniCircuits voltage-variable attenuators (ZX73-2500+) and switches (ZASWA-2-500R+).

coil	frequency range	position	z (mm)	n	r (mm)	$\varnothing$ (mm)
K hyperfine	1.1-1.3 GHz	main	34	1	19	0.54 (RG316)
Li hyperfine	200-400 MHz	main	34	1	10	0.5
Zeeman levels	0-10 MHz	main	34	7	10	0.5
Field calibration	1.0-2.0 GHz	appendix	15	1	6.5	0.5

Table 3.3: The antennas used to manipulate the hyperfine states of the potassium and lithium. The listed properties are the frequency range for operation, the position on the vacuum system, the distance from the sample z, the number of windings n, the coil radius r and wire diameter $\varnothing$.

RF and MW antennas

The generated RF and MW frequencies used to manipulate the ground state properties of the atoms are amplified and subsequently radiated by means of simple antennas. Four antennas are integrated in the setup (see table 3.3): one at the science cell to perform field calibration of the Feshbach field on the potassium hyperfine splitting (~ 1 GHz) and three in the main chamber: one for the potassium hyperfine splitting ($1.0-1.3$ GHz), one for the lithium hyperfine splitting ($200-400$ MHz) and one for the Zeeman splitting at low field ($0-10$ MHz). The 1.2 GHz coil for the potassium in the main chamber consists of a BNC cable of which the shielding is stripped and the core makes a loop of 19 mm radius ($\approx \lambda/2$ circumference). The coil radiates more than 50% of the power over the frequency range of $1.1-1.3$ GHz, however, there are strong resonances yielding a non-linear response. The coil is tuned to resonance with a triple-stub tuner to achieve a flat frequency response over the range $1.1-1.3$ GHz. The field calibration antenna is directly connected to the VCO output of the AD9956 evaluation board. For the field calibration and the Li hyperfine antennas three-port circulators (SIAM CT3.002 and McManus Microwave model 253) are connected to attenuate microwaves reflected from the antenna and protect the VCO and amplifier respectively.

3.5.3 Imaging

Three methods of imaging have been performed for the experiments described in this thesis, low field and high field absorption imaging and fluorescence imaging. In all cases (near)resonant light is scattered by the atomic sample. For absorption imaging light is scattered from a laser beam hitting the camera and the signal consists of the missing scattered photons. For fluorescence imaging the light is scattered from a laser beam *not* hitting the camera and the signal consists of the scattered photons which are collected by the camera. Fluorescence imaging is used for the lithium-beam measurements as presented in Chapter 4 and for MOT-recapture measurements. An atomic sample trapped in a MOT scatters many photons per atom without changing the number of trapped atoms, therefore the integration time for collecting fluorescent light can be very long yielding a good signal to noise ratio. Absorption images are generally taken on ballistically expanding or ultracold samples. This yields a short interaction time for the imaging pulse with the sample and few photons can be scattered per atom, thus a smaller signal to noise ratio is achieved as compared to fluorescence imaging in a MOT. In our experimental setup fluorescence imaging is only possible in the MOT area, therefore we have used this to characterize the MOT and magnetic trap. Obtaining absolute atom numbers from

fluorescence data is involved, the fluorescence signal of a MOT depends for example on the excited state fraction, ratio's of trap and repumper light and the solid angle of captured light. Therefore fluorescence imaging was only used to perform relative measurements and absolute atom numbers have always been obtained by absorption imaging.

Near-resonant imaging light for both species is obtained by means of double-pass AOM's (see figure 3.5 and 3.7). Each color is divided over two beams by half waveplates and polarizing cubes, recombined on bichromatic beamsplitters and coupled into polarization maintaining fibers (Schäfter + Kirchhoff PMC-630-4.5-NA011-3-APC-150-S). With this setup we have two fibers, one for imaging along the horizontal axis and one for the vertical axis, containing both colors controllable by the AOM's. The fiber for vertical imaging can be connected to either of two collimators for vertical imaging in the main chamber or in the science cell. Imaging along the horizontal axis is performed with linear polarized light and along the vertical axis with circular polarized (σ^+) light in both cases. During the imaging pulse a light pulse resonant with the repump transition is also applied to prevent leaking to dark states. These beams are under 45° with the imaging path, where the beams are retro-reflected to avoid a force being exerted on the atoms by the repump light.

During the imaging pulse the atoms absorb photons along the propagation axis of the imaging pulse and re-scatter photons in random directions. The former causes an acceleration which shifts the atoms out of resonance and the latter causes a random walk of the atoms during the imaging pulse which leads to blurring of the image [129, 61]. For a low saturation parameter $s_0 \ll 1$ the number of photons scattered off an on resonance light pulse is given by: $N_p = (s_0/2)\Gamma\ \Delta t$, with Γ the natural linewidth and Δt the duration of the imaging pulse. The longitudinal Doppler shift of an atom due to this pulse is $\omega_D = v_r N_p k$ where $v_r = \hbar k/m$ is the recoil velocity and k the wavevector of the imaging light. The transverse displacement is given by: $r_{rms} = \sqrt{N_p/3} v_r \Delta t$. Typical parameters in our experiment are a saturation parameter of $s_0 = 0.1$ (0.07) and a pulse duration of $\Delta t = 40$ (100) μs for the lithium(potassium), this results in a blurring of $r_{rms} = 19$ (9) μm and a shift out of resonance by $\omega_D/\Gamma = 1.8$ (0.4). During the imaging pulses for each species two counter-propagating beams of repump light are applied under 45° with the imaging path. This creates an one-dimensional optical molasses for atoms in the $F = 1/2$ and $F = 7/2$ hyperfine states for lithium and potassium respectively. Due to the unresolved hyperfine structure of the $^2P_{3/2}$ hyperfine state of lithium the lithium atoms spend a significant amount of time in the lower hyperfine state, resulting of a cooling of the atoms due to the counter-propagating repump beams. We have verified that for the lithium cloud the obtained atom number is insensitive to the imaging pulselength Δt, indicating that the repumper effectively cools the heat imposed by the imaging pulse and suppresses the shift out of resonance ω_D. Concluding, although the lithium imaging suffers strongly from the blurring effects the atom number can be reliably obtained in this manner. For analysis of the lithium density-profiles on the order of the r_{rms} a shorter pulselength or lower intensity should be used. The experiments presented in this thesis on lithium clouds do not require spatial analysis on the order of r_{rms}.

Images are analyzed by the conventional method where an absorption image is taken I_{abs}, subsequently a reference image I_{ref} of the optical field and a background image I_{bg} are taken without any imaging pulse. The signal is obtained as: $I/I_0 = (I_{abs} - I_{bg})/(I_{ref} - I_{bg})$. For the Sony camera's I_{bg} was found to be negligible, therefore this image is omitted in the analysis of the Sony data. For low saturation parameters the column-density of the

atomic distribution is obtained by evaluating the Lambert-Beer law:

$$\frac{I(x,y)}{I_0(x,y)} = e^{-OD},$$

where $OD = \sigma n(x,y)$ is the optical density, $n(x,y) = \int dz\, n(x,y,z)$ is the column density along the propagation axis of the imaging beam and σ is the optical scattering cross section of the imaging pulse with the atoms, given by

$$\sigma = \kappa \frac{3\lambda^2}{2\pi} \frac{1}{1+(2\delta/\Gamma)^2},$$

where κ accounts for the Clebsch-Gordan coefficients of the possible transitions, $\kappa_{Li} = 1/2$ and $\kappa_K = 2/5$ for linearly polarized light and $\kappa = 1$ for circular polarized light, for the lithium $F = 3/2 \rightarrow F' = 5/2$ and potassium $F = 9/2 \rightarrow F' = 11/2$ transitions. We have cross-checked the absolute atom number calibration by comparing the atom number of vertical imaging with horizontal imaging. The effective pixel-size of the horizontal cameras have been calibrated by measuring the free fall of an ultracold potassium cloud from the optical trap. The resulting vertical position scales according to: $y(t) = g/2\ t^2$ where $g = 9.8$ m/s is the gravitational acceleration. The effective pixel sizes of the vertical camera's have been calibrated on a 1951 USAF Resolution Target. For the Sony SX90 camera with a $1:1$ telescope on the science cell(main chamber) we find an effective pixel size of 3.60 μm(3.67 μm) and for the Apogee with a $\times 4$ objective we obtain 3.94 μm.
The absorption and reference image are taken within 500 ms with the Sony camera's, limited by readout time. The Apogee U13 camera is used in a fast kinetics mode. This method exposes only part of the CCD array which is shifted to a masked area before the next exposure is performed. This method allows fast consecutive image to be taken before the slow electronic readout is performed. The Apogee U13 camera is capable of shifting CCD-lines at a rate of 45 μs/line. For a 512-line kinetics image this results in a minimum of 25 ms between the absorption and reference image. For an optically trapped cloud after typical time of flights only 65 pixels are require to to image the complete cloud. This results in 3 ms between the absorption and reference image.
Four cameras are used to perform imaging of the ultracold sample. Two Sony SX90 Firewire cameras are imaging along the optical trap axis, where flippable mirror mounts allow to change between imaging in the main chamber and imaging in the science cell (see figure 3.16). Vertical images are taken in the main chamber by a Sony X710 camera and in the science cell by an Apogee Alta U13 camera.

High resolution imaging

The small dimensions of the science cell allow to image the ultracold sample with a high numerical aperture, resulting in a high optical resolution without the need of special optics. To test the high-resolution possibilities we have mounted a Sony SX90 camera with a standard DIN x4 microscope objective (Edmund Optics NT36-131) directly imaging the ultracold sample in the science cell without any additional optics. Using the $\times 4$ magnification the SX90 camera has an effective pixel size of 0.94 μm. Using the USAF test target we clearly resolve ($> 40\%$ contrast) the smallest elements, spaced at 4.4 μm. Taking this spacing to be the minimum resolved according to the Rayleigh criterion [130] we can obtain an upper limit for the imaging resolution. This corresponds to an imaging resolution of ~ 3 μm ($1/e^2$ radius) of a single point source.

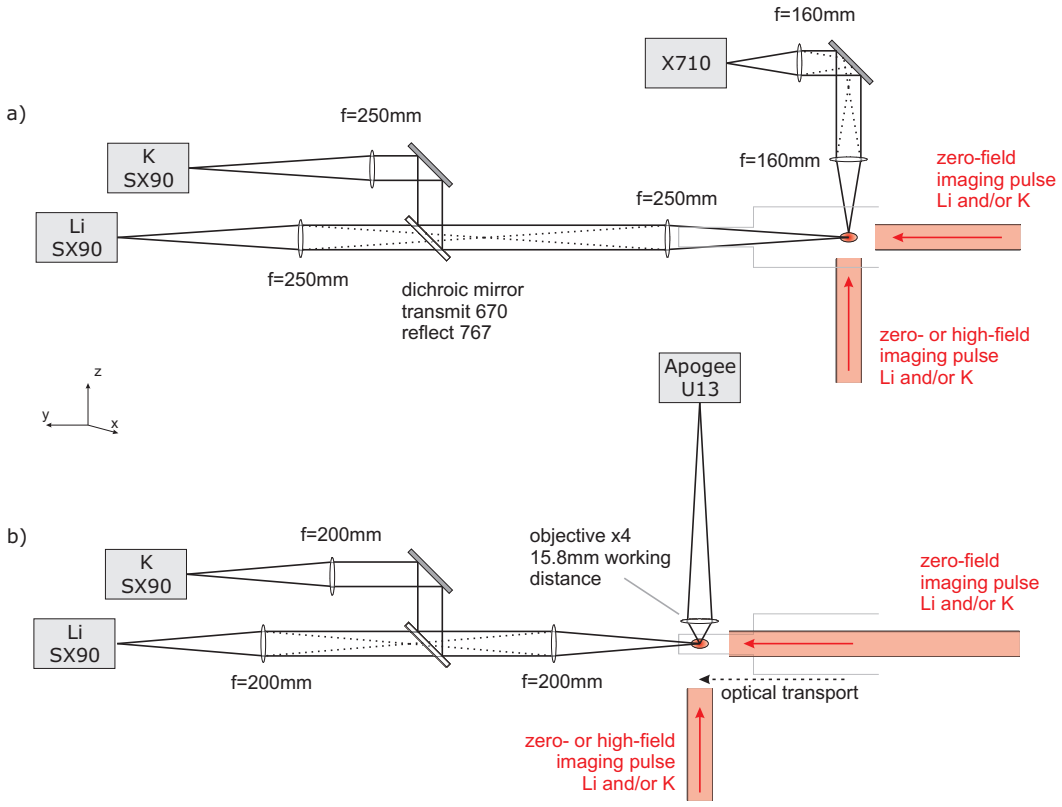

Figure 3.16: Imaging optics for imaging in a) the main chamber and b) the science cell. All $f = 250$mm and $f = 200$mm lenses are mounted on flippable mounts. This allows fast and reproducible switching between the two imaging setups. The vertical imaging in the science cell is done by directly imaging with a standard $\times 4$ microscope objective. The position of the vacuum system is shown in light grey.

3.5.4 Spin state preparation and purification

Control and characterization of spin states is an essential tool to perform experiments on ultracold gases. In particular systems involving a species with a high nuclear spin like ^{40}K require additional care since many spin states can be magnetically trapped. In this section a few methods will be discussed to manipulate the spin mixture of an ultracold potassium cloud.

Stern-Gerlach analysis The composition of spin states is measured by means of a Stern-Gerlach experiment. During the expansion of the ultracold sample a field gradient of $B' = 110$ G/cm is pulsed for the first 4 ms followed by a free expansion for 3 ms. The gradient is applied by pulsing on the quadrupole trap and the vertical shim coil generating a homogeneous field of 28 G. This method yields a gradient of $B' = 110$ G/cm with an absolute value of $B = 28$ G therefore the linear Zeeman effect dominates the separation of the spin states. Figure 3.19 shows typical Stern-Gerlach measurements. To perform a Stern-Gerlach experiment the atomic sample has to expand slower than the separation takes place. Due to the relatively small waist of the optical trap Stern-Gerlach analysis could only be performed on a cloud which was evaporatively cooled in the optical trap and had sufficiently low trapping frequencies. The measurements in figure 3.19 were taken with a radial trapping frequency of $\omega_r = 2\pi \times 560$ Hz and at a temperature of $T = 450$ nK.

State purification: microwave cleaning in the magnetic trap The optical plug induces an effective B_0 in the trap along the weak axis of the quadrupole field (see section 3.4.3) of 250 mG. Evaporation at the plug (inner) side of the cloud can be performed to selectively remove undesired spin states. Figure 3.17a and b show the truncation parameter $\eta = U_0/k_BT$ and the density as a function of the frequency f_0 to drive the $|F = 9/2, m_F\rangle$ state to an untrapped $|F = 7/2, m_F - 1\rangle$ state. These curves are calculated for a plug size(height) of 16 μm(670 μK) and a cloud of $T = 20$ μK. Evaporating from high frequency down spills spin states with preferably small m_F, purely selective spin addressing is only possible for temperatures of $\lesssim 1$ μK.

State purification: axial spilling After pre-cooling the ultracold sample in the magnetic trap it is transferred into the optical trap (see section 3.4.4). This transfer is performed by adiabatically ramping up the optical trap power followed by adiabatically ramping down the magnetic field. For the method considered here we consider the case that the optical trap is ramped on and the magnetic field is still at its full compression. At this moment the confinement of the ultracold cloud is radially determined by the optical trap and axially by the magnetic trap. Applying a homogeneous magnetic field shifts the magnetic trap center away and applies an offset field over the extent of the ultracold cloud. This offset field enables to drive the $|F = 9/2, m_F\rangle$ atoms to a $|F = 7/2, m_F - 1\rangle$ high field seeking state, therefore high field seeking states can be selectively evaporated along the axial dimension of the optical trap. Figure 3.18b shows the axial and radial trap shapes for a shifting field of 10.4 G and a trap depth of $U_0 = 150$ μK. A microwave sweep for 100 ms over a frequency span of 200 kHz is performed to evaporate the magnetically trapped states. Figure 3.18a shows the loss spectrum of a $T = 20$ μK cloud as a function of the starting microwave frequency. The features are well resolved therefore this method

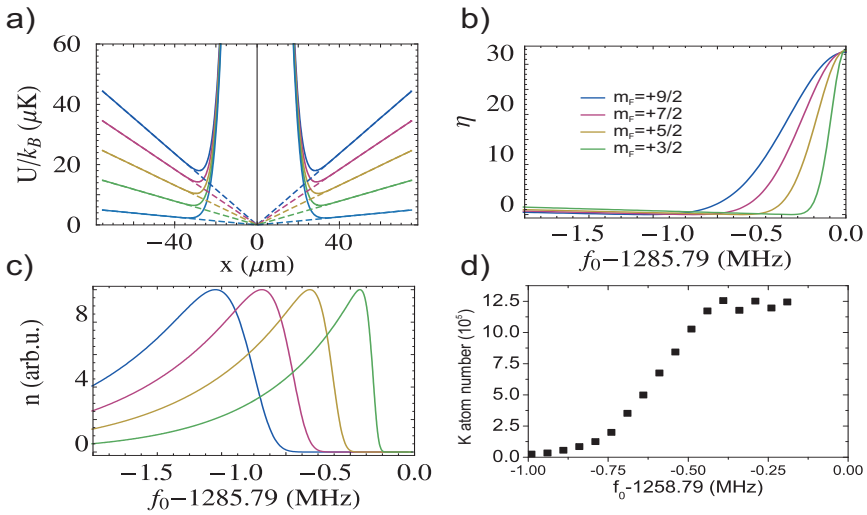

Figure 3.17: Microwave cleaning of the potassium spin states in the optically plugged quadrupole trap. a) The optically plugged quadrupole trap. Due to the plug a minimum magnetic field B_0 is experienced by the atoms. b) The calculated η parameter of various spin states as function of the microwave frequency for $T = 20\mu$K. For finite T the peaks overlap, for $T \to 0$ the peaks become isolated and selective addressing of the spin states is possible. c) Normalized density for each spin state. The spacing between the peaks is determined mainly by the plug parameters and the cloud temperature determines the wings towards the left (lower frequencies). d) A measurement of the atom number left after a microwave sweep from 1285.79 MHz down to a final frequency f_0 for a cloud of $T \simeq 20\mu$K.

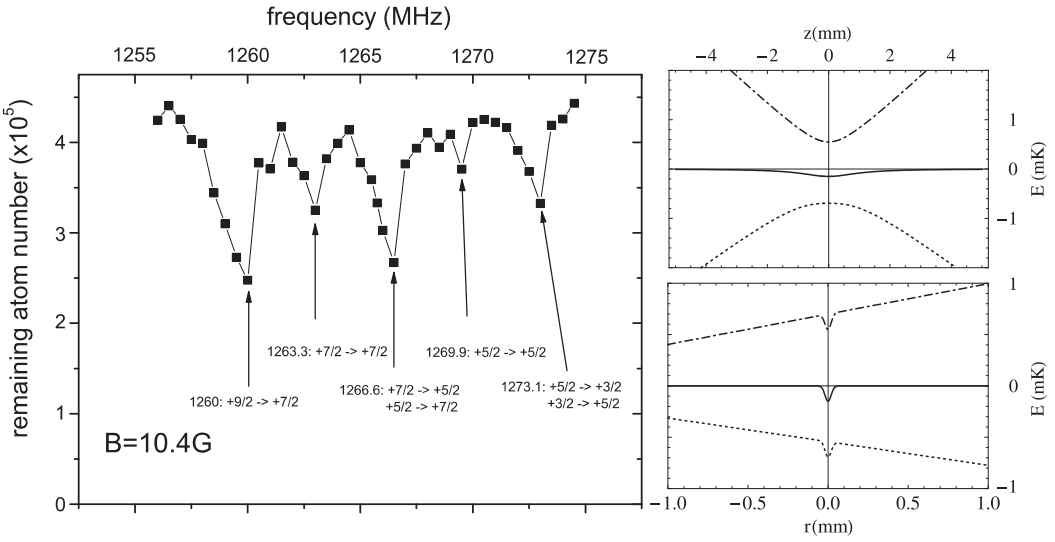

Figure 3.18: Selective axial spilling in a combined optical and magnetic trap. a) loss spectrum of a trapped spin mixture of ^{40}K, the various loss features are labeled. b) axial (radial) trap shape in the upper (lower) panel, the dash-dotted (dotted) line shows the combined optical and magnetic trapping potential for the $|9/2, +9/2\rangle$ ($|7/2, +7/2\rangle$) state and the solid line shows the optical potential. The magnetic trap is shifted radially by applying a homogeneous magnetic field, hardly affecting the radial potential but creating an axially anti-trapping potential for high field seeking states.

allows to selectively address each spin state and does not heat the sample, a disadvantage is that the method is only applicable to low field seeking states.

State purification: low field microwave + optical purification In an optically trapped sample with a homogeneous magnetic field the $F = 9/2$ hyperfine states can selectively be transferred to the $F = 7/2$ manifolds by means of an adiabatic microwave sweep. Subsequently the complete $F = 7/2$ manifold can be cleaned by an optical light pulse on the $^2S_{1/2} \rightarrow^2 P_{3/2}$ transition. For this experiment the ultracold sample is evaporatively cooled in the optical trap by ramping down the laser power to 2% of its initial value to enable a Stern-Gerlach analysis. Figure 3.19 shows the various stages of the cleaning process. Figure 3.19a shows the ^{40}K spin mixture in the optical trap after loading from the magnetic trap and evaporative cooling in the optical trap. Figure 3.19b is after an adiabatic sweep transferring the high m_F values on the low m_F values followed by the optical trap evaporation. The sweep is performed at a magnetic field of $B = 9.4$ G and the frequency is swept linearly from 3.0 MHz to 2.7 MHz in 10 ms. For figure 3.19c the optical trap evaporation is followed by a linear microwave sweep from $fs = 1302$ MHz to $fs = 1304$ MHz in 60 ms during which light resonant with the $^2S_{1/2}|F = 7/2\rangle \rightarrow {}^2P_{3/2}|F' = 9/2\rangle$ transition is switched on. This method selectively removes the $m_F = -7/2$ state, however due to optical pumping it populates the other m_F states. This optical pumping can be circumvented by applying the optical pulse on the $^2S_{1/2}|F = 7/2\rangle \rightarrow {}^2P_{3/2}|F' = 5/2\rangle$ transition since the $F' = 5/2$ excited state can only decay to the $F = 7/2$ groundstate.

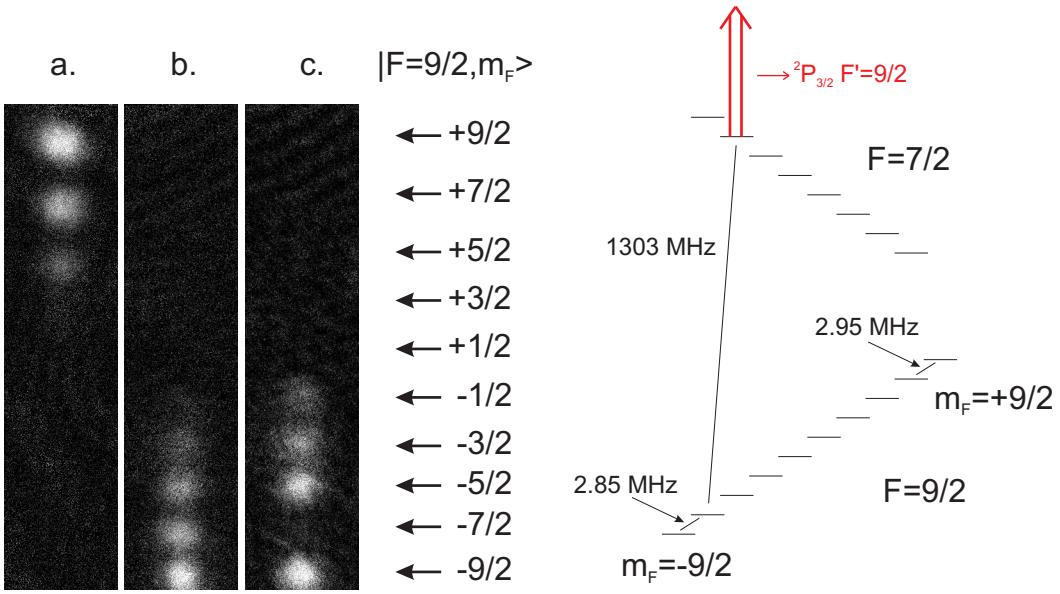

Figure 3.19: Purification of a spin mixture of ^{40}K. a) original spin mixture of high m_F states, b) after the adiabatic sweep transferring to the low m_F states, c) after the two-photon removal of the $m_F = -7/2$ state. d) level scheme at a magnetic field of $B = 9.3$G where this state purification is performed.

State purification: high field optical purification For high magnetic fields the Zeeman energy is much larger than the hyperfine energy. For the lithium (potassium) groundstate the hyperfine field corresponds to $B_{hf,Li} = 27$ G ($B_{hf,K} = 357$ G), see Fig. 2.2. For magnetic fields $B \gg B_{hf}$, the nuclear spin decouples from the electronic spin and a good basis to describe the hyperfine states is the $|m_I, m_J\rangle$ basis, where I is the nuclear spin and $J = L + S$ is the total electronic angular momentum: the sum of the orbital angular momentum and the electronic spin. An optical transition can couple a $m_J = +1/2$ groundstate to a $m_J = +3/2$ excited state. This state can only decay back to its originating $m_J = +1/2$ state. Therefore such a transition is a cycling transition and will efficiently exert a force on only one spin state. For intermediate fields the nuclear and electron spin are not completely decoupled, therefore, optical pumping of the potassium to different groundstates will occur. This method is therefore efficient to empty one specific spin state, however it will populate others if the magnetic field is not sufficiently high. We have used this method in the Feshbach width measurement (see chapter 6) to remove possible impurities from the potassium $|9/2, +3/2\rangle$ state, which due to a nearby Feshbach resonance could cause significant losses.

Adiabatic sweep state preparation To manipulate the potassium spin states we apply a homogeneous magnetic field of 9.3 G and sweep an RF frequency from $f_s = 3.0$ MHz downwards in 10 ms to a variable end frequency $2.7 < f_e < 3.0$ MHz. The end frequency determines the final spin composition of the mixture. Figure 3.19b shows the spin mixture after a sweep to $f_e = 2.7$ MHz showing a nearly complete transfer of the spin mixture before the sweep (see figure 3.19a) to the negative m_F values.
Lithium state preparation is performed by applying a fixed microwave frequency and sweeping the magnetic field. This method yields a smoother sweep and results in a higher

transfer efficiency as compared to sweeping the frequency for a fixed magnetic field value. Lithium in the state $|F = 3/2, m_F = +3/2\rangle$ is transferred to the $|F = 1/2, m_F = +1/2\rangle$ state with $\sim 50\%$ efficiency.

3.5.5 Feshbach Coils

The field of ultracold gases has been tremendously enriched by the ability to tune interactions by means of Feshbach resonances. To be able to control the scattering length accurately one needs to have a good control over the magnetic field applied to the ultracold sample. This requires a high stability, reproducibility, calibration and homogeneity of the magnetic field over the sample size. Since the properties of Feshbach resonances are very diverse in terms of positions and widths magnetic field coils have to be designed according to the needs for a specific system. We have chosen for a design with high field homogeneity and stability.

Mechanical Construction

Figures 3.20 and 3.21 show the design of the Feshbach coils as used in our setup. The concept of high field homogeneity and stability is achieved by having a Helmholtz configuration and many windings running a relatively small current to achieve a high and uniform current density with a square cross section. Additionally, the coils are wound anti-symmetrically; i.e., with opposing helicity, around the center. Therefore, the current-density of the coil system is also anti-symmetric around the origin

$$\vec{j}(\vec{r}) = -\vec{j}(-\vec{r}) \tag{3.3}$$

The total magnetic field in the origin is the sum of the magnetic field vectors generated by each coil. Expanding the total magnetic field in the origin in powers of r will only contain even terms due to Eq. 3.3. Any field inhomogeneity occurring from the finite size of wire bends or lead wires is cancelled to first order due to this configuration. The coil mount is chosen to be made from brass for the best compromise of high thermal conductivity and good mechanical properties[3]. The brass housing is cut to avoid creating an inductance loop and the brass volume is impoverished to reduce the volume where eddy-currents can occur.
Each coil contains of 126 windings wound as a continuous helix to avoid strong field inhomogeneities which would be caused by stepwise going to the next winding. The inhomogeneities caused by these types of steps would also be compensated by the second coil due to Eq. 3.3, however, it is very sensitive to the exact placement of the steps, therefore this method is much more sensitive to the winding procedure compared to a helix-wound coil. Additionally, with a helix-wound each layer can be easily filled up with an integer number of windings. To offset the thread at each layer, CNC machined glass-fiber (G10) spacers are included at the start of each layer. The step needed to lift the wire from one layer to the next layer is also performed in a gradual manner: the wire is lifted by its thickness over one complete circumference, this is also aided by including glass-fiber

[3] An interesting alternative are thermally conductive plastics, like the D5506 Thermally Conductive Liquid Crystalline Polymer from CoolPolymers. This polymer is electrically insulating and has a thermal conductivity of 10 $\mathrm{Wm^{-1}K^{-1}}$. We have performed preliminary tests on using this material for a coil mount, which yield good results.

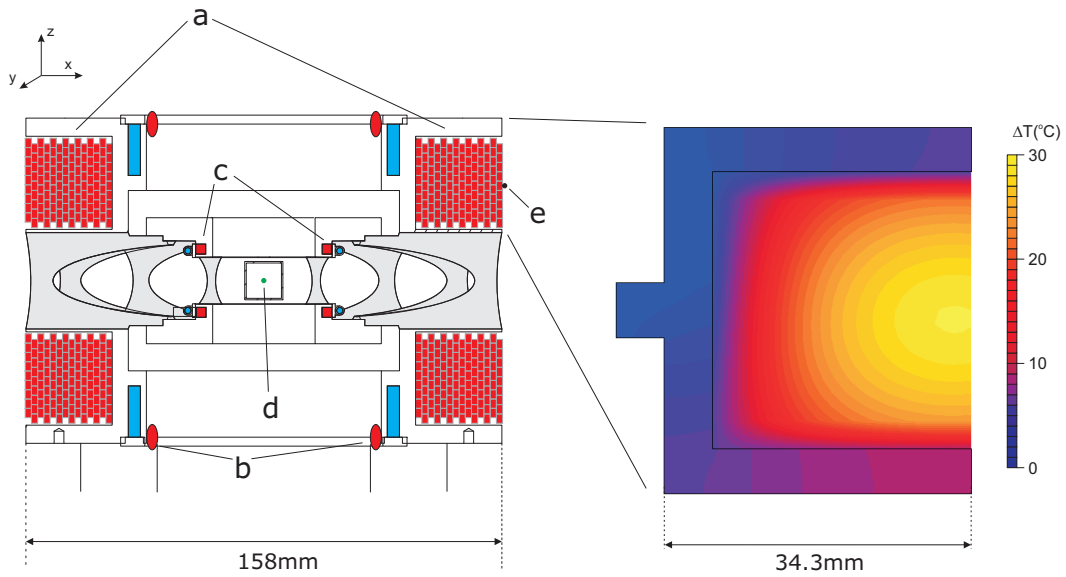

Figure 3.20: A schematic of the Feshbach coil (left) depicts the various sets of coils. a) main coils, b) trim coils, c) sweep coils, d) ultracold sample and e) thermistor location (see text). The grey indicates the brass, blue indicates the water cooling and red the coils. All coils create a magnetic field along the z-axis. A finite element calculation of the thermal distribution in the coil (right) depicts the maximum equilibrium temperature achieved in the coil while running $I = 28.5\text{A}$ to obtain a field of $B = 500\text{G}$.

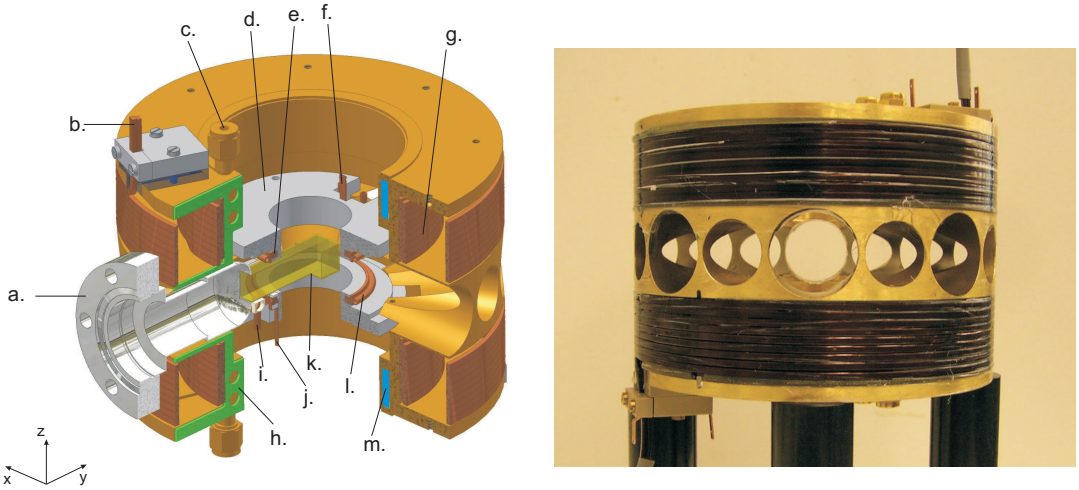

Figure 3.21: CAD drawing (left) and photograph (right) of the Feshbach coils. The monolithic brass mount (beige) ensures exact placing of the coil windings at the Helmholtz distance. The sweep coil is positioned also at the Helmholtz distance by a PEEK holder (light grey). To avoid eddy current the amount of brass is minimized and the mount is cut in two and rejoined with a glass-fiber spacer (green).

spacers. Rectangular 3×2 mm copper wire (Romal BV) is used to wind the coil, yielding a high copper filling fraction. While winding the coil, Stycast 1266 epoxy is applied to fix the positions of the windings and avoid air-pockets between the windings. Although epoxies with larger thermal conductivity coefficients are available the low viscosity of Stycast 1266 ensures a very thin film between the windings thus the heat conduction in the coil assembly is limited by the electrical isolation layer of the wires. During the winding procedure the wire is kept at a continuous tension of ~ 20 MPa to assure compression of the epoxy up to the maximum allowed operation temperature of $\Delta T \simeq 30°$ C above room temperature.
Two smaller coils (sweep coils) are mounted inside the large coils to provide the ability to do fast magnetic field sweeps. Figures 3.20 and 3.21 show the placement of the sweep coils with respect to the science cell. The mutual inductance between the coils is minimized to avoid crosstalk between the power supplies of the two pairs of coils. Each sweep coil has a diameter of 21 mm and consists of 10 windings of Laminax B-series foil (Alphacore). This copper foil has dimensions of 3.175×0.254 mm an a 25.4 μm thick Kapton isolation layer bonded on one side. The coil is wound on a PEEK holder which is mounted in the main coil mount. Water cooling of the sweep coil is applied from the outside by clamping a water cooled copper strip around the last layer. During the winding procedure Stycast 1266 epoxy is continuously applied to keep the windings in place and facilitate thermal conductivity. Just as the main coil set, this set of coils has an anti-symmetric current density with respect to the origin to cancel out finite size effects of the windings.
Furthermore two simple coils (trim coils) are placed at a spacing larger than the Helmholtz distance to allow trimming of reminiscent magnetic field gradients or curvatures. These coils have a radius of $r = 37$ mm and consist each of 15 windings of copper wire ($\varnothing$1 mm) fixed in place 5 cm from the field center by Araldite epoxy. No water cooling is applied to these coils since only small currents are required for trimming of the field. The coils yield a gradient of 43 mG/mm/A when running currents in opposite direction.

Field homogeneity

We characterized the magnetic field profile using a XEN-1200 (Xensor Integration) field probe, which has a digital resolution of 3.3 mG up to an absolute field value of 100 G. Figure 3.22a shows the measured axial field of the main coils where the environmental field gradient of 6 mG/cm has been subtracted, the red line indicates the design value without any fit performed. To characterize the remaining inhomogeneities we fit the magnetic field profile to a polynomial in the axial position z. An ideal Helmholtz coil would follow the form $B(z) = B_0 - B''''z^4 + \mathcal{O}(z^6)$, however to quantify the field inhomogeneities we include the first two orders of correction terms proportional to z and z^2: $B(z) = B_0 - B'z - B''z^2 - B''''z^4$. The fitted values of the main coil are $B'/B_0 = 1.5 \times 10^{-6}$ mm^{-1}, $B''/B_0 = 6 \times 10^{-6}$ mm^{-2} and $B''''/B_0 = 5 \times 10^{-8}$ mm^{-4}. Figure 3.22b shows the same characterization for the sweep coil, here the red line indicates the fitted curve with the fit parameters $B'/B_0 = 4 \times 10^{-4}$ mm^{-1}, $B''/B_0 = 9 \times 10^{-6}$ mm^{-2} and $B''''/B_0 = 4 \times 10^{-6}$ mm^{-4}. Clearly the magnetic field of the sweep coil is less homogeneous than that of the main coil due to its smaller size and less windings. However, the sweep coil is only used for a magnetic field of a few Gauss around the offset field generated by the main coil, therefore the absolute homogeneity is comparable for the two coils.
At the position of the ultracold sample magnetizable objects from the rest of the setup

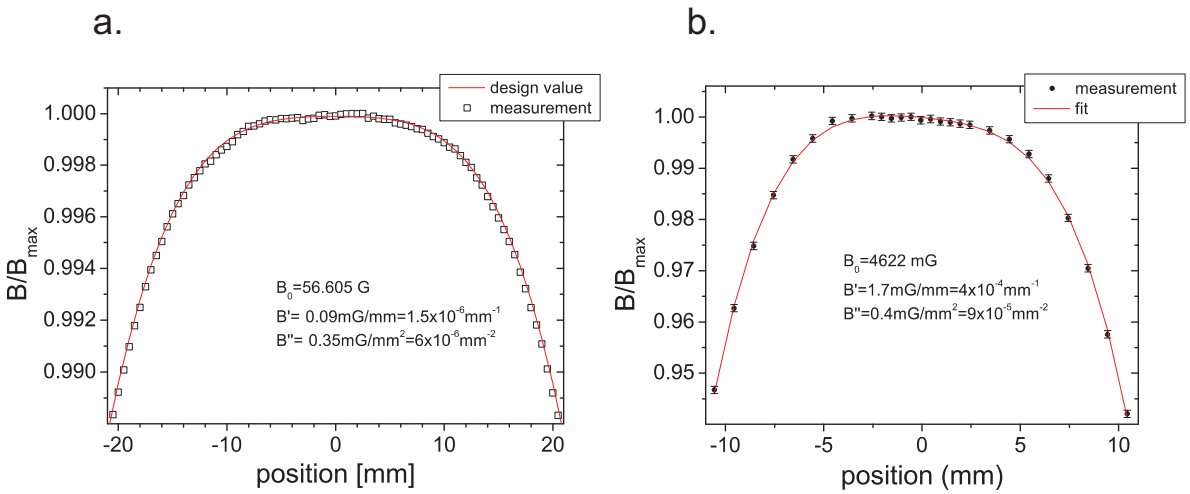

Figure 3.22: homegeneity measurements of the main coil (a) and of the sweep coils (b). The red curve in a) shows the design value, and the red curve in b) shows a fit (see text). The error bars in b) indicate the probe resolution (negligible in a))

generate a small gradient. The main source of this gradient originates from the reminiscent magnetization of the (non-magnetic) optical table, placing it higher above the table significantly reduces the gradient. Using a current density through both trim coils of $\vec{j}_{tr} = 0.005 \times \vec{j}_m$, where $\vec{j}_m$ is the current density through the main coil, the gradient is reduced again to $\sim 10^{-6}$ mm^{-1}.

Thermal properties

A finite element calculation has been performed by the UvA mechanical design office [131] to quantify the thermal and mechanical aspects of the coil design. The effective thermal conductivity of the wires filled with Stycast and the G10 fillings have been calculated separately. The radial(axial) thermal conductivity coefficient is $\kappa_r = 2.5$ Wm^{-1} K^{-1} ($\kappa_z = 3.7$ Wm^{-1}K^{-1}) for the Stycast filled windings and $\kappa_r \simeq \kappa_z = 1$ Wm^{-1}K^{-1} for the first and last winding of each layer filled with the G10-spacer. The thermal conductivity of brass is 109 Wm^{-1}K^{-1} therefore it suffices to apply water cooling only at one side of the coil. As can be seen in figure 3.20b the thick mass of the brass is chosen such that the coil is effectively cooled from three sides. The water cooling has a pressure of 2 bar. Figure 3.20b shows the calculated temperature for a current of $I = 28.5$ A, generating a field of $B_0 = 500$ G, at this field the maximum and average temperature of the coil are $T_{\max} = 28°$ C ($T_{av} = 20°$ C). For a field of 500 G the average temperature of the coil is measured by monitoring the change in resistivity of the copper coil wire, it increases to 23° C with an exponential time constant of ~ 4 min. During a run of the Feshbach resonance measurements the coil temperature is monitored at its hottest point with a thermistor (see Fig. 3.20) . The maximum temperature is found to be constant to within 0.1 °C for a period of two hours, limited by the temperature drift of the lab cooling water.

Current source and switching

The use of a brass coil mount with two 126-turn coils raises the question how fast the coil can be switched. Eddy currents which are induced due to switching the magnetic field and the large number of windings could slow down the rate at which the field can be controlled. We have characterized the switching speed of the coil by using the switching electronics of the magnetic trap (see section 3.4.3). The current is measured by means of a Hall probe, and switched off from a typical Feshbach field of 110 G. The current switches off with an initial slope of 849 G/ms. Although our coil design was not optimized for fast switching the coil turns out to be capable of switching at speeds comparable to reported from other Feshbach resonance experiments [44, 132]. A Danfysik Model 858 power supply is used as a high stability current supply for the Feshbach coils. The supply is specified to achieve a current stability of ±1ppm (30 min) and ±3ppm (8 hours). The power supply is programmed through RS232 and regulates the current at a constant speed of 2 A/s (=35 G/s). To allow fast switching of the magnetic field the current can be switched between the coil and a resistance-matched dummy load by means of two BUZ344 MOSFETs, protected with transient voltage suppressors to dissipate the voltage spike induced by the switch off of the MOSFET. The current is programmed to its set value at the beginning of an experimental cycle, running through the dummy load and switched to the coils at the start of the Feshbach experiment. The power supply adjusts to the change of the load to below the 5×10^{-5} detection level of the field probe within a few hundred milliseconds. Fast field sweeps or switching is performed by the sweep coil, which is operated by a Delta Elektronica ES075-2 power supply optionally equipped with a homebuilt transistor regulation to achieve linear field sweeps of up to 40 G/ms maintaining a current stability of $< 10^{-4}$ and a typical corresponding field stability of better than 10^{-5} during the sweep.

Field calibration

We have calibrated the absolute value of the magnetic field by driving transitions between hyperfine states of ^{40}K atoms. We prepare a spin mixture of potassium containing the $|F = 9/2, m_F = +9/2\rangle$ state in the science and apply a very weak microwave pulse connecting the $|9/2, +9/2\rangle$ and $|7/2, +7/2\rangle$ states for a period of 1 second. Subsequently the field is switched off and the number of atoms with $F = 9/2$ are detected in zero field on the $F = 9/2 \rightarrow F' = 11/2$ transition by absorption imaging. The loss signal has a width of 15 kHz corresponding to field noise or a field inhomogeneity of 6 mG around an offset field of 110 G. The field is calibrated for a few points between 110 and 120 G and found to be linear with respect to the power supply set current within the 6 mG accuracy. In future experiments a crossed dipole trap will be employed resulting in a sample with a much smaller volume. This will easily rule out if the 6 mG width is caused by field noise or field inhomogeneity. The most common source of field noise is low-frequency 50 Hz noise, therefore a higher accuracy can most likely be obtained by triggering the experimental sequence on the 50 Hz line.

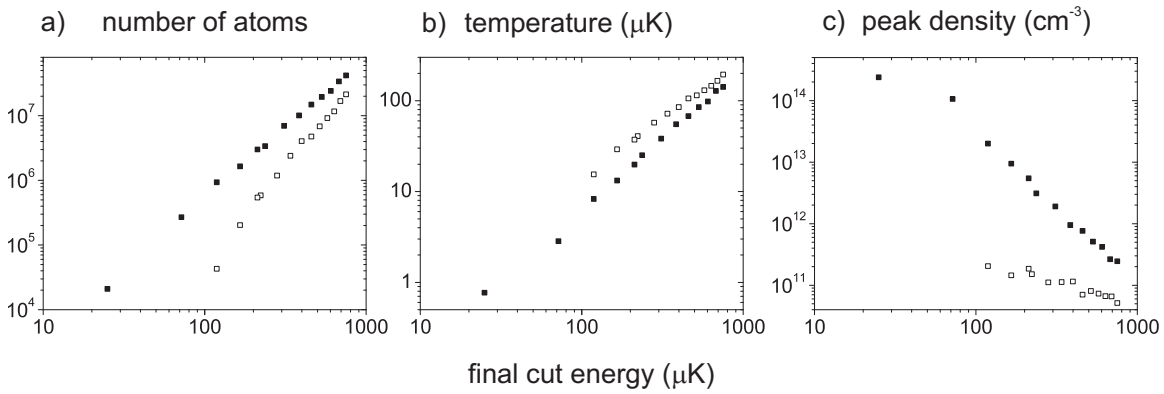

Figure 3.23: Forced evaporative cooling in the magnetic trap. The filled (open) squares are with (without) the plug beam. The plug allows density buildup during the evaporative cooling process. a) number of atoms, b) temperature as measured by time-of-flight, c) the peak density calculated numerically based on the plug and magnetic trap parameters. For low temperatures this value is sensitive to the exact plug shape, therefore the data points with the largest density should be considered as an order of magnitude estimate.

3.6 Ultracold Fermionic Mixtures

3.6.1 Quantum degenerate ^{40}K spin mixture

The first quantum degenerate Fermi gas in the field of ultracold atoms was created in 1999 by the group of D. Jin at JILA [7]. To achieve quantum degeneracy a spin-mixture of two hyperfine states $|9/2,+9/2\rangle$ and $|9/2,+7/2\rangle$ of ^{40}K was cooled by means of forced evaporation. Interspecies collisions between the $m_F = +9/2$ and $m_F = +7/2$ ensured rethermalization of the atom sample during the process of evaporative cooling. Since the achievement of quantum degeneracy many other groups have achieved quantum degeneracy of ^{40}K, however always by making use of ^{87}Rb as a bosonic species to ensure rethermalization. In this section I will describe the achievement of quantum degeneracy of a spin-mixture of ^{40}K atoms, much like the original approach of the JILA group.
We start our sequence by loading $\sim 10^9$ ^{40}K atoms in the 3D MOT, subsequently we optically pump the sample such that a mixture of hyperfine states is created. The mixture of spin states is optimized to have a high rethermalization rate in the magnetically trapped sample, this is performed by optimizing the atomic density after an initial stage of evaporative cooling in the magnetic trap. The transfer yields a total efficiency of $\sim 50\%$ yielding a trapped atom number of about 5×10^8, distributed over the $|9/2,+5/2\rangle$, $|9/2,+7/2\rangle$ and $|9/2,+9/2\rangle$ hyperfine states. The optically pumped sample is captured in the magnetic trap at a gradient of 90 G/cm and compressed to the full gradient of 180 G/cm in 300 ms. The sample is cooled for 23 seconds by forced evaporation on the microwave transitions of K $|9/2,+9/2\rangle \rightarrow |7/2,+7/2\rangle$, $|9/2,+7/2\rangle \rightarrow |7/2,+5/2\rangle$, etc.. Figure 3.23 shows the process of evaporative cooling with and without the optical plug. The cooling procedure is clearly improved by the presence of the optical plug, yielding a lower temperature and a higher phase-space density. For subsequent experiments the evaporative cooling process is stopped at a temperature of the potassium cloud of $T \simeq 12$ μK.
After pre-cooling in the optically plugged magnetic trap we transfer the spin mixture to the optical dipole trap (see section 3.4.4). The optical dipole trap is linearly ramped on to

a depth of $U_0/k_B = 140$ μK during the last 1 s of evaporative cooling in the magnetic trap. This method transfers $\sim 10^6$ atoms into the optical trap at a temperature of $T \simeq 9$ μK ($T/T_F \simeq 1.8$), corresponding to a peak density of $n_{0,K} = 6 \times 10^{13}$ cm^{-3}. The optical trap has a much tighter confinement than the magnetic trap, however, the temperature after the transfer into the optical trap is comparable to the temperature of the magnetically trapped cloud due to the rethermalizing collisions of the optically trapped atoms with the surrounding magnetically trapped cloud during the last stage of the evaporative cooling. This dimple-loading [133, 134] yields a strong increase in phase-space density compared to an adiabatic loading of the dipole trap.
Proof of quantum degeneracy is achieved by evaporative cooling in the optical trap. This experiment is performed in the main chamber. The optical trap power is exponentially ramped down in 3 s to a preselected final trap depth. The cloud is imaged along the optical trap axis after a variable time of flight, which is adjusted to achieve an optical density of $0.4 - 0.6$ for each image to reduce systematic errors obtained from fitting. The data is analyzed by a two-dimensional fit to the density profile and by a one-dimensional fit over an azimuthal average of the cloud distribution. The fit is performed to Eq. 2.36, where the fugacity, the cloud radius and maximum optical density are the fit parameters. The degeneracy parameter T/T_F is subsequently obtained from the fugacity by Eq. 2.39. Figure 3.24a shows the degeneracy obtained as a function of the final trap depth. For various points the consistency of the method to obtain the quantum degeneracy is verified by independent imaging along the vertical axis and performing a two-dimensional fit to the anisotropic cloud. Degeneracy parameters obtained from vertical and horizontal imaging are consistent within the scatter of the data. The spin mixture is analyzed by means of a Stern-Gerlach experiment (see section 3.5.4) and found to consist of 43% $|9/2, +9/2\rangle$, 36% $|9/2, +7/2\rangle$ and 21% $|9/2, +9/2\rangle$. Due to the comparable atom numbers in the various spin states and the weak dependence of the degeneracy parameter on the number of atoms ($T/T_F \sim N^{1/6}$) fitting the cloud to a single species Fermi distribution is a good approximation. This approximation has been verified by performing the fitting procedure on a numerically generated density profile of a spin mixture.
Figure 3.24b shows a large degenerate cloud after evaporating to a trap depth of $U_0/k_B = 5$ μK and 6 ms of time of flight. This measurement originates from a different dataset than the data in 3.24a. The data of Fig. 3.24b has been taken a few months after the dataset of Fig. 3.24a, with an optimized procedure resulting in a larger atom number and deeper degenerate clouds.

Prospects for ^{40}K spin mixtures

Due to the inverted hyperfine structure of ^{40}K, it exhibits peculiar properties with respect to spin-exchange collisions. Any mixture of two spin components in adjacent hyperfine states ($m_{F,1} - m_{F,2} = 1$, where $m_{F,1} > m_{F,2}$) in the $F = 9/2$ manifold will be stable against spin-exchange collisions due to the endothermic nature of the spin-exchange channels: $|m_{F,1}\rangle + |m_{F,2}\rangle \rightarrow |m_{F,1} + \Delta m\rangle + |m_{F,2} - \Delta m\rangle$, for $\Delta m \geq 1$. Figure 3.25 shows the thermal activation temperature T_{ac} required to drive the possible spin-exchange transitions for adjacent hyperfine states for $\Delta m = 1$, for channels with larger Δm the thermal activation temperature is even larger. Ultracold samples with $T = 1$ μK are collisionally stable for magnetic fields of $B \gtrsim 10$ G. Additionally, spin mixtures of two hyperfine states separated by *two* angular momenta ($m_{F,1} - m_{F,2} = 2$) are also collisionally stable because

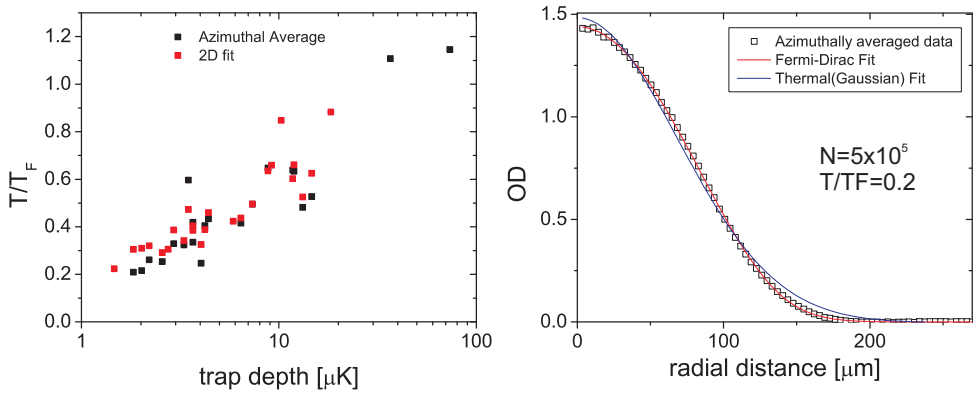

Figure 3.24: Quantum degeneracy of a ^{40}K spin mixture. (left) Degeneracy parameter T/T_F as a function of the final trap depth after evaporation. Two independent fitting procedures have been performed (see text). (right) Azimuthal average of the optical density of a degenerate cloud for an optimized sequence. This cloud consists of three spin states.

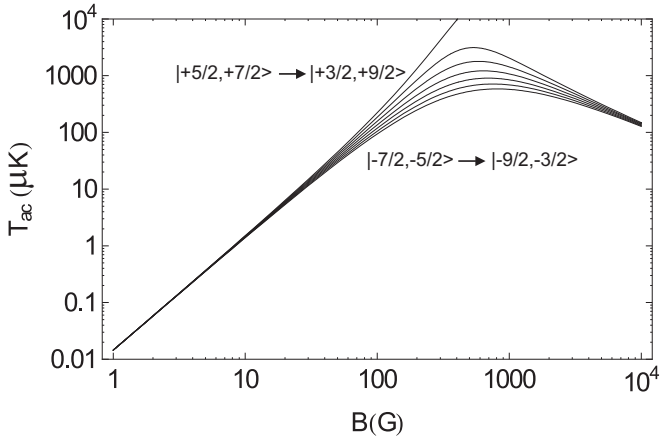

Figure 3.25: Thermal activation temperature T_{ac} required to drive a spin-exchange process for two adjacent states as a function of the magnetic field B. The curves correspond to spin exchange transitions involving exchange of one unit of angular momentum.

Pauli blocking suppresses the spin-exchange channel where both outgoing spin states are identical ($m_{F,1} - 1 = m_{F,2} + 1$). A consequence of the above is that spin mixtures of three *adjacent* hyperfine states in the $F = 9/2$ manifold are also collisionally stable.

An additional feature of ^{40}K is its relatively large nuclear spin, therefore many Feshbach resonances can occur in these spin mixtures. These properties make ^{40}K a promising and very rich system to perform studies on three strongly interacting fermions, in contrast to lithium where only one triple spin mixture and corresponding set of resonances is available [135]. In exploring experiments we have observed spin mixtures of three adjacent states to be stable for a period of many seconds (hundreds of collisions). We note that at high densities or near a Feshbach resonance dipolar relaxation may limit the stability of such systems.

3.6.2 Ultracold ^{6}Li-^{40}K mixture

To achieve an ultracold mixture of ^{6}Li and ^{40}K various approaches can be taken. One approach is to prepare large atom numbers of both species in their fully-stretched states, namely ^{6}Li $|F = 3/2, m_F = +3/2\rangle$ and ^{40}K $|F = 9/2, m_F = +9/2\rangle$. This mixture is the only combination which is stable against spin-exchange collisions. Due to the fermionic nature of both species rethermalizing collisions will occur by *inter*-species collisions only, therefore evaporative cooling has to be performed on both species simultaneously. Evaporating on one species only will initially cool the sample but will quickly become inefficient since the evaporated species will become a minority. As pointed out in section 2.2 the energy transfer per ^{6}Li-^{40}K collision is suppressed by a factor ξ and the time to rethermalize will be longer by $1/\xi$ as compared to collisions with equal mass. The ^{6}Li-^{40}K collisions in the fully stretched state collide through the triplet channel and therefore have a s-wave scattering length of $a = 64.41$ a$_0$ [136], and a collision cross-section of $\sigma_{K,Li} = 1.5 \times 10^{-10}$ m^2. Additionally the temperature of the ^{6}Li MOT is much higher than that of the ^{40}K MOT, therefore large volumes of ^{6}Li will pose a significant heat load on the ^{40}K resulting in a heating of the ^{40}K.
We have employed a more efficient procedure to achieve an ultracold mixture of ^{6}Li and ^{40}K. This is done by adding more hyperfine states of ^{40}K and load only a small amount of ^{6}Li. In this approach we use a spin mixture as described in section 3.6.1 with the $F = 9/2, m_F = +9/2$, $m_F = +7/2$ and $m_F = +5/2$ hyperfine states and ^{6}Li prepared in the $|F = 3/2, m_F = +3/2\rangle$ hyperfine state. This method has the various advantages over the fully-stretched approach. First the ^{40}K will mainly rethermalize due to *intra*-species collisions of the various hyperfine states and the ^{6}Li rethermalizes due to *inter*-species collisions. For typical magnetic fields in the magnetic trap ^{40}K scattering will mainly occur through the triplet channel. Therefore the scattering length between the various species will be (in the absence of Feshbach resonances) $a \simeq 170$ a$_0$ [137], resulting in an *intra*-species collision cross section of $\sigma_{K,K} = 1.0 \times 10^{-9}$ m^2, almost an order of magnitude larger than the *inter*-species collision cross section $\sigma_{K,Li}$. Additionally the use of a small lithium cloud in combination with the low MOT temperature of the potassium avoids the large heat load as it is present in the fully-stretched method. Rethermalization and cooling of the ^{40}K will fast and efficient. Rethermalizing collisions of the ^{6}Li with the ^{40}K will sympathetically cool the ^{6}Li.

Spin-exchange collisions

In contrast to the method with both lithium and potassium in the fully stretched states spin-exchange collisions can depolarize the ^{6}Li sample resulting in lithium atoms in untrapped states. Table 3.4 lists the possible spin-exchange channels with their respective decay rate coefficients K_2 obtained from Eq. 2.12. The rate coefficients are low due to the relatively small difference between the singlet a_s and triplet a_t scattering lengths. These collisions polarize the potassium sample, depolarize the lithium sample towards untrapped states and heat the ensemble.
Figure 3.26 depicts the cooling process towards an ultracold mixture of ^{6}Li and ^{40}K, the trajectory was optimized to achieve the maximum phase-space density of the mixture at $T \simeq 10$ μK where the optical dipole trap can be efficiently loaded. The potassium density is kept below 2×10^{12} cm^{-3} during the cooling process, yielding a lifetime due to spin-exchange losses of $\tau_{se,Li} \simeq 15 - 35$ s, comparable to the vacuum-limited lifetime. For

Li+K initial $\|\alpha\beta\rangle$	Li+K final $\|\alpha'\beta'\rangle$	K_2 (cm^3/s)
$\|3/2,+3/2\rangle + \|9/2,+7/2\rangle$	$\|3/2,+1/2\rangle + \|9/2,+9/2\rangle$	1.4×10^{-14}
$\|3/2,+3/2\rangle + \|9/2,+5/2\rangle$	$\|3/2,+1/2\rangle + \|9/2,+7/2\rangle$	2.4×10^{-14}
$\|3/2,+1/2\rangle + \|9/2,+7/2\rangle$	$\|3/2,-1/2\rangle + \|9/2,+9/2\rangle$	1.9×10^{-14}
$\|3/2,+1/2\rangle + \|9/2,+5/2\rangle$	$\|3/2,-1/2\rangle + \|9/2,+7/2\rangle$	3.3×10^{-14}

Table 3.4: Spin-exchange rates for various ^{6}Li-^{40}K channels calculated at $T = 10$ μK and $B = 1$ G

higher potassium densities we observe rapid loss of the ^{6}Li sample.
At truncation energies below ~ 50 μK the number of atoms in the mixture drops to $< 10^4$, too little to perform reliable measurements on the temperature. The mixture is transferred to the optical trap after evaporating to $\epsilon_t = 64$ μK, yielding a mixture of 10^5 atoms for each species and a temperature of $T = 10$ μK. During the adiabatic loading of the optical trap the trap volume for a $T = 10$ μK cloud shrinks by nearly two orders of magnitude, corresponding to a strong decrease in the ^{6}Li lifetime due to spin exchange. After switch-off of the magnetic trap, the cloud expands axially by about a factor 10, decreasing the spin-exchange losses again, however this still results in a lifetime too short to perform experiments. Figure 3.27 shows an optically trapped sample of $N_{Li} \simeq 10^5$ and $N_K \simeq 10^5$, at a temperature of $T \simeq 20$ μK,where the potassium consists of various spin states.
To achieve a heteronuclear mixture stable against spin-exchange collisions, we clean the potassium spin mixture before transferring it into the optical trap. This cleaning is performed by a microwave sweep at the inner (plug) side of the trap (see section 3.5.4). This method results in a loss of about 70% of the total number of ^{40}K atoms and is not purely state selective, however the lifetime of the mixture in the optical trap is increased to $\tau \simeq 15$ s. Removing remaining ^{40}K spin impurities by driving an optical transition in a high magnetic field (see Sect. 3.5.4) results in a mixture with the lifetime limited by background vapor ($\tau \simeq 25$ s at the time of these experiments).
A strong improvement and simplification to the cooling scheme can be achieved by employing a higher power optical dipole trap. With a proper choice of parameters the ultracold sample can be transferred to a less tight, but as deep optical trap yielding not as strong an increase of the density. Subsequently the spin mixture can be completely purified in the optical trap before compressing it to the final high density sample.

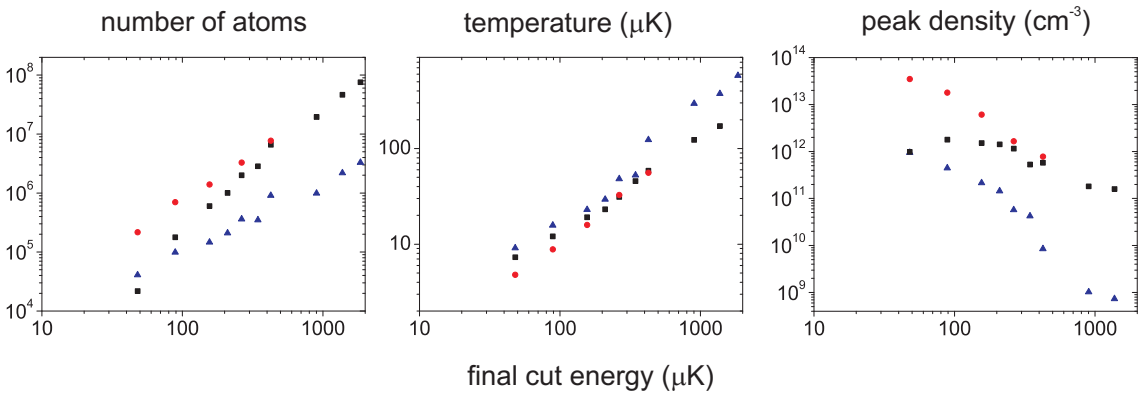

Figure 3.26: Sympathetic cooling of ^{6}Li by rethermalization with a ^{40}K spin mixture. The black squares is the potassium and the blue triangles the lithium. The trajectory is experimentally optimized and shows the density of the potassium levelling around 10^{12}cm^{-3} minimizing spin exchange collisions of the ^{6}Li-^{40}K sample. As a comparison the red circles are for the same trajectory with potassium only.

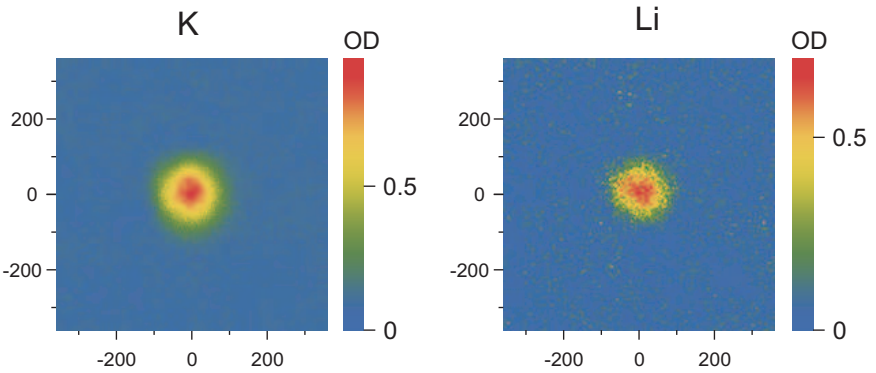

Figure 3.27: An optically trapped mixture of ^{6}Li in a pure hyperfine state and ^{40}K in a mixture of spin states. The color scale indicated the optical density of the sample. The temperature of the mixture is $T \simeq 20\mu\text{K} \simeq 2.5T_F$.

Chapter 4
Lithium 2D MOT

We demonstrate a novel 2D MOT beam source for cold ^{6}Li atoms. The source is side-loaded from an oven operated at temperatures in the range $600 \lesssim T \lesssim 700$ K. The performance is analyzed by loading the atoms into a 3D MOT located 220 mm downstream from the source. The maximum recapture rate of $\sim 10^9$ s^{-1} is obtained for $T \approx 700$ K and results in a total of up to 10^{10} trapped atoms. The recaptured fraction is estimated to be $30 \pm 10\%$ and limited by beam divergence. The most-probable velocity in the beam (α_z) is varied from 18 to 70 m/s by increasing the intensity of a push beam. The source is quite monochromatic with a full-width at half maximum velocity spread of 11 m/s at $\alpha_z = 36$ m/s, demonstrating that side-loading completely eliminates beam contamination by hot vapor from the oven. We identify depletion of the low-velocity tail of the oven flux as the limiting loss mechanism. Our approach is suitable for other atomic species.
This chapter has been published in Ref. [138] Physical Review A **80** (2009) 013409

4.1 Introduction

Since the first demonstration of a laser-cooled atomic beam by Phillips and Metcalf [139] the development and improvement of cold atom sources has evolved into an essential activity in atomic physics laboratories. In particular sources for cold Rb, K and Cs received a lot of attention and became compact and familiar standard devices [140]. However, for most other atomic and all molecular species the situation is less favorable and considerable time as well as resources remain necessary for the development of a source. Aside from optical cooling schemes many other cooling principles have been explored, we mention cryogenic cooling by surfaces [3] or buffer gas [141], filtering by magnetic [142, 143] or electric funnels [144] and Stark deceleration of molecules [145] as well as Rydberg atoms [146]. In spite of the success of these sources in specific cases, optical cooling is the preferred option whenever an appropriate optical transition is available.
The highest optically cooled atom fluxes to date have been produced from Zeeman-slowed atomic beams [147, 148, 149, 99]. Zeeman slowers have the additional advantage of a wide applicability. Unfortunately, their use adds a substantial engineering effort to system design and construction, in particular if beam-brightening and recycling principles are involved [150, 148]. The magnetic field inside the Zeeman slower must be very smooth and satisfy a particular profile in order to optimize the slowing. In addition, as the acceptance angle is small, the source oven has to be positioned on the beam axis and operated under high flux conditions. In typical applications this gives rise to a high background of hot atoms and results in maintenance because the oven has to be reloaded regularly.

An important simplification of cold atom sources was realized when Monroe *et. al.* [151] demonstrated that in a room-temperature vapor a fraction of the atoms can be optically captured and cooled into a magneto-optical trap (MOT) and subsequently loaded into a magnetic trap. The primary drawback of this vapor-cell MOT (VCMOT) is that the lifetime of the magnetically trapped atoms is limited by collisions with hot atoms from the vapor, thus limiting the time available for experiment. One approach to overcome this limitation is pulsed loading, starting from an alkali getter dispenser [152] or by ultraviolet light induced desorption [153, 154]. All other solutions involve a dual chamber arrangement in which a source chamber, containing some variation of the VCMOT source, is separated by a differential pumping channel from an ultra-high-vacuum (UHV) chamber in which the atoms are recaptured in a secondary MOT in preparation for experiments under UHV conditions .

Three basic types of VCMOT sources are used in the dual MOT configurations. In the first type a pulsed VCMOT serves to load the recapture MOT by a sequence of cold atom bunches, transferred with the aid of a push beam [155]. The second type is known as the LVIS (low-velocity intense source) [156]. In this case the VCMOT and the push beam are operated continuously, giving rise to a steady beam of cold atoms in the direction of the push beam. In the third type the standard three-dimensional (3D) MOT arrangement in the source chamber is replaced by a two-dimensional (2D) MOT configuration, with ($2D^+$-MOT) or without (2D MOT) push and cooling beams along the symmetry axis [109, 157, 158]. This has the important advantage that the source MOT can be optimized for capture because, with confinement in only two directions, the residence time and collisional losses are intrinsically low.

VCMOT sources work most conveniently for elements like Cs, Rb, and K, having a vapor pressure of $\sim 10^{-7}$ mbar around room temperature [159]. Elements such as Li, Yb, Cr and the alkaline earths must be loaded from atomic beams since their vapor pressures are only significant at temperatures far above the maximum baking temperature of a conventional UHV system [159, 149, 160, 161]. In the case of elements which are chemically reactive with glass, such as Li, a vapor cell is additionally impractical.

In this paper we present a novel 2D MOT source for cold lithium. It yields a cold flux comparable to the maximum achieved with lithium Zeeman slowers [162]. Contrary to previously realized 2D MOT systems our source is transversely loaded with a beam from an effusive oven, rather than longitudinally like in beam brighteners or isotropically like in vapor cells. This demonstrates the possibility to use 2D MOT sources in applications where a vapor cell cannot be used and avoids the background of hot atoms in the beam. An important *a priori* uncertainty of this arrangement is the risk of depletion of the low-velocity tail of capturable atoms by the onset of nozzling as occurred in the famous Zacharias fountain experiment [163, 164]. Our work shows that large cold atomic fluxes can be realized without this depletion becoming inhibitive. Recently this was also demonstrated with a Li oven loaded 3D MOT [165]. Another novelty of our source is the application of the 2D MOT concept to a light atom like lithium. Magneto-optical trapping of light species requires a high gradient for efficient capture. As this also compresses the cold atoms into a cloud of small volume, in particular in the 3D configuration trap losses are substantial even for small atom numbers. We demonstrate that in our dual MOT arrangement, the 2D MOT can be optimized for capture with a large gradient and without considerable losses, whereas the 3D recapture MOT can be optimized with a different gradient for maximum total atom number.

In the following sections we describe our experimental apparatus (section 4.2) and our results (section 4.4). In section 4.3 we present a simple model for the loading of the 2D MOT. The performance of our system and loss mechanisms are discussed in section 4.5 and in section 4.6 we summarize our findings and comment on the suitability of our approach for other atomic species.

4.2 Experimental

4.2.1 Vacuum system

The experimental setup of the lithium 2D MOT source is sketched in Fig. 4.1. The vacuum system consists of a stainless steel six-way cross of 40 mm tubing of which two CF40 ports define the horizontal symmetry axis of the source. The other four CF40 ports are configured under 45° and sealed with standard vacuum windows providing the optical access for the retroreflected 2D MOT beams with a waist ($1/e^2$ radius) $w = 9$ mm. A lithium oven is mounted with a CF16 flange onto the bottom of a water-cooled tube with inner radius $a = 8$ mm and connected along the vertical axis into the center of the cross. The source is connected horizontally onto the main UHV chamber, separated by a gate valve. Between the main vacuum and the source a 23 mm long differential pumping (DP) channel of 2 mm diameter can maintain a maximum pressure ratio of 10^{-3} between the main UHV chamber and the source. There is no direct line of sight from the oven to the main UHV chamber nor to the windows. When the oven is operated and the 2D MOT lasers are off, no lithium was detected in the main UHV chamber. Also no measurable gas load is observed on the main vacuum while the source is operated.

4.2.2 Lithium oven

The oven consists of a stainless steel lithium reservoir, 25 mm high and 50 mm in diameter, attached to a CF16 flange by a 15 mm long tube of 16 mm inner diameter. The oven is embedded in a simple heat shield of glass wool and aluminium foil and is connected to the vacuum system using a nickel gasket. The reservoir was loaded with ~ 6 g of ^{6}Li and ~ 2 g of ^{7}Li under an inert gas (argon) atmosphere. As commercial lithium contains a large fraction of LiH it has to be degassed by dissociating the hydride. For this purpose we baked the oven under vacuum in a separate setup for two hours at a temperature of ~ 943 K. Some 25% of the lithium was lost in this process. To protect the employed turbopump from alkali contamination a liquid nitrogen cold trap was used in this procedure.

Under typical conditions the oven is operated at $T = 623(12)$ K (350 C), well above the melting point of lithium at 454 K. All data presented in this paper, except those presented in Fig. 4.8, were obtained at this temperature. The oven temperature is calibrated by Doppler thermometry of the emerging Li flux using a probe beam under 50° with the vertical axis (see Fig. 4.1). Temperature stabilization is done with a thermocouple reference. Starting from room temperature the oven reaches the regulated value of 623 K in ~ 15 minutes. The ^{6}Li abundance was measured to be $a_6 = 0.74(5)$ using absorption spectroscopy on the ^{6}Li D_1 ($^2S_{1/2} \rightarrow ^2P_{1/2}$) line and the ^{7}Li D_2 ($^2S_{1/2} \rightarrow ^2P_{3/2}$) line.

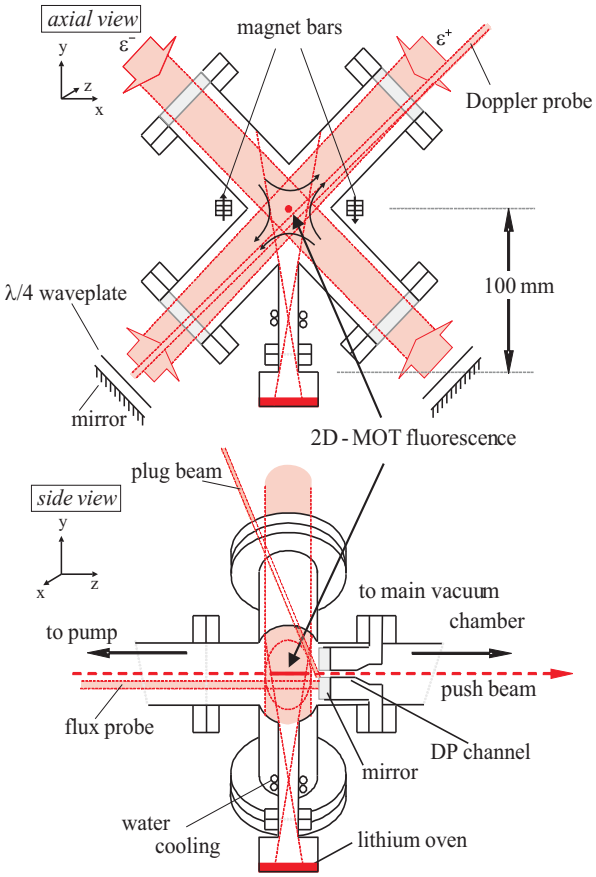

Figure 4.1: (Color online) Schematic drawing of the 2D MOT system. The oven tube is welded into the center of a six way cross as described in the text. *Upper drawing*: vertical cross section through the oven viewing along the beam axis; *lower drawing*: vertical cross section through the oven and through the DP-channel viewing the beam from the side. The Doppler probe is under 50 degrees with the vertical (y) axis and is used to calibrate the oven temperature. The flux probe is used to measure the hot flux emitted by the oven; a gold-plated mirror is included for this purpose. The plug beam is used to interupt the atomic beam for time-of-flight measurements. The two-dimensional quadrupole field required for the 2D MOT is provided by two permanent-magnet bars.

4.2.3 The 2D MOT configuration

As sketched in Fig. 4.1 the 2D MOT consists of a 2D quadrupole magnetic field in combination with two orthogonal pairs of retroreflected laser beams of opposite circular polarization, at a power of up to 50 mW per beam in a waist of 9 mm and red-detuned with respect to the optical resonance near 671 nm. Like in a standard 3D MOT [140], a cold atom moving in the crossed laser field is optically pumped to a state for which the Zeeman shift places it closer to resonance with a laser opposing the motion of the atom. Thus the atoms are trapped and cooled in the radial direction and collect along the symmetry axis of the 2D quadrupole field but are free to move in the axial direction. As a result only atoms with a sufficiently low axial velocity can be radially trapped; atoms with a residence time of less then 0.5 ms in the optical trapping region leave the 2D MOT before they are significantly cooled. Only the radially cooled atoms give rise to a sufficiently collimated beam to pass through the DP-channel and be recaptured by a 3D MOT in the middle of the UHV chamber.

For best performance the atoms are accelerated out of the source by a push beam, aligned along the symmetry axis and with a waist of 1.2 mm passing through the DP-channel. The detuning and intensity of the push laser determine the velocity of the atoms emerging from the source. This velocity is chosen below the capture limit of the recapture MOT but is sufficiently fast to assure that the atoms do not fall below the recapture region as a result of gravity. For this reason the push beam is essential for horizontal configurations but optional in vertical arrangements. In all arrangements the push beam acceleration increases the output flux because it reduces the residence time in the 2D MOT and therefore background-induced losses. In the literature on the $2D^+$ MOT [109, 157, 158] and the LVIS [156] control over the axial velocity is reported by using a pair of counter-propagating axial cooling beams over the entire trap but this method is not employed here.

The magnetic quadrupole field is provided by two sets of $Nd_2Fe_{14}B$ magnets (Eclipse magnets N750-RB) with a measured magnetization of $8.8(1)\times10^5$ A m^{-1}. Each set consists of two stacks of three $25\times10\times3$ mm magnet bars separated by 12 mm to make an effective dipole bar of 62 mm total length. The optimum position of the centers of the dipole bars was experimentally found to be $x = \pm42$ mm from the symmetry axis in the horizontal plane as sketched in Fig. 4.1. For this distance we calculate a field gradient of 0.50 T/m, constant within 2% along the 2D MOT symmetry axis over a total length of 20 mm. The use of permanent magnets simplifies the application of the high field gradients needed for light species. It combines a simple construction with convenient alignment and occupies much less space than the more traditional racetrack coils. The quadrupole field falls off over short distances along the symmetry axis. At the position of the recapture MOT, 23 cm downstream from the center of the 2D MOT, only a small gradient of 210 μT/m remains.

4.2.4 Hyperfine structure of ^{6}Li levels

Laser cooling of ^{6}Li differs from the familiar case of ^{87}Rb, in which a spectrally-well-resolved cycling transition on the D_2 line can be strongly driven to cool and trap the atoms while a weak repumping beam is sufficient to compensate for parasitic leakage to the dark state manifold. In the case of ^{6}Li the hyperfine splitting of the $2^2P_{3/2}$ excited

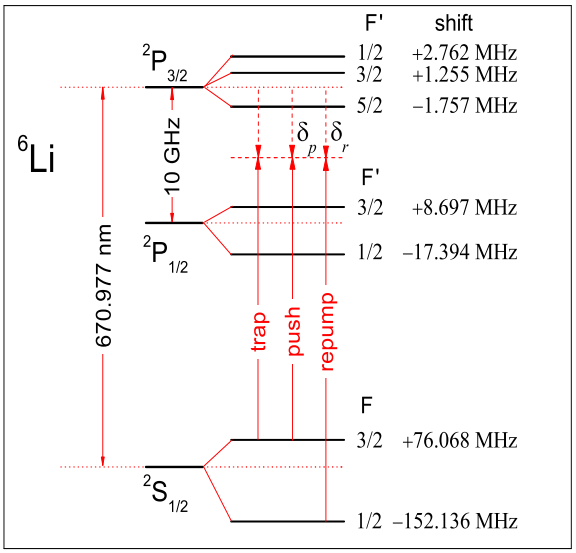

Figure 4.2: (Color online) Level structure of ^{6}Li. Note that the hyperfine splitting of the $^2P_{3/2}$ levels is smaller than the natural linewidth $\Gamma/2\pi = 5.9$ MHz of the D_2 $\left(^2S_{1/2} \rightarrow ^2P_{3/2}\right)$ transition.

state is of the order of the natural linewidth, $\Gamma/2\pi = 5.9$ MHz and all D_2 transitions from the $F = 3/2$ manifold, $|2^2S_{1/2}; F = 3/2\rangle \rightarrow |2^2P_{3/2}; F' = 1/2, 3/2, 5/2\rangle$ are excited simultaneously (see Fig. 4.2) [104]. Hence, there is no closed transition suitable for cooling and trapping and strong optical pumping to the $|2^2S_{1/2}; F = 1/2\rangle$ level cannot be avoided. As a consequence the 'trapping' and 'repumping' beams have to be of comparable intensities, which means that both beams contribute to the cooling and mutually serve for repumping. Also the detunings will have a strong influence in this respect [166]. In spite of these differences we stick to the conventional terminology, referring to the transition $|^2S_{1/2}; F = 3/2\rangle \rightarrow |^2P_{3/2}; F' = 1/2, 3/2, 5/2\rangle$ as the 'trapping' transition and to $|^2S_{1/2}; F = 1/2\rangle \rightarrow |^2P_{3/2}; F' = 1/2, 3/2\rangle$ as the 'repumping' transition.

4.2.5 Laser system

A laser system for wavelength $\lambda_L = 671$ nm was developed to serve the 2D (source) MOT and the 3D (recapture) MOT as well as to provide laser beams for ^{6}Li diagnostics. The laser system consists of a single master oscillator and four injection-locked slave lasers, all operating a 120 mW Mitshubishi ML101J27 diode heated to 70 C. The master oscillator is a home-built external-cavity diode laser (ECDL) [167], frequency stabilized using saturated absorption spectroscopy in a ^{6}Li heat pipe [107]. The power from the master laser is distributed over six beams, which can be independently shifted in frequency using ISOMET 1205-C acousto-optic modulators (AOM's). Of these six beams four are amplified by injection-locking of the slave lasers and of these four beams one pair is used for the retroreflected trapping and repumping beams of the 2D MOT while the other pair is equally distributed over six beams and similarly employed for the 3D MOT. The remaining two frequency-shifted ECDL beams serve as pushing beam, as probing beam or as plug beam in various diagnostic applications.

4.3 Source model

4.3.1 Oven flux

To establish the principle of our source and to enable comparison with experiment we present a semi-empirical kinetic model in which the oven is replaced by an emittance of area $A = \pi a^2 \approx 2$ cm^2 at the saturated vapor pressure of lithium. Around $T = 623$ K the saturated vapor pressure is given by $p_s = p_a \exp(-L_0/k_B T)$ where $p_a = 1.15(5) \times 10^{10}$ Pa and $L_0/k_B = 18474$ K is the latent heat of vaporization [159]. As p_s is only accurate to within 5% we neglect the small dependence on the isotopic composition. The total atomic flux Φ_{tot} emitted by the oven may be estimated by the detailed balance expression for the total flux onto and from the emittance under thermal equilibrium conditions,

$$\Phi_{tot} = \frac{1}{4} n_s \bar{v}\, A, \tag{4.1}$$

where n_s is the atomic density and $\bar{v} = [8k_B T/\pi m]^{1/2}$ the mean thermal speed, with k_B the Boltzmann constant and m the mass of the Li atoms. For $T = 623(12)$ K we have $p_s = 1.5^{+1.1}_{-0.7} \times 10^{-3}$ Pa, corresponding to a density $n_s = 1.8^{+1.2}_{-0.8} \times 10^{17}$ m^{-3}. With these numbers the total flux from the source is found to be $\Phi_{tot} \approx 1.3 \times 10^{16}$ s^{-1} $\approx 1.3 \times 10^{-10}$ kg s^{-1}. With 8 gram of Li this corresponds to ~ 17000 hours running time.
The flux of ^{6}Li atoms captured by a 2D MOT at a distance of $L = 100$ mm above the oven can be written as an integral over the velocity distribution

$$\Phi_c = a_6 n_s A \int_0^{\Omega_c} d\Omega \frac{\cos\theta}{4\pi} \frac{1}{\mathcal{N}} \int_0^{v_c} v^3 e^{-(v/\alpha)^2} dv, \tag{4.2}$$

where $a_6 = 0.74(5)$ is the ^{6}Li abundance, $\Omega_c = A_c/L^2 = 2 \times 10^{-2}$ the solid angle of capture (with A_c the capture surface), $d\Omega = 2\pi \sin\theta d\theta$ with θ the emission angle with respect to the oven axis, v_c the capture velocity, $\alpha = [2k_B T_0/m]^{1/2} = 1.31 \times 10^3$ m/s the most-probable atomic speed in the oven and $\mathcal{N} = \int v^2 e^{-(v/\alpha)^2} dv = \pi^{1/2}\alpha^3/4$ the normalization factor of the speed distribution. Note that by integrating Eq. (4.2) over a hemisphere we regain Eq. (4.1) in the limit ($a_6 \to 1; v_c \to \infty$). Because the solid angle of capture is small we have $\cos\theta \simeq 1$ and the flux Φ_s emitted by the oven within the solid angle of capture is given by

$$\Phi_s \simeq n_s \bar{v}\, A \frac{\Omega_c}{4\pi}. \tag{4.3}$$

For $T = 623(12)$ K we calculate a total flux density of $\Phi_s/A_c = 4^{+3.2}_{-1.6} \times 10^{13}$ s^{-1}cm^{-2} at $L = 100$ mm above the oven. Presuming the capture speed to be small, $v_c \ll \alpha$, the captured flux Φ_c may be approximated by

$$\Phi_c \simeq \frac{1}{2} a_6 n_s \bar{v}\, A \left(\frac{v_c}{\alpha}\right)^4 \frac{\Omega_c}{4\pi} = \frac{1}{2} a_6 \left(\frac{v_c}{\alpha}\right)^4 \Phi_s \tag{4.4}$$

This expression represents the theoretical maximum flux that can be extracted from the 2D MOT source.

4.3.2 Capture and cooling

To discuss the capture and cooling behavior in the 2D MOT we distinguish two coaxial spatial regions, crossing-over at $r = r_d$ defined by $\delta_Z(r_d) + \delta_L = 0$, *i.e.* the surface where

the Zeeman shift in the radial gradient of the quadrupole field, $\hbar\delta_Z(r) = \mu_B(\partial B/\partial r)\, r$, is compensated by the detuning of the laser, $\delta_L = \omega_L - \omega_0 < 0$, *i.e.*, to the red side of the cooling transition at angular frequency ω_0 in zero field.
In the outer region ($r > r_d$), the 2D MOT functions much like a Zeeman slower, while in the inner region ($r < r_d$) the motion of the atoms can be described by a damped harmonic oscillator model [140]. First we discuss the outer region. An atom with velocity $\mathbf{v}$ at distance r from the symmetry axis will be at resonance with the cooling laser if the difference of the Zeeman shift and the laser detuning equals the Doppler shift,

$$\delta_Z - \delta_L = -\mathbf{k}\cdot\mathbf{v}. \tag{4.5}$$

Here $k = |\mathbf{k}| = 2\pi/\lambda_L$ is the wavevector of the cooling laser. In view of the angle of 135° between the directions of the hot lithium beam and the opposing laser cooling beams the positive Doppler shift is reduced by a factor $-\cos(\mathbf{k},\mathbf{v}) = \sqrt{1/2}$ with respect to the fully counter-propagating configuration. Accordingly, the maximum available slowing distance is larger, $r_{\max} = \sqrt{2}w$, where $w = 9$ mm is the waist of the cooling beams. Substituting $r_{\max}$ in the expression for the Zeeman shift we rewrite Eq. (4.5) in the form of an expression for the highest atomic speed $v_{\max}$ for which the resonance condition is satisfied

$$v_{\max} = \lambda_L \frac{\sqrt{2}}{2\pi}\left[\frac{\mu_B}{\hbar}\frac{\partial B}{\partial r} r_{\max} - \delta_L\right]. \tag{4.6}$$

Note that with the left-circular (ϵ^+) and right-circular (ϵ^-) polarizations of the 2D MOT beams as indicated in Fig. 4.1 the atoms are σ^+ optically pumped into a fully stretched state with the magnetic field being orthogonal to the propagation direction of the hot flux. In the simplest 1D model for capture process (in which only the trajectory along the symmetry axis of the oven is considered) $r_{\max}$ represents the capture radius (r_c) and $v_{\max}$ the capture velocity (v_c) of the 2D MOT provided the resonant photon scattering force ($mdv/dt = \hbar k\Gamma/2$) is large enough to keep the atom in resonance with the cooling laser, $\hbar d\delta_Z/dt = -\mu_B(\partial B/\partial r)\, v_{\max}$. The resulting condition

$$v_{\max} \le \frac{\sqrt{1/8}\,(\hbar k)^2}{m\mu_B(\partial B/\partial r)}\Gamma \tag{4.7}$$

is satisfied in our experiment. Combining Eqs. (4.6) and (4.7) we obtain an equation quadratic in $(\partial B/\partial r)$, which reduces for $\delta_Z \gg \delta_L$ to

$$\frac{\partial B}{\partial r} \le \frac{(\hbar k)^{3/2}}{2\mu_B (m r_{\max})^{1/2}}\Gamma^{1/2}. \tag{4.8}$$

This expression shows that the optimal gradient for capture scales like $m^{-1/2}$, which is important for comparing the performance of the source for different atomic species. Substituting the optimal gradient into Eq. (4.7) we obtain

$$v_{\max} = (a_{\max} r_{\max})^{1/2}, \tag{4.9}$$

where $a_{\max} = \hbar k\Gamma/2m$ is the maximum attainable deceleration by the scattering force.
In spite of the insight it offers the 1D model is far too simple to justify the use $v_c = v_{\max}$ for reliable estimates of the captured flux. Therefore, we decided to estimate v_c experimentally

by measuring the loading rate of the 3D MOT as a function of the mean velocity in the cold beam and Eq. (4.6) is only used for scaling between the conditions of the 3D MOT and the 2D MOT. This procedure is discussed in section 4.5.

In the inner region ($r < r_d$) of the trap the atomic motion is described by an overdamped harmonic oscillator model with a spring constant κ and damping coefficient β [140]. The atoms approach the axis with the cooling time constant $\tau \simeq \beta/\kappa$. For our 2D MOT parameters $\tau \approx 0.5$ ms. Atoms entering the 2D MOT with velocity $v < v_c$ only contribute to the cold lithium beam if τ is less than the residence time $\tau_{\rm res}$ in the trapping beams ($\tau < \tau_{\rm res}$). In the absence of collisions with background gas $\tau_{\rm res}$ is determined by the velocity component $|v_z| \lesssim v_c a/L$ of the trapable lithium atoms along the symmetry axis of the 2D MOT and the entry point in the optical field. If even the atoms with the shortest residence time can still be cooled, *i.e.* for

$$|v_c| \lesssim \frac{w}{a}\frac{L}{\tau + \tau_Z} \simeq \frac{L}{\tau} \tag{4.10}$$

essentially all captured atoms contribute to the cold beam. For $L = 100$ mm we calculate with $\tau = 1$ ms that this condition is satisfied for $v_c \lesssim 100$ m/s, including the experimental value $v_c \approx 85$ m/s (see section 4.5).

4.4 Experimental results

4.4.1 Oven flux

To evaluate the merits of the 2D MOT it is essential to have a reliable estimate of the input flux from the lithium oven. For this purpose the oven flux was measured at $T = 623$ K by observing - in the absence of the $Nd_2Fe_{14}B$ magnets - the Doppler profile of the hot lithium beam using a horizontal probe beam with a waist of 1 mm running parallel to the 2D MOT axis and back-reflected by a gold-plated mirror (spring-mounted at the entrance of the DP-channel) as indicated in Fig. 4.1. To avoid optical pumping to dark states the probe intensity was kept at the low value of $\sim 0.018\, I_{sat}$. With a thermal velocity of $\bar{v}_{th} = 1500$ m/s the interaction time is 1.3 μs and the scattering rate is estimated to be 0.4 photons per atom. The effect of small fluctuations in the intensity of the probe laser was suppressed by measuring the intensity of the probe beam relative to that of a reference beam originating from the same laser diode. Both the probe beam and the reference beam were measured with Texas Instruments OPT101 photodiodes. The observed Doppler profile is shown in Fig. 4.3. The solid line represents a fit of the calculated Doppler profile for the oven temperature $T = 623$ K and presuming the measured ^{6}Li-abundance. The solid line is the sum of six overlapping Doppler broadened lines (dotted lines). The unusual lineshapes reflect the clipping profile of the oven tube. The two large peaks at 0 and 228 MHz correspond to the trapping and repumping transitions in ^{6}Li, respectively. Analogously the other four peaks at $199, 291, 1002$ and 1094 MHz are for the $F = 2 \rightarrow F' = 1, 2$ and $F = 1 \rightarrow F' = 1, 2$ transitions of the D_1 line of ^{7}Li [104]. The best fit is obtained for $\Phi_s = 8(3) \times 10^{13}\,\mathrm{s}^{-1}$, where the error reflects our estimate of systematic uncertainties. This result overlaps with the value $\Phi_s = 8^{+6.4}_{-3.2} \times 10^{13}\,\mathrm{s}^{-1}$ calculated with Eq. (4.3) of the semi-empirical model starting from the oven temperature.

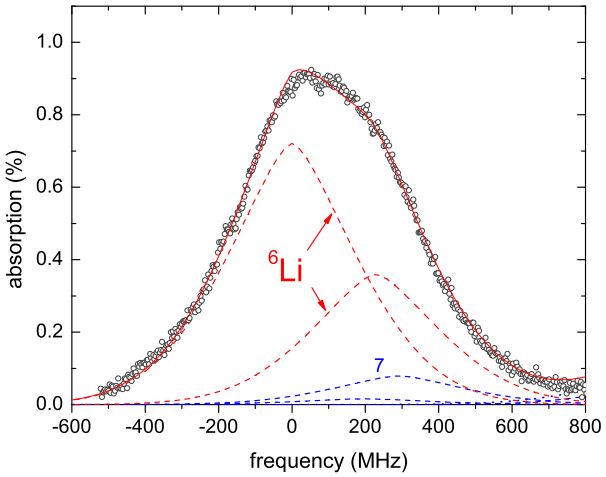

Figure 4.3: (Color online) The transverse Doppler profile of the hot lithium flux emerging from the oven as measured with the horizontal probe beam indicated in Fig. 4.1. The calculated profile (solid line) is the sum of six overlapping Doppler broadened transitions (dotted lines), two of which have a maximum outside the frequency range shown (see text). Only the amplitude has been fitted presuming the measured oven temperature $T = 623$ K and ^{6}Li-abundance of 74%.

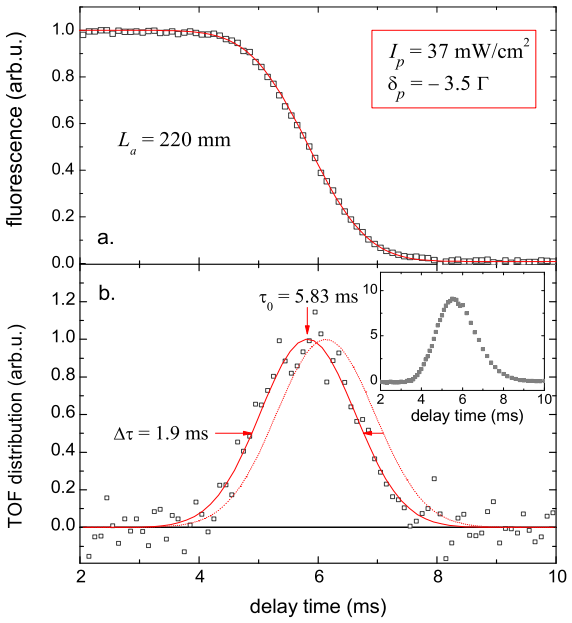

Figure 4.4: (Color online) a.) Typical fluorescence decay curve as a function of the probe delay time. The solid line is a fitted error function. Each datapoint represents the average over 200 cycles taken over a period of 6.7 s. b.) Derivative of the same data. The dashed line represents the true TOF-distribution (normalized to the same peak height) as calculated with the model presented in the text. The inset shows a TOF distribution as measured with a pulsed push beam.

4.4.2 Fluorescence detection - TOF distribution

We probe the intensity of the cold ^{6}Li beam in the middle of the main vacuum chamber by measuring the fluorescence after flashing a sheet of resonant laser light (knife-edge defined: $d = 1$ mm thick and $h = 5$ mm high) propagating horizontally through the middle of the UHV chamber orthogonal to the beam axis at position $z = L_a = 220$ mm downstream from the entry point of the DP-channel. The fluorescence flash is imaged vertically as a stripe onto a CCD camera. The length of the stripe provides information about the divergence of the beam. To remove stray-light fluctuations the integrated signal from the pixel area containing the stripe image is divided by the background signal from a reference area. For the probe beam we use 0.5 ms flashes of 0.3 W cm^{-2} in a ratio of 1 : 1.5 trap/repump light at zero detuning. The beam is retroreflected to prevent the atoms from being pushed out of resonance.
Velocity characterization of the cold ^{6}Li beam is done with a time-of-flight (TOF) method. For this purpose the beam is periodically interrupted at typically 30 Hz repetition rate with a resonant 0.6 W cm^{-2} 'plug' laser (2 : 1 trap/repump light) deflecting the atoms near the entrance of the DP-channel. From the decay of the fluorescence signal $\phi_{\rm fl}$ as a function time (see Fig. 4.4) we obtain the apparent TOF-distribution, which is proportional to $d\phi_{\rm fl}/d\tau$ and can be transformed into the axial velocity distribution using the flight distance of 220 mm. In a typical measurement we average over 200 cycles to reach a proper signal/noise ratio also for small fluxes traversing the light sheet at high velocity. The procedure is illustrated in Fig. 4.4 for a push-beam intensity of $I_p = 37$ mW cm^{-2} and a detuning $\delta_p = -3.5\,\Gamma$. Note that the derivative of $\phi_{\rm fl}$ can be nicely described by the gaussian function

$$d\phi_{\rm fl}/d\tau = (\pi^{1/2}\Delta\tau)^{-1}\exp[-(\tau-\tau_0)^2/\Delta\tau^2], \tag{4.11}$$

where $\tau_0 = 5.83$ ms is the mean apparent arrival time and $1.67\,\Delta\tau = 1.9$ ms is the full width at half maximum (FWHM). The absence of arrival times shorter than 3 ms reflects the absence of atoms with velocities $v_z \gtrsim 70$ m/s. This absence of 'hot' flux was verified up to 4 km/s and was anticipated because the cold beam is pushed horizontally out of the 2D MOT, *i.e.* orthogonally to the hot flux from the oven. The observed relative spread $\Delta\tau/\tau_0 \approx 0.2$ is insensitive to the push-beam intensity and comparable to the instrumental resolution for the shortest flight times investigated ($\tau_0 = 3$ ms). The value of τ_0 is entirely determined by the properties of the push beam and insensitive to other 2D MOT parameters. This behavior was previously also observed in other 2D MOT systems [158, 157]. Since optical pumping to different hyperfine states takes only a few optical cycles in ^{6}Li and $L_a/\tau_0 = 38$ m/s corresponds to ~ 380 photon recoils, the atoms must have been accelerated to their final velocity still within reach of the repump light, *i.e.* inside 2D MOT (the push beam does not contain repumper light). This limits the acceleration to a well-defined duration of time, which is consistent with the observed relatively narrow velocity distribution. The absence of slow atoms is not caused by gravity because for the lowest velocities measured ($L_a/\tau_0 = 22$ m/s) the gravitational drop is only 0.5 mm, less than half the height ($h/2 = 2.5$ mm) of the light sheet.
To relate the fluorescence signal $\phi_{\rm fl}$ to the velocity distribution in the atomic beam we have to account for the detection efficiency, which is inversely proportional to the velocity of the atoms and depends on the divergence of the beam. For this purpose we approximate the beam spot at the position of the light sheet ($z = L_a$) by a gaussian profile with $1/e$-radius R. The fraction $\chi_{\rm fl}$ of the beam giving rise to fluorescence is obtained by integrating

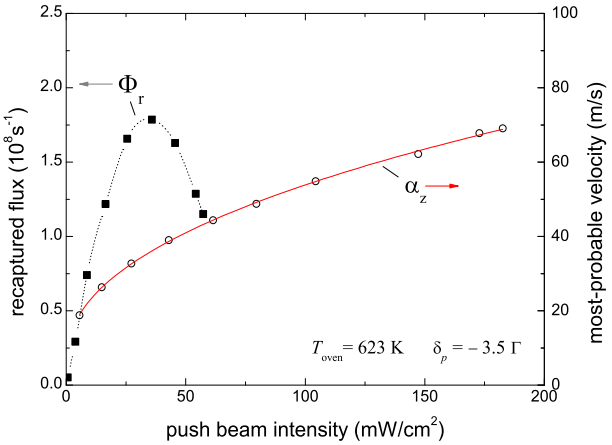

Figure 4.5: (Color online) Recapture rate into the 3D MOT (solid squares - left scale) and the most probable axial velocity (α_z) of the cold atomic beam (open circles - right scale) both as a function of the push beam intensity. The drawn lines provide a guide to the eye.

the normalized gaussian beam profile in horizontal and vertical direction over the surface area of the light sheet,

$$\chi_{\rm fl} = \mathrm{erf}(h/2R)\,\mathrm{erf}(S_0/R), \tag{4.12}$$

where $S_0 = 4.5$ mm is the radius of the optical field of view. Here we neglected some clipping by the DP-channel. Note that the divergence angle ζ of the cold beam equals the ratio of transverse to axial velocity of the atoms, $\zeta = R/L_a = v_t/v_z$. The length of the fluorescence stripe was found to vary only slightly with the intensity of the push beam. This sets a lower bound on the beam divergence, $S_0/R \lesssim 1$ for $v_z = 70$ m/s and on the characteristic transverse velocity, $v_t \gtrsim 1.4$ m/s. Since $h/2R \ll S_0/R \lesssim 1$ for all velocities studied Eq. (4.12) can be written in the form

$$\chi_{\rm fl}(v_z/v_t) \simeq \gamma v_z/v_t\,\mathrm{erf}\left(\eta v_z/v_t\right), \tag{4.13}$$

where $\eta = S_0/L_a = 0.02$ is the view angle and $\gamma = h/2L_a = 0.011$ the vertical acceptance angle.
The fluorescence decay signal $\phi_{\rm fl}$ can be expressed in the form

$$\phi_{\rm fl}(\tau) \sim \int_0^{L_a/\tau} \frac{\chi_{\rm fl}(v_z/v_t)}{v_z}\phi_0\left(v_z,\alpha_z\right)\,dv_z, \tag{4.14}$$

where $\phi_0\left(v_z,\alpha_z\right)$ is the normalized axial velocity distribution with α_z representing the most-probable velocity in the beam, and L_a/τ the velocity of the fastest atoms still arriving at the detector after delay time τ. Hence, the transformation between the beam property $\phi_0\left(v_z,\alpha_z\right)$ and the observed fluorescence decay is given by

$$\phi_{\rm TOF}\left(\tau\right) = \phi_0\left(L_a/\tau\right) \propto -\left(\tau/\chi_{\rm fl}\right) d\phi_{\rm fl}/d\tau. \tag{4.15}$$

Here $\phi_{\rm TOF}\left(\tau\right)$ represents the distribution of flight times in the beam. For $\Delta\tau/\tau \ll 1$ the prefactor $(\tau/\chi_{\rm fl})$ causes the distribution $d\phi_{\rm fl}/d\tau$ to shift to larger delay times but its shape remains well-described by a gaussian. In our case the shift is 5% ($\tau_{\rm max} \simeq 1.05\,\tau_0$)

as indicated by the dotted line in Fig. 4.4. Hence, the most-probable velocity in the beam is given by $\alpha_z \simeq 0.95\, L_a/\tau_0$. For the example of Fig. 4.4 we calculate $\alpha_z = 36$ m/s with a FWHM of 11 m/s. We have observed a ten-fold increase in $\phi_{\mathrm{TOF}}(\tau)$ at constant average flux by pulsing the push beam (see inset in Fig. 4.4). This indicates that the 2D MOT is not limited by its density when the push beam is continuously on. The most-probable velocity α_z was found to be the same for pulsed and continuous operation. The experimental results for α_z as a function of the push beam intensity are shown as the open circles in Fig. 4.5. Varying the push-beam intensity I_p over the range $5 - 180$ mW cm^{-2} we found α_z to increase from $18 - 70$ m/s.

4.4.3 Beam flux - dependence on push beam

The flux of the cold atomic beam is investigated as a function of the push-beam intensity (I_p) by recapture into the 3D MOT. The results are shown as the solid squares in Fig. 4.5. First of all we note that in the absence of the push beam the flux arriving at the recapture MOT is very small. Under these conditions the 2D MOT performance is very sensitive to the alignment of the quadrupole field, the MOT beams and the repumper. This low flux is attributed to the horizontal orientation of the beam axis, orthogonal to the direction of the hot flux from the oven. In view of this symmetry the trapped atoms have an axial velocity distribution centered around zero. Only the atoms with axial velocity $v_z \gtrsim 5$ m/s will reach the capture volume of the 3D MOT. Slower atoms drop below the trapping region as a result of gravity. High-field-seeking atoms will be deflected away from the recapture MOT by the quadrupole field outside the 2D MOT for axial velocities $v_z \lesssim 10$ m/s. Atoms with axial velocity $v_z \gtrsim 0.1\, v_c \approx 8.5$ m/s are absent due to clipping by the oven tube (v_c is the capture velocity of the 2D MOT).

As an aside we point out that by inclining the axis of the oven tube toward the beam axis direction it should be possible to realize a high flux cold beam with an axial velocity proportional to the inclination angle and without any (near)resonant light co-propagating with the atomic beam into the UHV chamber. In a more practical solution this may be realized by not retroreflecting the 2D MOT beams but tilting them so that the average **k**-vector points along the cold beam axis.

Measuring the loading rate Φ_r in the 3D MOT we obtain the 'useful' flux of the cold ^{6}Li beam. The rate is obtained from the leading slope of the loading curve, observing the 3D MOT fluorescence as a function of time using a CCD camera. This fluorescence is calibrated against an absorption image taken immediately after switching-off the 3D MOT. The measured rate Φ_r represents a lower limit for the flux emerging from the 2D MOT. Fig. 4.5 shows that Φ_r increases steeply until it reaches a maximum at $I_p \approx 34$ mW cm^{-2}. Further increase of the push-beam intensity causes the loading rate to decrease. This is attributed to the finite capture velocity of the 3D MOT (see section 4.5). For the data shown in Fig. 4.5 we used for the 3D MOT a magnetic field gradient of 0.19 T/m, 10 mW trapping light per beam at a detuning of $-6\,\Gamma$ and 11 mW repumping light per beam at a detuning of $-3.5\,\Gamma$. Both colors are distributed over six beams clipped at their beam waist of 9 mm, thus defining the acceptance radius $R_a = 9$ mm of the 3D MOT.

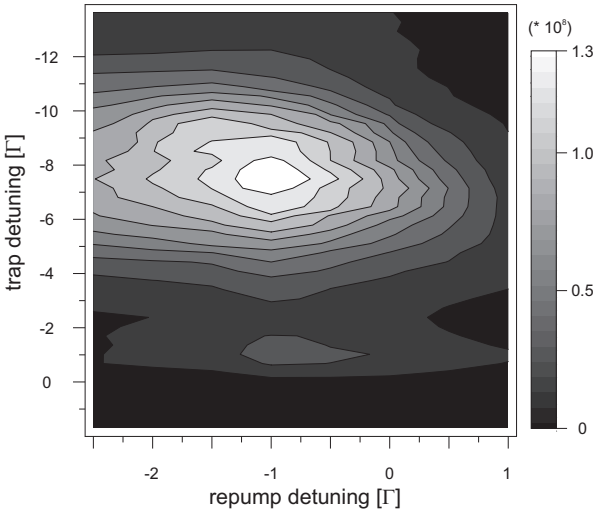

Figure 4.6: The 3D MOT loading rate as a function of the 2D MOT trap and repump detunings for an oven temperature $T = 623(12)$ K. These measurements were performed with maximum power for the 2D MOT trap and repump beams as given in Table 4.1. We find the maximum flux of $1.3 \times 10^8\,\mathrm{s}^{-1}$at a trap detuning of $\delta_t = -7.5\,\Gamma$ and $\delta_r = -1\,\Gamma$.

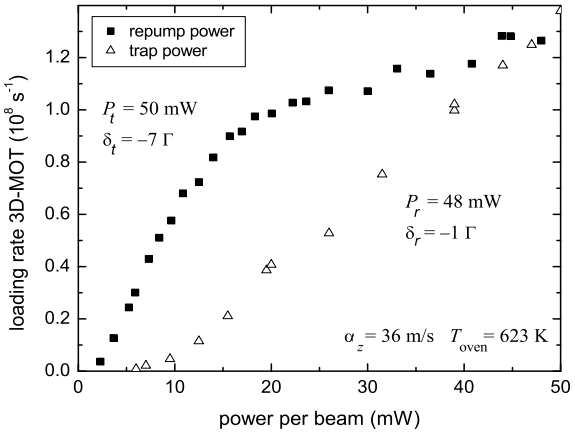

Figure 4.7: The 3D MOT loading rate as a function of the 2D trap and 2D repump laser powers (power per beam). Note that the 2D MOT is operated in a retroreflected configuration.

4.4.4 Beam flux - dependence on 2D MOT

We have optimized the total flux by varying both the trap and the repump detuning. For these measurements the laser power of the trap and repump lasers were set to their maximum values of 100 mW and 94 mW, respectively. The results are shown as a contour diagram in Fig. 4.6. The maximum flux is observed when the trap laser is far detuned ($\delta_t = -7.5\Gamma$) and the repump laser is close to resonance ($\delta_r = -1\Gamma$). We observe a small local maximum in flux if the trap laser is tuned close to resonance ($\delta_t = -1\Gamma$). We attribute this to better beam collimation because the 2D MOT is expected to be transversely colder when operated close to resonance [168, 166]. Apparently the advantage of better collimation cannot compensate loss in 2D MOT capture efficiency.

With optimized detunings we measured Φ_r as a function of the available optical power in the 2D MOT trap (P_t) and repump (P_r) beams. For this purpose either the trapping power is kept constant at $P_t \approx 50$ mW per beam and P_r is varied or the repumping power is kept constant at $P_r \approx 48$ mW per beam and P_t is varied. As is shown in Fig. 4.7 the loading rate increases linearly with P_t for $P_t \gtrsim 8$ mW, whereas Φ_r increases linearly with P_r for $P_r \gtrsim 2$ mW until it levels off for $P_r \gtrsim 18$ mW. The experimental parameters for optimal source performance are collected in Table 4.1. The output flux was reproducible to within 30% depending on the 2D MOT alignment.

4.4.5 Beam flux - dependence on oven temperature

Fig. 4.8 shows the loading rate as a function of the oven temperature. At low temperatures the loading rate increases exponentially with the oven temperature. This reflects the exponential increase of the effusive flux from the oven. Above $T \approx 650$ K a loss mechanism sets in. This limits further increase of the flux until at $T \approx 700$ K the cold atomic flux reaches its maximum value, corresponding to a loading rate of $\Phi_r = 8(3) \times 10^8\,\mathrm{s}^{-1}$ into the 3D MOT. The error reflects our best estimate of systematic uncertainties. As will be will be discussed in section 4.5 the losses are attributed to knock-out collisions in the effusive beam emerging from the oven. The dotted line shows the fraction of atoms surviving the loss mechanism.

Table 4.1: Experimental parameters for optimal performance of the Li 2D MOT.

parameter	trap	repump	push
detuning δ	-7.5 Γ	-1 Γ	-3.5 Γ
power per beam	50 mW	48 mW	0.8 mW
waist ($1/e^2$ radius)	9	9	1.2
gradient	0.5 T/m		
oven temperature	623 K		
most-probable velocity	36 m/s		
FWHM of velocity distribution	11 m/s		

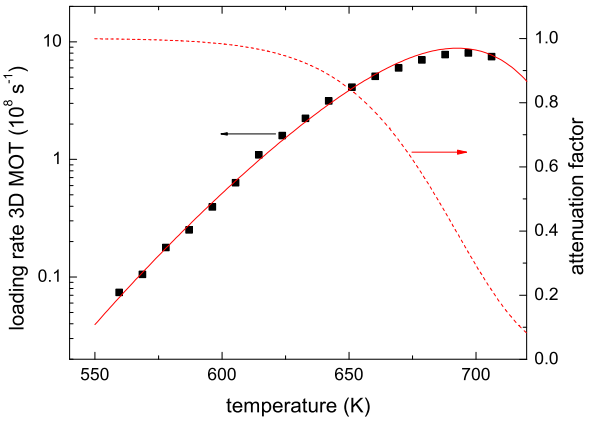

Figure 4.8: (Color online) The 3D MOT loading rate as a function of oven temperature (solid squares - left scale). The solid line shows a fit of the model presented in section 4.5. The loading rate reaches a maximum of $8 \times 10^8\,\mathrm{s}^{-1}$ at $T \approx 700$ K as a result of beam attenuation by hot background vapor. The calculated attenuation factor is shown as the dashed line (right scale).

4.5 Discussion

4.5.1 Recapture in the 3D MOT

To analyze the performance of the 2D MOT source we define the overall efficiency parameter χ as the ratio of the 3D MOT loading rate Φ_r and the maximum capturable flux Φ_c from the oven,

$$\Phi_r = \chi \Phi_c.$$

This efficiency is determined by the capture efficiencies of the 2D and 3D MOT as well as the transfer efficiency χ_t related to the divergence of the atomic beam. To determine χ_t as well as the capture velocity v_c we replotted the data of Fig. 4.5 in the form of Fig. 4.9, showing the capture rate Φ_r in the 3D MOT as a function of the most-probable axial velocity α_z in the cold atomic beam. Like in subsection 4.4.2 we approximate the atomic beam profile at the position of the 3D MOT ($z = L_a = 220$ mm) by the gaussian profile with $1/e$-radius R. The transfer efficiency is obtained by integrating the normalized profile from $r = 0$ on the beam axis to the acceptance radius $r = R_a = 9$ mm of the 3D MOT,

$$\chi_t(x_a) \simeq 2 \int_0^{x_a} (1 - x/x_0)\, e^{-x^2} x dx. \tag{4.16}$$

Here $x = r/R$, $x_a = R_a/R$ and $x_0 = R_0/R$. The factor $(1 - x/x_0)$ represents the conical approximation to the trapezoidal clipping profile imposed by the DP-channel, where $R_0 = 19$ mm marks the edge of the dark shadow. Defining the 3D MOT acceptance angle $\alpha = R_a/L_a$ and velocity ratio $\tilde{v}_z \equiv v_z/v_t = 1/\zeta$ we write compactly $x_a = \alpha \tilde{v}_z$. Similarly we define the clipping angle $\beta = R_0/L_a$ and write $x_0 = \beta \tilde{v}_z$. Substituting the expressions for x_a and x_0 into Eq. (4.16) and evaluating the integral we obtain for the transfer efficiency

$$\chi_t(\tilde{v}_z) = 1 - (1 - \alpha/\beta) e^{-(\alpha \tilde{v}_z)^2} - \frac{1}{2\beta \tilde{v}_z} \sqrt{\pi}\, \mathrm{erf}\,(\alpha \tilde{v}_z)\,. \tag{4.17}$$

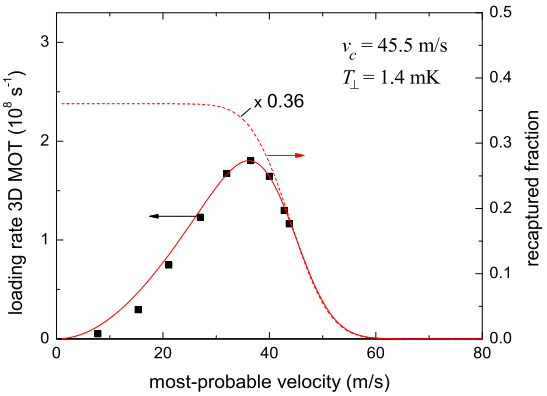

Figure 4.9: (Color online) Loading rate 3D MOT as a function of the most-probable velocity α_z in the beam (black squares - left scale). The drawn line represents the best fit to the data of the recapture model described in the text for $v_c = 45.5$ m/s (right scale). The result for zero beam divergence is shown as the dotted line, scaled down with a factor 0.36 for convenience of comparison.

The velocity-averaged transfer efficiency (recaptured fraction) into the 3D MOT is given by

$$\bar{\chi}_t(\alpha_z, v_c) = \int_0^{v_c} \chi_t(v_z/v_t)\phi_0\left(v_z, \alpha_z\right) dv_z, \tag{4.18}$$

where $\phi_0\left(v_z, \alpha_z\right)$ is the normalized axial velocity distribution defined by Eq. (4.15). The solid line in Fig. 4.9 is a plot of $\bar{\chi}_t(\alpha_z, v_c)$ for a fixed value of v_c. The position of the maximum is insensitive for the beam divergence and the best fit is obtained for a capture velocity of $v_c = 45.5$ m/s. In contrast the peak height $\bar{\chi}_{\max}$ depends strongly on the beam divergence. Using the lower limit for the characteristic transverse velocity ($v_t \gtrsim 1.4$ m/s) we calculate an upper limit for the recaptured fraction $\bar{\chi}_{\max} \lesssim 0.4$. For comparison also the result for zero beam divergence is shown in the plot (dotted line).
For the conditions used in experiment, $\partial B/\partial r = 0.19$ T/m and $\delta_L = -6\Gamma$, we calculate with Eq. (4.6) $v_c = 32 + 5.6\,|\delta_L/\Gamma| \approx 66$ m/s for $r_c = \sqrt{2}R_a = 12.7$ mm. Apparently the simple 1D model overestimates the capture velocity by some 50%. Because both the 2D MOT and the 3D MOT are configured in the 135° configuration with respect to the input beam and also $r_c = 12.7$ mm in both cases we presume a similar overestimate for the capture velocity of the 2D MOT. In the latter case we have $\partial B/\partial r = 0.50$ T/m and $\delta_L = -7.5\Gamma$ and calculate with Eq. (4.6) $v_c = 85 + 5.6\,|\delta_L/\Gamma| \approx 127$ m/s. Presuming somewhat arbitrarily that also this value overestimates the actual capture velocity by 50% we obtain $v_c \approx 85$ m/s as a reasonable estimate.
Starting from $\Phi_s = 8(3) \times 10^{13}$ s^{-1} we obtain with Eq. (4.4) for the theoretical maximum flux $\Phi_c = 5(2) \times 10^8$ s^{-1}. With the measured value $\Phi_r = 1.8(6) \times 10^8$ s^{-1} the overall efficiency $\chi = \Phi_r/\Phi_c$ is estimated to be $0.2 \lesssim \chi \lesssim 0.5$. This set a lower limit on the recaptured fraction, $0.2 \lesssim \bar{\chi}_{\max} \lesssim 0.4$, and (using our model) also an upper limit for the characteristic transverse velocity, $v_t \lesssim 2.5$ m/s. As the upper and lower limits more or less coincide our best estimate is $v_t \approx 2$ m/s, which corresponds to a transverse 2D MOT temperature of $T_\perp = 1.4$ mK. The corresponding beam divergence at optimal recapture for oven temperature $T = 623(12)$ K is $\zeta \approx 0.05$. For these conditions the brightness of the beam emerging from the 2D MOT is calculated to be $\sim 2 \times 10^{11}$ sr^{-1}s^{-1}.

4.5.2 Loss mechanisms

Because $\Phi_c \lll \Phi_s$ the output from the oven is well characterized by a small cold flux of capturable atoms overtaken by the hot flux of the full emittance. Once the hot flux exceeds a critical value we expect the cold flux to be attenuated by 'knock-out' collisions. This depletion of the low velocity class of atoms is a well-known phenomenon in close-to-effusive beam sources [163]. Comparing the total flux per unit area just above the emitting surface, $\Phi_{tot}/A \approx 6.5 \times 10^{15}\,\mathrm{s^{-1}cm^{-2}}$, with the flux per unit area in the capture region $\Phi_s/A \approx 4 \times 10^{13}\,\mathrm{s^{-1}cm^{-2}}$, we expect these knock-out collisions to occur primarily in the first few centimeters of the expanding beam. Once the atoms enter the 2D MOT the cross section increases because optically excited atoms interact resonantly with the hot background flux [169].
To model the attenuation we calculate the collision rate of an atom moving at velocity v_c along the symmetry axis at position l above the oven exit orifice with atoms from the hot background flux moving at typically the average velocity $\bar{v} \gg v_c$,

$$\dot{\Phi}/\Phi = \tfrac{1}{2}\sigma_6 n_s \int_0^{\theta_0(l)} v_r \sin\theta d\theta. \tag{4.19}$$

Here θ is the emission angle of the fast moving atoms with respect to the symmetry axis, $\tan\theta_0 = a/l$, σ_6 is the knock-out cross section and $v_r = (\bar{v}^2 + v_c^2 - 2v_c\bar{v}\cos\theta)^{1/2} \simeq \bar{v}$ is the relative velocity of the colliding atoms [163]. Using the substitution $dl = v_c dt$ we can solve the differential equation under the boundary condition $\Phi(l) = \Phi_c$ at $l = 0$ and obtain

$$\Phi(L) \simeq \Phi_c \exp[-\tfrac{1}{2}\sigma_6 n_s\,(\bar{v}/v_c)\int_0^L (1-\cos\theta_0)dl], \tag{4.20}$$

where $\cos\theta_0 = l/(l^2+a^2)^{1/2}$. In this model the density in the oven is taken to be uniform. Because for $l \gg a$ the collision probability vanishes we may freely extend the integral to infinity, $\int_0^\infty (1-\cos\theta_0)dl = a$. Hence, at the entrance of the 2D MOT the attenuated flux is given by

$$\Phi_{in} = \lim_{L\to\infty} \Phi(L) \simeq \Phi_c \exp(-\sigma_6 n_s \bar{v}\tau_6), \tag{4.21}$$

where $\tau_6 = a/2v_c \approx 47\ \mu$s is the characteristic duration of the attenuation process.
To estimate σ_6 we take the approach of ref. [170] and consider a slow atom moving at the capture velocity v_c along the symmetry-axis from the oven towards the capture region. Fast atoms flying-by with the thermal velocity $\bar{v}$ will give rise to momentum transfer as a result of Van der Waals interaction. As this happens most frequently close to the oven even a small momentum transfer $\Delta p \lesssim 0.1\, m v_c$ suffices to kick the atoms out of the capture cone Ω_c. Because $\bar{v} \gg v_c$ the trajectory of the fast atom is hardly affected and the momentum transfer to the cold atom can be calculated by integrating the transverse component of the Van der Waals force over time, $\Delta p = \frac{1}{2}\int_{-\infty}^{\infty} F_\perp(t)dt$. Here $F(r) = 6C_6/r^7$ with r the radial distance between the colliding atoms and $C_6 = 1389\, a_0^6\, E_h$ the Van der Waals coefficient [171] with $a_0 \approx 0.529 \times 10^{-10}$ m the Bohr radius and $E_h \approx 4.36 \times 10^{-18}$ J the Hartree energy. Changing from the time variable t to the angular variable θ using $\tan\theta = \bar{v}t/b$, where b is the distance of closest approach, we obtain using $F_\perp = F\cos\theta$ and $\cos\theta = b/r$,

$$\Delta p = \frac{6C_c}{2\bar{v}b^6}\int_{-\pi/2}^{\pi/2}\cos^6\theta d\theta = \frac{C_6}{\bar{v}b^6}\frac{15\pi}{16}. \tag{4.22}$$

The critical distance of closest approach for which the atoms are just scattered outside the capture cone Ω_c is given by

$$b_6 \simeq 1.8\,(C_6/mv_c\bar{v})^{1/6}\,. \tag{4.23}$$

Note that this quantity depends only very weakly on the precise values of v_c and $\bar{v}$. For $v_c \approx 85$ m/s and temperatures in the range $600 \lesssim T \lesssim 700$ K we calculate for the knock-out cross section $\sigma_6 = \pi b_6^2 \approx 4.4 \times 10^{-14}$ cm^2. Note that, in contrast to 'knock-out' collisions, 'knock-in' collisions are rare. The steep dependence of Δp on b implies that most of the atoms scattered outside the acceptance cone scatter over much larger angles than the minimum angle required for knock-out. Thus scattered atoms typically hit the wall of the oven tube and stick, rather than giving rise to knock-in.
Along the same lines we estimate the momentum transfer by resonant collisions inside the 2D MOT. As the relative velocities are large and the typical collision time is much shorter than the lifetime of the atoms in the excited state we may use again the classical scattering model discussed above. In the present case the critical distance of closest approach corresponds to momentum transfer just exceeding the escape value from the 2D MOT, $mv \gtrsim mv_c$ [170]. Neglecting the direction of the transition dipole the resonant-dipole force can be approximated by $F(r) = 3C_3/r^4$, where the C_3 coefficient is defined as [169, 172]

$$C_3 = e^2 a_0^2 D_{eg}^2/4\pi\varepsilon_0 = 3.7 \times 10^{-48}\,\mathrm{J\,m^3}. \tag{4.24}$$

Here $e \approx 1.60 \times 10^{-19}$ C is the elementary charge, $\varepsilon_0 \approx 8.85 \times 10^{-12}\,\mathrm{Fm^{-1}}$ the electric constant and $D_{eg} = 2.4$ a.u.the transition dipole moment for the $2s \rightarrow 2p$ transition in Li [140]. The corresponding critical distance of closest approach is in this case

$$b_3 \simeq 1.6\,(C_3/mv_c\bar{v})^{1/3}\,. \tag{4.25}$$

For $v_c \approx 85$ m/s and temperatures in the range $600 \lesssim T \lesssim 700$ K we calculate for the resonant cross section $\sigma_3 = \pi b_3^2 \approx 1.6 \times 10^{-13}$ cm^2. Accounting for the knock-out probability of trapped atoms the loading rate into the 3D MOT can be written as

$$\Phi_r = \bar{\chi}_t \Phi_{in} \exp[-\sigma_3 \tau_{\mathrm{res}} \Phi_s / A_c]. \tag{4.26}$$

Combining Eqs. (4.3) and (4.4) with the C_6 and C_3 loss exponents of Eqs. (4.21) and (4.26) and introducing the characteristic attenuation time $\tau_3 = A\tau_{\mathrm{res}}/4\pi L^2$ we obtain the following expression for the 3D MOT loading rate

$$\Phi_r \simeq \bar{\chi}_t a_6 n_s \bar{v}\, A \left(\frac{v_c}{\alpha}\right)^4 \frac{\Omega_c}{8\pi} \exp[-n_s \bar{v}\,(\sigma_6\tau_6 + \sigma_3\tau_3)], \tag{4.27}$$

Using $\tau_{\mathrm{res}} = 1$ ms we have $\tau_3 \approx 1.6$ μs. Note that only α, $\bar{v}$ and n_s are sensitive for the oven temperature. A best fit of Eq. (4.27) to the data using $\bar{\chi}_t$ and n_s (at $T = 623$ K) as free parameters is shown as the solid line in Fig. 4.8. The fit shown is obtained for $\bar{\chi}_t = 0.33$ and $n_s = 1.5 \times 10^{17}\,\mathrm{m^{-3}}$ at $T = 623$ K, which are both within the error limits given for these quantities. Thus also the position of the maximum confirms our model. As the result obtained for $\bar{\chi}_t$ strongly anti-correlates with the value presumed for v_c we cannot improve upon the estimate $\chi_{\max} = 30 \pm 10\%$ already given in subsection 4.5.1.
Interestingly, comparing the two loss mechanisms we find $\sigma_3\tau_3/\sigma_6\tau_6 \approx 0.1$, which shows that the resonance mechanism, dominating the background losses in the VCMOT [170,

109], is of minor importance in the present case. Since the output flux scales like $(v_c/\alpha)^4$ an obvious way to increase the output of MOT sources is to increase the capture velocity. Doubling the waist of the 2D MOT beams in the xy plane (see Fig. 1) in order to increase the capture radius we find with Eq. (4.9) that the capture velocity increases by $\sqrt{2}$ and the output by a factor 4. In addition, since τ_6 scales like $1/v_c$ the beam attenuation decreases slightly.

4.5.3 Comparison with Zeeman slowers

In several respects the 2D MOT source demonstrated in this paper represents an interesting alternative for the Zeeman slower. First of all the source yields a large controllable output flux of up to 3×10^9 s^{-1}, comparable to fluxes typically achieved in lithium Zeeman slowers. The transverse temperature of the source is low (1.4 mK) which makes it possible to recapture as much as 30% in a 3D MOT 220 mm downstream from the source. In contrast to Zeeman slowers, the 2D MOT source yields a clean and monochromatic cold atomic beam of which the most probable velocity can be varied over a wide range of velocities with the aid of a push beam. Permanent magnets for the creation of the quadrupole field add to the simplicity of the design. The resulting source is more compact than a typical Zeeman slower and is still capable of loading 10^{10} atoms in a 3D MOT.
Importantly, the 2D MOT principle works equally well with light atoms as with more heavy atoms like K, Rb and Cs. This shows that, like the Zeeman slower, also the 2D MOT beam source has a wide applicability. In cases with a sizable vapor pressure at room temperature the source will act as a VCMOT. As an example of a system for which a 2D MOT has not yet been realized we briefly discuss the case of Na. In this case the gradient of the quadrupole field should be scaled down proportional to $m^{1/2}$ in accordance with Eq. (4.8) to obtain the optimum value $\partial B/\partial r \approx 0.25$ T/m. In view of Eq. (4.9) the capture velocity scales down with the same factor. Using Eq. (4.27) we calculate for Na a maximum total output flux of 4×10^9 s^{-1} for an oven temperature $T \approx 471$ K. This output is lower than realized with Zeeman slowers but the oven is operated at much lower temperature [173, 149, 99].
Unlike the output of the Zeeman slower the output of the 2D MOT source is limited by a fundamental loss mechanism. As described in subsection 4.5.2 this is caused by Van der Waals forces between atoms leaving the oven and (to a lesser extent) by resonant-dipole forces between optically excited atoms in the 2D MOT and the hot background flux from the oven. These losses are quantified by the exponent in Eq. (4.27), which is shown as the dashed line in Fig. 8. Note that near maximum output at $T \approx 700$ K the attenuation factor is already as small as ~ 0.3. Therefore, the source is best operated at temperatures below 650 K, where the flux may be slightly smaller but the depletion time of the oven is comfortably long. Alternatively, one could incorporate a recycling principle [150, 148].

4.6 Summary and conclusion

We developed a novel beam source for cold ^{6}Li atoms. The source is based on the 2D MOT principle and yields a controllable output flux of up to $3 \times 10^9\,\mathrm{s}^{-1}$, comparable to fluxes typically achieved in lithium Zeeman slowers. Some 30% of the atoms are recaptured into a 3D MOT 220 mm downstream from the source. The source is side-loaded from

an oven and a push beam assures that only capturable atoms enter the main vacuum chamber. This yields a clean and quite monochromatic cold atomic beam of which the most-probable axial velocity α_z can be varied over the range $18 \lesssim \alpha_z \lesssim 70$ m/s by varying the intensity of the push beam. The 2D MOT can be fully optimized for capture because the push beam assures that the density of trapped atoms is intrinsically low. The push beam also drastically simplifies the alignment of the 2D MOT. Permanent magnets simplify the implementation of the quadrupole field. The resulting source is compact and enables us to load up to 10^{10} atoms into a 3D MOT, which is sufficient as a starting point for most experiments with quantum gases. The output flux increases exponentially with the oven temperature until at $T \approx 700$ K a loss mechanism limits the flux. We identify knock-out collisions near the oven exit as a result of Van der Waals forces between the atoms as the limiting mechanism. At maximum output the beam attenuation factor is ~ 0.35. Therefore, the source is more efficiently operated at a lower oven temperature. For $T = 623$ K we measured a loading rate of $\Phi_r = 1.8(6) \times 10^8\,\mathrm{s}^{-1}$ in the 3D MOT. At this temperature the uninterrupted running time on 8 g of lithium is ~ 17000 hrs. With our work we demonstrate that the 2D MOT principle works equally well with light atoms as with more heavy atoms and is likely to be suitable for any atomic system with an optical cooling transition.

Chapter 5
Asymptotic Bound-state Model

In this chapter we present an Asymptotic Bound-state Model which can be used to accurately describe all Feshbach resonance positions and widths in a two-body system. With this model we determine the coupled bound states of a particular two-body system. The model is based on analytic properties of the two-body Hamiltonian, and on asymptotic properties of uncoupled bound states in the interaction potentials. In its most simple version, the only necessary parameters are the least bound state energies and actual potentials are not used. The complexity of the model can be stepwise increased by introducing threshold effects, multiple vibrational levels and additional potential parameters. The model is extensively tested on the ^{6}Li-^{40}K system and additional calculations on the ^{40}K-^{87}Rb and ^{3}He* - ^{4}He* systems are presented.
This chapter will be submitted to Physical Review A. Parts of the model have been published in Ref. [18] and in Ref. [17] Physical Review Letters **100** 053201 (2008)

5.1 Introduction

The field of ultracold atomic gases has been rapidly growing during the past decades. One of the main sources of growth is the large degree of tunability to employ ultracold gases as model quantum systems [95, 174]. In particular the strength of the two-body interaction parameter, captured by the scattering-length a, can be tuned over many orders of magnitude. A quantum system can be made repulsive ($a > 0$), attractive ($a < 0$), non-interacting ($a = 0$) or strongly interacting ($|a| \to \infty$) in a continuous manner by means of Feshbach resonances. Feshbach resonances are induced by external fields: magnetically induced Feshbach resonances are conveniently used for alkali-metal atoms, while optically induced Feshbach resonances seem more promising for e.g. alkaline-earth atoms [62]. In this paper we consider magnetically induced resonances only.
Feshbach resonances depend crucially on the existence of an internal atomic structure, which can be modified by external fields. For alkali-metal atoms, this structure is initiated by the hyperfine interaction, which can be energetically modified by a magnetic field via the Zeeman interaction. For a given initial spin state, its collision threshold and its two-body bound states depend in general differently on the magnetic field. A Feshbach resonance occurs when the threshold becomes degenerate with a bound state. Accurate knowledge of the Feshbach resonance structure is crucial for experiments
The two-body system has to be solved to obtain the bound state solutions. Since the interactions have both orbital and spin degrees of freedom, this results in a set of radially coupled Schrödinger equations in the spin basis. The set of equations is referred to as Coupled Channels equations [175], and can be solved numerically. Quite often it is

far from trivial to obtain reliable predictions for the two-body problem, due to several reasons: the ab-initio interaction potentials are usually not accurate enough to describe ultracold collisions. Therefore these potentials have to be modelled by adding and modifying potential parameters. A full calculation for all spin combinations and all potential variations is very time-consuming. Moreover, one can easily overlook some features of the bound state spectrum due to numerical issues such as grid sizes and numerical accuracy. This is also due to a lack of insight of the general resonance structure, which is often not obvious from the numerical results.
Given the above, there is certainly a need for fast and simple models to predict and describe Feshbach resonances, which allow for a detailed insight in the resonance structure. In the last decade various simple models have been developed for ultracold collisions [47, 176, 177], which vary significantly in terms of complexity, accuracy and applicability. In all these models the radial equation plays a central role in finding the Feshbach resonances. In this paper we present in detail the Asymptotic Bound-state Model (ABM). This model, briefly introduced in Ref. [17], was successfully applied to the Fermi-Fermi mixture of ^{6}Li and ^{40}K. Here the observed loss features where assigned to 13 Feshbach resonances with high accuracy, and the obtained parameters served as an input to a full coupled channels analysis. The ABM builds on an earlier model by Moerdijk et al. [82] for homonuclear systems, which was also applied by Stan et al. [178] for heteronuclear systems. This model neglects the mixing of singlet and triplet states, therefore allowing the use of uncoupled orbital and spin states. In ABM we make use of the radial singlet and triplet eigenstates and include the coupling between them. This crucial improvement makes the whole approach in principle exact, and it allows for a high degree of accuracy given a limited number of parameters.
We show how we can systematically extend the most simple version of ABM to predict the width of the Feshbach resonances by including threshold behavior. Additionally we allow for the inclusion of multiple vibrational levels and parameter for the spatial wavefunction overlap. The fact that ABM is computationally light provides the possibility to map out the available Feshbach resonance positions and widths for a certain system, as has been shown in [18]. Throughout the paper we will use the ^{6}Li-^{40}K mixture as a model system to illustrate all introduced aspects. Additionally, we present ABM calculations on the ^{40}K-^{87}Rb mixture to demonstrate its validity on a more complex system, comparing it with accurate coupled channel calculations [179]. Finally, we make predictions for Feshbach resonances in the heteronuclear metastable helium (^{3}He*-^{4}He*) mixture.
In the following we describe the ABM model (Sec. 5.2) and various methods to obtain the required input parameters. In Sec. 5.3 the ABM is applied to the three physical systems and in Sec. 5.4 we introduce the coupling to the open channel to predict the width of Feshbach resonances. In section 5.5 we summarize our findings and comment on further extensions of the model.

5.2 Asymptotic Bound-state Model

We assume that the two colliding atoms both are initially prepared in a hyperfine state $|fm_f\rangle$, where f is the total spin and m_f its projection along the magnetic field axis. The two-body tensor product formed by the hyperfine states of the two atoms is called the *entrance channel*. To predict the position of a Feshbach resonance we calculate the energy

of the entrance channel and that of a coupled bound state as a function of the magnetic field. We expect Feshbach resonances at magnetic field values where the entrance channel energy equals the energy of the molecular state. In this section we will show how the ABM can be used to determine the energy of the entrance channel and of the coupled bound states.
The effective Hamiltonian describing the collision of two ground-state alkali atoms in the center of mass frame is given by [12]

$$\mathcal{H} = \frac{\mathbf{p}^2}{2\mu} + \mathcal{H}^{\text{int}} + \mathcal{V}, \tag{5.1}$$

where the first term is the relative kinetic energy with μ the reduced mass, $\mathcal{H}^{\text{int}}$ the internal energy of the two atoms and $\mathcal{V}$ the effective interaction between the atoms. We use the *bound* eigenstates $|\psi_\sigma\rangle$ of the relative Hamiltonian $\mathcal{H}^{\text{rel}} = \frac{\mathbf{p}^2}{2\mu} + \mathcal{V}$ as a basis for the secular equation

$$\det\left|(\epsilon_\sigma - E)\delta_{\sigma,\sigma'} + \left\langle \psi_\sigma \left| \mathcal{H}^{\text{int}} \right| \psi_{\sigma'} \right\rangle\right| = 0, \tag{5.2}$$

where the eigenvalues ϵ_σ are the binding energies of the uncoupled bound states of the relative Hamiltonian and σ is a label for all orbital and spin degrees of freedom. The solutions of the secular equation yield the energies of the coupled bound states as a function of magnetic field. Next we will specify the internal degrees of freedom of the two atoms, followed by a more detailed discussion of the relative Hamiltonian, the free parameters of the model and a description of asymptotic bound states.

5.2.1 Internal energy

The single atom internal Hamiltonian consists of hyperfine and Zeeman interactions

$$\mathcal{H}^{\text{hf}} = \frac{a_{\text{hf}}}{\hbar^2}\mathbf{i}\cdot\mathbf{s} + (\gamma_e\mathbf{s} - \gamma_i\mathbf{i})\cdot\mathbf{B}, \tag{5.3}$$

where $\mathbf{s}$ and $\mathbf{i}$ are the electron and nuclear spins respectively, γ_e and γ_i are their respective gyromagnetic ratios, a_{hf} is the hyperfine energy and $\mathbf{B}$ is the externally applied magnetic field. The hyperfine interaction couples the electron and nuclear spin which add to a total angular momentum $\mathbf{f} = \mathbf{s} + \mathbf{i}$. In Fig. 5.1 the well known hyperfine diagrams of ^{6}Li and ^{40}K are shown, the curves correspond to the eigenvalues of $\mathcal{H}^{\text{hf}}$. The one-atom hyperfine states are labeled $|fm_f\rangle$, although f is only a good quantum number in the absence of an external magnetic field. By labelling the colliding atoms with α and β, the interaction process can be described in the basis of the two-body internal states $|f_\alpha m_{f_\alpha}, f_\beta m_{f_\beta}\rangle$.
Since the effective interactions $\mathcal{V}$ can be neglected asymptotically, the threshold energy for two interacting atoms is completely determined by the two-body internal Hamiltonian $\mathcal{H}^{\text{int}} = \mathcal{H}^{\text{hf}}_\alpha + \mathcal{H}^{\text{hf}}_\beta$. Consequently, the threshold energy (E_{thr}) for a certain spin configuration (i.e. entrance channel) is the sum of the single atom internal energies. For a certain total energy E the threshold energy determines if a channel is open ($E > E_{\text{thr}}$) or closed ($E > E_{\text{thr}}$).

5.2.2 Relative Hamiltonian

The bound eigenstates of $\mathcal{H}^{\text{rel}}$ are crucial to determine the coupled bound states responsible for the Feshbach resonances. The relative Hamiltonian consists of effective interactions

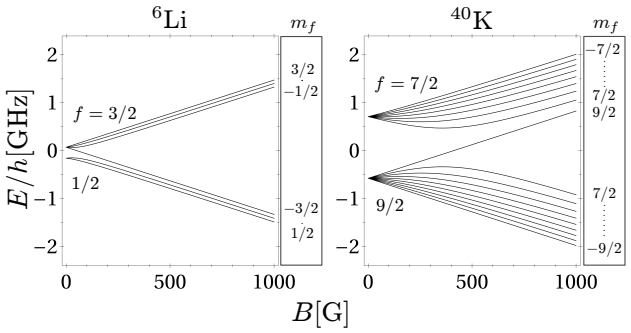

Figure 5.1: The single atom hyperfine diagrams for ^{6}Li and ^{40}K. The curves correspond to the eigenvalues of $\mathcal{H}^{\rm hf}$ and are labeled by the zero field quantum numbers $|fm_f\rangle$.

$\mathcal{V}$ resulting from all Coulomb interactions between the nuclei and electrons of both atoms [1]. These central interactions depend only on the quantum number S associated with the magnitude of the total electron spin $\mathbf{S} = \mathbf{s}_\alpha + \mathbf{s}_\beta$, therefore they can be decomposed as $\mathcal{V} = \sum_S |S\rangle \mathrm{V}_S \langle S|$ where the potential V_S is either the singlet ($S = 0$) or triplet ($S = 1$) potential. Note that for central interactions the two-body solutions will depend on orbital quantum number l, but not on its projection m_l. Both these quantum numbers are conserved.

We specify the ABM basis states $|\psi_\sigma\rangle$ as $|\psi_S^{\nu,l}\rangle|Sm_S\mu_\alpha\mu_\beta\rangle$. Here we define the spin basis states $|Sm_S\mu_\alpha\mu_\beta\rangle$ via spin quantum number S and the magnetic quantum numbers m_S, μ_α, and μ_β of the $\mathbf{S}$, $\mathbf{i}_\alpha$ and $\mathbf{i}_\beta$ operators respectively. The sum $m_F = m_S + \mu_\alpha + \mu_\beta$ is conserved, therefore limiting the number of spin states involved. The bound states for the singlet and triplet potentials, characterized by the vibrational and orbital quantum numbers ν and l, satisfy the eigenvalue equation for the relative motion, where we projected $\mathcal{H}^{\rm rel}$ on a specific S and l state:

$$\left[-\frac{\hbar^2}{2\mu}\frac{d^2}{dr^2} + V_S^l(r)\right]\psi_S^{\nu,l}(r) = \epsilon_S^{\nu,l}\psi_S^{\nu,l}(r). \tag{5.4}$$

Here $\psi_S^{\nu,l}(r) = \langle r|\psi_S^{\nu,l}\rangle$ is the relative reduced wavefunction, r the interatomic separation, and $V_S^l(r) \equiv l(l+1)\hbar^2/(2\mu r^2) + V_S(r)$. The corresponding binding energies are given by $\epsilon_S^{\nu,l}$. In this paper we focus on heteronuclear systems, however, the ABM works equally well for homonuclear systems. In the latter case one would rather use a symmetrized spin basis $|Sm_sIm_I\rangle$, where I is the total nuclear spin and m_I is the magnetic quantum number for $\mathbf{I}$ as described in Ref. [82].

Now that we have defined a complete basis, the internal Hamiltonian can be written as $\mathcal{H}_{\rm int} = \mathcal{H}_{\rm int}^+ + \mathcal{H}_{\rm int}^-$, where the $\mathcal{H}_{\rm int}^+$ part gives rise to hyperfine coupling within the separate singlet and triplet subspaces, while $\mathcal{H}_{\rm int}^-$ takes care of the coupling between the singlet and triplet manifolds. The latter term was neglected in the models of Refs. [82, 178].

For central interactions the orbital angular momentum is conserved, therefore we can solve Eq. (5.2) separately for every l-subspace:

[1] The much weaker magnetic dipole-dipole interactions are neglected.

$$\det|_{\nu,l}\langle Sm_S\mu_\alpha\mu_\beta|\left(\epsilon_S^{\nu,l}+\mathcal{H}_{\rm int}^{+}-E\right)\delta_{\nu,\nu'} \\ +\eta_{S,S'}^{\nu,\nu'}\mathcal{H}_{\rm int}^{-}|S'm_S'\mu_\alpha'\mu_\beta'\rangle_{\nu',l}|=0. \tag{5.5}$$

Here $\eta_{S,S'}^{\nu,\nu'}=\langle\psi_S^{\nu,l}|\psi_{S'}^{\nu',l}\rangle$ is the Franck-Condon factor which value generally is in the range $0\leq|\eta_{S,S'}^{\nu,\nu'}|\leq 1$, while only bound states within the same potential $V_S^l(r)$ are exactly orthonormal: $\langle\psi_S^{\nu,l}|\psi_S^{\nu',l}\rangle=\delta_{\nu,\nu'}$.

5.2.3 Free parameters

The free parameters of the ABM are the binding energies $\epsilon_S^{\nu,l}$ and the Franck-Condon factors $\eta_{S,S'}^{\nu,\nu'}$ describing the relative motion. These parameters can be obtained in a variety of manners. Here we discuss three methods which will be demonstrated in Sect. 5.3.
First, if the scattering potentials $V_S^l(r)$ are very well known, the bound state wavefunctions of the vibrational levels can be obtained by solving equation (5.4) for $\epsilon_S^{\nu,l}<0$. Numerical values of the Franck-Condon factors follow from the obtained eigenstates. This method is very accurate and can be extended to deeply bound levels, however accurate model potentials are only available for a limited number of systems.
A second method to obtain the free parameters is useful when the potentials are not very well or only partially known. For large interatomic distances the potentials can be parameterized by the asymptotically correct dispersion potential

$$V(r)=-\frac{C_6}{r^6}, \tag{5.6}$$

however, at short range this expression is no longer correct. Therefore we account for the inaccurate inner part of the potential by a boundary condition based on the accumulated phase method [86]. This boundary condition has a one-to-one relationship to the interspecies s-wave singlet and triplet scattering lengths. This method would then require only three input parameters: the van der Waals C_6 coefficient and the singlet (a_S) and triplet (a_T) scattering lengths. For an accurate description involving deeper bound states the accumulated phase boundary condition needs more parameters than only a scattering length.
The last method to obtain the free parameters is by comparing predicted positions of Feshbach resonances directly to experimental cold collision data, for instance by comparing it to atom loss. A loss feature spectrum can be obtained by holding an ultracold sample for a given time period at a particular magnetic field. The binding energies and Franck-Condon factors are obtained by fitting the calculated threshold crossings,which are the positions of the Feshbach resonances to the loss features. We used this method in Ref. [17], where it has proven to be very powerful due to the small computational time required to solve the eigenvalue equation.
The number of fit parameters is determined by the number of bound states which have to be considered. Depending on the atomic species and the magnetic field, a selected number of vibrational levels $\epsilon_S^{\nu,l}$ have to be taken into account. This number can be estimated by considering the maximum energy range involved. An upper bound results from comparing the maximum dissociation energy of the least bound vibrational level D^*

with the maximum internal energy of the atom pair $E_{\mathrm{int,max}}$. Using the dissociation energy of the N_ν-th vibrational level from [180] we obtain:

$$N_\nu \simeq \zeta \frac{\sqrt{\mu} C_6^{1/6}}{h} E_{\mathrm{int,max}}^{1/3} \tag{5.7}$$

where h is Planck's constant and ζ is a numerical constant. $E_{\mathrm{int,max}}$ is given by the sum of four terms; the hyperfine splitting of each of the two atoms at zero field, the maximum Zeeman energy for the free atom pair and the maximum Zeeman energy for the molecule. The constant ζ can be evaluated semi classically, yielding $\zeta = 1.8294$ [180], or numerically using the accumulated phase method, yielding $\zeta = 1.643$, in the following we will use the latter.

5.2.4 Asymptotic bound states

The most crucial parameters for ABM are the binding energies $\epsilon_S^{\nu,l}$, however, for accurate predictions of the Feshbach resonance positions, one also needs a rather accurate value for the Franck-Condon factors. For weakly bound states these factors are mainly determined by the binding energy difference between the bound states, rather than the potential shape. Therefore good approximations can be made with little knowledge of the scattering potential. For bound states with $r_c \gg r_0$, where r_c is the classical turning point and

$$r_0 = \frac{1}{2}\left(\frac{2\mu C_6}{\hbar^2}\right)^{1/4} \tag{5.8}$$

is the van der Waals range of the interaction potential, most of the probability density is at internuclear distances where the potential shape is unimportant. These bound states are commonly denoted as *halo states*[181]. The wavefunction is well described by $\psi(r) \sim e^{-\kappa r}$, where $\kappa = \sqrt{-2\mu\epsilon/\hbar^2}$ is the wavevector corresponding to a bound state with binding energy ϵ. The Franck-Condon factor of two weakly bound states with wavevectors κ_0 and κ_1 is given by

$$\langle \psi_0 | \psi_1 \rangle = \frac{2\sqrt{\kappa_0 \kappa_1}}{\kappa_0 + \kappa_1}. \tag{5.9}$$

This approximation is valid for states with $r_c \gg r_0$, i.e., for binding energies of $|\epsilon| \ll C_6/r_0^6$. The calculation of the Franck-Condon factors can be extended to deeper bound states by including the dispersive van der Waals tail. For $r \gg r_X$ where r_X is the radius where the van der Waals interaction equals the exchange interaction, the potential is well described by $-C_6/r^6$.The Franck-Condon factors can be calculated by numerically solving the Schrödinger equation (5.4) in the $-C_6/r^6$ potential for $r_X < r < \infty$ [182]. This method can be used for much deeper bound states, where $r_c \gg r_X$. We will define *asymptotic bound states* as states for which $r_c > r_X$. If even deeper bound states, with $r_c < r_X$, have to be taken into account, the potential can be extended by including the exchange interaction [79], or by using full model potentials.

To illustrate the validity of describing Feshbach resonances by asymptotic bound states we calculate the Franck-Condon factor for a contact potential (halo states), a van der Waals potential (asymptotic bound states) and a full model potential including short range behavior. Figure 5.2 shows the Franck-Condon factor η_{01}^{11} for ^{6}Li-^{40}K calculated numerically for the model potential, van der Waals potential, and analytically using equation (5.9).

The van der Waals coefficient used is $C_6 = 2322 E_h a_0^6$, where $E_h = 4.35974 \times 10^{-18}$J and $a_0 = 0.05291772$nm [183]. The η_{01}^{11} has been plotted as a function of the triplet binding energy ϵ_1 for three different values of the singlet binding energy ϵ_0. It is clear that the contact potential is only applicable for $\epsilon/h \lesssim 100$MHz, hence only for systems with resonant scattering in the singlet and triplet channels. The approximation based on the C_6 potential yields good agreement down to binding energies of $\epsilon \lesssim h \times 40$GHz, which is much more than the maximum possible vibrational level splitting of the least bound states ($D^* = h \times 8.2$GHz). The black circle indicates the actual Franck-Condon factor for the least bound state of ^{6}Li-^{40}K. For the contact, van der Waals and model potentials we find $\eta_{01}^{11} = 0.991$, $\eta_{01}^{11} = 0.981$ and $\eta_{01}^{11} = 0.979$ respectively.

5.3 Application to various systems

In this section we demonstrate the versatility of the ABM by applying it to three different systems using the three different approaches as discussed in Sect. 5.2.3.

5.3.1 ^{6}Li$-^{40}$K

Both ^{6}Li and ^{40}K have electron spin $s = 1/2$, therefore the total electron spin can be singlet $S = 0$ or triplet $S = 1$. We intend to describe all loss features observed in Ref. [17]. Since all these features where observed for magnetic fields below 300G we find that, by use of Eq. (5.7), it is sufficient to take only the least bound state ($\nu = 1$) of the singlet and triplet potential into account. This reduces the number of fit parameters to $\epsilon_1^{0,l}$ and $\epsilon_1^{1,l}$. Subsequently, we parameterize the $l > 0$ bound state energies by making use of model potentials as described by [184, 46] [2]. This allows us to reduce the number of binding energies to be considered to only two: $\epsilon_0^{1,0} \equiv \epsilon_0$ and $\epsilon_1^{1,0} \equiv \epsilon_1$. We now turn to the Franck-Condon factor η_{01}^{11} of the two bound states. As discussed in Sect. 5.2.4 its value is $\eta_{01}^{11} = 0.979$ and can be taken along in the calculation or approximated as unity. We first consider the case of $\eta_{01}^{11} \equiv 1$, this reduces the total number of fit parameters to only two. We fit the positions of the threshold crossings to the 13 observed loss features reported in Ref. [17] by minimizing the χ^2 value while varying ϵ_0 and ϵ_1. We obtain optimal values of $\epsilon_0/h = 716(15)$MHz and $\epsilon_1/h = 425(5)$MHz, where the error bars indicate one standard deviation. In Fig. 5.3, the threshold and spectrum of coupled bound states with $m_F = +3(-3)$ is shown for positive (negative) magnetic field values. The color scheme indicates the admixture of singlet and triplet contributions in the bound states. Feshbach resonances will occur at magnetic fields where the energy of the coupled bound state and the scattering threshold match. The strong admixture of singlet and triplet contributions at the threshold crossings emphasizes the importance of including the singlet-triplet mixing term $\mathcal{H}_{\rm int}^-$ in the Hamiltonian. All 13 calculated resonance positions have good agreement with the coupled channel calculations as described in Ref. [17], verifying that the ABM yields a good description of the threshold behavior of the ^{6}Li$-^{40}$K system for the studied field values.
We repeat the χ^2 fitting procedure now including the numerical value of the overlap. The η_{01}^{11} for both the s-wave and p-wave bound states are calculated numerically while varying

[2] Note that this procedure can also be applied with only a C_6 coefficient by utilizing the accumulated phase method

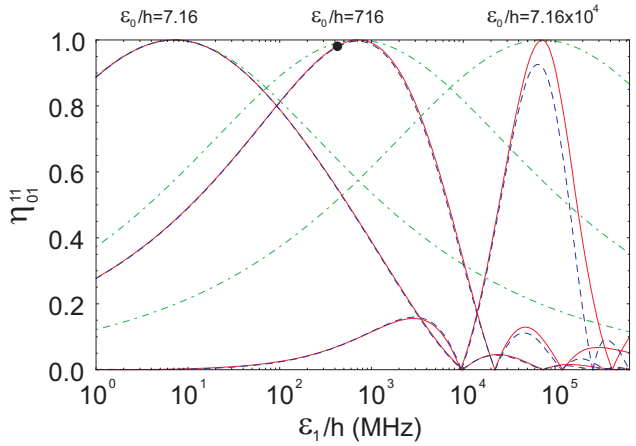

Figure 5.2: The Franck-Condon factor η_{01}^{11} for the ^{6}Li-^{40}K system calculated as a function of the triplet binding energy ϵ_1 for three different values of $\epsilon_0/h = 7.16$ MHz, $\epsilon_0/h = 716$ MHz and $\epsilon_0/h = 7.16 \times 10^4$ MHz. η_{01}^{11} is calculated for a model potential (dashed blue), a $-C_6/r^6$ potential (solid red) and a contact potential, equation (5.9) (dash-dotted green). The black circle indicates the actual value for the least bound state of ^{6}Li-^{40}K ($\epsilon_0/h =$ 716MHz and $\epsilon_1/h = 425$MHz). The nodes in η_{01}^{11} correspond to deeper lying vibrational states.

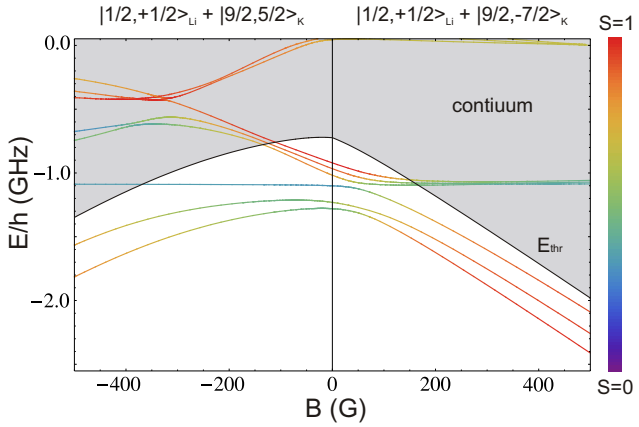

Figure 5.3: Here we have calculated the energies of all the coupled bound states for ^{6}Li-^{40}K with total spin $m_F = \pm 3$. The black solid line indicates the threshold energy of the entrance channel $|\{1/2, +1/2\}_{\mathrm{Li}}; \{9/2, +5/2\}_{\mathrm{K}}\rangle$ for $B < 0$ and $|\{1/2, +1/2\}_{\mathrm{Li}}; \{9/2, -7/2\}_{\mathrm{K}}\rangle$ for $B > 0$. The grey area represents the scattering continuum and the (colored) lines indicate the coupled bound states. Feshbach resonances occur when a bound state crosses the threshold energy. The color scheme indicates the admixture of singlet and triplet contributions in the bound states. The strong admixture near the threshold crossings at $B \simeq 150G$ demonstrate the importance of the singlet-triplet mixing in describing Feshbach resonance positions accurately. Since in the ABM the coupled bound states are not coupled to the entrance channel, they exist even for $E > E_{thr}$.

ϵ_0 and ϵ_1. This fit results in a slightly larger χ^2 value with corresponding increased discrepancies in the resonance positions. However, all of the calculated resonance positions are within the experimental widths of the loss features. Therefore, the analysis with $\eta_{01}^{11} \equiv 1$ and $\eta_{01}^{11} = 0.979$ can be safely considered to yield the same results within the experimental accuracy.

5.3.2 ^{40}K-^{87}Rb

We now turn to the ^{40}K-^{87}Rb mixture to demonstrate the application of the ABM model to a system including multiple vibrational levels and multiple non-trivial values for the overlap. Although accurate K-Rb scattering potentials are known [185], we choose to use the accumulated phase method as discussed in Sect. 5.2.3 using only three input parameters to demonstrate the accuracy of the ABM for a complex system like ^{40}K-^{87}Rb. We solve the radial Schrödinger equation (5.4) for $V_S^l(r) = -C_6/r^6$ and $\epsilon_S^{\nu,l} = \hbar^2 k^2/2\mu$ where $k \to 0$. We obtain the accumulated phase at $r_{in} = 18a_0$ by imposing a boundary condition at $r \to \infty$ using the s-wave phase shift $\delta_0 = \arctan(-ka)$, where a the s-wave scattering length. Subsequently we obtain binding energies for the three last bound states of the singlet and triplet potential by solving the same equation (5.4) but now with the accumulated phase at $r = r_{in}$ and $\psi(r \to \infty) = 0$ as boundary conditions. We numerically calculate the Franck-Condon factors by normalizing the wavefunctions for $r > r_{in}$, thereby neglecting the part of the wavefunction in the inner part of the potential ($r < r_{in}$). This assumption becomes less valid for more deeply bound states. We use as input parameters $C_6 = 4274 E_h a_0^6$ [183], $a_S = -111.5a_0$ and $a_T = -215.6a_0$ [185]. Figure 5.4 shows the spectrum of bound states with respect to the threshold energy for the mixture of ^{40}K $|f = 9/2, m_f = -9/2>$ and ^{87}Rb $|f = 1, m_f = +1>$ states. The red curves indicate the result of the ABM model and the blue curves are full coupled channel calculations [186]. The agreement between the two models is satisfactory, especially for the weakest bound states close to the threshold. The large negative scattering lengths indicates the presence of virtual bound states in both the singlet and triplet potentials. However, taking only the bound states into account already yields a good result. A conceptually different analysis of the K-Rb system using only three input parameters has been performed by Hanna, *et al.* [177].

5.3.3 ^{3}He* - ^{4}He*

In this section we briefly turn to the application of the ABM to a system of two two-electron atoms, namely the Fermi-Bose mixture of metastable helium-3 and helium-4. This system has recently been experimentally realized [39] and magnetic field tuning of the interaction parameters are of great interest. Up to now no field induced resonances have been reported experimentally nor theoretically. Based on potentials known from literature we calculate the binding energies of the least bound states and their corresponding Franck-Condon factors. Using these values as input parameters for the ABM we are able to predict Feshbach resonance positions. We use the adiabatic potential curves for the singlet ($1^1\Sigma_g^+$) and triplet ($1^3\Sigma_u^+$) potentials reported by Ref. [187] and the quintet ($1^5\Sigma_g^+$) potential we obtain from Ref. [188]. We obtain various Feshbach resonances at low magnetic field values. Two resonances of specific interest are at $B = 12.9$G in the ^{3}He* $|f = 3/2, m_f = -1/2\rangle$ ^{4}He* $|m_J = -1\rangle$ spin channel and at $B = 8.7$G in the ^{3}He* $|f = 3/2, m_f = +3/2\rangle$

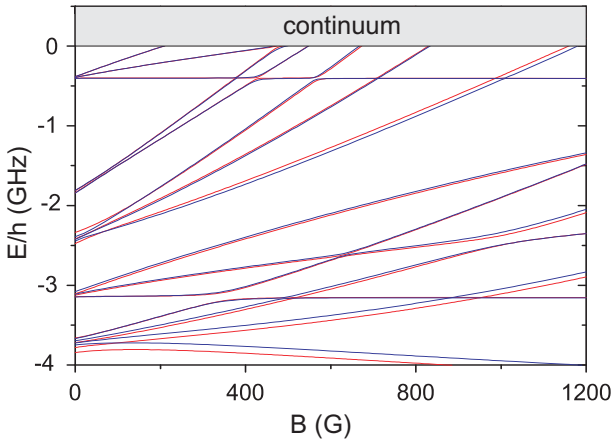

Figure 5.4: The bound state spectrum for ^{40}K-^{87}Rb for $m_F = -7/2$ plotted with respect to the threshold energy E_{thr} of the ^{40}K $|f = 9/2, m_f = -9/2 >$ + ^{87}Rb $|f = 1, m_f = +1 >$ hyperfine mixture. Red lines are ABM calculations and the blue lines are numerical coupled channels calculations. Good agreement between the two calculations is found in particular for the weakest bound levels.

^{4}He* $|m_J = 0\rangle$ spin channel. Both resonance positions are mainly determined by the accurately known quintet potential, and negligibly by the less accurately known triplet potentials. For temperatures in the ultracold regime, penning ionization collisions in the triplet potential are expected to be suppressed [189]. Spin exchange collisions of the ^{3}He* $|f = 3/2, m_f = -1/2\rangle$+^{4}He* $|m_J = -1\rangle \rightarrow$^{3}He* $|f = 3/2, m_f = -3/2\rangle$+^{4}He* $|m_J = 0\rangle$ type are suppressed for ultracold samples at $B = 12.9$G because a thermal activation of $\sim 580\mu K$ is required to drive the channel. Concluding, the $B = 12.9$G resonance is a promising candidate for manipulating interspecies interactions in the ^{3}He* - ^{4}He* mixture. However, due to the large background scattering length of the ^{3}He* - ^{4}He* system, the resonances are expected to be broad. Since the resonance position shifts by an amount of the order of the resonance width (see below) the actual resonance positions might be significantly different from the stated values.

5.4 Coupling to the open channel

The model, as introduced in section 5.2, has so far been used to determine the position of the Feshbach resonances. However, a Feshbach resonance is not only characterized by its position, but also by its width. The resonance width is for a collision process inversely proportional to the lifetime of the resonance. Its value plays an important role to determine whether a Feshbach resonance can be used to explore regimes of universal physics for strongly interacting quantum gases. Wide s-wave resonances give rise to universal behavior and can be described by the scattering length only, while narrow resonances need additional parameters such as the Effective Range parameter to describe the interactions properly. For practical experimental considerations, a resonance should be sufficiently wide to allow for an accurate control over the interaction strength.
The width of a resonance is determined by the coupling between the open collision threshold channel, and the closed-channel bound state which gives rise to the Feshbach resonance

[34, 35]. This coupling is contained in the AMB, however, to make it explicit in terms of a useful matrix element, it is crucial to partition the total Hilbert space, which describes the spin and spatial degrees of freedom, into two orthogonal subspaces $\mathcal{P}$ and $\mathcal{Q}$. The open channels are located in $\mathcal{P}$ space, and the closed channels in $\mathcal{Q}$ space. Within the ABM approach we obtain the coupling between the open and closed channels without the actual use of continuum states. In Sect. 5.4.1 we present the Feshbach theory tailored to suit the ABM, we give a mathematical description of the resonant coupling, and we demonstrate from a two-channel model how the ABM bound state compares to the associated $\mathcal{P}$-space bound state, and to the dressed molecular state from which one can deduce the resonance width. In Sect. 5.4.2 we summarize the results such that the width of the Feshbach resonances can be obtained for the general multi-channel case by performing two simple basis transformations. For a more thorough treatment of the Feshbach formalism we refer the reader to [34, 35] and for its application to cold atom scattering e.g. [82].

5.4.1 Tailored Feshbach theory

By introducing the projector operators P and Q, which project onto the subspaces $\mathcal{P}$ and $\mathcal{Q}$, respectively, the two-body Schrödinger equation can be split into a set of coupled equations [82]

$$(E - \mathcal{H}_{PP})|\Psi_P\rangle = \mathcal{H}_{PQ}|\Psi_Q\rangle, \tag{5.10}$$

$$(E - \mathcal{H}_{QQ})|\Psi_Q\rangle = \mathcal{H}_{QP}|\Psi_P\rangle, \tag{5.11}$$

where $|\Psi_P\rangle \equiv P|\Psi\rangle$, $|\Psi_Q\rangle \equiv Q|\Psi\rangle$, $\mathcal{H}_{PP} \equiv P\mathcal{H}P$, $\mathcal{H}_{PQ} \equiv P\mathcal{H}Q$, etc. Within $\mathcal{Q}$ space the Hamiltonian $\mathcal{H}_{QQ}$ is diagonal with eigenstates $|\phi_Q\rangle$ corresponding to the two-body bound state with eigenvalues ϵ_Q. The energy $E = \hbar^2k^2/2\mu$ is defined with respect to the open channel dissociation threshold.
We consider one open channel and assume that near a resonance it couples to a single closed channel. This allows us to write the S matrix of the effective problem in $\mathcal{P}$ space as [82]

$$S(k) = S_P(k)\left(1 - 2\pi i\frac{|\langle\phi_Q|\mathcal{H}_{QP}|\Psi_P^+\rangle|^2}{E - \epsilon_Q - \mathcal{A}(E)}\right), \tag{5.12}$$

where $|\Psi_P^+\rangle$ are scattering eigenstates of $\mathcal{H}_{PP}$, $S_P(k)$ is the direct scattering matrix describing the scattering process in $\mathcal{P}$ space in the absence of coupling to $\mathcal{Q}$ space.
The complex energy shift $\mathcal{A}(E)$ describes the dressing of the bare bound state $|\phi_Q\rangle$ by the coupling to the $\mathcal{P}$ space and is represented by

$$\mathcal{A}(E) = \langle\phi_Q|\mathcal{H}_{QP}\frac{1}{E^+ - \mathcal{H}_{PP}}\mathcal{H}_{PQ}|\phi_Q\rangle, \tag{5.13}$$

where $E^+ = E + i\delta$ with δ approaching zero from positive values. Usually the open channel propagator $[E^+ - \mathcal{H}_{PP}]^{-1}$ is expanded to a complete set of eigenstates of $\mathcal{H}_{PP}$, where the dominant contribution comes from scattering states. To circumvent the use of scattering states we expand the propagator to Gamow resonance states, which leads to a Mittag-Leffler expansion [190]

$$\frac{1}{E^+ - \mathcal{H}_{PP}} = \frac{\mu}{\hbar^2}\sum_{n=1}^{\infty}\frac{|\Omega_n\rangle\langle\Omega_n^D|}{k_n(k - k_n)}, \tag{5.14}$$

where n runs over all poles of the S_P matrix. The Gamow state $|\Omega_n\rangle$ is an eigenstate of $\mathcal{H}_{PP}$ with eigenvalue $\epsilon_{P_n} = \hbar^2 k_n^2/(2\mu)$. Correspondingly, the dual state $|\Omega_n^D\rangle \equiv |\Omega_n\rangle^*$, is an eigenstate of $\mathcal{H}_{PP}^\dagger$ with eigenvalue $(\epsilon_{P_n})^*$. Using these dual states, the Gamow states form a biorthogonal set such that $\langle\Omega_n^D|\Omega_{n'}\rangle = \delta_{nn'}$. For bound-state poles $k_n = i\kappa_n$, where $\kappa_n > 0$, Gamow states correspond to properly normalized bound states.
We assume the scattering in the open channel is dominated by a single bound state ($k_n = i\kappa_P$). This allows us to write the direct scattering matrix in Eq. (5.12) as

$$S_P(k) = e^{-2ika_{\rm bg}} = e^{-2ika_{\rm bg}^P}\frac{\kappa_P - ik}{\kappa_P + ik} \tag{5.15}$$

where $a_{\rm bg}$ is the open channel scattering length, and the P-channel background scattering length $a_{\rm bg}^P$ is on the order of the range of the interaction potential $a_{\rm bg}^P \approx r_0$. Since we only have to consider one bound state pole (with energy $\epsilon_P = -\hbar^2\kappa_P^2/2\mu$) in $\mathcal{P}$ space, the Mittag-Leffler series Eq. (5.14) is reduced to only one term. Therefore, the complex energy shift Eq. (5.13) reduces to

$$\mathcal{A}(E) = \frac{\mu}{\hbar^2}\frac{-i\mathrm{A}}{\kappa_P(k - i\kappa_P)}. \tag{5.16}$$

where $\mathrm{A} \equiv \langle\phi_Q|\mathcal{H}_{QP}|\Omega_P\rangle\langle\Omega_P^D|\mathcal{H}_{PQ}|\phi_Q\rangle$ is a positive constant. The coupling matrix element between open-channel bound state and the closed-channel bound state responsible for the Feshbach resonance is related to A.
The complex energy shift can be decomposed into a real and imaginary part such that $\mathcal{A}(E) = \Delta_{\rm res}(E) - \frac{i}{2}\Gamma(E)$. For energies $E > 0$ the unperturbed bound state becomes a quasi-bound state: its energy undergoes a shift $\Delta_{\rm res}$ and acquires a finite width Γ. For energies below the open-channel threshold, i.e. $E < 0$, $\mathcal{A}(E)$ is purely real and $\Gamma(E) = 0$. In the low-energy limit, $k \to 0$, Eq. (5.16) reduces to

$$\mathcal{A}(E) = \Delta - iCk, \tag{5.17}$$

where C is a constant characterizing the coupling strength between $\mathcal{P}$ and $\mathcal{Q}$ space [82], given by $C = \mathrm{A}(2\kappa_P|\epsilon_P|)^{-1}$ and $\Delta = \mathrm{A}(2|\epsilon_P|)^{-1}$. Note that if the direct interaction is resonant, $|a_{\rm bg}| \gg r_0$, the energy dependence of the complex energy shift is given by [191] $\mathcal{A}(E) = \Delta - iCk(1 + ika^P)^{-1}$ where $a^P = \kappa_P^{-1}$, yielding an energy dependence of the resonance shift.
Since we consider one open channel, the (elastic) S-matrix element can be written as $e^{2i\delta(k)}$, where $\delta(k)$ is the scattering phase shift. The scattering length, defined as the limit $a \equiv -\tan\delta(k)/k$, $(k \to 0)$, is found to be

$$a(B) = a_{\rm bg}\Big(1 - \frac{\Delta B}{B - B_0}\Big), \tag{5.18}$$

which shows the well known dispersive behavior. The direct scattering process is described by the scattering length $a_{\rm bg} = a_{\rm bg}^P + a^P$. At magnetic field value B_0, where the *dressed* molecular state crosses the P-threshold, the scattering length has a singularity. Near threshold, the shifted energy of the uncoupled molecular state, $\epsilon_Q + \Delta$, can be approximated by $\Delta\mu(B - B_0)$. The field width of the resonance is found to be equal to $\Delta B = C(a_{\rm bg}\Delta\mu)^{-1}$, where $\Delta\mu$ is the magnetic moment difference of the molecular state and the P-channel atoms.

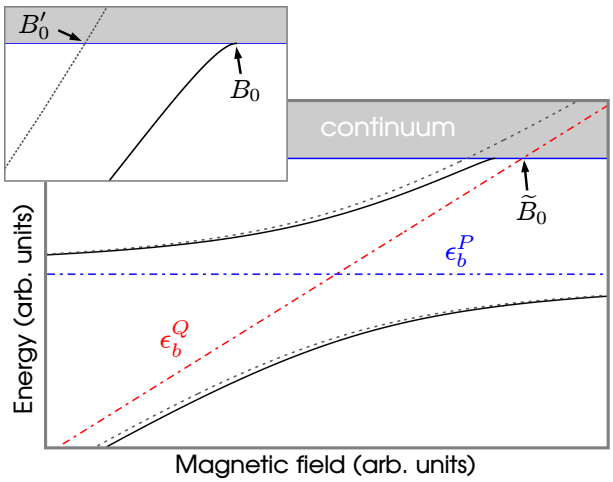

Figure 5.5: Different types of bound states, derived from a two-channel ABM model. The unperturbed molecular $\mathcal{Q}$ space bound state (dot-dashed red) is dressed by the coupling to $\mathcal{P}$ space, where ϵ_P is the uncoupled $\mathcal{P}$ space bound state (dot-dashed blue). Near threshold of the open channel (solid blue) the energy curve of the dressed molecular Feshbach state (solid black) will bend quadratically as a function of B and will cross the threshold at B_0. The uncoupled $\mathcal{Q}$ space bound state crosses the threshold at $\widetilde{B}_0$. For the original ABM bound state (gray) no threshold effects are seen and the coupled bound state crosses at B_0'.

The dressed state can be considered as a (quasi-) bound state of the total scattering system. The energy of these states is obtained by finding the poles of the total S matrix Eq. (5.12). This results in solving

$$(k - i\kappa_P)\,(E - \epsilon_Q - \mathcal{A}(E)) = 0, \tag{5.19}$$

for k. Due to the underlying assumptions, this equation is only valid for energies around threshold where the open and closed channel poles dominate.

We apply the above Feshbach theory to a (fictitious) two-channel version of ABM, and the results are shown in Fig. 5.5. This two-channel system is represented by a 2×2 Hamiltonian matrix, where there is only one open and one closed channel. The open and closed channel binding energies ϵ_P resp. ϵ_Q are given by the diagonal matrix elements, while the coupling is represented by the (identical) off-diagonal matrix elements. The closed channel bound state is made linearly dependent on the magnetic field, while the coupling is taken constant. In addition to ϵ_P and ϵ_Q, we plot the corresponding ABM solution, which in this case is equivalent to a typical two-level avoided crossing solution. The figure now nicely illustrates the evolution from ABM to the dressed ABM approach, where the latter solutions are found from the two physical solutions of Eq. (5.19), which are also plotted. Since the dressed ABM solutions account for threshold effects, they show the characteristic quadratic bending towards threshold as a function of magnetic field. From this curvature the resonance width can be deduced.

5.4.2 The dressed Asymptotic Bound state Model

To illustrate the presented model for a realistic case, we will discuss the ^{6}Li-^{40}K system prepared in the $|f_{\mathrm{Li}} m_{f_{\mathrm{Li}}}, f_{\mathrm{K}} m_{f_{\mathrm{K}}}\rangle = |1/2, +1/2, 9/2, -7/2\rangle$ two-body hyperfine state as an example throughout this section. This particular mixture is the energetically lowest spin combination of the $m_F = -3$ manifold, allowing to consider only one open channel. We note that the model can be utilized to cases containing more open channels.
In order to calculate the width of a Feshbach resonance using the method presented in Sect. 5.4.1 three quantities are required: the binding energy of the open channel ϵ_P, of the closed channel responsible for the Feshbach resonance ϵ_Q, and the coupling term between the two channels $\mathcal{H}_{PQ}$. In the following we will describe how to obtain these quantities from the ABM by two simple basis transformations.
For ultracold collisions the hyperfine and Zeeman interactions determine the threshold of the various channels and thus the partitioning of the Hilbert space into subspaces $\mathcal{P}$ and $\mathcal{Q}$, and therefore a natural basis for our tailored Feshbach formalism consists of the eigenstates of $\mathcal{H}^{\mathrm{int}}$. Experimentally a system is prepared in an eigenstate of the internal Hamiltonian $\mathcal{H}^{\mathrm{int}}$. This channel will be referred to as the entrance channel. Performing a basis transformation from the $|Sm_S\mu_\alpha\mu_\beta\rangle$ states to the eigenstates of $\mathcal{H}^{\mathrm{int}}$ allows us to identify the open and closed channel subspace. The open channel has the same spin-structure as the entrance channel.
We now perform a second basis transformation which diagonalizes within $\mathcal{Q}$ space without affecting $\mathcal{P}$ space. We obtain the eigenstates of $\mathcal{H}_{QQ}$ and are able to identify the bound state responsible for a particular Feshbach resonance. The bare bound states of $\mathcal{Q}$ space are defined as $\{|\phi_{Q_1}\rangle, |\phi_{Q_2}\rangle, \ldots\}$ with binding energies $\{\epsilon_{Q_1}, \epsilon_{Q_2}, \ldots\}$. For the one dimensional $\mathcal{P}$ space, which is unaltered by this transformation, the bare bound state $|\Omega_P\rangle$ of $\mathcal{H}_{PP}$ is readily identified with binding energy ϵ_P. In the basis of eigenstates of $\mathcal{H}_{PP}$ and $\mathcal{H}_{QQ}$ we easily find the coupling matrix elements between the i-th $\mathcal{Q}$ space bound state and the open channel bound state $\langle\phi_{Q_i}|\mathcal{H}_{QP}|\Omega_P\rangle$. This gives the coupling constant $\mathrm{A_i} = \langle\phi_{Q_i}|\mathcal{H}_{QP}|\Omega_P\rangle\langle\Omega_P|\mathcal{H}_{PQ}|\phi_{Q_i}\rangle$ that determines the resonance field B_0 by solving Eq. (5.19) at threshold, which is for $E = 0$:

$$\epsilon_{Q_i}\epsilon_P = \frac{\mathrm{A_i}}{2}. \tag{5.20}$$

The field width of this Feshbach resonance is proportional to the magnetic field difference between the crossings of the dressed (B_0) and uncoupled $\mathcal{Q}$ bound states ($\widetilde{B}_0$) with threshold since

$$\Delta B = \frac{a^P}{a_{\mathrm{bg}}}(B_0 - \widetilde{B}_0) = \frac{a^P}{a_{\mathrm{bg}}}\frac{\mathrm{A_i}}{2|\epsilon_P|\Delta\mu}. \tag{5.21}$$

We illustrate the dressed ABM for Li-K in Figs. 5.6 and 5.7, for $m_F = -3$. To demonstrate the effect of $\mathcal{H}_{PQ}$, we plotted for comparison both the uncoupled and dressed bound states [3]. Details of near-threshold behavior (gray shaded area in Fig. 5.6) are shown in Fig. 5.7 together with the obtained scattering length. We solved the pole equation of the total S-matrix Eq. (5.19) for each Q-state and plotted only the physical solutions which cause Feshbach resonances. The dressed bound states show the characteristic quadratic bending near the threshold. We have used C_6 to determine r_0 ($\approx a^P_{\mathrm{bg}}$) from Eq. 5.8.
Table 5.1 summarizes the results of the dressed ABM for the Li-K mixture. Note that the position of the Feshbach resonances will be slightly different compared to the results from

[3] For clarity only one of the two physical solutions is shown.

Table 5.1: The positions of experimentally observed s-wave Feshbach resonances of ^{6}Li−^{40}K. Column 2 gives the ^{6}Li ($m_{f_{Li}}$) and ^{40}K (m_{f_K}) hyperfine states. For all resonances $f_{Li} = 1/2$ and $f_K = 9/2$. Note that the experimental width of the loss feature $\Delta B_{\rm exp}$ is not the same as the field width ΔB of the scattering length singularity. Feshbach resonance positions B_0 and widths ΔB for ^{6}Li-^{40}K as obtained by the dressed ABM, obtained by minimizing χ^2. The last two columns show the results of full coupled channels (CC) calculations. All magnetic fields are given in (G). The experimental and CC values for $m_F < 0$ and $m_F > 0$ are taken from Ref. [17] and [18] respectively.

		Experiment		dressed ABM		CC	
m_F	$m_{f_{Li}}$,m_{f_K}	B_0	$\Delta B_{\rm exp}$	B_0	ΔB	B_0	ΔB
-5	$-\frac{1}{2}, -\frac{9}{2}$	215.6	1.7	216.2	0.16	215.6	0.25
-4	$+\frac{1}{2}, -\frac{9}{2}$	157.6	1.7	157.6	0.08	158.2	0.15
-4	$+\frac{1}{2}, -\frac{9}{2}$	168.2	1.2	168.5	0.08	168.2	0.10
-3	$+\frac{1}{2}, -\frac{7}{2}$	149.2	1.2	149.1	0.12	150.2	0.28
-3	$+\frac{1}{2}, -\frac{7}{2}$	159.5	1.7	159.7	0.31	159.6	0.45
-3	$+\frac{1}{2}, -\frac{7}{2}$	165.9	0.6	165.9	0.0002	165.9	0.001
-2	$+\frac{1}{2}, -\frac{5}{2}$	141.7	1.4	141.4	0.12	143.0	0.36
-2	$+\frac{1}{2}, -\frac{5}{2}$	154.9	2.0	154.8	0.50	155.1	0.81
-2	$+\frac{1}{2}, -\frac{5}{2}$	162.7	1.7	162.6	0.07	162.9	0.60
+5	$+\frac{1}{2}, +\frac{9}{2}$	114.47(5)	1.5(5)	115.9	0.91	114.78	1.82

the regular ABM, for equal values of $\epsilon_S^{\nu,0}$. Therefore, we have again preformed a χ^2 analysis and we found new values of the binding energies $\epsilon_0 = 713$[MHz] and $\epsilon_1 = 425$[MHz], which yields a lower χ^2 minimum as compared to the ABM calculation.
The obtained value of ΔB generally underestimates the field width of a resonance. This originates from the fact that only the dominant bound state pole corresponding to a^P has been taken into account. By including the pole of the dominant *virtual* state in the Mittag-Leffler expansion, ΔB will increase, and the value of a_{bg} will become more accurate.

5.5 Summary and Conclusion

We developed a novel method to describe Feshbach resonances. The model allows for fast and accurate prediction of resonance positions and widths with very little experimental input. The combination of the ABM with the accumulated phase allows to describe Feshbach resonances for a very large number of systems. We have demonstrated the application on three very different systems. The model underestimates the resonance width because we have neglected the dominant virtual state contribution in the Mittag-Leffler expansion. A further improvement of the model would be to take the virtual states into account. With this work we demonstrate that by performing simple matrix operations Feshbach resonances can be accurately described, allowing for a broad application for experiments working with ultracold gases.

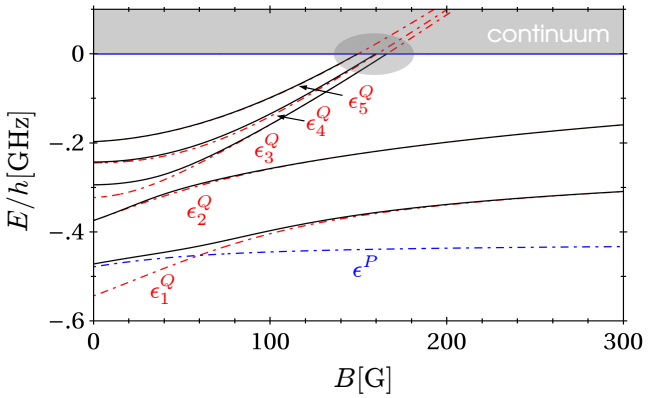

Figure 5.6: Dressed molecular states for Li-K for $m_F = -3$ (black lines, see also Table 5.1). The uncoupled $\mathcal{Q}$ and $\mathcal{P}$ bound states ($\mathcal{H}_{PQ} = 0$) are represented by the dot-dashed lines (red and blue respectively), indicating the effect of the $\mathcal{H}_{PQ}$ coupling.

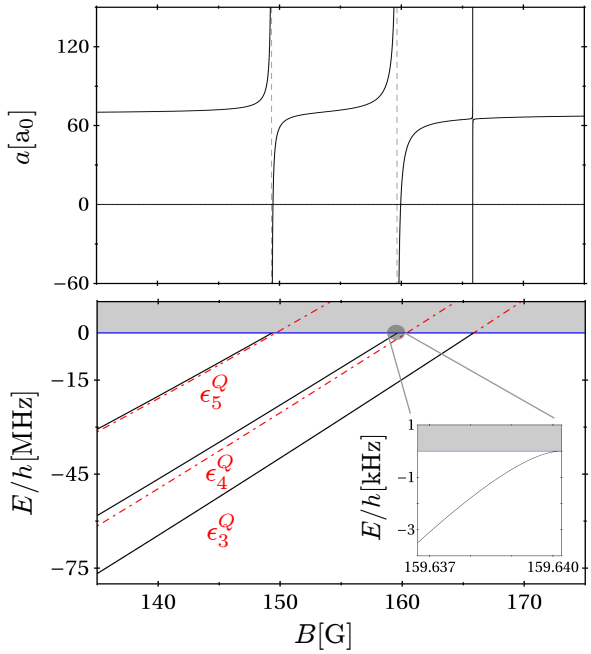

Figure 5.7: The dressed molecular states are shown near threshold (black). The field width of a resonance is related to the magnetic field difference of where the dressed and uncoupled $\mathcal{Q}$ bound state cross the threshold.

Chapter 6
Feshbach resonances in Li-K

We explore the widths of interspecies Feshbach resonances in a mixture of the fermionic quantum gases ^{6}Li and ^{40}K. Experimentally, we obtain the asymmetric lineshape of the interspecies elastic cross section by measuring the distillation rate of ^{6}Li atoms from an optically-trapped ^{6}Li/^{40}K mixture as a function of magnetic field. This provides us with the first experimental determination of the width of a resonance in this mixture, $\Delta B = 1.5(5)$ G, being one of the broadest. We present an extended version of the Asymptotic Bound-state Model and show that this model offers a convenient method to estimate the width and position of a large number of Feshbach resonances. Our results offer good perspectives for the observation of universal crossover physics in this mixture.
This chapter has been submitted to PRL [18]

6.1 Introduction

A decade of experiments with degenerate fermionic quantum gases has delivered major scientific advances as well as a whole new class of quantum many-body systems [7, 59, 95]. Feshbach resonances [192] played a central role in this development as they offer exceptional control over the interatomic interactions at low-temperatures [62]. In gases with the appropriate spin mixture the sign and magnitude of the s-wave scattering length a can be tuned to any positive or negative value by choosing the proper magnetic field in the vicinity of a resonance. In the case of fermionic atoms the role of Feshbach resonances is especially remarkable because Pauli exclusion dramatically suppresses three-body losses to deeply bound molecular states [193, 29]. The tunability has been used with great success in two-component Fermi gases of ^{6}Li and of ^{40}K to study and control pairing mechanisms, both of the Cooper type on the attractive side of the resonance ($a < 0$) [194] and of the molecular type on the repulsive side ($a > 0$) [195]. In particular the universal crossover from the superfluidity of a molecular Bose-Einstein condensate (BEC) towards the Bardeen, Cooper, Schrieffer (BCS) limit received a lot of attention [196].
Recently the study of heteronuclear fermionic mixtures, in particular the ^{6}Li/^{40}K mixture, has strongly gained in interest due to its additional mass imbalance. Experimentally unexplored properties of these mixtures include: superfluidity [20], phase separation [21], crystalline phases [197], exotic pairing mechanisms [198] and long-lived trimers [30]. In combination with spectroscopic measurements, precision measurements of Feshbach resonances can push the accuracy of the intermolecular potentials beyond the limitations of the Born-Oppenheimer approximation [136]. In the first experiment with the ^{6}Li/^{40}K mixture quantum degeneracy was reported by the Munich group, using a BEC of ^{87}Rb as a third species to assure thermalization of the fermions [199]. The basic interaction

properties of the ^{6}Li/^{40}K system were established in experiments by the Innsbruck group [17], in which the loss features of 13 Feshbach resonances were observed and assigned with the computationally-light Asymptotic Bound-state Model (ABM) as well as with a full coupled-channels analysis. The first ^{6}Li^{40}K molecules were recently reported from Munich [44].

In this Letter we report the first observation of the asymmetric lineshape (Fano profile) of the inter-species elastic cross section in the K-rich ^{6}Li/^{40}K mixture near a Feshbach resonance. Very recently, also the Li-rich mixture was studied [75]. Using a variation on the evaporation method [200], we measure the rate of distillation (preferential evaporation) of ^{6}Li atoms from a K-rich ^{6}Li/^{40}K mixture confined in an optical dipole trap. The line shape provides for this mixture the first precision determination of a resonance position as well as the first measurement of a resonance width. Extending the ABM approach we estimate the widths of all s-wave Feshbach resonances in stable two-component ^{6}Li/^{40}K mixtures below 500 G. The experimentally characterized resonance is one of the broadest of the ^{6}Li/^{40}K system.

6.2 Experimental procedure

The ultracold mixture of ^{6}Li and ^{40}K is created starting from two independent two-dimensional magneto-optical traps (2D MOTs) as beam sources for cold atoms [201]. From the cold beams we recapture about 10^9 K atoms and 10^6 Li atoms in a two-species 3D MOT. After optical pumping we transfer up to 80% of the ^{6}Li and 60% of the ^{40}K into an optically plugged magnetic quadrupole trap [5]. This trap is formed by a quadrupole field with a gradient of 180 G/cm along the tight vertical axis, plugged along the horizontal axis with a 7 W blue-detuned laser beam (532 nm) focused to a waist of 16 μm. The transfer is optimized to create a spin-polarized sample of ^{6}Li in the $|f, m_f\rangle = |3/2, +3/2\rangle$ hyperfine state and a three-component mixture of ^{40}K in the hyperfine states $|9/2, +5/2\rangle$, $|9/2, +7/2\rangle$ and $|9/2, +9/2\rangle$. The three-components assure effective thermalization of the potassium by *intra*-species collisions. The lithium thermalizes sympathetically by *inter*-species collisions with the potassium. The ^{6}Li/^{40}K mixture is cooled for 23 seconds by forced evaporation (from high field down) in the plugged trap on the microwave transitions of K ($|9/2, m_f\rangle \rightarrow |7/2, m_f - 1\rangle$) and Li ($|3/2, +3/2\rangle \rightarrow |1/2, +1/2\rangle$) simultaneously. Just before inter-species spin-exchange losses become prohibitive the evaporation is stopped to remove the non-stretched potassium states ($m_f < +9/2$) by a microwave spin-cleaning sweep (from zero field up), removing the undesired atoms in the plug-region of the trap. After cleaning, the remaining 30% of the ^{40}K is transferred together with the ^{6}Li into an optical dipole trap with a well depth of $U_0 = 360$ μK for K ($U_0 = 160$ μK for Li). The trap is created using a 5 W fiber laser ($\lambda = 1.07$ μm) focused to a waist of 19 μm and serving as an optical tweezer.

With an additional stage of forced evaporative cooling in the optical trap we reached - in pure ^{40}K - a quantum degenerate spin mixture at temperature $T \simeq 0.2\, T_F$, where T_F is the Fermi temperature. To prepare the ^{6}Li/^{40}K mixture we apply a holding field of ~ 10 G and succeed in transferring up to 50% of the ^{6}Li atoms to the $|1/2, +1/2\rangle$ state by adiabatic fast passage on the microwave transition using a field sweep downwards across the resonant field chosen at ~ 9 G. The residual population of the $f = 3/2$ manifold is removed by a resonant light pulse on the $^2S_{1/2} \rightarrow {}^2P_{3/2}$ transition. For the Feshbach measurements the

resulting clean mixture is optically transported without substantial losses by moving the optical tweezer in 3.5 s over a distance of 21.5 cm to a $12.7 \times 12.7 \times 42$ mm quartz cell extending from the main vacuum chamber. The transport is realized by moving a lens mounted on a precision linear air-bearing translation stage. In the Feshbach cell we can apply homogeneous fields (< 10 ppm/mm) of up to 500 G. At this point we have prepared a $|1/2, +1/2\rangle_{\mathrm{Li}} - |9/2, +9/2\rangle_{\mathrm{K}}$ mixture consisting of 4×10^3 lithium and 2×10^4 potassium atoms at temperature $T \approx 21(2)$ μK.

6.3 Extended ABM

In search for broad and accessible Feshbach resonances we analyzed the ^{6}Li/^{40}K two-body system with an extended version of the ABM [17]. We start from the two-body Hamiltonian for the relative motion

$$\mathcal{H} = \mathbf{p}^2/2\mu + \mathcal{V} + \mathcal{H}^{int} = \mathcal{H}^{rel} + \mathcal{H}^{int}, \tag{6.1}$$

containing the relative kinetic energy with μ the reduced mass, the electron spin dependent central interatomic interaction $\mathcal{V}$, and the internal energy $\mathcal{H}^{int}$ of the two atoms. Here we restrict $\mathcal{H}^{int}$ to the hyperfine and Zeeman terms and consider s-wave interactions only. Instead of solving coupled radial Schrödinger equations, the ABM approach relies on knowledge of the binding energies of the highest bound states in the two-body system, which is sufficient to determine the scattering properties, and, in particular, the position of Feshbach resonances. For ^{6}Li/^{40}K only the least bound levels of $\mathcal{H}^{rel}$ are relevant and can be obtained using the eigenvalues E_S of the least bound states in the electron-spin singlet ($S = 0$) and triplet ($S = 1$) potentials as free parameters; here we adapt E_0 and E_1 from Ref. [17].

The mixture is prepared in one of the two-body hyperfine eigenstates of $\mathcal{H}^{int}$ at magnetic field B, referred to as the P-channel or open channel; for $B = 0$ denoted via the hyperfine quantum numbers as $|f_\alpha, m_{f_\alpha}; f_\beta, m_{f_\beta}\rangle$. The corresponding energy of two free atoms at rest in the mixture defines the B-dependent threshold between the scattering states ($E > 0$) and the bound states ($E < 0$) of $\mathcal{H}$. In the following we define $\mathcal{H}$ relative to this threshold energy. A complete basis for the spin properties is defined via the quantum numbers S, its projection M_S, and the projection of the nuclear spins μ_α and μ_β, while demanding that the total projection $M_S + \mu_\alpha + \mu_\beta = m_{f_\alpha} + m_{f_\beta} = M_F$ is fixed. By diagonalizing $\mathcal{H}$ starting from this 'singlet-triplet' basis we find the energies of the bound states, and the Feshbach resonances are localized at the magnetic fields where they intersect with the energy of the threshold.

Threshold effects cause the approximately linear magnetic field dependence of the bound-state energies to change to quadratic behavior close to the field of resonance [95, 62]. This provides information about the width of a Feshbach resonance. The ABM, as discussed thus far, does not show these threshold effects, which is not surprising because the threshold is not explicitly build into the theory; it is merely added as a reference value for comparison with the ABM eigenvalues.

However, the ABM contains all ingredients to obtain also the resonance width. Here we give a brief description [202]. The width depends on the coupling between the open channel and the various closed channels, which is determined in two steps. First we separate the open channel P, as defined above, from all other channels: the closed channels Q [82]. This

is realized with a basis rotation from the singlet-triplet basis to the basis of the eigenstates of $\mathcal{H}^{int}$ at field B. Next we diagonalize the closed-channel subspace, leaving the open-channel unaffected. We refer to the diagonal sub-spaces as $\mathcal{H}_{PP}$, a single matrix element that we identify with the (bare) open-channel bound-state energy $\epsilon_P = -\hbar^2\kappa_P^2/2\mu$, and as $\mathcal{H}_{QQ}$, a matrix containing the (bare) closed-channel bound-state energies ϵ_Q. The coupling between the open and the resonant closed channel is referred to as $\mathcal{H}_{PQ}$.
The bare bound states (in both open and closed channel) are 'dressed' by $\mathcal{H}_{PQ}$. This is nicely treated in Feshbach's resonance theory [203, 204]: a closed-channel bound state acquires a finite width Γ and its energy undergoes a shift Δ_{res}. If the binding energy of a certain Q-channel bound state $|\phi_Q\rangle$ is sufficiently close to the threshold the complex energy shift is given by [204]

$$\mathcal{A}(E) = \Delta_{res}(E) - \frac{i}{2}\Gamma(E) = \frac{\mu}{\hbar^2}\frac{-i\mathrm{A}}{\kappa_P(k - i\kappa_P)}, \tag{6.2}$$

where $\mathrm{A} = |\langle\phi_Q|\mathcal{H}_{QP}|\phi_P\rangle|^2$ is the coupling strength to the P-channel bound state $|\phi_P\rangle$. For $k \to 0$ the expression $\Gamma \equiv \hbar^2 k/\mu R^*$ defines the characteristic length R^* [83]. The negative energy $E = \hbar^2k^2/2\mu$ of the dressed bound state follows by solving the pole equation $E - \epsilon_Q - \mathcal{A}(E) = 0$. From the energy dependence of the dressed bound state we obtain an expression for the magnetic field width ΔB of the corresponding Feshbach resonance as defined by the dispersive formula for the field dependence of the scattering length,

$$a(B) = a_{bg}\left(1 - \frac{\Delta B}{B - B_0}\right). \tag{6.3}$$

The resonance width ΔB is given by

$$\mu_{rel}\Delta B = \frac{a^P}{a_{bg}}\frac{\mathrm{A}}{2\epsilon_P}. \tag{6.4}$$

Here $\mu_{rel} = \partial\epsilon_Q/\partial B|_{B=B_0}$ is the magnetic moment of the bare Q channel relative to the open channel threshold. Note that $R^* = -\hbar^2\epsilon_P/(\mu a^P\mathrm{A}) = \hbar^2/(2\mu a_{bg}\mu_{rel}\Delta B)$. The off-resonance scattering is described by the background scattering length $a_{bg} = a_{bg}^P + a^P$, where $a_{bg}^P \approx r_0$ and $a^P = \kappa_P^{-1}$. Here $r_0 \equiv (\mu C_6/8\hbar^2)^{1/4} \simeq 41\,a_0$ is the inter-species Van der Waals range, with C_6 the Van der Waals coefficient and a_0 the Bohr radius.
The results for all s-wave resonances in stable two-component ^{6}Li/^{40}K mixtures below 500 G are shown in Fig. 6.1. The widest resonances for the ^{6}Li/^{40}K mixture are found to be of the order of 1 Gauss. For the experiment we selected a resonance in the fully-stretched ($M_F = 5$) manifold $|1/2, +1/2\rangle_{\mathrm{Li}} \otimes |9/2, +9/2\rangle_{\mathrm{K}}$ with the predicted position of $B_0 = 114.7$ G as obtained with the ABM parameters $E_{0,1}$ from Ref. [17]. The predicted width is $\Delta B = 0.9$ G. This value is known to slightly underestimate the actual width [202, 205].

6.4 Feshbach resonance width measurement

To observe the resonance we first ramp the field up to 107.112 G where any remaining potassium spin impurities are selectively removed by resonant light pulses. The Fano profile of the resonance is observed by measuring the distillation rate of the Li from the

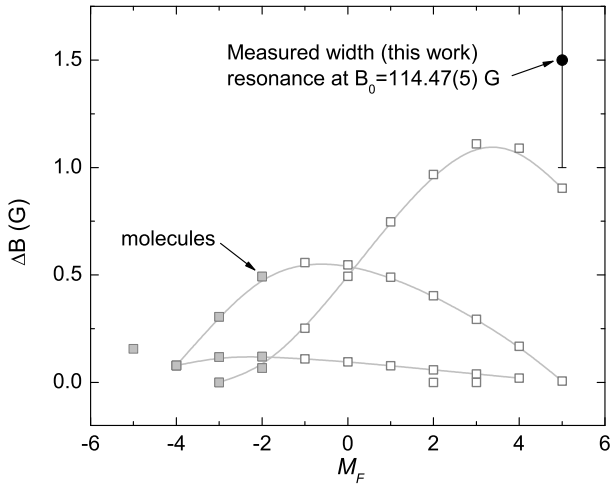

Figure 6.1: ABM calculated widths of all s-wave Feshbach resonances in stable two-component ^{6}Li/^{40}K mixtures below 500 G. The lines are a guide to the eye. The point at $M_F = -5$ corresponds to the $|1/2, -1/2\rangle_{\mathrm{Li}} - |9/2, -9/2\rangle_{\mathrm{K}}$ mixture. All other mixtures contain the ^{6}Li ground state $|1/2, +1/2\rangle_{\mathrm{Li}}$. Solid black dot: width measurement reported in this work. The mixtures with $-M_F = 5, 4, 3, 2$ (gray squares) where studied in Ref. [17]. The resonance used in Ref. [44] for molecule formation is indicated with an arrow.

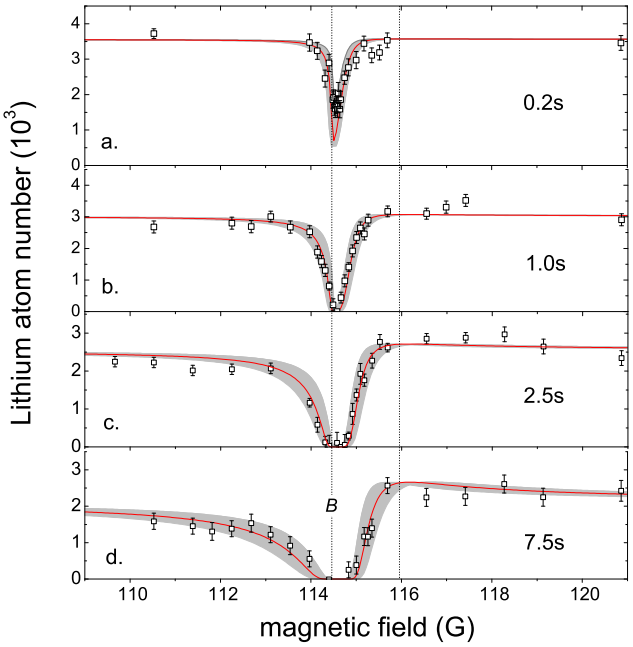

Figure 6.2: (Color online) Measurement of the Feshbach resonance width. The red solid line indicates the best fit obtained for $B_0 = 114.47(5)$ G and $\Delta B = 1.5(5)$ G. The gray shaded area indicates the combined error in B_0 and ΔB.

potassium-rich Li-K mixture in the optical trap as a function of magnetic field. To initiate this process we decrease the depth of the dipole trap in 10 ms to $U/U_0 \approx 0.15$. Aside from a small spilling loss of the ^{6}Li this decompresses the mixture with a factor $(U/U_0)^{3/4} \approx 0.24$ in the adiabatic limit and reduces the temperature accordingly by a factor $(U/U_0)^{1/2} \approx 0.39$. The truncation parameter for evaporation, $\eta = U/k_BT$, drops for both species by the same amount $\eta/\eta_0 \approx 0.39$. After decompression the central density of the potassium is $n_{\rm K} \approx 2 \times 10^{11}\,{\rm cm}^{-3}$ ($n_{\rm Li} \approx 9 \times 10^9\,{\rm cm}^{-3}$ for Li) and the temperature of the mixture is $T = 9(1)$ μK. As the truncation parameter of the lithium ($\eta_{\rm Li} \approx 2.7$) is much smaller than that of potassium ($\eta_{\rm K} \approx 6.2$) the Li preferentially evaporates at a rate proportional to the inter-species elastic cross section. As the lithium is the minority component this distillation process proceeds at an approximately constant rate. We have verified that a pure lithium cloud experiences no rethermalization by itself. The final trap depth U was determined from the total laser power and the measured trap frequency for the potassium, $\omega_r/2\pi = 1.775(6)$ kHz. In Fig. 6.2 we plot the atom number after various holding times and as a function of magnetic field. We analyze our data by modelling the distillation rate. Before decompression ($\eta_{Li} \approx 7$) we observe a loss of 30% for 1s holding time on resonance. As the decompression reduces the density by a factor 4 the three-body losses can be neglected in the decompressed trap. The distillation of the lithium as a function of time t is described by $N(t) = N_0\, e^{-t/\tau_{ev}} e^{-t/\tau_{bg}}$, where $N_0 \approx 3 \times 10^3$ is the initial number of lithium atoms, $\tau_{bg} = 25$ s the vacuum limited lifetime and $\tau_{ev}^{-1} \simeq n_{\rm K} \langle \sigma\,(k)\, \hbar k/\mu \rangle e^{-\eta_{Li}}$ the thermally-averaged evaporation rate. Here is

$$\sigma(k) = 4\pi \frac{a^2(k)}{1 + k^2 a^2(k)} \tag{6.5}$$

the elastic cross section with

$$a(k) = a_{bg} + \frac{a_{bg}\mu_{rel}\Delta B}{\hbar^2 k^2/2\mu - \mu_{rel}\,(B - B_0)} \tag{6.6}$$

the 'Doppler shifted' scattering length, with $a_{bg} = 56.6$ a$_0$ at the resonance position B_0, and $\mu_{rel} = 1.57\,\mu_B$. Note that for $kR^* \ll 1$ Eqs. (6.6) and (6.3) yield the same result for the cross section (6.5).

The solid lines in Fig. 6.2 show the best simultaneous fit of the thermally-averaged Eq. (6.5) to the four sub-figures, accounting for 25% variation in N_0 from one day to the next. The best fit is obtained for $B_0 = 114.47(5)$ G and $\Delta B = 1.5(5)$ G ($R^* \approx 100$ nm), where B_0 is mostly determined by the data of Fig. 6.2a and ΔB by those of Fig. 6.2d. Uncertainties in T and $n_{\rm K}$ can result in broadening of the loss features but the difference in asymmetries between Fig. 6.2a-d can only originate from the asymmetry of the elastic cross section around the resonance. The zero crossing of $a(k)$, prominently visible in systems with a resonantly enhanced a_{bg} like ^{6}Li [206] and ^{40}K [207], remains within the noise band of our distillation measurements because in the ^{6}Li/^{40}K system a_{bg} is non-resonant ($\sigma_{bg} = 1 \times 10^{-12}{\rm cm}^{-2}$). Close to the expected zero crossing a narrow $M_F = +2$ Feshbach resonance occurs at 115.6 G in the $|1/2, +1/2\rangle_{\rm Li} \otimes |9/2, +3/2\rangle_{\rm K}$ manifold. We have observed this resonance in impure spin mixtures.

6.5 Conclusion

The chosen resonance offers good perspectives to meet the conditions for universal crossover physics in this mixture: $E_F, \mu_{rel} |B - B_0| \ll \Gamma/2$, where $E_F \equiv \hbar^2 k_F^2 / 2\mu$ is the characteristic relative energy of a colliding pair of atoms at their Fermi energy. The former condition corresponds to $k_F R^* \ll 1$ and is satisfied for Fermi energies $E_F \ll E^* \equiv \hbar^2 / 2\mu R^{*2} \sim 5$ μK; the latter condition corresponds to $k_F a \gg 1$ and is satisfied for $\mu_{rel} |B - B_0| / E^* < k_F R^* \ll 1 \Leftrightarrow |B - B_0| \ll 43$ mG.

Chapter A
Potassium Properties

A.1 Introduction

This section is meant to provide an overview of the properties of atomic potassium to be used in ultracold gases experiments. A very thorough review of the properties of lithium has been given in the thesis of Michael Gehm [208, 209]. The properties of potassium are well discussed in the thesis of Robert Sylvester Williamson III [120], and a lot of properties in this appendix are obtained from it. For the other alkali atoms extended reviews have been given for Na, Rb and Cs by Daniel Steck [210].

A.2 General Properties

Potassium is an alkali-metal occurring with the symbol K and atomic number 19. It has been discovered in 1807 by deriving it from potassium hydroxide KOH. Being an alkali atom it has only one electron in the outermost shell and the charge of the nucleus is being shielded by the core electrons. This makes the element very chemically reactive due to the relatively low ionization energy of the outermost electron. The basic physical properties of potassium are listed in Table A.1. Potassium has a vapor pressure given in mbar by [159]:

$$\begin{aligned} &\text{(solid)} && \log\ p = 7.9667 - \frac{4646}{T} && 298\ \text{K} < T < T_m. \\ &\text{(liquid)} && \log\ p = 7.4077 - \frac{4453}{T} && T_m < T < 600\ \text{K} \end{aligned} \tag{A.1}$$

Figure A.1 depicts the vapor pressure over the valid range of Eq. A.1.

Potassium has a chemical weight of 39.0983(1) [212] and appears naturally in three isotopes, ^{39}K, ^{40}K and ^{41}K which are listed in Table A.2. The fermionic isotope ^{40}K has

Melting point	63.65°C (336.8 K)	[211]
Boiling point	774.0°C (1047.15 K)	[211]
Density at 293 K	0.862 g/cm^3	[211]
Ionization energy	418.8 kJ mol^{-1}	[211]
	4.34066345 eV	[89]
Vapor pressure at 293 K	1.3×10^{-8} mbar	[159]
Electronic structure	$1s^2 2s^2 p^6 3s^2 p^6 4s^1$	

Table A.1: General properties of potassium

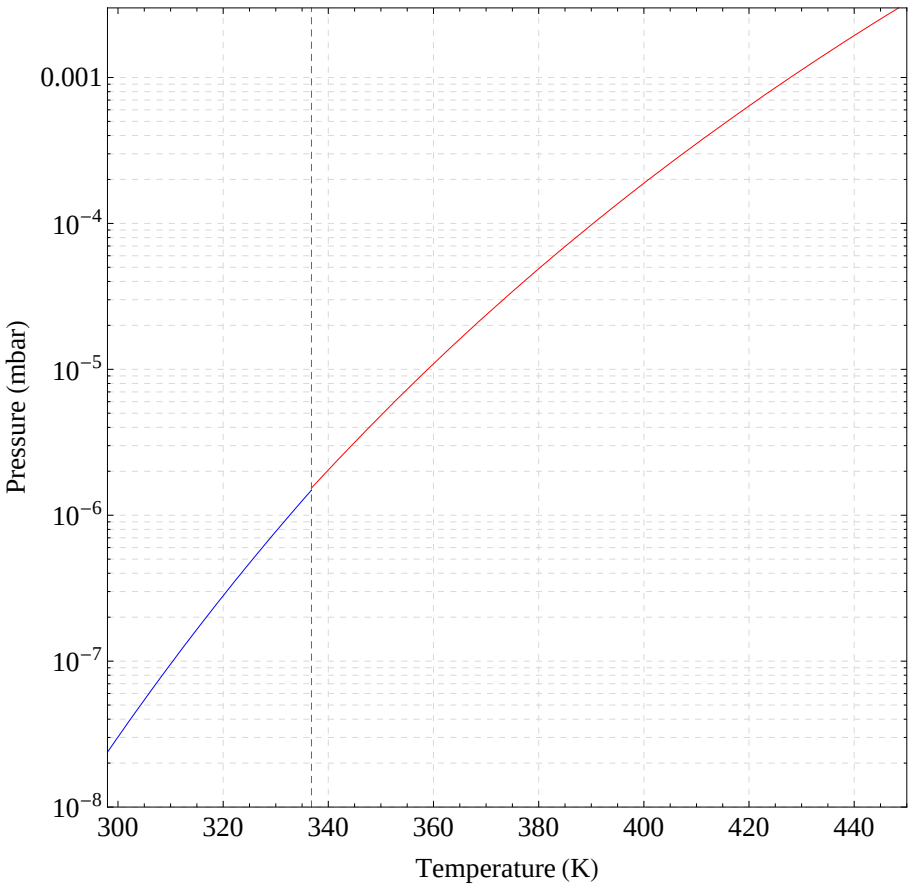

Figure A.1: Vapor pressure of potassium taken from [159]. The green dashed line indicates the melting point of $T = 336.8°\mathrm{C}$.

Isotope A	Neutrons N	Abundance (%)[212]	m (u)[214]	τ[120]	I[120]
39	20	93.2581(44)	38.96370668(20)	stable	3/2
40	21	0.0117(1)	39.96399848(21)	1.28×10^9 y	4
41	22	6.7302(44)	40.96182576(21)	stable	3/2

Table A.2: Naturally occurring isotopes of potassium. The atomic number of potassium is $Z = 19$. The given properties are the atomic number A, the number of neutrons in the nucleus N, the abundance, the atomic mass m, the lifetime τ and the nuclear spin I.

two radioactive decay channels. In 89% of the cases it decays through a β^- decay of 1.311MeV resulting in the stable ^{40}Ar. In the remaining 11% it decays through electron capture (K-capture) to ^{40}Ca [213]. The former decay channel is commonly used for dating of rocks.

A.3 Optical properties

The most strong lines of the ground state potassium atom are the D1 ($^2S \rightarrow {}^2P_{1/2}$) and D2 ($^2S \rightarrow {}^2P_{3/2}$) lines. The most recent high precision measurements of the optical transition frequencies of potassium have been published by Falke *et al.* [102]. Table A.3 and A.4 list the properties of the D1 and D2 lines respectively. The natural lifetime τ of an excited state is related to the linewidth of the associated transition by

$$\Gamma = \frac{1}{\tau} \tag{A.2}$$

where Γ is the natural linewidth. A temperature can be related to this linewidth, which is referred to as the *Doppler temperature*

$$k_B T_D = \frac{\hbar\Gamma}{2}$$

where k_B is the Boltzmann constant. The wavenumber k and frequency ν of a transition are related to the wavelength λ by

$$k = \frac{2\pi}{\lambda}, \qquad \nu = \frac{c}{\lambda} \tag{A.3}$$

When an atom emits or absorbs a photon the momentum of the photon is transferred to the atom by the simple relation

$$m v_{rec} = \hbar k \tag{A.4}$$

where m is the mass of the atom, v_{rec} is the recoil velocity obtained (lost) by the absorption (emission) process and $\hbar = h/2\pi$ is the reduced Planck constant. A temperature can be associated to this velocity, which is referred to as the recoil temperature

$$k_B T_{rec} = \frac{1}{2} m v_{rec}^2 \tag{A.5}$$

Finally, we can define a saturation intensity for a transition. This intensity is defined as the intensity where the optical Rabi-frequency equals the spontaneous decay rate. The optical Rabi-frequency depends on the transition. For the cycling transition $F = 9/2 \rightarrow F = 11/2$ it is given by

Property	symbol	value	reference
Frequency	ν	389.286184353 THz	[102]
Wavelength	λ	770.108136507 nm	
Wavenumber	$k/2\pi$	12985.1893857 cm^{-1}	
Lifetime	τ	26.37(5) ns	[215]
Natural linewidth	$\Gamma/2\pi$	6.03(1) MHz	
Recoil velocity	v_{rec}	1.2965411 cm/s	
Recoil Temperature	T_{rec}	0.40399576 μK	
Doppler Temperature	T_D	145 μK	

Table A.3: Optical properties of the ^{40}K D1-line.

Property	symbol	value	reference
Frequency	ν	391.016296050 THz	[102]
Wavelength	λ	766.700674699 nm	
Wavenumber	$k/2\pi$	13042.8997000 cm^{-1}	
Lifetime	τ	26.37(5) ns	[215]
Natural linewidth	$\Gamma/2\pi$	6.03(1) MHz	
Recoil velocity	v_{rec}	1.3023033 cm/s	
Recoil Temperature	T_{rec}	0.40759471 μK	
Doppler Temperature	T_D	145 μK	
Saturation intensity	I_s	1.75 mW/cm^2	

Table A.4: Optical properties of the ^{40}K D2-line.

$$I_s = \frac{\pi hc}{3\lambda^3\tau}$$

A.4 Fine structure, Hyperfine structure and the Zeeman effect

The fine structure interaction originates from the coupling of the orbital angular momentum **L** of the valence electron and its spin **S** with corresponding quantum numbers L and S respectively. The total electronic angular momentum is given by:

$$\mathbf{J} = \mathbf{L} + \mathbf{S}$$

and the quantum number J associated with the operator **J** is in the range of $|L - S| \leq J \leq L + S$. The electronic ground state of ^{40}K is the $4^2S_{1/2}$ level, with $L = 0$ and $S = 1/2$, therefore $J = 1/2$. For the first excited state $L = 1$ and $S = 1/2$ therefore $J = 1/2$ or $J = 3/2$ corresponding to the states $4^2P_{1/2}$ and $4^2P_{3/2}$ respectively. The fine structure interaction lifts the degeneracy of the $4^2P_{1/2}$ and $4^2P_{3/2}$ levels, splitting the spectral lines in the D_1 line ($4^2S_{1/2} \rightarrow 4^2P_{1/2}$) and the D_2 line ($4^2S_{1/2} \rightarrow 4^2P_{3/2}$).

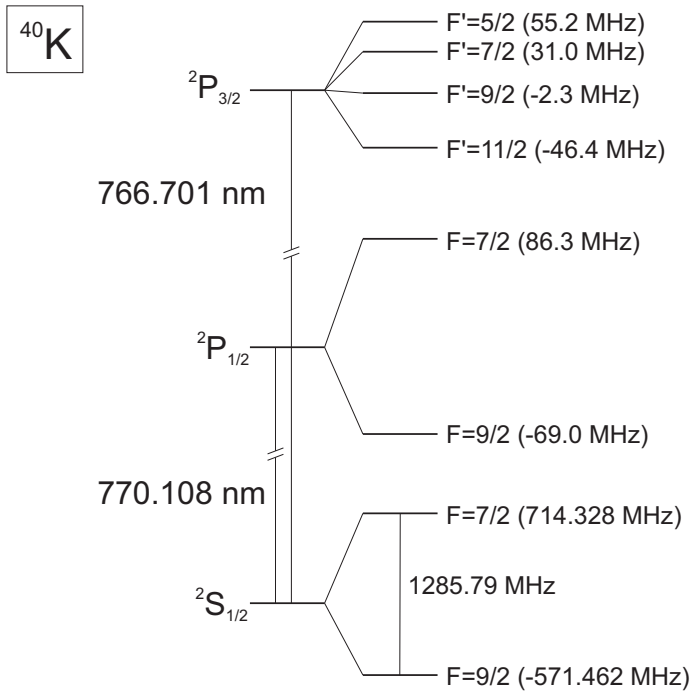

Figure A.2: Optical transitions of the D1 and D2-lines of ^{40}K and the transitions used for trapping, cooling and diagnostics. Numerical values are taken from [102] and [77]. Note the inverted hyperfine structure.

The hyperfine interaction originates from the coupling of the nuclear spin $\mathbf{I}$ with the total electronic angular momentum

$$\mathbf{F} = \mathbf{J} + \mathbf{I}$$

where the quantum number F associated with the operator $\mathbf{F}$ is in the range of $|J - I| \leq F \leq J + I$, where I is the quantum number corresponding to the operator $\mathbf{I}$. For ^{40}K the fine-structure splitting is $\Delta E_{FS} \simeq h \times 1.7$ THz, therefore the two excited states can be considered separately when considering smaller perturbations like the hyperfine or Zeeman interaction which are on the order of a few GHz or less.
The Hamiltonian describing the hyperfine structure for the two excited states described above is given by [77, 78]

$$\mathbf{H}^{\mathrm{hf}} = \frac{a_{hf}}{\hbar^2}\mathbf{I}\cdot\mathbf{J} + \frac{b_{hf}}{\hbar^2}\frac{3(\mathbf{I}\cdot\mathbf{J})^2 + \frac{3}{2}(\mathbf{I}\cdot\mathbf{J}) - \mathbf{I}^2\mathbf{J}^2}{2I(2I-1)J(2J-1)},$$

where a_{hf} and b_{hf} are the magnetic dipole and electric quadrupole constants respectively. The dot product is given by

$$\mathbf{I}\cdot\mathbf{J} = \frac{1}{2}(\mathbf{F}^2 - \mathbf{I}^2 - \mathbf{J}^2)$$

In the presence of an external magnetic field the Zeeman interaction has to be taken into account

$$\mathbf{H}^{\mathrm{Z}} = (g_J\mathbf{J} - g_I\mathbf{I})\cdot\mathbf{B},$$

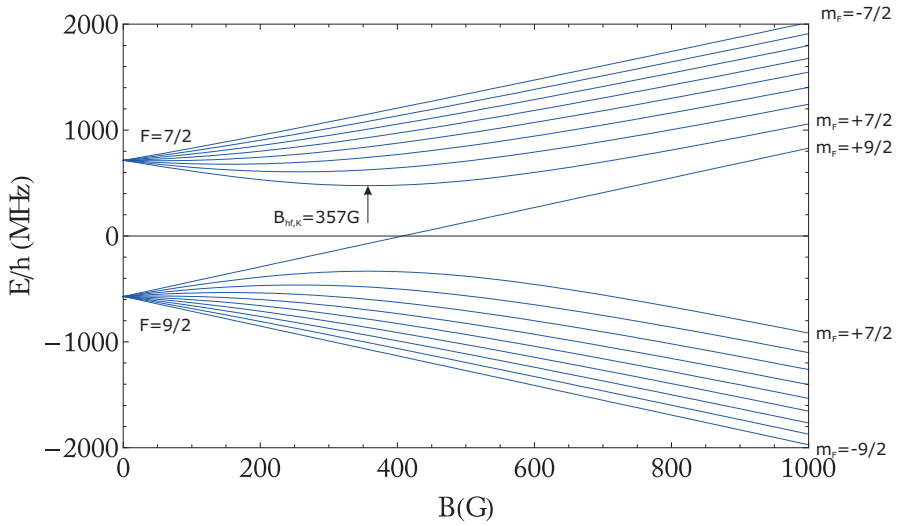

Figure A.3: The hyperfine structure of the $^2S_{1/2}$ groundstate of ^{40}K. The states are labeled with their low-field quantum numbers $|F, m_F\rangle$. Note the inverted hyperfine structure.

Property	symbol	value	Ref.
$4p^2S_{1/2}$ Magnetic dipole constant	a_{hf}	$h \times -285.7308(24)$ MHz	[77]
$4p^2P_{1/2}$ Magnetic dipole constant	a_{hf}	$h \times -34.523(25)$ MHz	[102]
$4p^2P_{3/2}$ Magnetic dipole constant	a_{hf}	$h \times -7.585(10)$ MHz	[102]
$4p^2P_{3/2}$ Electric quadrupole constant	b_{hf}	$h \times -3.445(90)$ MHz	[102]

Table A.5: Hyperfine structure coefficients for the ground state and the first exited state.

where g_J is the Landé g-factor of the electron and g_I the nuclear gyromagnetic factor, with the sign convention such that $\boldsymbol{\mu}$=$g_I\mu_B\mathbf{i}$. The factor g_J can be written as

$$g_J = g_L\frac{J(J+1)-S(S+1)+L(L+1)}{2J(J+1)} + g_S\frac{J(J+1)+S(S+1)-L(L+1)}{2J(J+1)},$$

where $g_S \simeq 2.002319$ is the electron g-factor, g_L is the gyromagnetic factor of the orbital, given by $g_L = 1-m_e/m_n$, where m_e is the electron mass and m_n is the nuclear mass. The total hyperfine interaction in the presence of an external magnetic field is now given by the internal hamiltonian

$$\mathbf{H}^{\text{int}} = \mathbf{H}^{\text{hf}} + \mathbf{H}^{\text{Z}} \tag{A.6}$$

Figures A.3 and A.4 show the eigenvalues of Eq. A.6 for the $^2S_{1/2}$ ground state and the $^2P_{1/2}$ and $^2P_{3/2}$ excited states respectively.

A.5 Scattering properties

The scattering properties of ultracold atoms are essential for the evaporative cooling processes and most experiments performed with ultracold gases. At typical densities temperatures the scattering reduces to s-wave scattering For ultracold scattering only lower partial waves play a role and the scattering properties are determined by the positions of

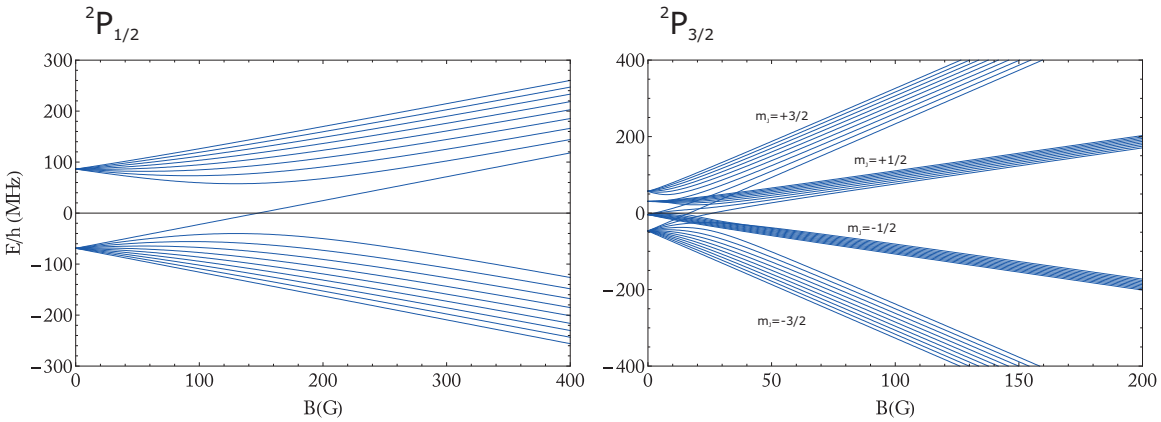

Figure A.4: Hyperfine structure of the $^2P_{1/2}$ (D1) and the $^2P_{3/2}$ (D2) levels of ^{40}K.

Property	symbol	value	reference
Total nuclear g-factor	g_I	$-0.000176490(34)$	[77]
Total electronic g-factor	$g_J(4p^2S_{1/2})$	2.00229421(24)	[77]
Total electronic g-factor	$g_J(4p^2P_{1/2})$	2/3	
Total electronic g-factor	$g_J(4p^2P_{3/2})$	4/3	

Table A.6: Electronic and nuclear gyromagnetic factors. Experimental values for the g_J values are not available, therefore, we use the Russel-Saunders values which agree within the error margins for all other alkali atoms [77]. An experimental value for g_J can be obtained by fitting to the data of Ref. [137].

isotope	a_s	a_t
39/39	138.49(12)	−33.48(18)
39/40	−2.84(10)	−1985(69)
39/41	113.07(12)	177.10(27)
40/40	104.41(9)	169.67(24)
40/41	−54.28(21)	97.39(9)
41/41	85.53(6)	60.54(6)

Table A.7: s-wave scattering lengths for the various isotope-combinations of potassium, values are taken from Ref. [137]

	value	units
C_6	3925.9	$E_h a_0^6$
C_8	4.224×10^5	$E_h a_0^8$
C_{10}	4.938×10^7	$E_h a_0^{10}$
r_0 (^{39}K)	64.61	a_0
r_0 (^{40}K)	65.02	a_0
r_0 (^{41}K)	65.42	a_0

Table A.8: Van der Waals properties of the scattering potential of potassium. $V_{vdw}(r) = -C_6/r^6 - C_8/r^8 - C_8/r^8$.

only the last few bound states of the potentials. The scattering can be described by the radial Schrödinger equation

$$\left[-\frac{\hbar^2}{2\mu}\left(\frac{\partial^2}{\partial r^2} + \frac{2}{r}\frac{\partial}{\partial r} - \frac{l(l+1)}{r^2}\right) + V(r)\right] R(r) = \epsilon R(r), \tag{A.7}$$

where $R(r)$ is the radial wavefunction, l is the angular momentum quantum number and $V(r)$ is the scattering potential. As has been pointed out in Chapter 5 many ultracold scattering properties with sufficient accuracy for general use in the lab can be obtained by only using the accumulated phase method and $V(r) = -C_6/r^6$. However, for Potassium accurate potentials have been published by Falke, *et al.* [137]. Because potassium has $S = 1/2$ the total spin of the potassium dimer can be either singlet ($S = 0$) or triplet ($S = 1$). Figure A.5 shows the Born-Oppenheimer potentials for the singlet $X^1\Sigma$ and triplet $a^3\Sigma$ potentials. Solving Eq. A.7 for $\epsilon \downarrow 0$ one can obtain the scattering length. Table A.7 lists the s-wave scattering lengths of the various potassium isotopes [137].

To qualitatively described the scattering for ^{40}K we compare the scattering lengths to the the van der Waals range. The van der Waals range is a measure for the typical range of the potential for an atomic species and is given by [62]

m_{f1}, m_{f2}	s/p	B_0 (G)	ΔB (G)	Ref.
-9/2 + -7/2	s	202.10 ± 0.07	7.8 ± 0.6	[65, 50, 216]
-9/2 + -5/2	s	224.21 ± 0.05	9.7 ± 0.6	[65, 217]
-9/2 + -5/2	p	~ 198.8		[65, 50, 218]

Table A.9: All resonances are between spin states in the $F = 9/2$ manifold. This table has been adapted from Ref. [65]

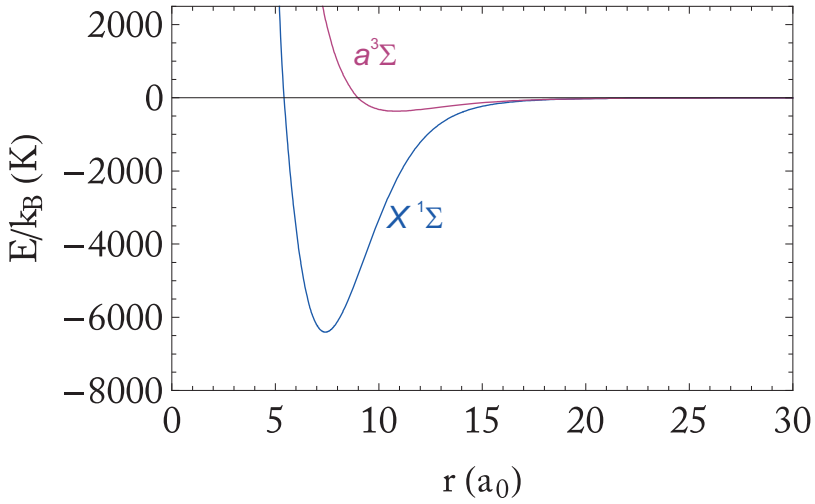

Figure A.5: Born-Oppenheimer potentials $V_S(r)$ for the singlet $S = 0$, $X^1\Sigma$ and the triplet $S = 1$, $a^3\Sigma$ states.

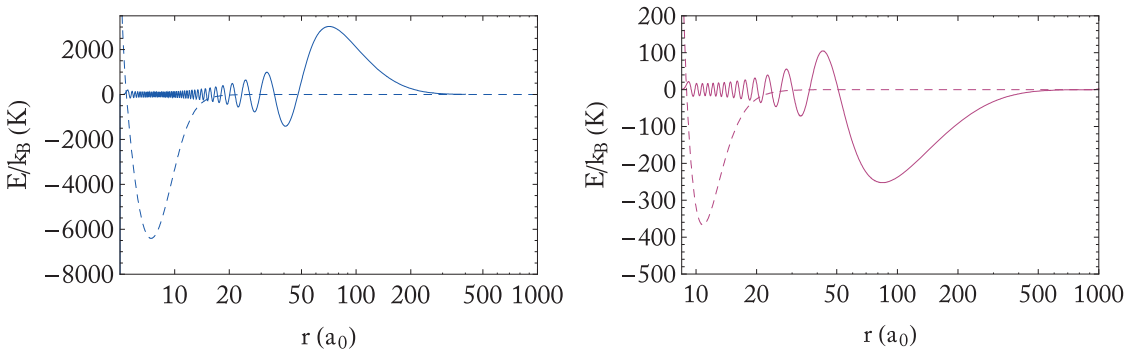

Figure A.6: Wavefunctions of the least bound states of ^{40}K for the singlet (left) and triplet (right) potentials. The dashed curve indicates the potential and the solid curve the radial wavefunction of the least-bound vibrational levels. Note the horizontal logarithmic scale and the asymptotic character of the wavefunctions.

$$r_0 = \frac{1}{2}\left(\frac{2\mu C_6}{\hbar^2}\right)^{1/4}$$

Using the van der Waals coefficient of $C_6 = 3925.9\ \mathrm{E}_h\mathrm{a}_0^6$ [137] for ^{40}K we obtain a van der Waals range of $r_0 \simeq 65\ \mathrm{a}_0$. The scattering lengths of both the singlet and triplet potentials are much larger than r_0 indicating resonant scattering due to the presence of a weakly bound state in both the singlet and triplet scattering potentials. Figure A.6 shows the wavefunctions of the least bound states in the singlet and triplet potentials for ^{40}K. Note the horizontal logarithmic scale. The wavefunctions extend far into the asymptotic van der Waals tail of the potentials.

As has been pointed out often throughout this thesis the use of Feshbach resonances are essential for the study of ultracold gases. Due to the resonant scattering in the open channels (i.e. a large background scattering length) the Feshbach resonances of ^{40}K are considered broad resonances. In ^{40}K two experimentally characterized s-wave Feshbach

resonances and one p-wave resonance have been published. The resonances are summarized in Table A.9.

Chapter B
Li-K properties

B.1 General properties

In this appendix some properties of the Li-K system are tabulated. Table B.1 lists general properties of the ^{6}Li-^{40}K system. Table B.2 lists the scattering lengths of the various combination of isotopes.
Accurate scattering potentials for the Li-K system are described in Ref. [136]. To use the accumulated phase method in its most simple form the complete potentials are not required, but only the van der Waals tail suffices. This is given by

$$V_{vdW}(r) = -\frac{C_6}{r^6} - \frac{C_8}{r^8} - \frac{C_{10}}{r^{10}}$$

where the C_8 and C_{10} terms can be omitted to obtain an even simpler form. Table B.3 lists the van der Waals coefficients for the ^{6}Li-^{40}K system. To obtain a more accurate potential the exchange interaction can be included in the potential, where the singlet and triplet potentials are given

$$V_S(r) = V_{vdW}(r) \mp \frac{1}{2}J(r)$$

where the minus sign corresponds to the singlet ($S = 0$) potential and the plus sign to the triplet ($S = 1$) potential. The exchange interaction is given by [79]

$$J(r) = J(\gamma_\alpha, \gamma_\beta, r) r^{\frac{2}{\gamma_\alpha} + \frac{2}{\gamma_\beta} - \frac{1}{\gamma_\alpha + \gamma_\beta} - 1} e^{-(\gamma_\alpha + \gamma_\beta)r}$$

where

$$J(\gamma_\alpha, \gamma_\beta, r) = J_0 + r(\beta - \alpha)J_1 + \frac{1}{2}r^2(\beta - \alpha)^2 J_2$$

where the parameters are given in Table B.3
In experiments with ^{40}K^{87}Rb the Ramsauer-Townsend minimum at $T \simeq 630$ μK plays a significant role during the sympathetic cooling process [219]. During evaporative cooling

isotope	a_s [17]	Ref.
m_{Li6}	6.015122795(16) u	[214]
m_{K40}	39.96399848(21) u	[214]
m_{Li6}/m_{K40}	6.64392	
μ	5.22821 u	
D	3.510(5) D	[45, 46]

Table B.1: General properties of the ^{6}Li-^{40}K system. The atomic masses and reduced mass μ are given, additionally, the dipole moment D of the vibrational ground state of the singlet potential is given.

isotope	a_s [17]	a_t [17]	a_s[136]	a_t[136]	r_0 (Eq.2.7)
6/39	64.4	67.7	64.93	68.59	40.75
6/40	52.1	63.5	52.61	64.41	40.78
6/41	42.3	59.9	42.75	60.77	40.81
7/39	29.1	81.2	29.83	81.99	42.11
7/40	13.9	74.5	14.88	75.27	42.15
7/41	−7.92	69.1	−6.375	69.76	42.19

Table B.2: s-wave scattering lengths and van der Waals ranges r_0 in units of a_0 for the various isotope-combinations of lithium-potassium mixtures. Values in the second and third column are calculated based on the model potentials used in Ref. [17], using mass scaling between the isotopes. The last two columns are taken from Ref. [136]

symbol	value
C_6	2322 $E_h a_0^6$
C_8	1.95×10^5 $E_h a_0^8$
C_{10}	2.646×10^7 $E_h a_0^{10}$

symbol	value
α	0.630
β	0.567
J_0	1.26×10^{-2}
J_1	5.4×10^{-4}
J_2	1.44×10^{-3}

Table B.3: Parameters for the van der Waals and exchange potential of Li-K. The C_6, C_8 and C_{10} values are taken from Ref. [136] and other values from Ref. [79]. Units are atomic units.

described in this thesis ^{6}Li-^{40}K collisions occur mostly in the triplet channel. For the triplet potential the first Ramsauer-Townsend minimum occurs at $T \simeq 57$ mK. Due to the comparable scattering lengths for the singlet and triplet potentials no different behavior is expected for hyperfine mixtures scattering through a superposition of the singlet and triplet channels. Therefore, the Ramsauer-Townsend minima plays no role during the evaporative cooling process.

B.2 Feshbach resonances

Table B.4 lists all s-wave Feshbach resonances in ^{6}Li-^{40}K below $B = 500$ G and their widths. The data is based on a binding energy of $E_0/h = 715.5$ MHz and $E_1/h = 422.0$ MHz for the singlet and triplet potentials respectively. These values are obtained from a least-squares fitting procedure to the experimental data of Ref. [17] and the resonance measured in Chapter 6.

The Feshbach resonance optimal for studies in the lab is chosen to the the resonance at $B_0 \sim 115$ G in the $|1/2, +1/2\rangle_{\mathrm{Li}} + |9/2, +9/2\rangle_{\mathrm{K}}$ mixture. This resonance is only 20% narrower than the broadest available in ^{6}Li-^{40}K mixtures stable against spin-exchange collisions. The potassium $m_F = +9/2$ hyperfine level has the advantage of having an optical cycling transition to the $|11/2, +11/2\rangle$ excited state which facilitates absorption imaging at intermediate magnetic fields where these resonances occur (see Appendix A). This optimal resonance is indicated with an arrow in Fig. B.1. Detailed ABM calculations for this resonance are shown in Fig. B.2. For $B - B_0 < 5$ mG and $E_F < 100$ nK the dressed bound state is well described by the universal quadratic behavior. Since the ABM underestimates the width of a resonance the real physical case will be slightly more

M_F	B_0 (G)	ΔB (G)	Ref.
-5	216.2	0.16	[17]
-4	157.4	0.08	[17]
-4	168.4	0.08	[17]
-3	148.8	0.12	[17]
-3	159.6	0.32	[17]
-3	165.9	4×10^{-5}	[17]
-2	141.0	0.12	[17]
-2	154.7	0.51	[17, 44]
-2	162.5	0.08	[17]
-1	133.6	0.11	
-1	149.3	0.57	
-1	158.5	0.27	
0	126.7	0.10	
0	143.5	0.56	
0	153.9	0.52	
1	120.2	0.08	
1	137.2	0.50	
1	148.6	0.77	
2	114.2	0.06	
2	130.5	0.41	
2	142.5	1.00	
2	476.1	3.6×10^{-5}	
3	108.9	0.04	
3	123.6	0.30	
3	135.3	1.13	
3	367.5	4.7×10^{-5}	
4	104.4	0.02	
4	116.6	0.18	
4	126.5	1.11	
5	101.3	0.01	
5	115.4	0.92	[18]

Table B.4: s-wave Feshbach resonances for $B < 500$ G in the ^{6}Li-^{40}K mixture for hyperfine states stable against spin-exchange. Values are calculated using the extended ABM as presented in Chapter 5. References are to the experimental observation of the specific resonance. The $M_F = -5$ resonance is for the mixture: $|9/2, -9/2\rangle_{\mathrm{K}} + |1/2, -1/2\rangle_{\mathrm{Li}}$, all other resonances are in systems with lithium in the absolute groundstate ($|1/2, +1/2\rangle_{\mathrm{Li}}$) and potassium in another hyperfine state in the $F = 9/2$ manifold.

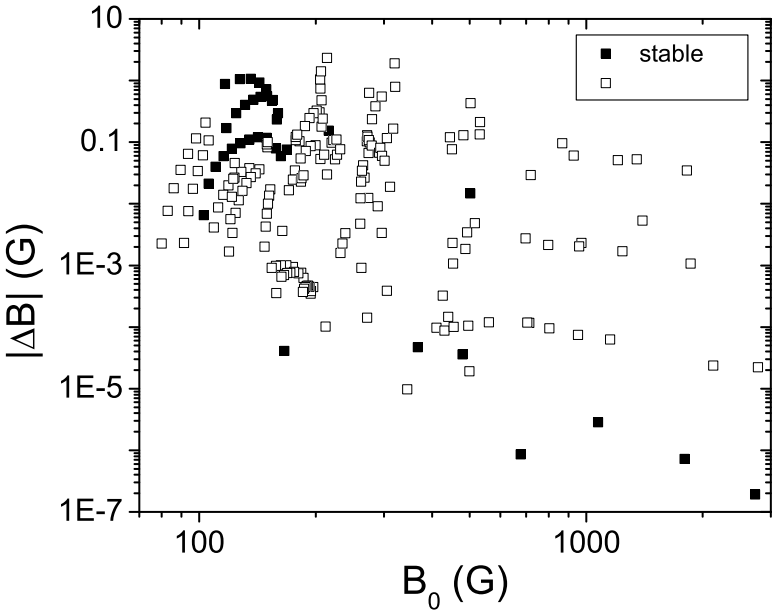

Figure B.1: All s-wave Feshbach resonances in the ^{6}Li-^{40}K system below $B_0 = 3$ kG. Plotted is the absolute value of the resonance width $|\Delta B|$ versus the resonance position B_0. The arrow indicates the optimal resonance discussed in the text.

favorable.

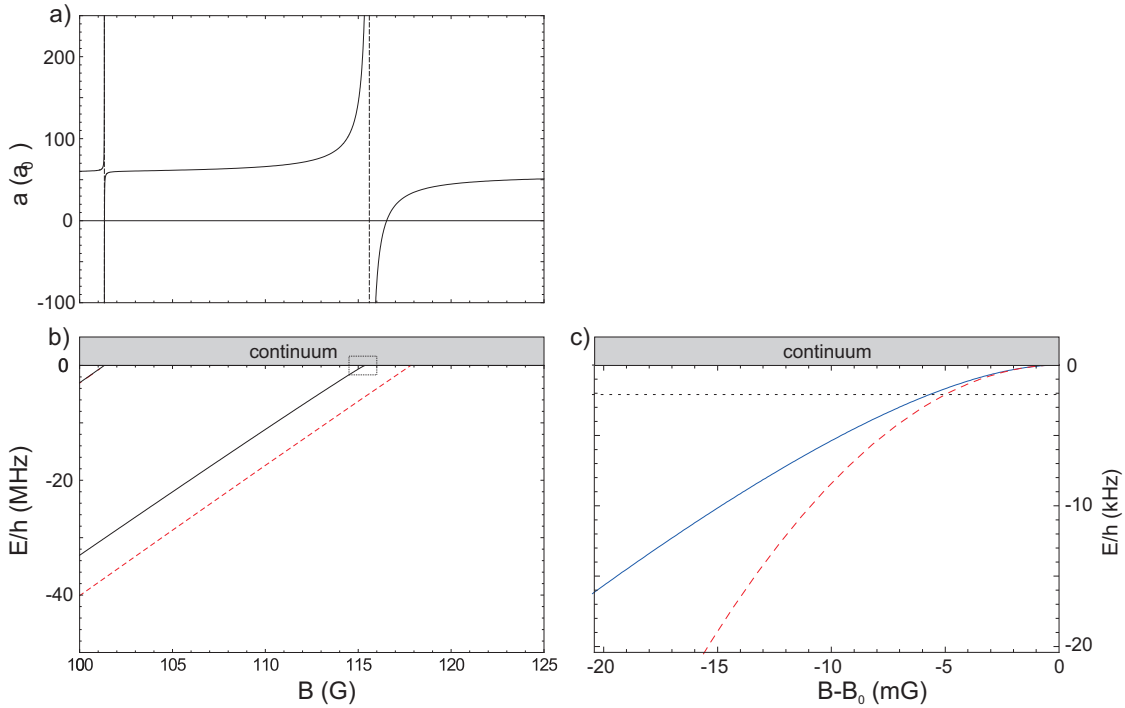

Figure B.2: ABM calculations for the resonance characterized in Chapter 6, occurring in the channel $|1/2, +1/2\rangle_{\mathrm{Li}} + |9/2, +9/2\rangle_{\mathrm{K}}$. a) The scattering length behavior of the two resonances in this channel b) the bound state behavior below threshold, the solid black line shows the dressed state and the dashed red line the uncoupled bound state in $\mathcal{Q}$-space. c) a zoom around the broadest resonance, the solid line is the dressed state calculation, the dashed red line is the quadratic universal behavior near threshold and the dotted line indicates a typical Fermi energy of $E_F = 100$ nK.

Bibliography

[1] Jr. J. V. Dugan and R. D. Etters. Ground state properties of spin-alined atomic hydrogen. *The Journal of Chemical Physics*, 59(11):6171–6172, 1973.

[2] Richard D. Etters, Jr. John V. Dugan, and Raymond W. Palmer. The ground state properties of spin-aligned atomic hydrogen, deuterium, and tritium. *The Journal of Chemical Physics*, 62(2):313–319, 1975.

[3] Isaac F. Silvera and J. T. M. Walraven. Stabilization of Atomic Hydrogen at Low Temperature. *Phys. Rev. Lett.*, 44(3):164–168, Jan 1980.

[4] M. H. Anderson, J. R. Ensher, M. R. Matthews, C. E. Wieman, and E. A. Cornell. Observation of Bose-Einstein Condensation in a Dilute Atomic Vapor. *Science*, 269(5221):198–201, 1995.

[5] K. B. Davis, M. O. Mewes, M. R. Andrews, N. J. van Druten, D. S. Durfee, D. M. Kurn, and W. Ketterle. Bose-Einstein Condensation in a Gas of Sodium Atoms. *Phys. Rev. Lett.*, 75(22):3969–3973, Nov 1995.

[6] Isaac F. Silvera and J. T. M. Walraven. Spin-Polarized Atomic Deuterium: Stabilization, Limitations on Density, and Adsorption Energy on Helium. *Phys. Rev. Lett.*, 45(15):1268–1271, Oct 1980.

[7] B. DeMarco and D. S. Jin. Onset of Fermi Degeneracy in a Trapped Atomic Gas. *Science*, 285(5434):1703–1706, 1999.

[8] J. Cubizolles, T. Bourdel, S. J. J. M. F. Kokkelmans, G. V. Shlyapnikov, and C. Salomon. Production of Long-Lived Ultracold Li_2 Molecules from a Fermi Gas. *Phys. Rev. Lett.*, 91(24):240401, Dec 2003.

[9] D. S. Petrov. Three-body problem in Fermi gases with short-range interparticle interaction. *Phys. Rev. A*, 67(1):010703, Jan 2003.

[10] William C. Stwalley. Stability of Spin-Aligned Hydrogen at Low Temperatures and High Magnetic Fields: New Field-Dependent Scattering Resonances and Predissociations. *Phys. Rev. Lett.*, 37(24):1628–1631, Dec 1976.

[11] M. W. Reynolds, I. Shinkoda, R. W. Cline, and W. N. Hardy. Observation of inverse predissociation of spin-polarized atomic hydrogen at low temperatures. *Phys. Rev. B*, 34(7):4912–4915, Oct 1986.

[12] E. Tiesinga, A. J. Moerdijk, B. J. Verhaar, and H. T. C. Stoof. Conditions for Bose-Einstein condensation in magnetically trapped atomic cesium. *Phys. Rev. A*, 46(3):R1167–R1170, Aug 1992.

[13] E. Tiesinga, B. J. Verhaar, and H. T. C. Stoof. Threshold and resonance phenomena in ultracold ground-state collisions. *Phys. Rev. A*, 47(5):4114–4122, May 1993.

[14] S. Jochim, M. Bartenstein, A. Altmeyer, G. Hendl, C. Chin, J. Hecker Denschlag, and R. Grimm. Pure Gas of Optically Trapped Molecules Created from Fermionic Atoms. *Phys. Rev. Lett.*, 91(24):240402, Dec 2003.

[15] D. S. Naik and C. Raman. Optically plugged quadrupole trap for Bose-Einstein condensates. *Phys. Rev. A*, 71(3):033617, Mar 2005.

[16] T. L. Gustavson, A. P. Chikkatur, A. E. Leanhardt, A. Görlitz, S. Gupta, D. E. Pritchard, and W. Ketterle. Transport of Bose-Einstein Condensates with Optical Tweezers. *Phys. Rev. Lett.*, 88(2):020401, Dec 2001.

[17] E. Wille, F. M. Spiegelhalder, G. Kerner, D. Naik, A. Trenkwalder, G. Hendl, F. Schreck, R. Grimm, T. G. Tiecke, J. T. M. Walraven, S. J. J. M. F. Kokkelmans, E. Tiesinga, and P. S. Julienne. Exploring an Ultracold Fermi-Fermi Mixture: Interspecies Feshbach Resonances and Scattering Properties of ^{6}Li and ^{40}K. *Physical Review Letters*, 100(5):053201, 2008.

[18] T.G. Tiecke, M. Goosen, A. Ludewig, S.D. Gensemer, S. Kraft, S. J. J. M. F. Kokkelmans, and J.T.M. Walraven. Search for broad Feshbach resonances in the 6Li-40K mixture. *arXiv:0908.2071*.

[19] Sadhan K. Adhikari. Superfluid Fermi-Fermi mixture: Phase diagram, stability, and soliton formation. *Physical Review A (Atomic, Molecular, and Optical Physics)*, 76(5):053609, 2007.

[20] M. A. Baranov, C. Lobo, and G. V. Shlyapnikov. Superfluid pairing between fermions with unequal masses. *Physical Review A (Atomic, Molecular, and Optical Physics)*, 78(3):033620, 2008.

[21] I. Bausmerth, A. Recati, and S. Stringari. Chandrasekhar-Clogston limit and phase separation in Fermi mixtures at unitarity. *Physical Review A (Atomic, Molecular, and Optical Physics)*, 79(4):043622, 2009.

[22] G. J. Conduit, P. H. Conlon, and B. D. Simons. Superfluidity at the BEC-BCS crossover in two-dimensional Fermi gases with population and mass imbalance. *Physical Review A (Atomic, Molecular, and Optical Physics)*, 77(5):053617, 2008.

[23] Roberto B. Diener and Mohit Randeria. BCS-BEC crossover with unequal mass fermions. *arXiv:0906.4300v1*.

[24] K. B. Gubbels, J. E. Baarsma, and H. T. C. Stoof. Lifshitz Point in the Phase Diagram of Resonantly Interacting 6Li-40K Mixtures. *arXiv:0907.1867v2*.

[25] Hao Guo, Chih-Chun Chien, Qijin Chen, Yan He, and K. Levin. Finite-temperature behavior of an interspecies fermionic superfluid with population imbalance. *Physical Review A (Atomic, Molecular, and Optical Physics)*, 80(1):011601, 2009.

[26] W. Vincent Liu and Frank Wilczek. Interior Gap Superfluidity. *Phys. Rev. Lett.*, 90(4):047002, Jan 2003.

[27] Yusuke Nishida and Shina Tan. Confinement-induced Efimov resonances in Fermi-Fermi mixtures. *Physical Review A (Atomic, Molecular, and Optical Physics)*, 79(6):060701, 2009.

[28] G. Orso, L. P. Pitaevskii, and S. Stringari. Equilibrium and dynamics of a trapped superfluid Fermi gas with unequal masses. *Physical Review A (Atomic, Molecular, and Optical Physics)*, 77(3):033611, 2008.

[29] D. S. Petrov, C. Salomon, and G. V. Shlyapnikov. Weakly Bound Dimers of Fermionic Atoms. *Phys. Rev. Lett.*, 93(9):090404, Aug 2004.

[30] J. Levinsen, T. G. Tiecke, J. T. M. Walraven, and D. S. Petrov. Atom-dimer scattering and long-lived trimers in fermionic mixtures. *arXiv:0907.5523*, 2009.

[31] J. G. Bednorz and K. A. Müller. Possible highTc superconductivity in the Ba-La-Cu-O system. *Zeitschrift für Physik B*, 64:189–193, 1986.

[32] Henning Heiselberg. Fermi systems with long scattering lengths. *Phys. Rev. A*, 63(4):043606, Mar 2001.

[33] K. M. O'Hara, S. L. Hemmer, M. E. Gehm, S. R. Granade, and J. E. Thomas. Observation of a Strongly Interacting Degenerate Fermi Gas of Atoms. *Science*, 298(5601):2179–2182, 2002.

[34] Herman Feshbach. Unified theory of nuclear reactions. *Annals of Physics*, 5(4):357 – 390, 1958.

[35] Herman Feshbach. A unified theory of nuclear reactions. II. *Annals of Physics*, 19(2):287 – 313, 1962.

[36] M. Girardeau. Relationship between Systems of Impenetrable Bosons and Fermions in One Dimension. *Journal of Mathematical Physics*, 1(6):516–523, 1960.

[37] Belen Paredes, Artur Widera, Valentin Murg, Olaf Mandel, Simon Folling, Ignacio Cirac, Gora V. Shlyapnikov, Theodor W. Hansch, and Immanuel Bloch. Tonks-Girardeau gas of ultracold atoms in an optical lattice. *Nature*, 429(6989):277–281, May 2004.

[38] Markus Greiner, Olaf Mandel, Tilman Esslinger, Theodor W. Hansch, and Immanuel Bloch. Quantum phase transition from a superfluid to a Mott insulator in a gas of ultracold atoms. *Nature*, 415(6867):39–44, Jan 2002.

[39] J. M. McNamara, T. Jeltes, A. S. Tychkov, W. Hogervorst, and W. Vassen. Degenerate Bose-Fermi Mixture of Metastable Atoms. *Physical Review Letters*, 97(8):080404, 2006.

[40] Andrew G. Truscott, Kevin E. Strecker, William I. McAlexander, Guthrie B. Partridge, and Randall G. Hulet. Observation of Fermi Pressure in a Gas of Trapped Atoms. *Science*, 291(5513):2570–2572, 2001.

[41] F. Schreck, L. Khaykovich, K. L. Corwin, G. Ferrari, T. Bourdel, J. Cubizolles, and C. Salomon. Quasipure Bose-Einstein Condensate Immersed in a Fermi Sea. *Phys. Rev. Lett.*, 87(8):080403, Aug 2001.

[42] Takeshi Fukuhara, Yosuke Takasu, Mitsutaka Kumakura, and Yoshiro Takahashi. Degenerate Fermi Gases of Ytterbium. *Physical Review Letters*, 98(3):030401, 2007.

[43] K.-K. Ni, S. Ospelkaus, M. H. G. de Miranda, A. Pe'er, B. Neyenhuis, J. J. Zirbel, S. Kotochigova, P. S. Julienne, D. S. Jin, and J. Ye. A High Phase-Space-Density Gas of Polar Molecules. *Science*, 322(5899):231–235, 2008.

[44] A.-C. Voigt, M. Taglieber, L. Costa, T. Aoki, W. Wieser, T. W. Hänsch, and K. Dieckmann. Ultracold Heteronuclear Fermi-Fermi Molecules. *Physical Review Letters*, 102(2):020405, 2009.

[45] F. Engelke, H. Hage, and U. Sprick. The B 1[Pi]-X 1[Sigma]+ system of 39K6Li and 39K7Li: High-resolution laser excitation and fluorescence spectroscopy using selectively detected laser-induced fluorescence (SDLIF) in molecular beam and injection heat pipe (IHP). *Chemical Physics*, 88(3):443 – 453, 1984.

[46] M. Aymar and O. Dulieu. Calculation of accurate permanent dipole moments of the lowest $^{1,3}\Sigma^+$ states of heteronuclear alkali dimers using extended basis sets. *The Journal of Chemical Physics*, 122(20):204302, 2005.

[47] M. Houbiers, H. T. C. Stoof, W. I. McAlexander, and R. G. Hulet. Elastic and inelastic collisions of $6Li$ atoms in magnetic and optical traps. *Phys. Rev. A*, 57(3):R1497–R1500, Mar 1998.

[48] M. Bartenstein, A. Altmeyer, S. Riedl, R. Geursen, S. Jochim, C. Chin, J. Hecker Denschlag, R. Grimm, A. Simoni, E. Tiesinga, C. J. Williams, and P. S. Julienne. Precise Determination of ^{6}Li Cold Collision Parameters by Radio-Frequency Spectroscopy on Weakly Bound Molecules. *Physical Review Letters*, 94(10):103201, 2005.

[49] John L. Bohn, James P. Burke, Chris H. Greene, H. Wang, P. L. Gould, and W. C. Stwalley. Collisional properties of ultracold potassium: Consequences for degenerate Bose and Fermi gases. *Phys. Rev. A*, 59(5):3660–3664, May 1999.

[50] C. A. Regal, C. Ticknor, J. L. Bohn, and D. S. Jin. Tuning p-Wave Interactions in an Ultracold Fermi Gas of Atoms. *Phys. Rev. Lett.*, 90(5):053201, Feb 2003.

[51] Rudolf Grimm, Matthias Weidemüller, and Yurii B. Ovchinnikov. Optical dipole traps for neutral atoms. *Advances in Atomic, Molecular and Optical Physics*, 42:95–170, 2000.

[52] David E. Pritchard. Cooling Neutral Atoms in a Magnetic Trap for Precision Spectroscopy. *Phys. Rev. Lett.*, 51(15):1336–1339, Oct 1983.

[53] T. Bergeman, Gidon Erez, and Harold J. Metcalf. Magnetostatic trapping fields for neutral atoms. *Phys. Rev. A*, 35(4):1535–1546, Feb 1987.

[54] E. L. Surkov, J. T. M. Walraven, and G. V. Shlyapnikov. Collisionless motion of neutral particles in magnetostatic traps. *Phys. Rev. A*, 49(6):4778–4786, Jun 1994.

[55] H. Metcalf and P. van der Straten. *Laser Cooling and Trapping*. Springer, 1999.

[56] Wolfgang Ketterle and N.J. Van Druten. Evaporative Cooling of Trapped Atoms. 37:181 – 236, 1996.

[57] O. J. Luiten, M. W. Reynolds, and J. T. M. Walraven. Kinetic theory of the evaporative cooling of a trapped gas. *Phys. Rev. A*, 53(1):381–389, Jan 1996.

[58] W. Ketterle M. Inguscio and C. Salomon, editors. *Making, probing and understanding ultracold Fermi gases*. IOS Press, Amsterdam, 2008.

[59] Stefano Giorgini, Lev P. Pitaevskii, and Sandro Stringari. Theory of ultracold atomic Fermi gases. *Reviews of Modern Physics*, 80(4):1215, 2008.

[60] C. J. Pethick and H. Smith. *Bose-Einstein Condensation in Dilute Gases*. Cambridge University Press, Cambridge, 2002.

[61] Alex Martin Michael A. Joffe, Wolfgang Ketterle and JOSA B Vol. **10** Iss. 12 pp. 2257-2262 David E. Pritchard, *Transverse cooling and deflection of an atomic beam inside a Zeeman slower*. Making Probing and Understanding Bose. 1993.

[62] C. Chin, R. Grimm, Julienne, and E. P. S., Tiesinga. Feshbach Resonances in Ultracold Gases. *arxiv*, 2008.

[63] Cheng Chin. A simple model of Feshbach molecules. *http://arxiv.org/abs/cond-mat/0506313*, 2005.

[64] Jook Walraven. Elements of Quantum Gases: Thermodynamic and Collisional Properties of Trapped Atomic Gases.

[65] Cindy Regal. *Experimental realization of BCS-BEC crossover physics with a Fermi gas of atoms*. PhD thesis, University of Colorado, 2005.

[66] Florian Schreck. *Mixtures of ultracold gases: Fermi sea and Bose-Einstein condensate of Lithium isotopes*. PhD thesis, Universite Paris VI, 2002.

[67] K. Dieckmann. *Bose-Einstein Condensation with High Atom Number in a Deep Magnetic Trap*. PhD thesis, University of Amsterdam, 2001.

[68] Dale G. Fried, Thomas C. Killian, Lorenz Willmann, David Landhuis, Stephen C. Moss, Daniel Kleppner, and Thomas J. Greytak. Bose-Einstein Condensation of Atomic Hydrogen. *Phys. Rev. Lett.*, 81(18):3811–3814, Nov 1998.

[69] S. C. Doret, C. B. Connolly, W. Ketterle, and J. M. Doyle. A buffer-gas cooled Bose-Einstein condensate. *Physical Review Letters*, #, 2009.

[70] Z. Hadzibabic, C. A. Stan, K. Dieckmann, S. Gupta, M. W. Zwierlein, A. Görlitz, and W. Ketterle. Two-Species Mixture of Quantum Degenerate Bose and Fermi Gases. *Phys. Rev. Lett.*, 88(16):160401, Apr 2002.

[71] C. Silber, S. Günther, C. Marzok, B. Deh, Ph. W. Courteille, and C. Zimmermann. Quantum-Degenerate Mixture of Fermionic Lithium and Bosonic Rubidium Gases. *Phys. Rev. Lett.*, 95(17):170408, Oct 2005.

[72] G. Roati, F. Riboli, G. Modugno, and M. Inguscio. Fermi-Bose Quantum Degenerate $K40 - R87b$ Mixture with Attractive Interaction. *Phys. Rev. Lett.*, 89(15):150403, Sep 2002.

[73] Takeshi Fukuhara, Seiji Sugawa, Yosuke Takasu, and Yoshiro Takahashi. All-optical formation of quantum degenerate mixtures. *Physical Review A (Atomic, Molecular, and Optical Physics)*, 79(2):021601, 2009.

[74] S. R. Granade, M. E. Gehm, K. M. O'Hara, and J. E. Thomas. All-Optical Production of a Degenerate Fermi Gas. *Phys. Rev. Lett.*, 88(12):120405, Mar 2002.

[75] F. M. Spiegelhalder, A. Trenkwalder, D. Naik, G. Hendl, F. Schreck, and R. Grimm. Collisional Stability of 40K Immersed in a Strongly Interacting Fermi Gas of 6Li. *arXiv:0908.1101v1.*

[76] N. F. Mott and H. S. W. Massey. *Theory of Atomic Collisions.* Oxford; 3rd edition, 1965.

[77] E. Arimondo, M. Inguscio, and P. Violino. Experimental determinations of the hyperfine structure in the alkali atoms. *Rev. Mod. Phys.*, 49(1):31–75, Jan 1977.

[78] Mitchel Weissbluth. *Atoms and Molecules.* Academic Press, 1980.

[79] B. M. Smirnov and M. I. Chibisov. Electron exchange and changes in the hyperfine state of colliding alkaline metal atoms. *JETP*, 21(3):624–628, Sep 1965.

[80] David J. Griffiths. *Introduction to Quantum Mechanics.* Prentice-Hall, Inc., 1995.

[81] U. Fano. Effects of Configuration Interaction on Intensities and Phase Shifts. *Phys. Rev.*, 124(6):1866–1878, Dec 1961.

[82] A. J. Moerdijk, B. J. Verhaar, and A. Axelsson. Resonances in ultracold collisions of ^{6}Li, ^{7}Li, and ^{23}Na. *Phys. Rev. A*, 51(6):4852–4861, Jun 1995.

[83] D. S. Petrov. Three-Boson Problem near a Narrow Feshbach Resonance. *Phys. Rev. Lett.*, 93(14):143201, Sep 2004.

[84] G. Breit and E. Wigner. Capture of Slow Neutrons. *Phys. Rev.*, 49(7):519–531, Apr 1936.

[85] A. J. Moerdijk and B. J. Verhaar. Prospects for Bose-Einstein Condensation in Atomic ^{7}Li and ^{23}Na. *Phys. Rev. Lett.*, 73(4):518–521, Jul 1994.

[86] B. J. Verhaar, E. G. M. van Kempen, and S. J. J. M. F. Kokkelmans. Predicting scattering properties of ultracold atoms: Adiabatic accumulated phase method and mass scaling. *Physical Review A (Atomic, Molecular, and Optical Physics)*, 79(3):032711, 2009.

[87] J. Dalibard and C. Cohen-Tannoudji. Dressed-atom approach to atomic motion in laser light: the dipole force revisited. *J. Opt. Soc. Am. B*, 2(11):1707–1720, 1985.

[88] Anthony E. Siegman. *Lasers*. University Science Books, 1986.

[89] NIST Atomic Spectra Database http://physics.nist.gov/PhysRefData/ASD/index.html.

[90] József Fortágh and Claus Zimmermann. Magnetic microtraps for ultracold atoms. *Reviews of Modern Physics*, 79(1):235, 2007.

[91] G. Breit and I. I. Rabi. Measurement of Nuclear Spin. *Phys. Rev.*, 38(11):2082–2083, Dec 1931.

[92] Wolfgang Petrich, Michael H. Anderson, Jason R. Ensher, and Eric A. Cornell. Stable, Tightly Confining Magnetic Trap for Evaporative Cooling of Neutral Atoms. *Phys. Rev. Lett.*, 74(17):3352–3355, Apr 1995.

[93] Georg M. Bruun and Charles W. Clark. Ideal gases in time-dependent traps. *Phys. Rev. A*, 61(6):061601, May 2000.

[94] Eric Wille. *Preparation of an Optically Trapped Fermi-Fermi Mixture of ^6Li and ^{40}K Atoms and Characterization of the Interspecies Interactions by Feshbach Spectroscopy*. PhD thesis, University of Innsbruck, 2009.

[95] For reviews see *Proceedings of the International School of Physics "Enrico Fermi," Course CLXIV*, Varenna, 20–30 June 2006, M. Inguscio, W. Ketterle, and C. Salomon (Eds.), IOS Press, Amsterdam, 2008.

[96] G. Ferrari, M. Inguscio, W. Jastrzebski, G. Modugno, G. Roati, and A. Simoni. Collisional Properties of Ultracold K-Rb Mixtures. *Phys. Rev. Lett.*, 89(5):053202, Jul 2002.

[97] S. Inouye, J. Goldwin, M. L. Olsen, C. Ticknor, J. L. Bohn, and D. S. Jin. Observation of Heteronuclear Feshbach Resonances in a Mixture of Bosons and Fermions. *Phys. Rev. Lett.*, 93(18):183201, Oct 2004.

[98] Erik W. Streed, Ananth P. Chikkatur, Todd L. Gustavson, Micah Boyd, Yoshio Torii, Dominik Schneble, Gretchen K. Campbell, David E. Pritchard, and Wolfgang Ketterle. Large atom number Bose-Einstein condensate machines. *Review of Scientific Instruments*, 77(2):023106, 2006.

[99] K. M.R. van der Stam, E. D. van Ooijen, R. Meppelink, J. M. Vogels, and P. van der Straten. Large atom number Bose-Einstein condensate of sodium. *Review of Scientific Instruments*, 78:013102, 2007.

[100] Markus Greiner, Immanuel Bloch, Theodor W. Hänsch, and Tilman Esslinger. Magnetic transport of trapped cold atoms over a large distance. *Phys. Rev. A*, 63(3):031401, Feb 2001.

[101] B. DeMarco, H. Rohner, and D. S. Jin. An enriched ^{40}K source for fermionic atom studies. *Review of Scientific Instruments*, 70(4):1967–1969, 1999.

[102] Stephan Falke, Eberhard Tiemann, Christian Lisdat, Harald Schnatz, and Gesine Grosche. Transition frequencies of the D lines of ^{39}K, ^{40}K, and ^{41}K measured with a femtosecond laser frequency comb. *Physical Review A (Atomic, Molecular, and Optical Physics)*, 74(3):032503, 2006.

[103] Maarten Koot. Het maken van een diodelasersysteem voor het maken van een magneto-optische val van rubidium-atomen. Master's thesis, University of Amsterdam, 2007.

[104] Dipankar Das and Vasant Natarajan. Absolute frequency measurement of the lithium D lines: Precise determination of isotope shifts and fine-structure intervals. *Physical Review A (Atomic, Molecular, and Optical Physics)*, 75(5):052508, 2007.

[105] L. Ricci, M. Weidemüller, T. Esslinger, A. Hemmerich, C. Zimmermann, V. Vuletic, W. König, and T. W. Hänsch. A compact grating-stabilized diode laser system for atomic physics. *Optics Communications*, 117:541–549, 1995.

[106] K. G. Libbrecht and J. L. Hall. A low-noise high-speed diode laser current controller. *Review of Scientific Instruments*, 64(8):2133–2135, 1993.

[107] C. R. Vidal and J. Cooper. Heat-Pipe Oven: A New, Well-Defined Metal Vapor Device for Spectroscopic Measurements. *Journal of Applied Physics*, 40(8):3370–3374, 1969.

[108] Erling Riis, David S. Weiss, Kathryn A. Moler, and Steven Chu. Atom funnel for the production of a slow, high-density atomic beam. *Phys. Rev. Lett.*, 64(14):1658–1661, Apr 1990.

[109] K. Dieckmann, R. J. C. Spreeuw, M. Weidemüller, and J. T. M. Walraven. Two-dimensional magneto-optical trap as a source of slow atoms. *Phys. Rev. A*, 58(5):3891–3895, Nov 1998.

[110] J. Schoser, A. Batär, R. Löw, V. Schweikhard, A. Grabowski, Yu. B. Ovchinnikov, and T. Pfau. Intense source of cold Rb atoms from a pure two-dimensional magneto-optical trap. *Phys. Rev. A*, 66(2):023410, Aug 2002.

[111] Saptarishi Chaudhuri, Sanjukta Roy, and C. S. Unnikrishnan. Realization of an intense cold Rb atomic beam based on a two-dimensional magneto-optical trap: Experiments and comparison with simulations. *Physical Review A (Atomic, Molecular, and Optical Physics)*, 74(2):023406, 2006.

[112] S. Weyers, E. Aucouturier, C. Valentin, and N. Dimarcq. A continuous beam of cold cesium atoms extracted from a two-dimensional magneto-optical trap. *Optics Communications*, 143(1-3):30 – 34, 1997.

[113] P. Berthoud, A. Joyet, G. Dudle, N. Sagna, and P. Thomann. A continuous beam of slow, cold cesium atoms magnetically extracted from a 2D magneto-optical trap. *Europhys. Lett.*, 41(2):141–146, jan 1998.

[114] J. Catani, P. Maioli, L. De Sarlo, F. Minardi, and M. Inguscio. Intense slow beams of bosonic potassium isotopes. *Physical Review A (Atomic, Molecular, and Optical Physics)*, 73(3):033415, 2006.

[115] S. Ospelkaus, C. Ospelkaus, R. Dinter, J. Fuchs, M. Nakat, K. Sengstock, and K. Bongs. Degenerate K-Rb Fermi-Bose gas mixtures with large particle numbers. *Journal of Modern Optics*, 54(5):661 – 673, 2007.

[116] Silke Ospelkaus-Schwarzer. *Quantum Degenerate Fermi-Bose Mixtures of 40K and 87Rb in 3D Optical Lattices*. PhD thesis, Universitaet Hamburg, 2006.

[117] Saptarishi Chaudhuri. Presented at FerMix 2009, Trento. 2009.

[118] U. Schunemann, H. Engler, M. Zielonkowski, M. Weidemuller, and R. Grimm. Magneto-optic trapping of lithium using semiconductor lasers. *Optics Communications*, 158:263–272, 1998.

[119] J. Kawanaka, K. Shimizu, and H. Takuma. Decay rate measurement of lithium in a magneto-optical trap. *Applied Physics B: Lasers and Optics*, 57(2):113–118, 1993.

[120] Robert Sylvester Williamson. Magneto-optical trapping of potassium isotopes. 1997.

[121] F. S. Cataliotti, E. A. Cornell, C. Fort, M. Inguscio, F. Marin, M. Prevedelli, L. Ricci, and G. M. Tino. Magneto-optical trapping of Fermionic potassium atoms. *Phys. Rev. A*, 57(2):1136–1138, Feb 1998.

[122] G. Modugno, C. Benkő, P. Hannaford, G. Roati, and M. Inguscio. Sub-Doppler laser cooling of fermionic $40K$ atoms. *Phys. Rev. A*, 60(5):R3373–R3376, Nov 1999.

[123] Brian DeMarco. *Quantum Behavior of an Atomic Fermi Gas*. PhD thesis, University of Colorado, 2001.

[124] N. W. M. Ritchie, E. R. I. Abraham, Y. Y. Xiao, C. C. Bradley, R. G. Hulet, and P. S. Julienne. Trap-loss collisions of ultracold lithium atoms. *Phys. Rev. A*, 51(2):R890–R893, Feb 1995.

[125] W. Jastrzebski, P. Kowalczyk, A. Pashov, and J. Szczepkowski. The potential energy barrier of the $^1\Pi$ state in KLi. *Spectrochimica Acta Part A: Molecular and Biomolecular Spectroscopy*, 73(1):117 – 120, 2009.

[126] S. Aubin, M. H. T. Extavour, S. Myrskog, L. J. LeBlanc, J. Estève, S. Singh, P. Scrutton, D. McKay, R. McKenzie, I. D. Leroux, A. Stummer, and J. H. Thywissen. Trapping Fermionic 40K and Bosonic 87Rb on a Chip. *Journal of Low Temperature Physics*, 140(5):377–396, 2005.

[127] Florian Schreck and Todd Meyrath. http://www.nintaka.com/Control.

[128] The Robotics Insitute CMU 1394 Digital Camera Driver. http://www.cs.cmu.edu/ iwan/1394/index.html.

[129] Michael A. Joffe, Wolfgang Ketterle, Alex Martin, and David E. Pritchard. Transverse cooling and deflection of an atomic beam inside a Zeeman slower. *J. Opt. Soc. Am. B*, 10(12):2257–2262, 1993.

[130] Eugene Hecht. *Optics (4th Edition)*. Addison Wesley, August 2001.

[131] Mechanical Design Workshop. Internal Report. Technical report, University of Amsterdam, 2008.

[132] G. Thalhammer, K. Winkler, F. Lang, S. Schmid, R. Grimm, and J. Hecker Denschlag. Long-Lived Feshbach Molecules in a Three-Dimensional Optical Lattice. *Physical Review Letters*, 96(5):050402, 2006.

[133] P. W. H. Pinkse, A. Mosk, M. Weidemüller, M. W. Reynolds, T. W. Hijmans, and J. T. M. Walraven. Adiabatically Changing the Phase-Space Density of a Trapped Bose Gas. *Phys. Rev. Lett.*, 78(6):990–993, Feb 1997.

[134] D. M. Stamper-Kurn, H.-J. Miesner, A. P. Chikkatur, S. Inouye, J. Stenger, and W. Ketterle. Reversible Formation of a Bose-Einstein Condensate. *Phys. Rev. Lett.*, 81(11):2194–2197, Sep 1998.

[135] T. B. Ottenstein, T. Lompe, M. Kohnen, A. N. Wenz, and S. Jochim. Collisional Stability of a Three-Component Degenerate Fermi Gas. *Physical Review Letters*, 101(20):203202, 2008.

[136] E. Tiemann, H. Knöckel, P. Kowalczyk, W. Jastrzebski, A. Pashov, H. Salami, and A. J. Ross. Coupled system a $^3\Sigma^+$ and $X^1\Sigma^+$ of KLi: Feshbach resonances and corrections to the Born-Oppenheimer approximation. *Physical Review A (Atomic, Molecular, and Optical Physics)*, 79(4):042716, 2009.

[137] Stephan Falke, Horst Knöckel, Jan Friebe, Matthias Riedmann, Eberhard Tiemann, and Christian Lisdat. Potassium ground-state scattering parameters and Born-Oppenheimer potentials from molecular spectroscopy. *Physical Review A (Atomic, Molecular, and Optical Physics)*, 78(1):012503, 2008.

[138] T. G. Tiecke, S. D. Gensemer, A. Ludewig, and J. T. M. Walraven. High-flux two-dimensional magneto-optical-trap source for cold lithium atoms. *Physical Review A (Atomic, Molecular, and Optical Physics)*, 80(1):013409, 2009.

[139] W.D. Phillips and H.J. Metcalf , Phys. Rev. Lett. **48**, 596 (1982).

[140] H.J. Metcalf and P. van der Straten, *Laser Cooling and Trapping*, Springer 1999.

[141] J.D. Weinstein, R. deCarvalho, T. Guillet, B. Friedrich, and J.M. Doyle, Nature **395**, 148 (1998).

[142] B. Ghaffari, J. M. Gerton, W.I. McAlexander, K.E. Strecker, D.M. Homan, and R.G. Hulet, Phys. Rev A **60**, 3878 (1999).

[143] E. Nikitin, E. Dashevskaya, J. Alnis, M. Auzinsh, E. R. I. Abraham, B. R. Furneaux, M. Keil, C. McRaven, N. Shafer-Ray and R. Waskowsky, Phys. Rev. A **68**, 023403 (2003).

[144] S.A. Rangwala, T. Junglen, T. Rieger, P.W.H. Pinkse and G. Rempe, Phys. Rev. A **67**, 043406 (2003).

[145] H.L. Bethlem, G. Berden and G. Meijer, Phys. Rev. Lett. **83**, 1558 (1999).

[146] E. Vliegen and F. Merkt, J. Phys. B: At. Mol. Opt. Phys. **39**, L241 (2006).

[147] F. Lison, P. Schuh, D. Haubrich, and D. Meschede, Phys. Rev. A **61**, 013405 (1999).

[148] C. Slow, L. Vernac, L.V. Hau, Rev. Sci. Instrum. **76**, 103101 (2005).

[149] C.A. Stan and W. Ketterle, Rev. Sci. Instr., **76**, 63113 (2005).

[150] See e.g. L. Vestergaard Hau, J.A. Golovchenko, and M.M. Burns, Rev. Sci. Instrum. **65**, 3746 (1994).

[151] C. Monroe, W. Swann, H. Robinson, and C. Wieman, Phys. Rev. Lett. **65**, 1571 (1990).

[152] K.L. Moore, T.P. Purdy, K.W. Murch, S. Leslie, S. Gupta, and D.M. Stamper-Kurn, Rev. Sci. Instr. **76**, 023106 (2005).

[153] A. Gozzini, F. Mango, J. H. Xu, G. Alzetta, F. Maccarone, and R. A. Bernheim, Nuovo Cimento D **15**, 709 (1993).

[154] C. Klempt, T. van Zoest, T. Henninger, O. Topic, E. Rasel, W. Ertmer, and J. Arlt, Phys. Rev. A **73**, 13410 (2006).

[155] C. J. Myatt, N. R. Newbury, R. W. Ghrist, S. Loutzenhiser, and C. E. Wieman, Optics Letters, **21**, 290 (1996).

[156] Z.T. Lu, K.L. Corwin, M.J. Renn, M.H. Anderson, E.A. Cornell, and C.E. Wieman, Phys. Rev. Lett. **77**, 3331 (1996).

[157] J. Schoser, A. Batär, R. Löw, V. Schweikhard, A. Grabowski, Yu. B. Ovchinnikov, and T. Pfau, Phys. Rev. A **66**, 023410 (2002).

[158] J. Catani, P. Maioli, L. De Sarlo, F. Minardi, and M. Inguscio, Phys. Rev. A **72**, 033415 (2006).

[159] C. B. Alcock, V. P. Itkin, and M. K. Horrigan. Vapor pressure equations for the metallic elements: 298-2500K. *Canadian Metallurgical Quarterly*, 23:309, 1984.

[160] K. Honda, Y. Takahashi, T. Kuwamoto, M. Fujimoto, K. Toyoda, K. Ishikawa, and T. Yabuzaki, Phys. Rev. A, **59**, R934 (1999).

[161] A. Griesmaier, J. Werner, S. Hensler, J. Stuhler, and T. Pfau, Phys. Rev. Lett. **94**, 160401 (2005).

[162] W. Ketterle, private communication.

[163] I. Estermann, O.C. Simpson, and O. Stern, Phys. Rev. **71**, 238 (1947).

[164] J. Vanier and C. Audoin. *The Quantum Physics of Atomic Frequency Standards.* Bristol, 1989.

[165] K. Ladouceur, B.G. Klappauf, J. van Dongen, N. Rauhut, B. Schuster, A.K. Mills, D.J. Jones, and K.W. Madison, J. Opt. Soc. Am. B **26**, 210 (2009).

[166] U. Schünemann, H. Engler, M. Zielonkowski, M. Weidemüller, and R. Grimm, Optics Commun. **158**, 263 (1998).

[167] L. Ricci, M. Weidemüller, T. Esslinger, A. Hemmerich, C. Zimmermann, V. Vuletic, W. König and T.W. Hänsch, Opt. Commun. **117**, 541 (1995).

[168] J. Kawanaka, K. Shimizu, H. Takuma, Appl. Phys. B **57**, 113 (1993).

[169] H. Margenau and N.R. Kestner, *Theory of intermolecular forces*, Pergamon Press, Oxford 1971.

[170] A.M. Steane, M. Chowdhury, and C. J. Foot, J. Opt. Soc. Am. B. **9**, 2142 (1992).

[171] A. Derevianko, J.F. Babb, and A. Dalgarno, Phys. Rev. A **63**, 052704 (2001).

[172] P.R. Fontana, Phys.Rev. 123, 1871 (1961).

[173] M.A. Joffe, W. Ketterle, A. Martin, and D.E. Pritchard, J. Opt. Soc. Am. B **10**, 2257 (1993).

[174] Immanuel Bloch, Jean Dalibard, and Wilhelm Zwerger. Many-body physics with ultracold gases. *Reviews of Modern Physics*, 80(3):885, 2008.

[175] H. T. C. Stoof, J. M. V. A. Koelman, and B. J. Verhaar. Spin-exchange and dipole relaxation rates in atomic hydrogen: Rigorous and simplified calculations. *Phys. Rev. B*, 38(7):4688–4697, Sep 1988.

[176] J. M. Vogels, B. J. Verhaar, and R. H. Blok. Diabatic models for weakly bound states and cold collisions of ground-state alkali-metal atoms. *Phys. Rev. A*, 57(5):4049–4052, May 1998.

[177] Thomas M. Hanna, Eite Tiesinga, and Paul S. Julienne. Prediction of Feshbach resonances from three input parameters. *Physical Review A (Atomic, Molecular, and Optical Physics)*, 79(4):040701, 2009.

[178] C A Stan, M W Zwierlein, C H Schunck, S M F Raupach, and W Ketterle. *Phys. Rev. Lett.*, 93:143001, 2004.

[179] P. Julienne. Private communication. 2009.

[180] Robert J. LeRoy and Richard B. Bernstein. Dissociation Energy and Long-Range Potential of Diatomic Molecules from Vibrational Spacings of Higher Levels. *The Journal of Chemical Physics*, 52(8):3869–3879, 1970.

[181] A. S. Jensen, K. Riisager, D. V. Fedorov, and E. Garrido. Structure and reactions of quantum halos. *Rev. Mod. Phys.*, 76(1):215–261, Feb 2004.

[182] Bo Gao. Solutions of the Schrödinger equation for an attractive $1/r6$ potential. *Phys. Rev. A*, 58(3):1728–1734, Sep 1998. Analytical solutions are provided by ...

[183] A Dervianko, J F Babb, and A Dalgarno. *Phys. Rev. A*, 63:052704, 2001.

[184] H. Salami, A. J. Ross, P. Crozet, W. Jastrzebski, P. Kowalczyk, and R. J. Le Roy. A full analytic potential energy curve for the a $^3\Sigma^+$ state of KLi from a limited vibrational data set. *The Journal of Chemical Physics*, 126(19):194313, 2007.

[185] A. Pashov, O. Docenko, M. Tamanis, R. Ferber, H. Knöckel, and E. Tiemann. Coupling of the $X^1\Sigma^+$ and a $^3\Sigma^+$ states of KRb. *Physical Review A (Atomic, Molecular, and Optical Physics)*, 76(2):022511, 2007.

[186] Julienne Paul S. Ultracold molecules from ultracold atoms: a case study with the KRb molecule. *arXiv:0812.1233v2*, 2009.

[187] M. W. Müller, A. Merz, M. W. Ruf, H. Hotop, W. Meyer, and M. Movre. Experimental and theoretical studies of the Bi-excited collision systems He*(23S) + He*(23S, 21S) at thermal and subthermal kinetic energies. *Zeitschrift für Physik D*, 21:89–112, 1991.

[188] Michael Przybytek and Bogumil Jeziorski. Bounds for the scattering length of spin-polarized helium from high-accuracy electronic structure calculations. *The Journal of Chemical Physics*, 123(13):134315, 2005.

[189] V. Venturi and I. B. Whittingham. Close-coupled calculation of field-free collisions of cold metastable helium atoms. *Phys. Rev. A*, 61(6):060703, May 2000.

[190] B Marcelis, E G M van Kempen, B J Verhaar, and S J J M F Kokkelmans. *Phys. Rev. A*, 70:012701, 2004.

[191] Bout Marcelis and Servaas Kokkelmans. Fermionic superfluidity with positive scattering length. *Physical Review A (Atomic, Molecular, and Optical Physics)*, 74(2):023606, 2006.

[192] E. Tiesinga, *et al.*, Phys. Rev. A **47**, 4114 (1993).

[193] J. Cubizolles, *et al.*, Phys. Rev. Lett. **91**, 240401 (2003); S. Jochim, *et al.*, Phys. Rev. Lett. **91**, 240402 (2003); C.A. Regal, *et al.*, Phys. Rev. Lett. **92**, 083201 (2004).

[194] C.A. Regal, *et al.*, Phys. Rev. Lett. **92**, 40403 (2004); M.W. Zwierlein, *et al.*, Phys. Rev. Lett. **92**, 120403 (2004).

[195] M. Greiner, *et al.*, **426**, 537 (2003); S. Jochim, *et al.*, Science **302**, 2101 (2003); M. W. Zwierlein, *et al.*, Phys. Rev. Lett. **91**, 250401 (2003).

[196] K.M. O'Hara, *et al.*, Science **298**, 2179 (2002); G.B. Partridge, *et al.*, Phys. Rev. Lett. **95**, 020404 (2005); M. Greiner, *et al.*, Phys. Rev. Lett. **94**, 070403 (2005); M.W. Zwierlein, *et al.*, Nature **435**, 1047 (2005); cf. C.A. Regal and D.S. Jin, Adv. At. Mol. Phys. **54**, 1 (2006); Ref. [95].

[197] D. S. Petrov, G. E. Astrakharchik, D. J. Papoular, C. Salomon, and G. V. Shlyapnikov. Crystalline Phase of Strongly Interacting Fermi Mixtures. *Phys. Rev. Lett.*, 99:130407, 2007.

[198] M.M. Forbes, *et al.*, Phys. Rev. Lett. **94**, 017001 (2005).

[199] M. Taglieber, *et al.*, Phys. Rev. Lett. **100**, 010401 (2008).

[200] C. Chin, *et al.*, Phys. Rev. Lett. **85**, 2717 (2000).

[201] T.G. Tiecke, *et al.*, Phys. Rev. A 80 013409 (2009).

[202] For details see T.G. Tiecke, *et al.*, to be published.

[203] H. Feshbach, Ann. of Phys. (N.Y.) **5**, 357 (1958); *ibid.* **19**, 287 (1962).

[204] B. Marcelis, *et al.*, Phys. Rev. A **70**, 012701, (2004).

[205] We thank prof. E. Tiemann for sharing with us his coupled-channel result $B_0 = 114.78$ G, $a_{bg} = 57.1\ a_0$, $\Delta B = 1.82$ G, based on the potential of Ref. [136].

[206] S. Jochim, *et al.*, Phys. Rev. Lett. 89, 273202 (2002); K.M. O'Hara, *et al.*, Phys. Rev. A **66**, 041401(R) (2002).

[207] T. Loftus, *et al.*, Phys. Rev. Lett. 88, 173201 (2002).

[208] M. E. Gehm. *Preparation of an Optically-Trapped Degenerate Fermi Gas of 6Li: Finding the Route to Degeneracy.* PhD thesis, Duke University, 2003.

[209] Michael Gehm. Properties of Lithium. http://www.phy.duke.edu/research/photon/qoptics/techdocs/pdf/PropertiesOfLi.pdf.

[210] Daniel Steck. Alkali D Line Data. http://steck.us/alkalidata/.

[211] Chemical properties of the elements. http://www.chemicalelements.com/elements/k.html.

[212] NIST Atomic Weigths and Isotopic Compositions. http://physics.nist.gov/PhysRefData/Compositions/index.html.

[213] A. Azman, A. Moljk, and J. Pahor. Electron Capture in Potassium 40. *Zeitschrift ffir Physik*, 208:234–237, 1968.

[214] G. Audi, A. H. Wapstra, and C. Thibault. The 2003 atomic mass evaluation: (II). Tables, graphs and references. *Nuclear Physics A*, 729(1):337 – 676, 2003. The 2003 NUBASE and Atomic Mass Evaluations.

[215] H. Wang, P. L. Gould, and W. C. Stwalley. Long-range interaction of the ^{39}K(4s)+^{39}K(4p) asymptote by photoassociative spectroscopy. I. The 0_g^- pure long-range state and the long-range potential constants. *The Journal of Chemical Physics*, 106(19):7899–7912, 1997.

[216] C. A. Regal, M. Greiner, and D. S. Jin. Observation of Resonance Condensation of Fermionic Atom Pairs. *Phys. Rev. Lett.*, 92(4):040403, Jan 2004.

[217] C. A. Regal and D. S. Jin. Measurement of Positive and Negative Scattering Lengths in a Fermi Gas of Atoms. *Phys. Rev. Lett.*, 90(23):230404, Jun 2003.

[218] C. Ticknor, C. A. Regal, D. S. Jin, and J. L. Bohn. Multiplet structure of Feshbach resonances in nonzero partial waves. *Phys. Rev. A*, 69(4):042712, Apr 2004.

[219] S. Aubin, S. Myrskog, M. H. T. Extavour, L. J. LeBlanc, D. McKay, A. Stummer, and J. H. Thywissen. Rapid sympathetic cooling to Fermi degeneracy on a chip. *Nat Phys*, 2(6):384–387, Jun 2006.

[220] T.G. Tiecke, M. Goosen, J.T.M. Walraven, and S. J. J. M. F. Kokkelmans. An asymptotic bound state model to predict Feshbach resonances. *arXiv:0908.xxx.*

Summary

This thesis describes the study of two atomic gases close to the absolute zero of temperature. At these ultralow temperatures the quantum nature of the atomic species is essential for an accurate description of the gases. Many systems which occur in nature, but which have not been understood completely, consist of strongly interacting fermions. These systems are often hard to describe theoretically or to study experimentally. Ultracold gases offer a large degree of tunability and this makes such systems suited to study quantummechanical phenomena in various regimes. In particular the interaction strength between the two particles can be tuned by means of Feshbach resonances, which allows to study the regime of strongly interacting fermions. For certain experimental conditions universal behavior can be achieved, i.e. details of the ^{6}Li-^{40}K interactions are irrelevant and the only relevant interaction parameter is the scattering length a.

The atomic species chosen for the work presented in this thesis are the two fermionic alkali metals ^{6}Li and ^{40}K. Such a mixture of fermions with unequal mass is suited to study a large variety of novel quantum phenomena. The mass imbalance allows to study mediated interactions, which, for the ^{6}Li/^{40}K system in particular, can be used to study long-lived p-wave trimers. Additionally, ^{6}Li^{40}K molecules in the groundstate of the singlet potential have a large dipole moment, which is essential to study dipolar bosonic quantum gases.

This thesis provides a description of the realization and study of a ^{6}Li/^{40}K mixture. In Chapter 1 an introduction of the field of ultracold gases is given from the point of view of the performed experiments, followed by the theoretical background of the presented work in Chapter 2. Chapter 3 gives a detailed description of the state-of-the-art machine which has been developed to study the ^{6}Li/^{40}K mixture in the strongly interacting regime. The machine incorporates a variety of novel techniques and experimental approaches to cool an ultracold gas to degeneracy. As a point of experimental innovation in the field of ultracold atoms a novel high-flux source for cold lithium has been developed. The source operates according to a two-dimensional magneto-optical trap (2D MOT) principle, is bright and monochromatic. Compared to the conventional source for cold lithium, the Zeeman slower, it yields a comparable flux, however, its design is strongly simplified. Additionally, due to transverse loading from the hot beam, the source beam contains only cold, capturable, atoms and has no hot background. Furthermore, the realization of a 2D MOT loaded from an effusive oven and the use of a light species as lithium demonstrates the wide applicability of the 2D MOT principle.

The ability to tune the interaction strength between ^{6}Li and ^{40}K is crucial to perform studies on such a system. This tunability can be realized by using Feshbach resonances. Such resonances occur due to resonant coupling with a lithium-potassium molecular bound state, and allow to change the interaction strength from zero to infinity being repulsive or attractive. The molecular bound state can have a different magnetic moment than the

free atoms, therefore resonances can occur as a function of the external magnetic fields. Knowledge about the magnetic field spectrum of these Feshbach resonances is essential to reach the strongly interacting regime and possibly study universal behavior of the ^{6}Li/^{40}K system. To describe the Feshbach resonances in the ^{6}Li/^{40}K system a novel theoretical model has been developed. In Chapter 5 the model is explained in detail. The model is intuitive and can be stepwise extended to become more complete. This allows the degree of complexity and the corresponding accuracy to be chosen to suit the atomic species being studied. Using two experimental input parameters the model can be used to predict the positions and widths of all Feshbach resonances in a certain system. This possibility has allowed us to select the optimal resonance to perform studies in the ^{6}Li/^{40}K system. Chapter 6 presents a precision measurement of the position and the width of this optimal resonance. This is performed by measuring the distillation of a weakly confined ^{6}Li sample by rethermalizing collisions with a bath of ^{40}K. The distillation rate is a measure of the elastic cross section and provides the observation of the asymmetric Fano-profile. To this profile a model is fitted, yielding both the position and the width of the resonance. The identification and characterization of the optimal Feshbach resonance in the ^{6}Li/^{40}K system paves the way to perform future studies on mass-imbalanced fermionic quantum gases in the universal regime.

Samenvatting

Dit proefschrift beschrijft de studie van een mengsel van twee ultrakoude gassen. Ultrakoud betekent dat de atomen waaruit het gas bestaat zo koud zijn dat de quantum mechanische aspecten van belang zijn om het gas te kunnen beschrijven. Volgens de quantummechanica is een deeltje (bijvoorbeeld een atoom) niet een puntdeeltje, maar een golf die beschreven wordt met een golffunctie. Alle deeltjes zijn onder te verdelen in twee soorten: bosonen en fermionen. Deze twee typen gedragen zich fundamenteel verschillend: twee identieke bosonen kunnen wél dicht bij elkaar komen en twee identieke fermionen níet. Veel systemen die in de natuur voorkomen, maar die nog niet goed begrepen zijn, blijken te bestaan uit fermionen die onderling sterke interactie hebben. Deze systemen zijn moeilijk te beschrijven en vaak experimenteel moeilijk te bestuderen.

Ultrakoude gassen zijn bijzondere systemen omdat de eigenschappen van het gas experimenteel heel goed gecontroleerd kunnen worden. Dit maakt ultrakoude gassen tot ideale systemen om quantummechanische fenomenen in gassen te bestuderen. In het bijzonder kan de interactiesterkte van twee atomen veranderd worden met behulp van zogeheten Feshbach resonanties. Rond een resonantie kan de interactiesterkte afgestemd worden van nul tot oneindig positief én negatief. Zo kunnen ultrakoude gassen van fermionische atomen met een geschikte Feshbach resonantie gebruikt worden om sterk wisselwerkende fermionen te bestuderen.

Het systeem dat beschreven wordt in dit proefschrift is een ultrakoud mengsel van de twee isotopen lithium-6 en kalium-40, beide fermionische atomen. Het gebruik van fermionische atomen met verschillende massa voegt een extra dimensie aan het systeem toe, die de studie van een nieuwe klasse quantum-mechanische systemen mogelijk maakt. Voordat het onderzoek voor dit proefschrift begon was dit systeem nog nooit gerealiseerd. Op dit moment zijn er wereldwijd drie experimenten operationeel die het ^{6}Li-^{40}K systeem bestuderen, waarvan de opstelling aan de Universiteit van Amsterdam er een is. In dit proefschrift wordt de experimentele realisatie van dit ultrakoude mengsel beschreven. Daarnaast wordt een uitgebreide studie van de Feshbach resonanties in het ^{6}Li-^{40}K systeem gegeven, zowel vanuit theoretisch als experimenteel perspectief.

Hoofdstuk 1 geeft een algemene introductie over ultrakoude gassen in de context van het proefschrift. Hoofdstuk 2 geeft de theoretische achtergrond van de concepten die gebruikt worden in het proefschrift. Hoofdstuk 3 beschrijft in detail de experimentele opstelling die gebouwd is om het ^{6}Li-^{40}K systeem te realiseren. Er wordt ingegaan op de verschillende experimentele methoden en technieken die gebruikt worden. Hierna volgen drie hoofdstukken die als publicaties verschenen zijn of zullen verschijnen. Hoofdstuk 4 geeft een uitgebreide karakterisatie van de lithium 2D MOT, een bron ontwikkeld voor dit onderzoek die een koude atomaire bundel genereert. Deze bundel heeft een hoge intensiteit en is erg schoon. In vergelijking met de conventionele bron die voor lithium gebruikt wordt

is de intensiteit hetzelfde, daarentegen is de bundel erg schoon doordat de koude van de hete atomen worden gescheiden. Hoofdstuk 5 geeft een beschrijving van het Asymptotic Bound-state Model. Dit theoretische model hebben we ontwikkeld om de Feshbach resonanties in een nieuw systeem als ^{6}Li-^{40}K te kunnen beschrijven. Dit model maakt het mogelijk om de eigenschappen van alle Feshbach resonanties te berekenen. Deze informatie kan gebruikt worden om de optimale resonantie van ons systeem te selecteren. Hoofdstuk 6 beschrijft tenslotte de experimentele karakterisatie van de optimale Feshbach resonantie. Het resultaat toont aan dat met deze resonantie het mogelijk is om vervolg experimenten te generaliseren naar algemene systemen van fermionen met verschillende massa.

Acknowledgments

In the time between entering an empty lab and finishing this thesis many, many people have contributed to the work presented here. I would like to take this opportunity to express my thanks to them.

First of all, I thank Jook for being my supervisor. The amount of interaction we had seems to have been growing exponentially towards the end and no matter how busy, your door was always open and there was always time to discuss physics, lab problems, university politics and of course to push unhealthy amounts of coffee. One thing you definitely taught me is to keep going until every single detail of a certain problem is understood. In particular while writing the lithium source paper I learned to keep on going to understand every aspect better and better. This way of doing physics, trying to understand everything in detail, ranging from glue to few body physics, is an extremely valuable lesson I learned, thank you!

Then I would like to thank Steve. The first period at the UvA was a really intense time in which you taught me all the neat tricks to become a real lab-physicist. In particular working towards a goal and not getting stuck in details is a valuable lesson I learned from you. It's a pity you left, but I definitely have good memories of seeing the first lithium 2D MOT and the many pizza's and mensa meals we have had. And of course you showed me how to keep up the humor when things went horribly wrong. Also later on this has proven to be quite valuable. Thank you for these lessons!

During the last years Servaas turned out to be a sort of supervisor as well. The very fruitful collaboration on the ABM was a lot of fun. I enjoyed working with you and you were always very motivating and stimulating to continue figuring out new aspects of the model. Most of our contact was by phone and email and every time we met there was always work to be done, but I definitely owe you a boat trip on the canals.

Then I would like to thank my fellow lab-mate Antje for the work we did together in the lab. We spent many hours together in K.10 and I was really impressed by your discipline on the projects you were working on. Finally, I would like to thank Sebastian for his contributions to the experiment, in particular the tapered amplifier and DDS's have proven to be reliable pieces of equipment.

I would like to thank Maikel for our collaboration on extending the ABM. The discussions we had to compare results and consider the possibilities and limitations of the model provided me with a lot of insight in the resonance physics. I enjoyed our collaboration very much, thank you!

Dan is er de technische staf van de UvA die ik wil bedanken. Tijdens m'n promotieonderzoek heb ik met alle werkplaatsen gewerkt en ik denk dat ik met vrijwel iedereen een keer individueel te maken heb gehad. Het wikkelen van de Feshbach spoel in de zomer van 2008, waarbij heel veel mensen betrokken waren en ik veel haast had, was een erg bijzon-

dere ervaring voor mij. Ik wil de hele technische staf bedanken voor alle bijdragen, zonder jullie was dit proefschrift er niet geweest, bedankt daarvoor! Drie mensen wil ik expliciet bedanken: Joost, Bert en Johan omdat jullie extra veel voor ons gedaan hebben en altijd bereid waren te helpen, de UvA bureaucratie kwam dan later wel. Bedankt!

I would like to thank the members of the Quantum Gases group at the UvA. Although it is never enough, I enjoyed the interaction we had at the Quantum Collective meetings, the lunch meetings and occasionally at Kriterion. Klaasjan, Robert, Ben, Phil, Carolijn, René, Jan-Joris, Shannon, Thomas, Atreju, Vlad, Caspar, Rutger, Richard for always being able to show a nice YouTube movie, Thomas for the audio-visual entertainment and of course the many games of tabletennis we played, Tom for sharing his beautiful views on science, the economic crisis and the JSF, which provided a nice form of entertainment, but also for all the useful (and less useful) discussions on physics we had. I want to thank Aaldert for the many discussions we had, at many occasions and many different places on getting our experiments up and running. I learned a lot from your experiences with the 1D-BEC setup, and it definitely accelerated the progress of my research. And finally Paul for keeping his patience while I was systematically emptying his optics drawers and of course for a memorial St. Patrick's day. I would like to thank the theory group of Gora. I had many nice discussions with Micha, Pjotr and Carlos. And I would like to thank Dima in particular for the useful tips of how to deal with supervisors and of course, in between all the chatting, we had very nice discussions on the physics of what I was doing in the basement. Thank you all!

Finally, I would like to thank the collaborators I have had. When we were trying to understand the Feshbach resonance structure as measured by the group of Florian Schreck and Rudi Grimm I found it very special how we became collaborators although we started as 'competitors'. Working with Paul Julienne, Eite Tiesinga, Florian, Rudi and the rest of the FeLiKx team were very exciting times for me. In particular, when the collaborative effort reached its peak in the summer of 2007, by concluding the resonance assignment. I think this is really what science should be like, thank you!

En natuurlijk zijn er veel mensen die bijgedragen hebben aan dit proefschrift op een ander niveau. In het bijzonder Henk en Marieke, jullie hebben me altijd gesteund als ik mijn frustraties uitte en waren altijd in staat de situatie te relativeren en me weer goede moed te geven. Ook bleken veel dingen die ik in mijn jeugd van jullie geleerd heb uitermate nuttig te zijn voor een promotieonderzoek in de atoomfysica. Bedankt voor alles! Eva and Barry, during the course of my thesis you have moved quite a few times, but my visits to you were always of great joy, with great food, nice hikes and a lot of fun. These trips have been quite special to me and seem to become addictive. See you soon again! *En Liza, jij hebt wel het vervelendste van een promotieonderzoek meegemaakt al voordat je zelf aan de beurt was. De nachten dat ik je wakker hield en de avonden dat ik moedeloos thuis kwam, waren aan het einde meer regelmaat dan uitzondering. Altijd wist je me weer goede moed te geven, niet alleen door te laten zien dat doorslapen best mogelijk was, maar meer nog door de ontelbare peptalks en het blinde vertrouwen dat je had in dat het zou lukken. En je had gelijk. Dank je!*

Dan wil ik afsluiten met het bedanken van iedereen die (onbewust) afleiding van de wereld van het lab wist te verzorgen. Dit varieerde van het traditionele biertje met kipsaté, ijs eten in de Pijp, schaatsen over de Gouwzee, kiten, catten en met name cappuccino's drinken op Zandvoort, vroege uren in obscure clubs, op ski's door de Alpen, aan een touw door de rotsen of op een bouldermat in Sloterdijk en degenen die het op een gegeven moment wel

mooi geweest vonden met het antwoord: "ik ben druk". Jullie waren allemaal essentieel voor het slagen van dit proefschrift.

List of Publications

- I. Shvarchuck, Ch. Buggle, D.S. Petrov, K. Dieckmann, M. Zielonkovski, M. Kemmann, T. Tiecke, W. von Klitzing, G.V. Shlyapnikov, and J.T.M. Walraven, *Bose-Einstein condensation into non-equilibrium states studied by condensate focusing*, Physical Review Letters **89** (2002) 270404

- T.G. Tiecke, M. Kemmann, Ch. Buggle, I. Schvarchuck, W. von Klitzing and J.T.M. Walraven, *Bose-Einstein condensation in a magnetic double-well potential*, Journal of optics B **5** (2003) S119-S123

- I. Shvarchuck, Ch. Buggle, D.S. Petrov, M. Kemmann, T.G. Tiecke, W. Von Klitzing, G.V. Shlyapnikov and J.T.M. Walraven, *Focusing of Bose-Einstein condensates in free flight*, In: Interactions in ultracold gases: from atoms to molecules. - Weinheim: Wiley, 2003. - pp 415-420

- E. Wille, F. M. Spiegelhalder, G. Kerner, D. Naik, A. Trenkwalder, G. Hendl, F.Schreck, R. Grimm, T. G. Tiecke, J. T. M. Walraven, S. J. J. M. F. Kokkelmans, E. Tiesinga and P. Julienne, *Exploring an Ultracold Fermi-Fermi Mixture: Interspecies Feshbach Resonances and Scattering Properties of ^6Li and ^{40}K*, Physical Review Letters **100** 053201 (2008) [17]

- T. G. Tiecke, S. D. Gensemer, A. Ludewig and J. T. M. Walraven, *High-flux two-dimensional magneto-optical-trap source for cold lithium atoms*, Physical Review A **80** 013409 (2009) [138]

- J. Levinsen, T. G. Tiecke, J. T. M. Walraven and D. S. Petrov, *Atom-dimer scattering and long-lived trimers in fermionic mixtures*, Physical Review Letters **103** 153202 (2009) [30]

- T. G. Tiecke, M. R. Goosen, A. Ludewig, S. D. Gensemer, S. Kraft, S. J. M. M. F. Kokkelmans and J. T. M. Walraven, *Search for a broad Feshbach resonance in the ^6Li-^{40}K mixture*, submitted to Physical Review Letters (arXiv:0908.2071) [18]

- T. G. Tiecke, M. Goosen, J. Walraven and S. J. J. M. F. Kokkelmans, *An asymptotic bound state model to predict Feshbach resonances*, in preparation for Physical Review A [220]